University of Oxford

St Catherine's College



# Muon Reconstruction Performance and Constraints on Off-shell Higgs Boson Production and the Higgs Boson Total Width with the ATLAS Detector
# and
# Charm Production at Low Transverse Momentum with the CDF Detector

*Supervisor*
Prof. Ian Peter Shipsey

*Candidate*
Luigi Marchese

Thesis submitted in partial fulfillment of the requirements for the degree of Doctor of Philosophy at the University of Oxford

Department of Physics
Trinity Term 2019

# Muon Reconstruction Performance and Constraints on Off-shell Higgs Boson Production and the Higgs Boson Total Width with the ATLAS Detector and Charm Production at Low Transverse Momentum with the CDF Detector

Luigi Marchese

St Catherine's College, University of Oxford

Trinity Term 2019

# Abstract

The latest constraints on the signal strength of the off-shell Higgs boson production and the Higgs boson total width in the $ZZ \to \ell\ell\nu\nu$ final state are presented. The Higgs boson is studied in decays to a pair of on-shell $Z$ bosons where one of the two $Z$ bosons decays to a pair of leptons - $\ell$ stands for either an electron or a muon - and the other to a pair of neutrinos. The analysis is based on proton-proton collision data collected by the ATLAS detector in 2015 and 2016 at a centre-of-mass energy of 13 TeV at the Large Hadron Collider (LHC), corresponding to a total integrated luminosity of 36.1 fb$^{-1}$. An observed (expected) upper limit on the off-shell Higgs signal strength, defined as the event yield normalised to the Standard Model prediction, of 5.3 (4.4) is obtained at 95% confidence level (CL) in the $ZZ \to \ell\ell\nu\nu$ channel. After the combination with similar results from the $ZZ \to 4\ell$ channel the reported observed (expected) limit is 3.8 (3.4) at 95% CL. Assuming the ratio of the Higgs boson couplings to the Standard Model predictions is independent of the

momentum transfer of the Higgs production mechanism considered in the analysis, a combination with the on-shell signal-strength measurements yields an observed (expected) 95% CL upper limit on the Higgs boson total width of 14.4 (15.2) MeV.

The ATLAS simulation includes the best knowledge of the detector geometry, material distribution, and physics modeling of the muon interaction with the material of the ATLAS sub-detectors. However, this is not enough to reproduce the muon momentum scale(resolution) of data at the needed level of permille(percent) precision for important measurements, such as the Higgs boson mass. Additional corrections are applied to achieve such data/MC agreement. They are based on $J/\psi \to \mu\mu$ and $Z \to \mu\mu$ decays. A new independent validation of these corrections is possible using the $\Upsilon \to \mu\mu$ resonance. At ATLAS this is challenging as the momentum resolution is not sufficient to fully resolve the $\Upsilon(1S)$, $\Upsilon(2S)$ and $\Upsilon(3S)$ resonances. Results are based on proton-proton collision data collected by the ATLAS detector in 2015 and 2016 at a centre-of-mass-energy of 13 TeV at the LHC, corresponding to a total integrated luminosity of 36.5 fb$^{-1}$. They demonstrate that the $\Upsilon$ resonance is a reliable validation channel. The corrected MC is in very good agreement with data, with the momentum scale within the scale systematic uncertainty of 0.05% in the barrel region and up to 0.25% in the forward region, $|\eta| \sim 2.5$. The muon momentum resolution is measured to be of 1.7% and 2.9% in the centre of the detector and in the endcaps, respectively. The observed level of agreement demonstrates that the ATLAS simulation provides a very accurate description of the muon momentum scale and resolution in all $\eta$ regions, over a wide $p_T$ range.

A measurement of the $D^+$-meson production cross section as a function of the transverse momentum is reported. Results are based on the full dataset of proton-antiproton collisions collected by the CDF detector at 1.96 TeV centre-of-mass energy at the Tevatron Run II and corresponding to 10 fb$^{-1}$ of integrated luminosity. Fully reconstructed $D^+ \to K^-\pi^+\pi^+$ decays in the central rapidity region $|y| < 1$ with transverse momentum down to 1.5 GeV are used. This is a range previously unexplored in $p\bar{p}$ collisions, close to a kinematic range where it is challenging to make predictions in perturbative QCD. Inelastic $p\bar{p}$-scattering events are selected online using minimally biasing requirements followed by an optimized offline selection. The $K^-\pi^+\pi^+$ mass distribution is used to identify the $D^+$ signal, and the $D^+$ transverse

impact-parameter distribution is used to separate prompt production, occurring directly in the hard-scattering process, from secondary production from $b$-hadron decays. The final number of prompt $D^+$ candidates is 2950 corresponding to a total cross section $\sigma(D^+, 1.5 < p_T < 14.5 \text{ GeV}, |y| < 1) = 71.9 \pm 6.8(\text{stat}) \pm 9.3(\text{syst}) \ \mu\text{b}$. While the measured cross sections are consistent with theoretical estimates in each $p_T$ bin, the shape of the observed $p_T$ spectrum is softer than the expectation from QCD. This is the first time the $D^+$-meson production cross section in $p\bar{p}$ collisions has been measured at such low transverse momenta. It provides important input to improve future QCD predictions. In addition, in searches for astrophysical neutrinos, knowledge of charm production cross-sections may improve estimations of background rates from neutrinos produced in decays of charm hadrons from cosmic-ray interactions with atmospheric nuclei.

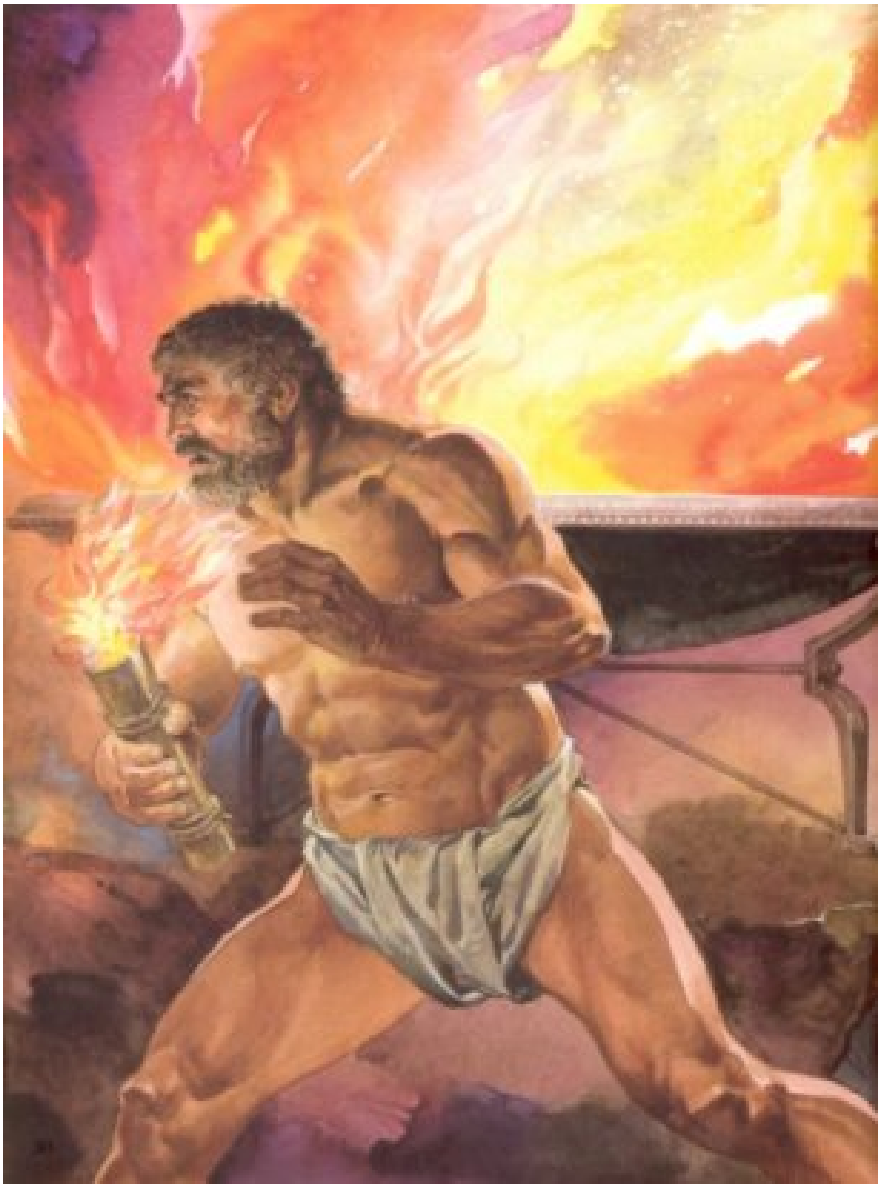

*"Hèphaistos: For thine own pride, even flashing fire, source of all arts, he hath purloined and bestowed upon mortal creatures."* Aischỳlos, Prometheus Bound

Only a pure thirst for knowledge
can make people and memories alive.
In loving memory of Luisa

# Acknowledgements

This thesis summarizes my 4-year research experience as a PDhil student at the university of Oxford and at CERN. This period of time has definitely shaped my personality as physicist and as a person. It has also changed my way of looking, and thinking about, the universe.

The list of people to thank is very long. I will for sure miss someone. Apologies for that.

First and foremost, I would like to deeply thank my supervisor, Prof. Ian Shispey. From the first time we met at a conference in 2015 and we briefly talked of physics I knew he was the perfect supervisor for me. He has been a fantastic physicist to discuss several topics with, but also a great person to work with. Thanks to him I have also learned, in addition to physics, several management skills which are needed in our field. I didn't think they were so relevant before I started my DPhil. He gave me a large degree of freedom as his student and I always enjoyed my chats with him, from physics to several other topics. I truly consider him as an academic father and a source of incredible inspiration. He will be no doubt my role model as a physicist in the years to come. I am deeply proud of having been is "first Oxford student", as he likes to introduce me when talking with colleagues.

I would like to thank all the Oxford HEP group. I have met several colleagues and friends during my year in Oxford and during my long stay at CERN. A big thanks to the Bortoletto - Shipsey team at the university of Oxford. A big thanks to Prof. Daniela Bortoletto for reviewing several conference talks and her guidance on several occasions. Many people of this group are now friends I am in touch with, such as Mariyan Petrov and Luigi Vigani. I am sure we will be friends also after the end of our DPhil. I will remember several coffee breaks and chats with Maria Giovanna Foti, Gabriel Gallardo, Santiago Paredes, Elisabeth Schopf and Kathrin Becker at building 104 at CERN. Also, a special thank to Mike Nelson, Jesse Liu and Gabija

Zemaityte. We started together this wonderful DPhil adventure sharing funny and challenging moments and some home-made limoncello at some conferences. I am also truly thankful to Miha Zgubic for the nice chats we had in Oxford and at CERN and for the massive help during the final submission of this thesis.

I cannot forget the ATLAS Muon Combined Performance (MCP) and HZZ family at CERN. I spent about 3 years with them. In as small a group as MCP it is easy to know more or less each member of the group. I am particularly thankful to Gaetano Barone, Giacomo Artoni, Federico Sforza and Stefano Zambito - the Italian MCP subgroup - for their valuable support and help which allowed me to finalize the $\Upsilon$ Public Note. A special thank to the off-shell team, which, in the most crucial (and final) year, was composed of just three people: Monica Trovatelli, Lailin Xu (the two contact editors) and me. It was a real pleasure to work with both of them. I worked mostly with Lailin. His help was significant in several difficult moments during the publication of the off-shell paper. Always available, I very much enjoyed discussing with him some coding issues and physics ideas. I also want to thank the Higgs conveners Fabio Cerruti and Kerstin Tackmann and the HZZ sub-conveners R.D. Schaffer and (again) Giacomo Artoni for their helpful support in getting this paper published.

A big thanks also to the ATLAS Early Career Scientist Board, which I joined last year. Working with Ana Peixoto, Dimitrii Krasnopevtsev, Lesya Horyn, Stefan Richter, Xingguo Li and Reina Coromoto Camacho has been educational since this is the first board I am a member of. I enjoyed working in an international team with so many different personalities and nationalities. I hope I have learned something from each of them. Also, I am really thankful to the several shift crews I met in the ATLAS Control Room. We shared so many afternoon and nights taking data that will allow us to discover new physics and consolidate the Standard Model.

I would like to thank prof. Roxanne Guenette and Mrs Sue Geddes for all their help with the Oxford Summer Student Program, which is now a well-established international program. I am particularly thankful to Sue also for her support for conferences, organization of events etc. Sue is really a 'fundamental particle' for all the activities organized in the Oxford Particle Physics department.

I am also thankful to the whole Italian young@CERN community, especially to Nello Bruscino, Andrea Sciandra, Francesco Cirotto and Marco Arzeo for some needed breaks in several burnout moments. There is nothing you cannot get through

if you have some good Italian pizza, wine and friends!

I cannot conclude this section without thanking my family. This is the third academic degree I have been awarded. None of this would have been possible without the inexhaustible moral and financial support of my parents and sisters throughout the past years. We now live a thousand kilometers away, but I am always with them. I wish in future I will be able to visit them more often. This DPhil came with an additional value since my parents finally got over their fear of flight and visited me at CERN. I am now looking forward to seeing them in Oxford for the graduation ceremony!

# Contents

# List of Figures

# List of Tables

# Introduction

In this thesis I present the results produced during my DPhil in particle physics at the University of Oxford with both the ATLAS and CDF collaborations on Higgs, muon and charm physics, respectively. All the measurements presented have been produced in a collaborative effort with other ATLAS and CDF members and led to three publications during my DPhil.

After more than forty years of Higgs hunting, on the $4^{th}$ of July 2012 the discovery of a new boson - consistent with the expected Higgs boson in the Standard Model (SM) of particle physics - was reported by the ATLAS and CMS collaborations. P. Higgs and F. Englert were awarded the Nobel Prize in Physics in 2013. The Higgs boson discovery is a milestone in the quest to understand the SM electroweak symmetry breaking mechanism. The observation of the Higgs boson is direct evidence of the existence of the Higgs field and provides one of the most powerful tests of the SM, the prevailing theory of particle physics. The SM is a theory able to describe all the known elementary particles and their interactions.

For the first time we have been able to recreate the conditions present a picosecond after the Big Bang 100 meters underground, in the Large Hadron Collider (LHC) particle accelerator of CERN. The ATLAS and CMS experiments have confirmed that the observed particle, with a mass of 125 GeV, is a SM Higgs boson since its spin, parity and couplings are fully consistent with the SM expectations. However, some Higgs boson properties are still to be discovered and studied.

The Higgs boson is not a stable particle, it quickly decays. The Higgs boson total width is a fundamental measurement given its global information on the Higgs boson decays. By measuring the width one can check how many different ways the Higgs boson is decaying. Even if it decays to particles not visible in the LHC detectors, these decays will influence the width, making it larger than the expected value in the SM because the Higgs boson will decay faster. Several theories beyond

the SM (BSM) predict the existence of new heavier Higgs bosons - which can change the SM Higgs boson couplings in the high-mass regime - or new exotic decays for the SM Higgs boson, such as the decay to dark matter and/or other exotic particles. Even if these decays are not visible, by measuring the Higgs boson total width BSM models could be indirectly tested. Therefore, the measurement of the Higgs boson width is one of the most interesting physics results to determine its nature and to both test the SM and search for new physics at the LHC.

A direct width measurement at the resonance peak is limited by experimental resolution - which is about 1 GeV - and is only sensitive to values larger than the SM expectation of 4 MeV. Recent studies have shown that the high-mass off-peak regions beyond $2m_V$ ($V = Z, W$), well above the measured Higgs boson mass of about 125 GeV, in the $H^* \to ZZ$ and $H^* \to WW$ channels are sensitive to Higgs boson production through off-shell and background interference effects. This presents a novel way of characterizing the properties of the Higgs boson in terms of the off-shell event yields, normalised to the SM prediction (referred to as signal strength $\mu_{off-shell}$), and the associated off-shell Higgs boson couplings. Such studies also provide sensitivity to new BSM physics that alters the interactions between the Higgs boson and other fundamental particles in the high-mass region. In addition, the off-shell production method can be used to set an indirect limit on the Higgs boson total width, based on the relative measurement of the off-shell to the on-shell production cross section. However, Higgs couplings to particles in the off-shell and on-shell region need to be assumed the same in order to extract a constraint on the Higgs boson total width.

The ATLAS part of this thesis summarizes the status of the Higgs width measurement at the ATLAS experiment focusing on the $H^* \to ZZ$ decays mode, where one on-shell $Z$ boson decays to a pair of leptons $Z \to \ell\ell$ and the other decays to a neutrino pair $Z \to \nu\bar{\nu}$. First, the measurement of the off-shell signal strength is presented and later - after a combination with the on-shell signal strength - a measurement of the Higgs boson total width is reported. My four-year contribution on muon reconstruction performance is also presented. All the ATLAS results in this thesis are obtained from the analysis of $\sqrt{s} = 13$ TeV $pp$ collision events corresponding to an integrated luminosity of 36.1 fb$^{-1}$ (36.5 fb$^{-1}$ for the muon performance results) collected by the ATLAS detector in 2015 and in 2016.

The SM also provides a powerful description of the strong interaction of the

coloured quarks and gluons via a quantum field theory known as Quantum chromodynamics (QCD). However, QCD cannot predict the behaviour of the strong interactions at low 4-momentum transfer because in this kinematic region the strong coupling constant, $\alpha_s$, is of order unity. Thus, a perturbative expansion is no longer permitted and the colour confinement behaviour is not yet understood. Phenomenological models are only able to partially describe the behaviour of the physical observables. Experimental results are then crucial input to guide theory. Measurements of production cross-sections of hadrons containing bottom or charm quarks in hadron collisions offer essential information to test and refine phenomenological models of the strong interactions at small four-momentum transfer, where perturbative expansions of QCD are challenging.

The CDF part of this thesis reports on the measurement of the $D^+$-meson production cross section in the low transverse momentum region, down to 1.5 GeV. The data were collected by the CDF II detector at the Tevatron $p\bar{p}$ collider of the Fermi National Accelerator Laboratory (FERMILAB) at $\sqrt{s}$ = 1.96 TeV corresponding to an integrated luminosity of 10 fb$^{-1}$.

This thesis is structured as follows:

**Chapter 1** : I describe the theoretical motivation for both measurements within and beyond the Standard Model. I remark on the uniqueness of these two measurements.

**Chapter 2** : I briefly describe the CERN $pp$ Large Hadron Collider and the ATLAS detector.

**Chapter 3** : I describe the reconstruction of physics objects (such as electrons, muons, jets, missing transverse momentum) at ATLAS. I focus more on muons since in this chapter I also introduce the work I performed with the ATLAS Muon Combined Performance Group (MCP). This was initially my qualification task to become an author of the ATLAS Collaboration. After completion of my task I stayed in the group contributing to new studies on the $\Upsilon \to \mu\mu$ decay. I was involved in several Public Plots needed for International Conferences, such as ichep2016 and Moriond2017. In May 2019 I was Contact Editor and Analysis Contact for a Public Note on such activities,

which was published during the fourth year of my DPhil - ATL-PHYS-PUB-2019-018. I finally presented these results in a summary talk on behalf of ATLAS and CMS at LHCP2019 with a talk titled "Lepton and photon reconstruction and identification performance in ATLAS and CMS".

**Chapter 4** : I describe the methodology of the ATLAS analysis for the measurement of the off-shell signal strength for the Higgs boson production and later for the measurement of the Higgs boson total width. I focus more on the results in the $\ell\ell\nu\nu$ channel since this is the subgroup of the $HZZ$ group I joined at CERN. Details on the signal selection, optimization, background estimation and systematic uncertainties are given.

**Chapter 5** : I present and interpret the results of the ATLAS analysis in the $\ell\ell\nu\nu$ channel and their combination with the $4\ell$ results since I was responsible for the combination to provide the final constraints. An interpretation of these results in the context of effective field theories is also included. Also, future improvements in the analysis strategy and the expected sensitivity with the full ATLAS Run 2 dataset are discussed. I was one of the three main ATLAS members working on this analysis in a group of about 40 people. I contributed to the data analysis - MC validation, theoretical corrections, background estimation, final limits and systematic uncertainties - editorial production and review of the analysis. These results were published at the end of my third year of DPhil - Phys. Lett. **B 786** (2018) 223 - and I presented them in a summary talk on behalf of the ATLAS and CMS collaborations at HiggsHunting2018 with a talk titled "Higgs width at LHC and ILC" and on behalf of the ATLAS collaboration at LISHEP2018 with a talk titled "Measurement of cross sections and properties of the Higgs boson using the ATLAS detector". I also gave more than ten seminars on the topic in Europe and in the USA (Heidelberg, Zurich, Princeton, Harvard, Scuola Normale di Pisa, FERMILAB, SLAC, Imperial College, CALTECH etc.).

***Chapter 6*** : I briefly describe the FERMILAB $p\bar{p}$ Tevatron collider and the CDF II detector. I later focus on the methodology of the CDF analysis to measure the $D^+$-meson production cross section at low-$p_T$ providing details on

the signal selection, optimization, background estimation and systematic uncertainties. Finally, results and comparisons with the theoretical model and the previous high-$p_T$ CDF measurement are reported. I performed all the measurement from the first data selection to the final publications. These results were published at the end of my second year of DPhil - Phys. Rev. **D 95**, 092006 - and I presented them in a summary talk on behalf of the CDF collaboration at CHARM2016, QCD16 and ICHEP2016 with a talk titled "MEASUREMENT OF LOW-$p_T$ $D^+$-MESON PRODUCTION CROSS SECTION AT CDF II". At CHARM2016 I also presented a poster on such results and I was awarded the "Best Poster" prize. In addition, I gave three seminars on the topic in Europe and in the USA (University of Siena, Bologna and Harvard).

***Chapter 7*** : I conclude with a brief discussion of the significance of the results in this thesis.

# Chapter 1

# Theoretical Introduction

*In this chapter I introduce both the measurements presented in this thesis focusing on their importance and uniqueness. First, I briefly illustrate the Standard Model which is the reference model for all the measurements reported in this thesis. Later, I focus on Higgs physics and on Quantum Chromodynamics (QCD) - the quantum field theory, which describes the strong interaction. A short section about physics beyond the Standard Model is also included. Finally, I discuss the two measurements and their motivation.*

## 1.1 Introduction

Research in high energy physics is primarily aimed at understanding how the Universe works at the most fundamental level. This is achieved by discovering and studying elementary particles and their interactions at energies not seen since the Big Bang. These energies are reachable by using accelerators. Given the cost of such machines, high energy physics is an international endeavor. Physicists work at laboratories all over the world, such as CERN and FERMILAB in Europe and in the USA, respectively.

The Standard Model (SM) is the best model available to describe fundamental particles and their interactions at the energy scales experimentally achievable at the present. It is the result of experimental measurements and theoretical insights over a period of more than one century. Despite being enormously successful in describing a large number of phenomena, some are still not explainable in the context of the SM

formalism. This has triggered a new set of models, known in literature as Beyond the SM (BSM) models.

This Chapter is organized as follows: Sec. 1.2 briefly describes the SM and its formalism, including electro-weak symmetry breaking and mass generation in the SM in Sec. 1.2.2 and the quantum field theory for strong interactions in Sec. 1.2.3. BSM models of relevance for the contents of this thesis are presented in Sec. 1.3. Finally, the motivation for the two measurements in Higgs and charm physics are described in Sec. 1.4 and Sec. 1.5, respectively.

## 1.2 The Standard Model of Particle Physics

The SM is a quantum field theory (QFT) describing all elementary particles and three of the fundamental interactions known today: weak, electromagnetic (EM) and strong [1] [2]. The first two forces are unified into the electroweak interaction, confirmed in 1983 by the discovery of the $W$ and $Z$ particles at the CERN $p\bar{p}$ collider [3–5]. And most importantly, the SM provides a unified description of the electroweak and strong interactions based on the local gauge symmetries of the unitary group $G_{SM} = SU(3)_C \times SU(2)_L \times U(1)_Y$[1]. The symmetries of the $SU(3)_C$ group - where $C$ is the colour charge - describe the strong interaction and those of the $SU(2)_L \times U(1)_Y$ group - where $L$ refers to the weak isospin coupling to left-handed particles only and left-handed particle refers to the chirality eigenstate meaning that the particle transforms in a left-handed representation of the Poincaré group; $Y$ finally refers to the weak hypercharge, a single-charge operator relating the electric charge and the third component of weak isospin - describe the electroweak interaction. Gravity is still not included in the model, but many efforts move in this direction.

Matter and forces are described as a physical manifestation of quantum fields with point-like particles representing the quanta of these fields. Several properties distinguish one particle from another, such as charge, spin, mass. Fundamental interactions are the immediate consequences of local gauge invariance. The SM gauge invariance of $SU(2)_L \times U(1)_Y$ implies massless weak bosons and fermions since massive fields would make the theory non-renormalizable. This is in total contradiction

[1] $U(N)$ refers to a group of $N \times N$ unitary matrices where $SU(N)$ is a subset with unitary determinant.

with the reality where weak bosons ($W$ and $Z$) and almost all fermions are experimentally observed to be massive. The most widely accepted solution to this problem is the Higgs mechanism [6] [7] - a spontaneously symmetry breaking process of the EW group responsible for generating the masses of the weak gauge bosons and fermions. This mechanism breaks the $SU(2)_L \times U(1)_Y$ symmetry resulting in the subgroup $U(1)_{QED}$, which describes the EM force.

*Quantum Electrodynamics (QED)* and *Quantum Chromodynamics (QCD)* are the names of the QFTs which describe the EM and strong interaction, respectively.

Over time and through many experiments, the SM has become established as a well-tested physics theory [8]. The recent observation of the Higgs boson [9–11] has strengthened even more the reliability of the SM. Sometimes it is regarded as the "theory of almost everything" because of its completeness in explaining a huge variety of phenomena and processes.

### 1.2.1 Elementary Particles

The SM includes different types of elementary particles. In this model the elementary particles appear as irreducible representation of the $G_{SM}$ symmetry group. Matter is composed by spin-1/2 particles which follow the Fermi-Dirac statistics and, therefore, they are called *fermions*. SM Interactions are transmitted via spin-1 particles called *bosons* since they obey the Bose-Einstein statistics.

Fermions are classified into two types: *leptons* and *quarks* depending on how they interact. There are six quarks: up ($u$), charm ($c$), top ($t$), down ($d$), strange ($s$), and bottom ($b$). Similarly, six leptons have been classified: electron ($e$), electron neutrino ($\nu_e$), muon ($\mu$), muon neutrino ($\nu_\mu$), tau ($\tau$) and tau neutrino ($\nu_\tau$). Both quarks and leptons are arranged in three family generations in increasing mass order. Quarks carry a fractional electric charge, weak isospin and an additional charge called colour. They interact with other fermions via the EM, weak and strong interaction. On the contrary, leptons do not carry colour charge and, therefore, they cannot interact via the strong interaction. Neutrinos do not carry electric charge either, thus, their interactions with other fermions are via the weak interaction only. In addition, there are corresponding antiparticles for each fermion.

Bosons mediate the strong, weak and EM interactions. The generators of the symmetry group $G_{SM}$ are the mediators of the fundamental interactions described

in the SM. Depending on the interaction there are different mediators: photons ($\gamma$) mediate the EM interaction between electrically charged particles. Photons are massless and electrically neural. The weak bosons ($W^{\pm}$ and $Z^0$) mediate the weak interaction between quarks and leptons of different flavours. The $W$ bosons carry electric charge, while the $Z$ boson is electrically neutral. They are all massive particles. These weak bosons are generally grouped together with photons as gauge bosons of the electroweak interaction. Finally, eight gluons ($g$) mediate the strong interaction between quarks and gluons themselves. They are massless and carry colour charge. As better described in Sec. 1.2.3, quarks and gluons are confined in hadrons, such as neutrons and protons, because of asymptotic freedom. Figure 1.1 summarizes all the elementary particles in the SM.

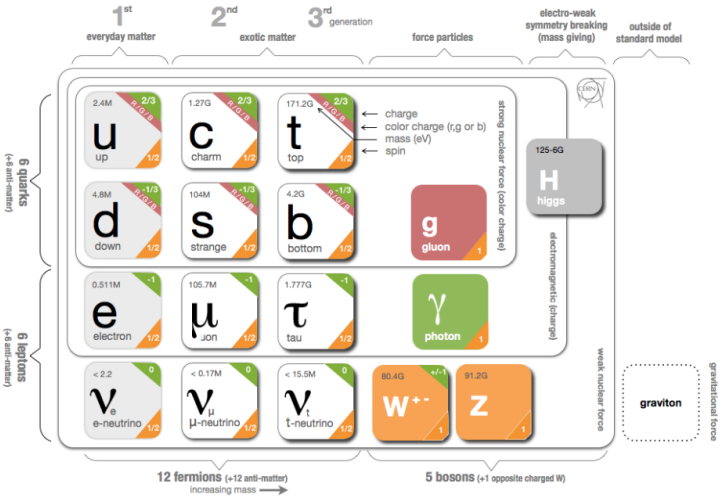


Figure 1.1: Elementary particles in the SM. Figure from [12].

### 1.2.2 Electro-weak Symmetry Breaking

In mechanics, the equations of motion follow from the application of the variational *principle of least action* to the SM Lagrangian density[2] $\delta S = 0$ where $S = \int \mathcal{L} dx$ and $\mathcal{L}$ is the SM Lagrangian and $x$ the space-time coordinates, $x^{\mu} = (x, y, z, t)$. SM

[2]The Lagrangian density of a system is a function of its fields and its derivatives. It is also known as the Lagrangian.

interactions are the result of the invariance of the SM Lagrangian under appropriate transformations [13], the *local gauge transformations*, which imply a different behavior of the system for different space-time points. In fact, such an invariance requires additional terms in the Lagrangian, which are interpreted as interactions between fundamental constituents mediated by quanta of gauged fields. The gauge invariance of $SU(2)_L \times U(1)_Y$ implies massless unphysical weak bosons - called Goldstone bosons [14] - and fermions since massive fields would make the theory non-renormalizable violating the gauge invariance. This is in total contradiction with reality where weak bosons ($W$ and $Z$) and all fermions are experimentally observed to be massive. The most accepted solution to this problem is the *Englert-Brout-Higgs (EBH) mechanism* [6] [7]. This solution arises from some considerations on the energy of the lowest vacuum state [15, 16]. For a non-zero vacuum expectation value (VEV), the symmetry of the theory can be *spontaneously broken* completing the Lagrangian with the needed mass terms and no violation of the gauge invariance. In the SM, spontaneous symmetry breaking of the $SU(2)_L \times U(1)_Y$ gauge symmetry successfully generates mass terms for the gauge bosons. However, a new field - the *Higgs field* - needs to be introduced. The EBH mechanism proves how the massless unphysical Goldstone bosons can be completely removed from the theory with an appropriate choice of gauge.

For the simple rotational $U(1)$ symmetry, this mechanism predicts the existence of a scalar field, $\Phi$, whose corresponding Lagrangian density has the following form:

$$\mathcal{L}_\Phi = (\partial_\mu \Phi)^\dagger (\partial^\mu \Phi) - V(\Phi) \tag{1.1}$$

where $\Phi$ is a complex scalar doublet, $\Phi(x) = (\Phi_1(x) + i\Phi_2(x))/\sqrt{2}$ made from two real fields, $\Phi_1$ and $\Phi_2$ and $V(\Phi)$ is the simplest potential field which gives rise to mass terms:

$$V(\Phi) = \mu^2 \Phi^\dagger \Phi + \lambda (\Phi^\dagger \Phi)^2. \tag{1.2}$$

where the parameter $\mu$ stands for the field mass term and $\lambda$ is the self-coupling term. If $\lambda > 0$ and $\mu^2 < 0$ the potential has a minimum for $\Phi^\dagger \Phi = -\mu^2/2\lambda \equiv v^2/2$ where $v$ is the non-zero VEV of the field $\Phi$. Under this assumption, the field $\Phi$ has a non-zero VEV. Fig. 1.2 shows the shape of the potential. The potential is in a meta-stable state on top and will move to a stable ground state. The transition to the stable state gives rise to the Higgs field and consequently the the Higgs field

mass couplings. However, the transition can occur at any point in a set of ground states. There is a symmetry since the ground state of minimum energy is degenerate. The electroweak symmetry is spontaneously broken choosing one of the degenerate states of minimum energy. According to the Goldstone theorem, fields that acquire a VEV will have an associated massless boson which will disappear, transformed into the longitudinal component of a massive gauge boson.

Formally, one expands the field $\Phi$ around the true minimum of the theory obtaining:

$$\Phi(x) = \frac{1}{\sqrt{2}} e^{i\theta(x)/v}(v + H(x)) \tag{1.3}$$

where $H(x)$ is the Higgs field and $\theta(x)$ is the non-physical Goldstone boson. Since the gauge is arbitrary, one can choose the physical, *unitary gauge* $\theta(x) = 0$. Thus, in this representation of $\Phi$ the Goldstone boson vanishes:

$$\Phi(x) \to \Phi'(x) = \frac{1}{\sqrt{2}}(v + H(x)) \tag{1.4}$$

and the gauge boson acquires a term which can be identified as a mass term. In this gauge, the Lagrangian $\mathcal{L}$ takes the form

$$\mathcal{L} = \left[\frac{1}{2}(\partial_\mu H)^2 - \lambda v^2 H^2\right] + \frac{1}{2} q^2 v^2 A_\mu A^\mu + \frac{1}{2} q^2 A_\mu A^\mu H^2 + \tag{1.5}$$

$$+ \quad q^2 v A_\mu A^\mu H - \lambda v H^3 - \frac{\lambda}{4} H^4 - \frac{1}{4} F_{\mu\nu} F^{\mu\nu} + \frac{\lambda v^4}{4} \tag{1.6}$$

where there is no Goldstone boson anymore. It correctly describes the interaction of two massive particles: the Higgs boson of mass

$$m_H = \sqrt{-2\mu^2} = \sqrt{2\lambda v^2} \tag{1.7}$$

and the gauge boson $A_\mu$ of mass:

$$m_A = qv \tag{1.8}$$

and the term $F^{\mu\nu} = \partial^\mu A^\nu - \partial^\nu A^\mu$ is the kinetic term of the field $A$. The other terms describe the interaction between fields and the self-interactions.

In the SM, the EBH mechanism is applied to the $SU(2)_L \times U(1)_Y$ gauge symmetry. As seen for $U(1)$ , the spontaneously broken symmetry leaves three Goldstone

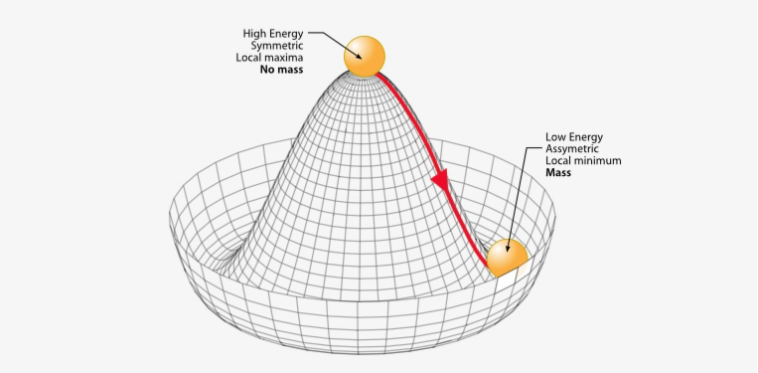


Figure 1.2: Higgs potential $V(\Phi)$ for a complex doublet field.

bosons, which represent the longitudinal polarization degrees of the $W^{\pm}$ and $Z^0$ bosons, which acquire a mass term. The mass terms of the three bosons are related to the VEV of the Higgs field by:

$$m_W = \frac{1}{2} g_W v, m_Z = \frac{1}{2} v \sqrt{g_W^2 + g^{`2}} = \frac{m_W}{cos(\theta_W)}, m_A = 0, m_H = v\sqrt{2\lambda} \tag{1.9}$$

where $g_W$ and $g^{`}$ are gauge couplings of the weak fields and $m_W$, $m_Z$, $m_A$ and $m_H$ are the masses of the $W$, $Z$, $\gamma$ and Higgs particles, respectively.

Similar to bosons, the mass terms for fermions are generated through Yukawa couplings - $g_\ell$ and $g_q$ - in the Yukawa Lagrangian resulting in $m_\ell = g_\ell v/\sqrt{2}$ and $m_q = g_q v/\sqrt{2}$ for the charged leptons and quarks, respectively.

### 1.2.3 Quantum Chromodynamics

Quantum chromodynamics (QCD) is the QFT describing the strong interactions of the coloured quarks and gluons. It is based on the non-abelian $SU(3)_C$ gauge group. Quarks possess a colour charge (there are three types of colour charges, arbitrarily labeled *red*, *blue* and *green*) while gluons carry a colour and an anti-colour (for a total of eight possible combinations). A hadron is a colour-singlet combination of quarks, anti-quarks and gluons. QCD predictions are well tested at high energies where perturbative approaches are possible because of the small value of the strong coupling constant, $\alpha_s$ (see Figure 1.3). On the other hand, in the low-energy region, QCD becomes a strongly-coupled theory and a perturbative approach cannot be

applied. QCD is a relativistic QFT of quarks and gluons interacting according to the laws of non-abelian forces between colour charges. The QCD Lagrangian is defined as follows:

$$\mathcal{L}_{QCD} = -\frac{1}{4} G_a^{\mu\nu} G^a_{\mu\nu} + \sum_f \bar{q}_f [i\gamma^\mu D_\mu - m_f] q_f \tag{1.10}$$

where $q$ represents the quark field and $f$ for the quark flavors relevant in the interaction, while $G_a^{\mu\nu}$ is the gluon field strength tensor:

$$G_a^{\mu\nu} = \partial^\mu A_a^\nu - \partial^\nu A_a^\mu + g f_a^{bc} A_b^\mu A_c^\nu \tag{1.11}$$

$A_a^\nu$ is the gluon field, $f_a^{bc}$ the antisymmetric structure constants and $g$ a constant related to the strong coupling constant, $\alpha_S$, via the formula $\alpha_S = g^2/4\pi$. $D^\mu$ is the gauge covariant derivative, namely

$$D^\mu = \partial^\mu - i\frac{g}{2} A_a^\mu \lambda^a \tag{1.12}$$

The world of hadronic and nuclear physics is governed by this QCD Lagrangian. Quarks and gluons represent the fundamental QCD degrees of freedom. How this elegant and simple theory can give rise to the complexity of hadrons is only qualitatively understood today. The QCD field equations are non-linear since the gluons that mediate the interaction carry colour charge and hence they can interact among themselves. This means that even the simplest strongly-interacting system is a multi-body problem: many quark-antiquarks pairs and gluons are always involved.

An intrinsic QCD scale, $\Lambda_{QCD}$, is set through the process of the renormalization in quantum field theory: below the QCD scale the standard perturbation theory is no longer valid because the coupling constant becomes larger.

Two of the prominent features of QCD are:

1. *Colour confinement*, which means that any strongly interacting system at temperatures below a critical value, $T_c$ (about 0.2 GeV), and at low baryon density must be a colour singlet at a scale of distance larger than $1/\Lambda_{QCD}$. As a consequence, isolated free quarks cannot exist in nature (quark confinement). The force between quarks increases with distance; this bounds them into hadrons, such as the proton, the neutron and so on. The colour confinement of QCD is

a theoretical conjecture consistent with experimental data.

2. *Asymptotic freedom*, which states that the interaction strength between quarks, $\alpha_S$, becomes smaller as the distance between them gets shorter.

Confinement is dominant in low-energy scales while asymptotic freedom becomes dominant as energy increases.

It has been said that QCD is the most elegant theory among the renormalisable QFTs based on the $SU(3)$ gauge group. The QCD Lagrangian has several other important symmetries, such as the number of quarks minus that of antiquarks for each flavour is conserved, corresponding to an automatic invariance of the Lagrangian under phase rotations of the quark fields of each flavour separately.

Still today, about forty years after the first QCD theoretical formulation, strong interactions are not completely understood: features of low transfer momentum QCD phenomena are far from being theoretically predictable. That is why experiments which test QCD in the non-perturbative regime are crucial to improve our understanding of the strong interactions.

**QCD Coupling Constant.** The qualitative understanding of QCD is based on the classical calculation of the renormalization scale dependence of the QCD coupling constant $\alpha_s$. The best way to show this dependency is to define the so-called $\beta$-function at an energy scale $\mu$:

$$\beta(\alpha_s) \equiv \frac{\mu}{2}\frac{\partial \alpha_s}{\partial \mu} = -\frac{\beta_0}{4\pi}\alpha_s^2 - \frac{\beta_1}{8\pi^2}\alpha_s^3 - \dots \tag{1.13}$$

where

$$\beta_0 = 11 - \frac{2}{3}n_f \tag{1.14}$$

$$\beta_1 = 51 - \frac{19}{3}n_f \tag{1.15}$$

and $n_f$ is the number of *effective quarks* (i.e. quarks with mass less than $\mu$). One introduces the arbitrary scale $\Lambda$ for solving this differential equation for $\alpha_s$ and to provide the $\mu$ dependence of $\alpha_s$. A first order approximate solution is the following:

$$\alpha_s(\mu^2) = \frac{\alpha_s(\Lambda^2)}{1 + \frac{\alpha_s(\Lambda^2)}{12\pi}\beta_0 \ln\frac{\mu^2}{\Lambda^2}} \tag{1.16}$$

The solution demonstrates the two famous QCD properties: asymptotic freedom

$$\alpha_s \xrightarrow{\mu \to +\infty} 0 \tag{1.17}$$

and the increasing value of the strong coupling at scales below $\mu \sim \Lambda$. As shown

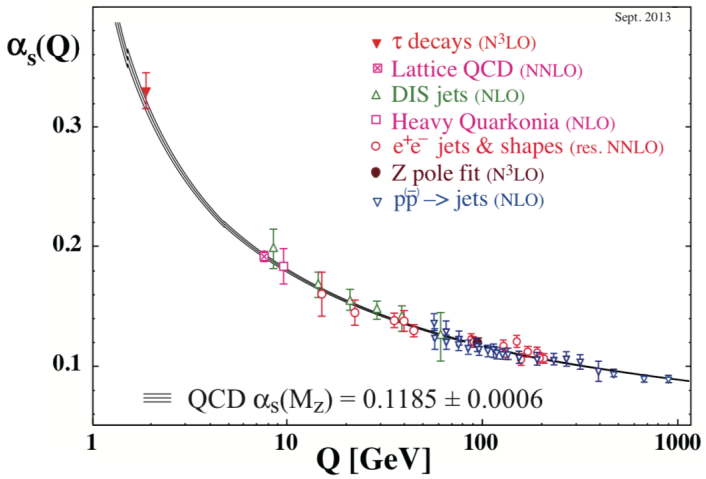


Figure 1.3: The QCD running coupling constant as a function of the transferred momentum $Q$ [17].

in Figure 1.3, it is possible to roughly divide the strong interaction physics into two regions as a function of the energy of the process: the area of perturbative QCD (pQCD) for high momentum transfer (small $\alpha_S$) and that of non-perturbative QCD for low momentum transfer (large $\alpha_S$). The pQCD has been well-tested in quantitatively describing phenomena where Feynman standard rules apply. In the perturbative regime, the magnitude of the coupling constant is the fundamental parameter for theoretical predictions. Its value as a function of the energy determines a host of phenomena, such as scaling violations in deep inelastic scattering, high-energy hadron collisions, $e^+e^-$ collisions and jet rates in $ep$ collisions etc. One of the most important example is the $e^+e^-$ annihilation: the multi-particle hadronic final-state system reveals the pQCD physics in the form of the quark and gluon jets. The different values of the coupling constant derived from these processes are listed in Figure 1.4; they are consistent with each other leading to an average value of [17]:

$$\alpha_s(m_Z^2) = 0.1181 \pm 0.0011. \tag{1.18}$$

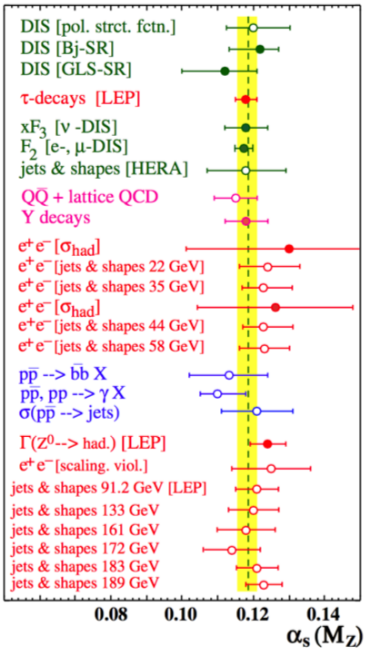


Figure 1.4: Summary of $\alpha_s(m_Z^2)$ measurements and world average value [18].

The non-perturbative regime is quantitatively much less understood: important questions still wait to be answered.

## 1.3 Physics Beyond the Standard Model

Despite being the most successful theory of particle physics to date - able to explain and predict a large variety of phenomena across a range of energies - the SM is not complete. Some of the fundamental physics phenomena that are not predicted in the SM are:

1. *Dark matter and dark energy.* From studies of the cosmic microwave background and other astronomical observations, about 26.8% of the total mass-energy of the known Universe is composed of non-luminous dark matter, 68.3% of dark energy - a mysterious energy believed to be responsible for the acceleration of the expansion of the Universe [19, 20] - and only about 4.9% of the visible ordinary matter. Therefore, the SM is able to describe only a tiny fraction of the mass-energy of the Universe. In addition, it doesn't provide any

dark matter candidates. At the moment, dark matter has been observed only indirectly through gravitational effects in a wide range of astronomical scales.

2. *Neutrino masses.* SM neutrinos are massless particles. However, recent observations of neutrino oscillations [21] have proven that neutrinos do have mass. In principle, it is possible to add neutrino masses by hand in the SM, but this is not straightforward. In fact, neutrino masses are extremely small and it is not clear if they arise in the same way as for the other SM particles.

3. *Gravity.* At the moment, the most successful theory to describe gravity is still Einstein's theory of General Relativity. The quantum behavior of gravity is still a mystery preventing Gravity from being unified with the other interactions in the SM.

   The EBH mechanism, as explained in Sec. 1.2.2, introduces the Higgs field to generate the mass of fermions and weak bosons. For the model to be consistent, the Higgs boson mass should not be too different from the $W$ mass. This is the case since the Higgs boson mass is measured to be around 125 GeV [9, 10]. However, the tree-level (bare) Higgs mass receives quadratically-divergent corrections from some loop diagrams shown in Fig. 1.5 and, thus:

$$m_H^2 = (m_H^2)_{bare} + \mathcal{O}(\lambda, g^2, h^2)\Lambda^2 \tag{1.19}$$

   where $\Lambda$ is the next higher scale in the theory. Several theorists consider the Planck scale $m_P = G_N^{-1/2} \sim 10^{19}$ GeV the best candidate for the natural scale of $m_H$, $\mathcal{O}(\Lambda)$. However, this is much larger than the observed values. As a consequence, the bare value and the corrections have to cancel out in order to give the observed value for $m_H$. This cancellation is known as the *fine tuning problem*. The SM can be seen as an effective field theory, valid at the electroweak energy scale, but breaking down close to the Planck scale where effects of gravity become relevant. This is the core of the *hierarchy problem*. Several solutions have been considered. One is the supersymmetrical TeV-scale, where quadratically divergent contributions originating from fermion and boson loops cancel, leaving only effects of the order of the supersymmetry breaking. Other non-supersymmetrical SM extensions include the Twin-Higgs models [23] or little Higgs models [24]. However, there is no experimental

evidence for any of these models.

4. *Strong $CP$.* Some theoretical speculations claim that the SM should include a term able to break the $CP$ symmetry in the strong interaction sector, i.e. in QCD. So far, no experimental violation of $CP$ symmetry in the strong interaction has been observed. Since there is no known a priori reason for it to be conserved, this fine tuning problem is often considered unnatural. In the context of QCD, also the theoretical approach for non-perturbative QCD includes several BSM models.

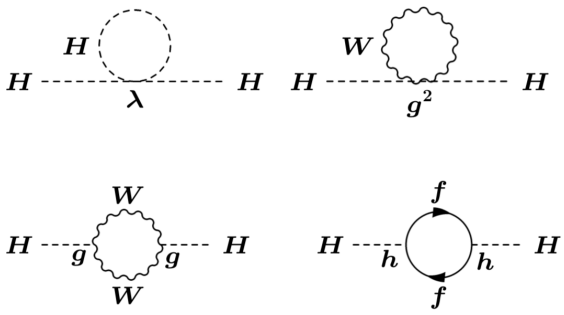


Figure 1.5: Radiative corrections to the Higgs mass. The list of corrections include loop diagrams for self-interactions, interactions with gauge bosons and interactions with fermions [22].

The SM is still far from being a *theory of everything* in Nature. Theoretically, it is more an approximate theory since 19 parameters need to be determined by experiments and added in an ad hoc way, such as the masses of fermions, of the Higgs boson, the gauge couplings etc. This opens new windows into BSM models. Several models have been proposed over time to solve the SM inconsistencies, such as the hierarchy problem. Some of them invoke the existence of *superpartners* for the SM particles, defining the Supersymmetry (SUSY) models [25]. Such models also require additional Higgs fields to generate masses for the full spectrum of SUSY particles. Other models, such as the Randall-Sundrum model [26] solve the hierarchy problem by compacting the extra dimensions which bridge the gap between the Planck and electroweak scale.

In the following sections, a brief introduction to the *Two Higgs Doublet Model*, the *Randal-Sundrum Model* and to some models for non-perturbative QCD is given.

### 1.3.1 Two Higgs Doublet Models

The two Higgs Doublet model (2HDM) is an extension of the SM which adds an additional doublet to the SM Higgs sector [27]. Through spontaneous symmetry breaking, *five* physical Higgs bosons appear: two $CP$-even[3] neutral scalar Higgs particles - $h$ and $H$ - a $CP$-odd neutral pseudoscalar - $A$ - and two charged scalar partners - $H^{\pm}$. The mass terms in the Lagrangian for each of the Higgs bosons are given by a mass matrix.

The free parameters of the 2HDM are:

- the masses of the five Higgs bosons: $m_h$, $m_H$, $m_A$ and $m_{H^{\pm}}$
- $\tan\beta = v_1/v_2$ where $v_1$ and $v_2$ are vacuum expectation values of the two doublets;
- $\alpha$, the mixing angle between the two $CP$-even Higgs bosons.

However, the number of free parameters can be reduced by identifying the observed SM $m_h = 125$ GeV with the $h$ boson and by imposing the gauge invariance, which results in the following constraints on the couplings of the two neutral $CP$-even bosons: $g^{2HDM}_{hVV}/g^{SM}_{hVV} = \sin(\beta-\alpha)$ and $g^{2HDM}_{HVV}/g^{SM}_{HVV} = \cos(\beta-\alpha)$. The alignment limit - $\sin(\beta-\alpha) = 1$ and $\cos(\beta-\alpha) = 0$ - allows for $m_h < m_H$. Another degree of freedom comes from the choice of the symmetry of the Yukawa sector which models the interaction of the two fields with the fermions. Several 2HDM models are possible depending on this choice. It is possible to define two main possible types of models: *type I* where all the right-handed quarks couple to the same Higgs doublets and *type II* where all the right-handed up-type quarks ($u$, $c$, $t$) couple to one of the Higgs doublets and the right-handed down-type quarks ($d$, $s$, $b$) couple to the other. SUSY models, such as the Minimal Supersymmetric Standard Model, require *type II* option, but *type I* is also studied. More details can be found in [28].

### 1.3.2 Randal-Sundrum Model

The Randal-Sundrum (RS) model - also known as a 5-dimensional warped geometry model - tries to solve the hierarchy problem by a different route. According to this

[3] After a $CP$ transformation, $CP$-even pseudoscalars have a +1 eigenvalue, while $CP$-odd pseudoscalars have a -1 eigenvalue.

model, the Universe is a 5D anti-de-Sitter (adS) space - a bulk extremely warped - which contains two branes[4]: the *Planckbrane*, where the Planck scale is located and gravity is a relatively strong interaction, and the 4D *Tevbrane*, where the SM scale is located. This spacetime is warped only along the fifth dimension. In this model gravity is mediated through Kaluza-Klein gravitons which follow a spin-2 mode with mass and couplings at the TeV scale. The graviton's probability function is extremely high at the Planckbrane, but drops with an exponential distribution when one moves closer towards the Tevbrane. As a result, gravity is much weaker on the Tevbrane rather than on the Planckbrane. The hierarchy problem is automatically solved in this model. In fact, the two branes are separated by approximately 16 units (units are based on the brane and bulk energies) causing the scale to change by 16 order of magnitude when moving from the Planckbrane to the Tevbrane with strings on the Planckbrane $10^{-33}$ cm in size, but only $10^{-17}$ cm on the Tevbrane. Therefore, there is no longer a strange range of masses and energies. However, the RS model makes specific predictions for the masses of gravitons which should be observed at the LHC energies [29]. At present, gravitons have not been observed at the LHC [30].

### 1.3.3 Non-perturbative QCD

The theoretical approaches to the non-perturbative QCD region are essentially two: Lattice QCD (LQCD) and the Effective Field Theory (EFT).

LQCD is a numerical approach. This approach uses a discrete set of space-time points, the so-called lattice, to reduce the analytically intractable path integrals of the continuum theory to a very difficult numerical computation which is then carried out on supercomputers, constructed for precisely this purpose. The discretization is removed by letting the lattice spacing tend to zero, thus restoring the continuum. LQCD theoretical principles were originally proposed in 1974. This approach has made enormous progress over the last decades, mainly due to the empowerment of the computer technology.

An EFT is a theoretical prescription for constructing theory spanning multiple energy scales, under a series of approximations. For instance, if we assume negligible

[4] A brane is a physics object which generalizes the notion of a point particle to higher dimensions in string theories or supergravity theories.

mass of the $u$, $d$ and $s$ quarks with respect to $\Lambda_{QCD}$, it is possible to formulate an EFT equivalent to QCD in a certain scale range. The most successful approach is the heavy-quark effective theory (HQET) for hadrons containing a quark $c$ or $b$ because their mass is $m_Q \gg \Lambda_{QCD}$. In the limit $m_Q \to +\infty$ the heavy quark becomes on-shell and the dynamics becomes independent of its mass. The hadronic matrix elements can be expanded as a power series in $1/m_Q$ resulting in symmetry relations between various matrix elements [31].

In recent years a great variety of EFTs with quark and gluon degrees of freedom have been developed. The best solution is obtained combining LQCD with EFT because there is a remarkable simplification in the theoretical calculations.

## 1.4 Higgs Physics at the Large Hadron Collider

As seen in Sec. 1.2.2, in the EBH mechanism an additional quantum field, the Higgs field, is introduced to give mass to the gauge bosons and cancel out the massless Goldstone bosons. The quantization of this field results in the production of the quanta of the Higgs field, the Higgs bosons. As a consequence, the experimental observation of the Higgs boson is the best experimental evidence of the Higgs field and the EBH mechanism. The Higgs boson mass is a free parameter in the SM since couplings to other fields are predicted, but the energy scale is not. The Higgs boson mass needs to be added by hand and, thus, its experimental measurements are crucial to complete the SM. The SM Higgs particle is expected to be a spin-0 electrically neutral scalar boson and $CP$-even (i.e. invariant under charge and parity transformation) [32].

After more than forty years of Higgs hunting, on July $4^{th}$, 2012 the discovery of a new boson consistent with the SM Higgs boson was reported by the ATLAS and CMS Collaboration [9] [10]. The Higgs discovery is a milestone in the quest to understand the SM electroweak symmetry breaking.

After the Higgs discovery, a new Higgs precision era has recently started. The Higgs boson mass was measured to be $m_h = 125.09 \pm 0.21(\text{stat}) \pm 0.11(\text{syst})$ GeV [33] corresponding to a VEV of 246 GeV. Recently, ATLAS has reported a similar 1.9 permille precision level on the Higgs boson mass without a need for a combination with CMS results [34]. The particle properties, spin, parity and those couplings to SM particles that have been measured by ATLAS and CMS are fully consistent

with the prediction of the SM Higgs particle, favouring the scalar, $J^{PC} = 0^{++}$, hypothesis [35–38]. A recent paper produced by the ATLAS collaboration based on a combination of measurements of the Higgs couplings to other SM particles can be found here [39]. No deviations from the SM expectations are observed.

### 1.4.1 Higgs production

At the Large Hadron Collider (LHC), the Higgs boson is produced via four leading production modes:

- Gluon-Gluon fusion (ggF) process, mediated by a top quark loop (88% of total production at N$^3$LO QCD + NLO EW);
- Vector Boson Fusion (VBF) process, with a clear signature of two scattered quarks in addition to the produced Higgs boson (7% of total production at NNLO QCD + NLO EW);
- Associated production with a vector boson $W$ or $Z$, VH (4% of total production at NNLO QCD + NLO EW);
- Associated production of the Higgs boson with a $t\bar{t}$ pair, $t\bar{t}H$ (1% of total production at NLO QCD + NLO EW).

The tree-level Feynman diagrams for the four processes are shown in Fig. 1.6 and the cross sections as a function of the Higgs boson mass at $\sqrt{s} = 13$ TeV are shown in Fig. 1.7. The Higgs results reported in this thesis mainly focus on the ggF and VBF production modes, which were observed during the LHC Run 1 data-taking operations. The other two production modes, VH and $t\bar{t}H$, were finally observed at the end of LHC Run 2 data-taking operations in 2018 [40] [41].

The gluon-gluon fusion process, $gg \to H$, proceeds via triangular diagrams of virtual quarks, as the Higgs boson does not couple directly to gluons. In the SM the triangular loop is largely dominated by top quarks, with a bottom quark contribution that does not exceed the 10% level at leading order (LO). The top quark mass in the loop is assumed to be infinite, allowing for computational calculations of the cross section up to the theoretical next-to-next-leading order (NNLO) and next-to-next-to-next-leading order (N$^3$LO) in $\alpha_S$ for a Higgs boson with mass of 125 GeV. The total ggF production cross section at $\sqrt{s} = 13$ TeV for a Higgs boson with mass of 125

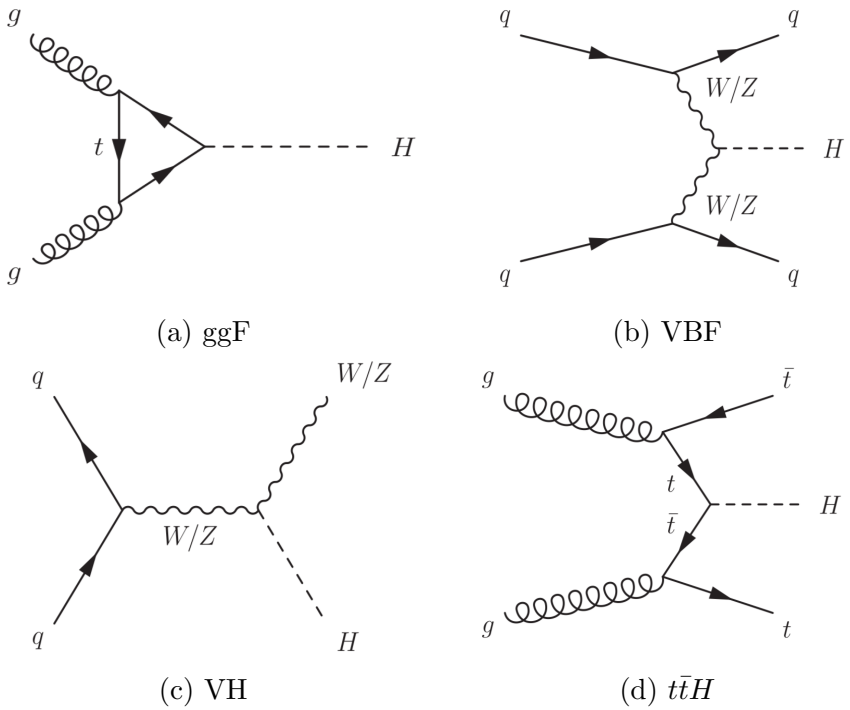


Figure 1.6: Tree-level Feynman diagrams for the Higgs production at the LHC.

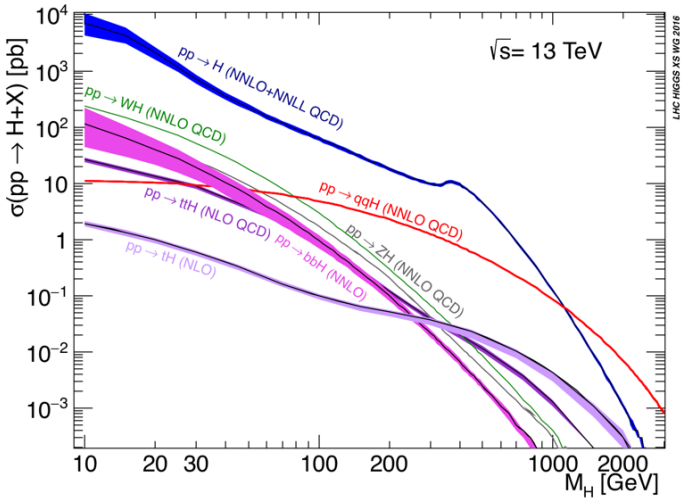


Figure 1.7: Higgs production cross section for the various production modes as a function of the Higgs boson mass, $M_H$, at $\sqrt{s} = 13$ TeV [42].

GeV is: $\sigma_{ggF} = 48.68^{+2.07}_{-3.16}(\text{theory})^{+1.25}_{-1.26}(\alpha_S) \pm 0.89(\text{PDF})$ pb [42]. The LO and QCD NLO corrections amount to about 80% of the total cross section given above, the

NNLO QCD corrections further increase the cross section by an additional 30% and the N$^3$LO corrections by 3%. In addition, NLO EW corrections increase the cross section by 5%. A detailed introduction on the ggF theoretical corrections for the off-shell[5] production of the Higgs boson will be given in Sec. 4.2 when introducing the analysis idea to indirectly constrain the Higgs boson total width.

The vector-boson-fusion VBF process is the second most copious production mode at the LHC. Two vector bosons ($W$s or $Z$s) are radiated from the quarks of the incoming protons which collide, providing the hard interaction. A Higgs is produced centrally, while the two quarks from which the vector bosons are radiated, shower and manifest themselves as two highly energetic jets in the forward regions of the detector. Despite VBF having a smaller cross section than ggF, it is characterized by a distinctive signature: two well-separated jets in the forward regions of the detector with little extra hadronic activity and the decay products of the Higgs boson in the central region. The total VBF production cross section at NNLO QCD and NLO EW corrections at $\sqrt{s} = 13$ TeV for a Higgs boson with mass of 125 GeV is $\sigma_{VBF} = 3.78 \pm 0.08$ pb, where the uncertainty corresponds to the total theoretical systematic uncertainties calculated by adding in quadrature the QCD scale and PDF+$\alpha_S$ uncertainties [42]. The NNLO QCD corrections reduce the residual scale uncertainties on the inclusive cross section to approximately 2%.

### 1.4.2 Higgs decays

The Higgs boson is not a stable particle, it quickly decays to particles with smaller masses converting the initial Higgs rest mass energy into momentum of the decay products in order to conserve the four-momentum. As discussed in Sec. 1.2.2, the SM Higgs boson interacts with other particles via gauge couplings and Yukawa couplings with couplings strengths proportional to the particle masses. Therefore, the Higgs boson prefers to decay into the heaviest pair which is allowed. In particle physics one defines the Branching Ratio (BR) for a specific decay as the fraction of times the particle decays to this specific final state with respect to the total

[5]For a particle, for instance the $W$ boson, the notation $W^*$ means that the boson is a virtual quantum particle which doesn't have to have the mass of a real $W$ boson - 80 GeV - but it can have a different mass since it can live (briefly) off mass-shell or simply *off-shell*. This is meant to distinguish it from a real 80 GeV $W$ boson which is on mass-shell or simply *on-shell*. In the decay $H \to WW^*$, the on-shell Higgs boson can only decay to one on-shell $W$ boson and to one off-shell $W$ boson in order to conserve the four-momentum of the system.

number of its decays. Among the various Higgs decay channels, the most abundant are $b\bar{b}$(BR = 58%), $WW^*$(BR = 21%), $gg$(BR = 8.2%), $\tau\tau$(BR = 6.2%), $c\bar{c}$(BR = 2.9%), $ZZ^*$(BR = 2.6%), $\gamma\gamma$(BR = 0.2%), $Z\gamma$(BR = 0.15%) and $\mu\mu$(BR = 0.02%). They are also shown as a function of the Higgs boson mass in Fig. 1.8.

At the end of the LHC Run 2 data-taking operations in 2018, the leading decay mode $H \to b\bar{b}$ was finally observed [40].

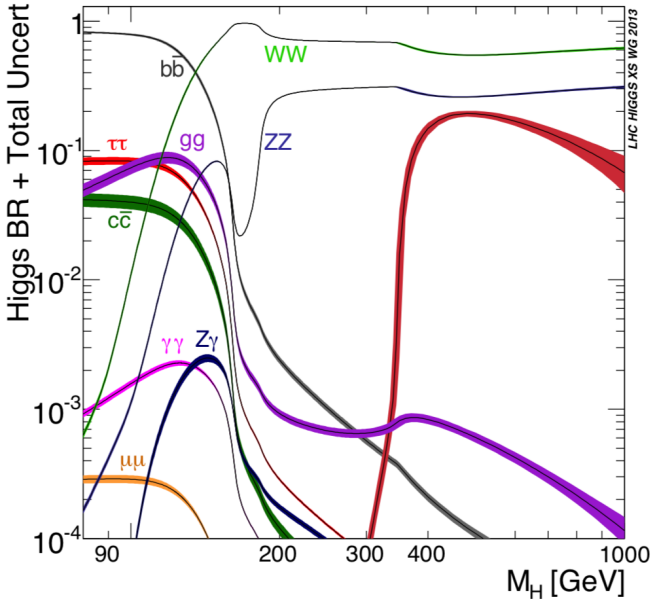


Figure 1.8: Branching ratios of the different SM Higgs boson decay modes as a function of the Higgs boson mass [42].

### 1.4.3 Higgs boson total width

The total width of the Higgs boson, $\Gamma_H$, is the sum of the partial widths, $\Gamma_i$, of the various Higgs decay modes:

$$\Gamma_H = \sum_i \Gamma_i \tag{1.20}$$

where $BR_i = \Gamma_i/\Gamma_H$ is the branching ratio of the $i^{th}$ decay mode. The Higgs boson total width varies as a function of the Higgs boson mass, as reported in Fig. 1.9. For a Higgs boson of mass of 125 GeV, the SM expectation is 4.07 MeV [43].

The Higgs boson total width is a fundamental measurement providing global information on the Higgs decays. By measuring the width one can check how many

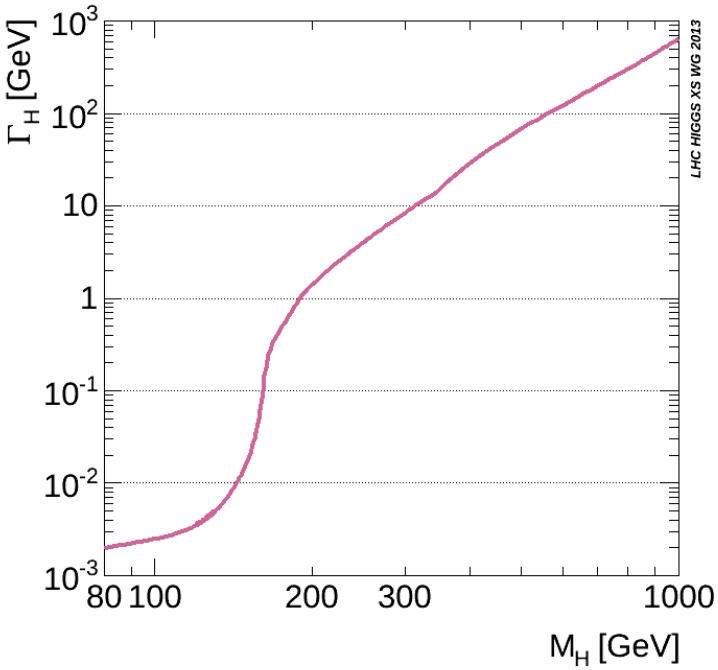


Figure 1.9: SM Higgs boson total width as a function of the Higgs boson mass $M_H$ [43].

different ways the Higgs boson is decaying; even if it decays to particles not visible in the LHC detectors, these decays will influence the width, making it larger than the expected value in the SM because the Higgs boson will decay faster. As seen in Sec. 1.3, there are several BSM theories which look for new heavier Higgs bosons or the Higgs boson could decay to exotic dark matter particles. Even if these decays are not visible, by measuring the Higgs boson total width BSM models could be indirectly tested. Therefore, the measurement of the Higgs boson width at the LHC is important to determine its nature.

A direct width measurement at the resonance peak is limited by experimental resolution, about 1 GeV [44–46], and is only sensitive to values larger than the SM expectation [43, 47]. The CMS collaboration has also tried to constrain the Higgs boson total width by measuring the Higgs boson lifetime[6] from the flight distance in the CMS detector resulting in a lower bound of $\Gamma_H > 3.5 \cdot 10^{-9}$ MeV at 95% confidence level (CL) [48].

[6] According to Heisenberg's uncertainty principle $\Gamma_H > 1/\tau_H$ where the expected SM $H$ boson average lifetime is $\tau_H \sim 16\ \ 10^{-8}$ fs (or 48 fm/$c$).

Several studies in [49–52] have shown that the high-mass off-peak regions beyond $2m_V$ ($V = Z, W$), well above the measured resonance mass of about 125 GeV, in the $H^* \to ZZ$ and $H^* \to WW$ channels are sensitive to Higgs boson production through off-shell and background interference effects. This presents a novel way of characterizing the properties of the Higgs boson in terms of the off-shell event yields, normalised to the SM prediction (referred to as signal strength $\mu_{off-shell}$), and the associated off-shell Higgs boson couplings. As said before, such studies also provide sensitivity to new physics that alters the interactions between the Higgs boson and other fundamental particles in the high-mass region [53–58]. In addition, the off-shell production method can be used to set an indirect limit on the Higgs boson total width, based on the relative measurement of the off-shell to the on-shell production cross section [59]. However, Higgs couplings to particles in the off-shell and on-shell region need to be assumed the same in order to extract a constraint on the Higgs boson total width.

During the LHC Run 1, both the CMS and ATLAS collaborations have set constraints of $\Gamma_H < 22$ MeV(22.7 MeV for ATLAS) at 95% CL on the Higgs boson total width using the off-shell production method [60, 61]. This value is 5.4(5.5 for ATLAS) times the SM value of $\Gamma_H$ at the measured mass of 125.09 GeV.

The off-shell decay channels studied by the CMS Collaboration in Run 1 are $H^* \to ZZ \to 4\ell$ or $H^* \to ZZ \to 2\ell 2\nu$ with $\ell = e, \mu$. The combination with the corresponding observed Higgs boson signal strength in the resonance peak region leads to constraints on the Higgs boson total width $\Gamma_H$. The $2\ell 2\nu$ decay channel, which benefits from a higher branching fraction, is used in the high-mass region to further increase the sensitivity to the Higgs boson width. The measurement is based on $pp$ collision data collected by the CMS detector at the LHC in 2011, corresponding to an integrated luminosity of 5.1 fb$^{-1}$ at the centre-of-mass energy of $\sqrt{s} = 7$ TeV ($4\ell$ channel), and in 2012, corresponding to an integrated luminosity of 19.7 fb$^{-1}$ at $\sqrt{s} = 8$ TeV ($4\ell$ and $2\ell 2\nu$ channels). The $4\ell$ and $2\ell 2\nu$ channels are combined in a simultaneous binned maximum likelihood fit to the measured kinematic distributions near the resonance peak and above the $Z$-boson pair production threshold to extract an upper limit on the Higgs boson width of $\Gamma_H < 22$ MeV at a 95% CL.

Similar to CMS, the ATLAS Collaboration has measured the off-shell Higgs boson signal strength in the high-mass $WW \to \ell\nu\ell\nu$, $ZZ \to 4\ell$ and $ZZ \to 2\ell 2\nu$ channels, setting a 95% CL upper limit on $\Gamma_H/\Gamma_H^{SM}$ of 5.5 with an expected value of 8.0.

The data collected correspond to an integrated luminosity of 20.3 fb$^{-1}$ at a collision energy of $\sqrt{s} = 8$ TeV. One of the main challenges for these measurements arises from the theoretical predictions. During Run 1, while higher-order QCD and EW corrections were known for the off-shell signal process in the form of a next-to-next-to-leading order (NNLO) $K$-factors defined as $K(m_{ZZ}) = \sigma^{NNLO}_{gg\to H^*\to ZZ}/\sigma^{LO}_{gg\to H^*\to ZZ}$[7], no higher-order QCD calculations were available for the LO $gg \to ZZ$ background process. As a consequence, the ATLAS results were given as a function of the $K$-factor ratio $R^B_{H^*} = K(gg \to ZZ)/K(gg \to H^* \to ZZ)$ to make their dependence on the unknown $K$-factor explicit. The limits reported above - 95% CL upper observed limit on $\Gamma_H/\Gamma^{SM}_H$ of 5.5 and an expected value of 8.0 - are based on the assumption that the $K$-factor for the $gg \to ZZ$ background is the same as the $K$-factor for the $gg \to H^* \to ZZ$ signal. Table 1.1 reports the individual-channel contribution for off-shell signal strength ($\mu_{off-shell}$) measured by ATLAS in Run 1. It will be explained in Chapter 4 that the theoretical situation has improved in Run 2 with no need for such a caveat anymore.

| | Observed | | | Median expected | | |
|---|---|---|---|---|---|---|
| $R^B_{H^*}$ | 0.5 | **1.0** | 2.0 | 0.5 | **1.0** | 2.0 |
| $ZZ \to 4\ell$ | 6.1 | **7.3** | 10.0 | 9.1 | **10.6** | 14.8 |
| $ZZ \to 2\ell 2\nu$ | 9.9 | **11.0** | 12.8 | 9.1 | **10.6** | 13.6 |
| $WW \to e\nu\mu\nu$ | 15.6 | **17.2** | 20.3 | 19.6 | **21.3** | 24.7 |

Table 1.1: The observed and expected 95% CL upper limit on $\mu_{off-shell}$ within the range of $0.5 < R^B_{H^*} < 2.0$, with $R^B_{H^*}$ defined in the text, for the individual channels used in the Run-1 ATLAS analysis [61]. The bold numbers correspond to the limit assuming $R^B_{H^*} = 1$.

Early in 2019 the CMS collaboration updated the measurement for the $4\ell$ channel with an additional 80.2 fb$^{-1}$ of data collected in 2016-2017 [62]. The combination with the Run 1 dataset leads to an observed(expected) upper constraint of 9.16(13.7) MeV at 95% CL on $\Gamma_H$. In Fig. 1.10 the likelihood scan for both the CMS (Run1+Run2) and ATLAS (Run 1) results are shown.

In this thesis, a new analysis of the off-shell signal strength in the $ZZ \to 4l$ and $ZZ \to 2\ell 2\nu$ final states is presented. Similar to Run 1, the off-shell results are

[7]Similar considerations are valid for the $WW$ channel.

combined with the on-shell result for the Higgs production in order to derive a limit on the Higgs boson total width. Results are based on data collected by the ATLAS detector in 2015-2016 during the Run 2 data-taking operations, corresponding to 36.1 fb$^{-1}$ and were published in 2018 by the ATLAS collaboration [63].

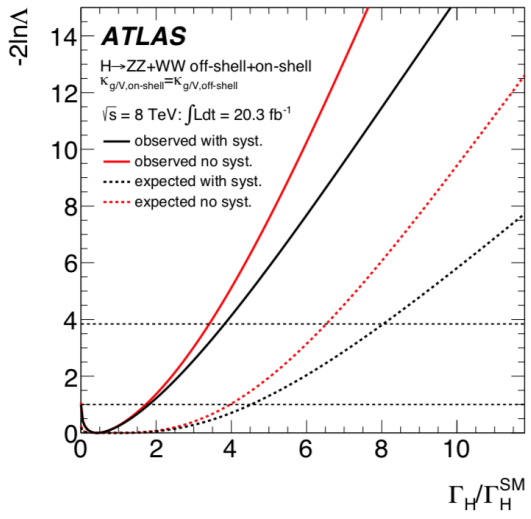


(a) ATLAS results

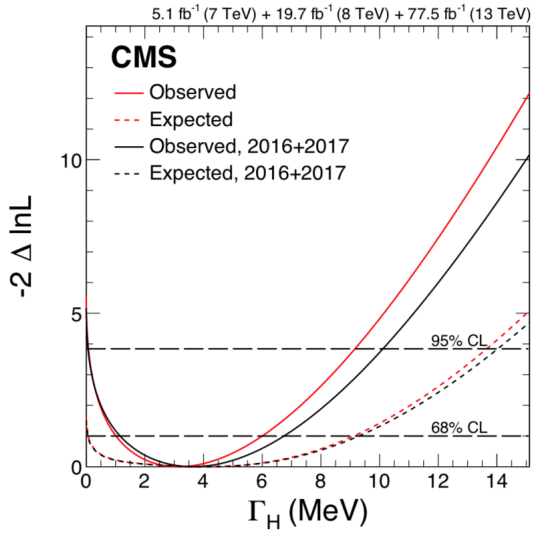


(b) CMS results

Figure 1.10: Scan of the negative log-likelihood as a function of $\Gamma_H/\Gamma_H^{SM}(\Gamma_H)$ with data collected by the ATLAS collaboration in Run 1 (a) [61] and the CMS collaboration in Run 1 and Run 2(2016-2017) (b) [62].

## 1.5 Charmed-hadron Production at High Energy Colliders

After the discovery of several hadrons made up by $u$, $d$ and $s$ quarks, the existence of a fourth quark had been postulated by a number of authors around 1964. However, its prediction is usually credited to Sheldon Glashow, John Iliopoulos and Luciano Maiani in 1970 with the so-called *GIM mechanism*.

A firmly established experimental fact is that flavor changing weak processes obey certain selection rules. One of them, known as the $\Delta S = 1$ rule, states that the flavor number, in this case strangeness $S$, changes by at most one unit. A second rule is that flavor changing neutral current (FCNC) processes, must occur only at second order in the weak interactions[8]. In order to explain the non observation of FCNC processes at tree level, the existence of a second *up*-type quark was postulated, which pairs with the $s$ quark in a doublet of $SU(2)_L$. In 1974 two independent research groups, one at the Stanford Linear Accelerator Center - headed by Burton Richter - and one at the Brookhaven National Laboratory - headed by Samuel Ting - announced the discovery of the first meson consisting of a charm quark and a charm antiquark, namely $J/\psi$ (charmonium).

Among the *up*-type quarks, the quark charm, $c$, occupies a unique place since it is the only *up*-type quark whose hadronization (and the subsequent decay) can be studied. This is due to the fact that the $t$ quark decays before it can hadronize and the $u$ quark can be considered stable.

The main features of charm quarks are the following:

- $c$ quarks are similar to $u$ quarks, but they are heavier (about 2 GeV);
- They form charged and neutral hadrons, of which (in the $C = 1$ sector) three mesons and four baryons decay only weakly with lifetimes of about $10^{-13}s$. The $D$ family is composed of the ground state $D^0(c\bar{u})$, $D^+(c\bar{d})$ and $D_s(c\bar{s})$ meson and their antiparticles.
- Charm decays via the weak interaction preferentially to strange.

[8]The best experimental evidence is the measurement of the branching ratio $\frac{Br(K^+\to\pi^+\nu\bar{\nu})}{Br(K^+\to\pi^0\mu^+\nu_\mu)} \sim 10^{-8}$, where $K^+ \to \pi^+\nu\bar{\nu}$ is a neutral current process with $\Delta S = 1$ and $K^+ \to \pi^0\mu^+\nu_\mu$ is a charged current process with $\Delta S = 1$.

Today, after about 50 years of research in the charm sector, these assumptions are well established. Experimentally, charm has some distinct advantages compared to the $B$-system: fully reconstructed modes are characterized by branching fractions at the level of the ~10%, much higher than branching fractions of modes used to fully reconstruct $B$-decays $\mathcal{O}(1\%)$. Moreover, very specific tags are present in the charm decays, allowing distinguishable signatures. For instance about one third of the $D^0$ comes from a $D^{*+} \to D^0\pi^+$ decay: the charge of the slow pion tags the $D^0$ flavor at production with an efficiency of almost 100%.

Measurements of production cross sections of hadrons containing bottom or charm quarks in hadron collisions offer essential information to test and refine phenomenological models of the strong interaction at small four-momenta transfer, a regime in which perturbative expansions are challenging. In addition, in searches for astrophysical neutrinos, charm production cross sections allow for improved estimations of background rates from neutrinos produced in decays of charm hadrons from cosmic-ray interactions with atmospheric nuclei [64].

Charm physics has been deeply studied by fixed target experiments, such as E687/FOCUS, and at colliders, such as the Tevatron and the LHC. At present, some of the best results in charm physics are from the LHC ALICE and LHCb collaborations. Both published measurements of charm production cross sections at centre-of-mass energies $\sqrt{s}$ = 2.76, 7, 8 and 13 TeV [65–68] including measurements of $D$-mesons differential cross sections. The total charm production cross section dependence on $\sqrt{s}$ was estimated using the extrapolation of the $D$-meson cross section measurements to the full kinematic phase space. In Figure 1.11 the $pp \to c\bar{c}$ cross section as a function of the centre-of-mass energy for various experiments is shown [69].

One of the important contributions in the charm sector is also from CDF. Before CDF, charm physics had not been studied at $p\bar{p}$ colliders. The CDF Silicon Vertex Tracker (SVT) was designed to collect large data samples of $b$-hadrons in fully hadronic final states, but thanks to this particular tracker, CDF was also able to collect huge samples containing $D$-meson decays, becoming competitive in terms of sensitivity to previous charm factories [70]. During Run I (1992–1996) of the FERMILAB Tevatron collider, the CDF experiment pioneered the study of bottom-meson cross sections, using proton-antiproton collisions at centre-of-mass energy of $\sqrt{s} = 1.8$ TeV [71]. Observed cross sections were significantly larger than predicted

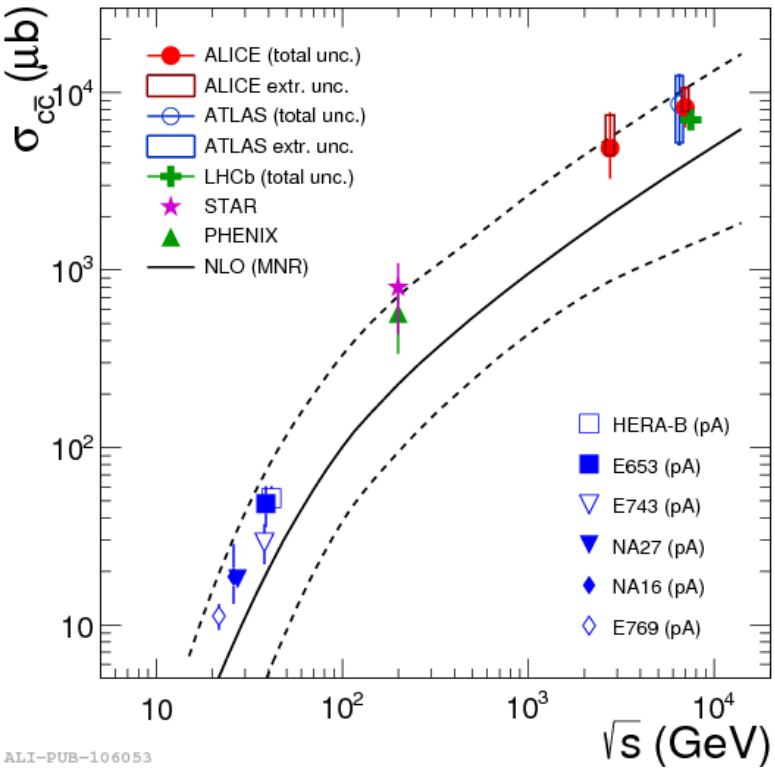


Figure 1.11: Total charm production cross section as a function of centre-of-mass energy for various experiments [69].

values [72,73] and prompted a dedicated and continuing effort to refine calculations, which resulted in reduced discrepancies. In Tevatron Run II (2001–2011), CDF complemented this program with the world's first measurements of charm-meson hadroproduction cross sections, using $p\bar{p}$ collisions at $\sqrt{s}$ = 1.96 TeV [74]. These measurements used charm mesons, such as the $D^+$-meson, reconstructed down to minimum transverse momenta of 6.0 GeV because of the biases introduced by the online event selection based on displaced tracks. They are shown in Fig. 1.12.

In this thesis a new measurement of the $D^+$-meson production cross section as a function of transverse momentum is reported. Samples of $D^+ \to K^-\pi^+\pi^+$ decays are reconstructed using the full CDF Run II dataset - corresponding to 10 fb$^{-1}$ - in the transverse-momentum range down to 1.5 GeV, at the time still unexplored in $p\bar{p}$ collisions. The event sample is selected online using minimally biasing requirements and a data-driven optimization for each $p_T$ bin is used to determine the offline selection. A two-dimensional simultaneous fit of the $K^-\pi^+\pi^+$-mass and $D^+$ Impact-

Parameter (IP) distributions allows to determine, in each transverse-momentum bin, the number of $D^+$ decays produced directly in the hard scattering. These numbers are later combined with reconstruction and selection efficiencies derived from simulation, but validated with data, to determine the differential cross section. The low-$p_T$ extension of the previous measurement strengthens significantly the experimental leverage to refine current knowledge.

Even though the best charm results are now published by the LHC collaborations, the Tevatron results presented in this thesis are still of unique importance. In fact, different admixtures of quark-level processes contribute at different energy scales and with different initial states and, therefore, proton-antiproton collision measurements at the lower energy of 1.96 TeV remain crucial to extend comprehension in a regime in which QCD perturbative expansions are challenging. These results are complementary to similar results published by the LHC collaborations and were published as the $700^{th}$ paper of the CDF collaboration [75] in 2017.

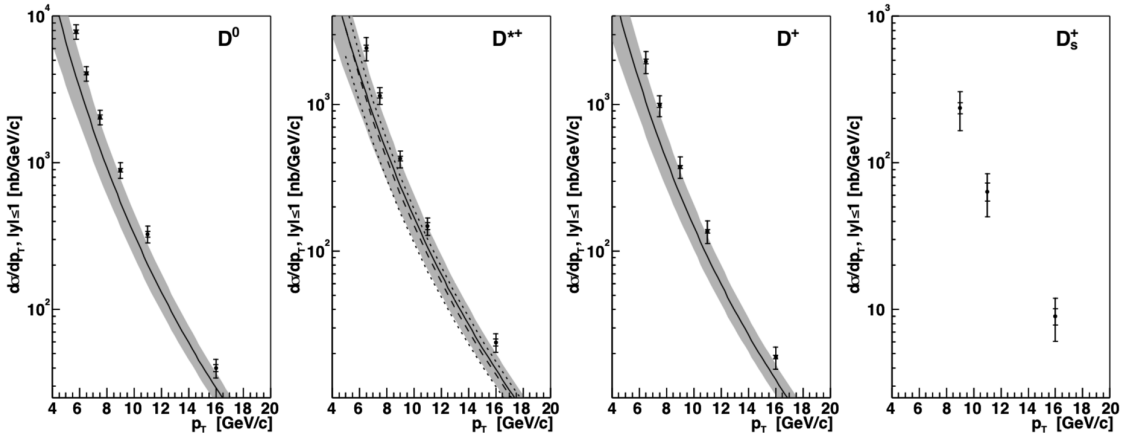


Figure 1.12: The differential cross section measurements for the $D$-mesons at $\sqrt{s}$= 1.96 TeV at CDF II. The inner bars represent the statistical uncertainties, while the outer bars are the quadratic sum of the statistical and systematic uncertainties. The solid and dashed curves represent the theoretical predictions and the shaded bands indicate the corresponding uncertainties. For the $D_s^+$ production there is no theoretical prediction [74].

# Chapter 2

# The Large Hadron Collider and the ATLAS Experiment

*In this chapter I describe the Large Hadron Collider (LHC) facility and the ATLAS detector focusing on all its sub-detectors. All the data used for the measurement of the Higgs boson off-shell production and the muon momentum performance presented in this thesis were collected by the ATLAS detector during the Run 2 data-taking operations in 2015 and in 2016.*

## 2.1 Introduction

The Large Hadron Collider (LHC) is the largest and most powerful particle collider ever built by humans [76]. It is located in the heart of Europe, at the European Organization for Nuclear Research (CERN), near Geneva in Switzerland. It serves as a microscope to study and probe the behaviour of matter and interactions on the very small scales $\mathcal{O}(10^{-18}$ m) recreating energy conditions similar to those just after the Big Bang. It is a proton-proton collider with a 27-kilometer ring of superconducting magnets and a number of accelerating structures to boost the energy of the particles along the way. Beams inside the LHC tunnel collide in four different locations of the accelerator ring, corresponding to the position of four particle detectors: ATLAS, CMS, LHCb and ALICE.

ATLAS - short for *A Toroidal Lhc ApparatuS* - is the largest-volume detector ever

constructed. The volume is comparable to half the size of the cathedral of Notre Dame in Paris. It is also a record scientific collaboration with more than 3000 scientific authors from 183 institutions around the world (as of 2019). ATLAS, along with the CMS detector, is a multipurpose detector which has been designed to detect a wide range of particles, to test the validity of the SM and to search for new physics. It takes advantage of the LHC energy allowing for the observation of highly massive particles - such as the Higgs boson - which were not observable with lower-energy accelerators before the LHC.
In this Chapter a brief introduction to the LHC facility, its structure and function, is given in Sec. 2.2. Later, ATLAS is described in Sec. 2.3 focusing on all the ATLAS sub-detectors: the Inner Detector (ID) is described in Sec. 2.3.1, the Electromagnetic and Hadronic CALorimeters (ECAL and HCAL) are described in Sec. 2.3.2, the Muon System (MS) in Sec. 2.3.3 and the Trigger System in Sec. 2.3.4. Finally, the ATLAS data used in this thesis are summarized in Sec. 2.4, along with a short description of the detector simulation infrastructure.
The descriptions in this Chapter closely follow the ATLAS Technical Design Report [77] [78].

## 2.2 The Large Hadron Collider

The LHC is hosted in the tunnel formerly used for the Large Electron-Positron Collider (LEP). The tunnel has a 27-kilometer circumference at a depth ranging from 50 to 175 meters underground at the French-Swiss border near Geneva. The collider facility consists of two adjacent parallel beamlines, each containing a proton beam traveling in opposite direction around the ring. Proton beams consist of packed short-pulse bunches with about $10^{11}$ protons assembled together in a bunch train. Inside the accelerator, the two high-energy proton beams travel at close to the speed of light before they are made to collide. They are guided around the accelerator ring by a strong magnetic field maintained by superconducting electromagnets. The dipole magnetic field strength reaches the unprecedented level of 8.3 T. This high field can only be achieved via the implementation of superconducting materials made of niobium-titanium (NbTi) coils cooled down to 1.9 K - a temperature cooler than outer space - using superfluid helium. As a consequence, much of the accelerator is connected to a distribution system of liquid helium, which cools the magnets, as

well as to other supply services. A total number of 1232 dipole magnets is used to keep the beams on their circular path, while 474 quadrupole magnets squeeze and bunch together all the protons to avoid dispersion of proton beams. In total, more than 1600 magnets are installed with an overall weight of about 28 tonnes. The temperature isolation of the system is achieved via an high insulating vacuum ($\sim 10^{-6}$ mbar) [76].

The LHC accelerator collides protons with protons - each proton beam is accelerated to energies of 6.5 TeV resulting in a centre-of-mass energy $\sqrt{s} = 13$ TeV, close to the designed maximum centre-of-mass energy of 14 TeV. Protons originate from a hydrogen source where they are stripped from their electron. In order to reach the needed energy in the LHC tunnel, protons undergo several cycles of acceleration. They are schematically indicated in Fig. 2.1. The protons' path starts with a linear accelerator (LINAC) where protons are accelerated up to 50 MeV. Due to residual magnetic fields present in the ring cavities, there is no direct injection in the ring section. Protons are injected into the Booster ring where their energy increases up to 1.4 GeV and next to the Proton Synchrotron (PS) where their energy is increased up to 26 GeV. The protons are then transferred to the Super Proton Synchrotron (SPS) - the CERN proton-antiproton machine which allowed the Nobel-prize-winning observations of the $W$ and $Z$ bosons in 1983 - where the proton beams gain an energy of 450 GeV. Finally the protons are injected into the LHC ring where the beam energy ($E_b$) reaches the final goal of 6.5 TeV resulting in $\sqrt{s} = 2 \times E_b = 13$ TeV.

The collisions at the LHC take place in four different locations, where each of the four main detectors are located:

- ATLAS and CMS, the two large general-purpose experiments;
- LHCb designed to study $b$-quark physics, $CP$-violation and rare decays;
- ALICE designed to study multi-track events produced by heavy-ion or proton collisions and the nature of the quark-gluon plasma.

### 2.2.1 LHC Key Parameters

The performance of a collider is evaluated in terms of two key parameters: the available centre-of-mass energy, $\sqrt{s}$, and the instantaneous luminosity, $\mathcal{L}$.

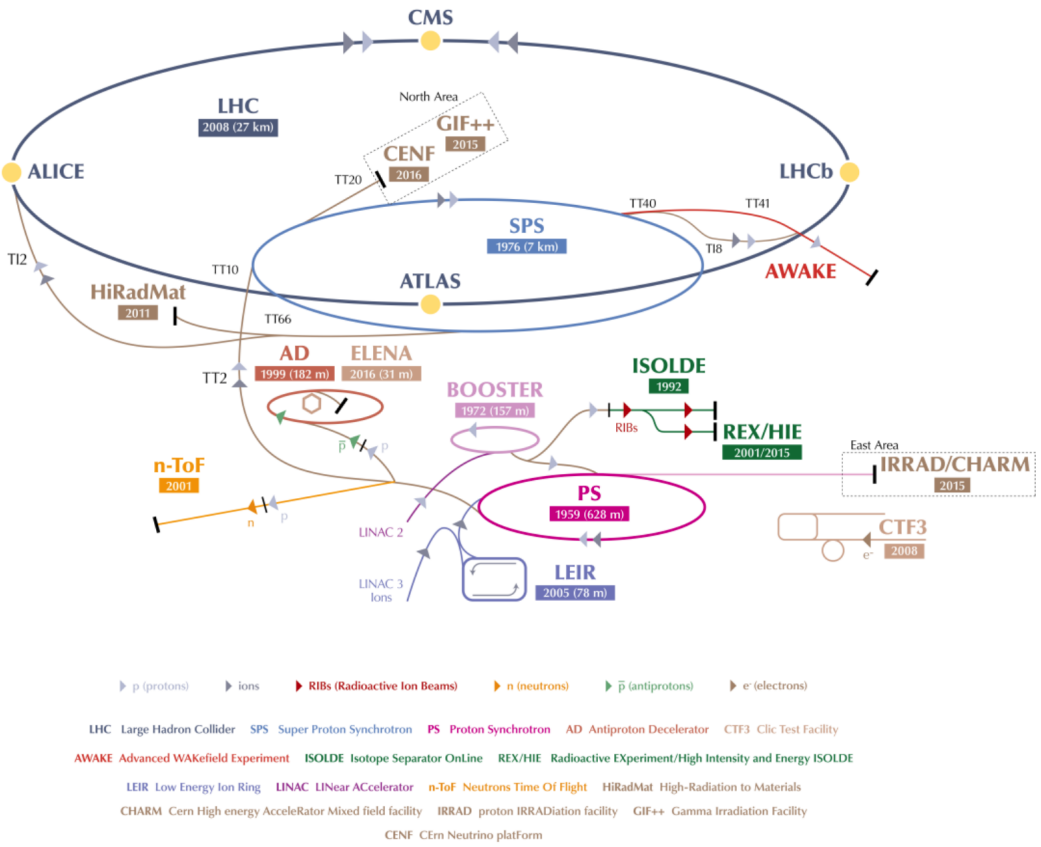


Figure 2.1: The LHC Collider chain at CERN. Protons are accelerated in several stages: linear accelerators (LINACs), the Booster, the Proton Synchrotron (PS), the Super Proton Synchrotron (SPS) and finally the Large Hadron Collider (LHC). Proton beams are accelerated in opposite directions before colliding in four different locations at the centres of the four detectors ATLAS, LHCb, CMS and ALICE. Figure from [79].

**Luminosity.** In the measurement of the cross section of a given process, the luminosity is fundamental because it represents the proportionality between the rate of the process, $R$, and its predicted cross section $\sigma$:

$$\mathrm{R}\ [\text{events s}^{-1}] = \mathcal{L}\ [\text{cm}^{-2}\text{s}^{-1}] \times \sigma\ [\text{cm}^{2}] \tag{2.1}$$

where $\mathcal{L}$ is the luminosity that is determined by the accelerator design since it reflects the amount of colliding particles. The cross section is constant in time, so the time integral of the luminosity (*integrated luminosity*) is therefore a measurement of the

expected number of events, $N$, produced in a finite time $\Delta T$:

$$N(\Delta T) = \sigma \int_{\Delta T} \mathcal{L}(t)\, dt \tag{2.2}$$

From this definition, the luminosity must be as high as possible for the study of very rare events. Assuming an ideal head-on $pp$ collision, the instantaneous luminosity depends only on the beam parameters and can be written as follows for a Gaussian beam profile:

$$\mathcal{L} = \frac{N_b n_1 n_2 f}{4\pi\sigma_x\sigma_y} F \tag{2.3}$$

where $N_b$ is the number of bunches in a beam, $n_i$ is the number of protons in a bunch, $f$ is the LHC revolution frequency (11.245 kHz), $\sigma_x$ and $\sigma_y$ characterize the rms transverse beam sizes in the horizontal (bend) and vertical directions at the interaction point and $F$ is a reduction factor due to the crossing angle differences between the two beams. At the LHC the instantaneous luminosity reached the record values of $\mathcal{L} = 2 \times 10^{34}$ cm$^{-2}$s$^{-1}$ in 2017-2018. Later, in Sec. 6.2.1 the Tevatron collider will also be introduced since one measurement in this thesis is based on collision data produced at the Tevatron collider and collected by the CDF experiment. Before the advent of the LHC, the Tevatron accelerator held the record instantaneous luminosity of $4 \times 10^{32}$ cm$^{-2}$s$^{-1}$.

Most of the parameters for the LHC luminosity, including the revolution frequency and the beam intensity parameters, are accurately measured from various beam monitors. In more detail, the measurement of the beam profile is performed via dedicated scans, known as *van der Meer* (vdM) scans [80]. These special scans consist of moving the $pp$ beams across each other step-wise in the transverse plane. At each point the collision rate is measured providing with an effective determination of the beam height. The reduction factor and the beam profiles are measured by the various experiments using dedicated sub-detectors called lumino-meters. In ATLAS several lumino-meters measure the luminosity with multiple algorithms.

The high luminosity delivered by the LHC implies high collision rates - needed to search for new physics and probe the SM. As a direct consequence, multiple proton-proton collisions occur whenever two bunches of protons cross. Interesting hard high-energy events - events characterized by a *hard scatter vertex* - are then contaminated by multiple soft QCD interactions - characterized by additional soft vertices. These

soft vertices, along with the signal hard scatterer vertex, form what are better known as pile-up events or simply *pile-up*. Based on their origins, there are two categories for pile-up events: *in-time pile-up*, caused by multiple soft collisions within the same event bunch crossing, and *out-of-time pile-up*, caused by collisions from different bunch crossings. The in-time pile-up is measured through the number of reconstructed primary events [81], while the out-of-time pile-up is measured through the average number of interactions [82]:

$$< \mu >= \frac{\mathcal{L}_{bunch} \cdot \sigma_{inel}}{f \cdot n_{bunch}} \tag{2.4}$$

where $\mathcal{L}_{bunch}$ is the per-bunch instantaneous luminosity, $n_{bunch}$ is the number of colliding bunches, $f$ is the LHC revolution frequency and $\sigma_{inel}$ is the inelastic cross section which is 80 mb at 13 TeV and was 73 (71.5) mb at 8 (7) TeV, as measured by the ATLAS collaboration [83]. The pile-up profile is shown in Fig. 2.2, as measured by the ATLAS collaboration in Run 2. From the plots it is evident how changes in the beam conditions (to increase the luminosity) result in a higher total average, $\mu$, with a pile-up peak of about 65 reported in 2017. This is an extraordinary performance for a collider. Before the advent of the LHC, at the Tevatron's luminosity peak $\mu$ was measured to be 10. At the LHC, the designed pile-up peak value of 25 has been passed after only ten years of operation.

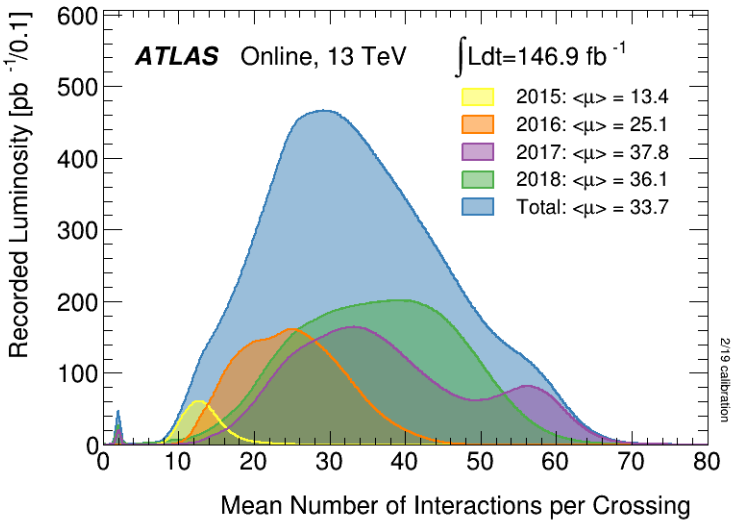


Figure 2.2: LHC pile-up profile in Run 2, as measured by the ATLAS detector [83].

**Centre-of-mass Energy.** Another key parameter for a collider is the centre-of-mass energy, $\sqrt{s}$, which defines the accessible phase space for the production of resonances in the final states. At the LHC $\sqrt{s}$ was increased after the upgrade from Run 1 to Run 2 moving from 7-8 TeV to 13 TeV thanks to an improvement of the performance of the superconducting-magnet cooling system. This is a record value for an accelerator (although it is still 1 TeV below the design value). In fact, at the Tevatron the maximum value achieved was 1.96 TeV.

Compared to $e^+e^-$ colliders, such as LEP, hadron colliders offer some advantages. Because of the emission of synchrotron radiation, LEP suffered very large energy losses compared to the LHC. Additionally, compared to the Tevatron, the LHC can benefit from higher luminosity since antiprotons are harder to produce compared to protons. However, at LEP the initial state energy was well known depending only on the beam energies since electrons and positrons are fundamental particles. On the contrary, protons and antiprotons are composed of quarks and gluons. Since the colliding quarks and gluons carry some fraction of the mother proton/antiproton momentum, the energy of the initial state is unknown at hadron colliders.

## 2.3 The ATLAS Detector

The ATLAS experiment [77] is a multi-purpose detector with a forward-backward symmetric cylindrical geometry with respect to the interaction and a nearly $4\pi$ solid angle coverage. The detector is 46 meters long, 25 meters in diameter and weighs approximately 7 000 tonnes. It has a total of 100 million readout channels which process particle collisions at a rate of 40 MHz, in time with the LHC fast 25 ns bunch crossings. ATLAS was designed to study 14 TeV $pp$ collisions and is able to precisely:

- detect electrically charged particles by bending their trajectories with a magnetic field and, exploiting the Lorentz force, to measure their electrical charge and momentum;
- reconstruct the primary collision vertex and possible secondary interaction vertices originating from long lived particles or pile-up events;
- obtain a measurement of hadronic and electromagnetic energy losses, which

are detected in electromagnetic calorimeters with scintillating material and hadronic calorimeters, respectively;

- detect muons which reach specific muon tracking chambers whose information is combined with that from the inner tracker to also provide a robust momentum measurement.

The excellent hermeticity of the detector allows for the reconstruction of the missing transverse momentum ($E_T^{miss}$ which is properly defined in Sec. 3.3.4) - which is a good indicator of the non-visible energy carried away by weakly or non-interacting particles, such as neutrinos, or new particles, such as dark matter candidates or the other weakly interacting particles described in Sec. 1.3. The identification of final states including these challenging signatures is crucial to either probe the SM or to search for new BSM physics - the main purposes of the ATLAS experiment and of the LHC. The observation of a new physics signal is experimentally performed by looking for an excess of data events over the SM expectation of the background.

**Coordinate System.** The ATLAS experiment uses a right-handed coordinate system with its origin at the nominal collision point (CP) in the centre of the detector and the $z$-axis along the beam pipe, as shown in Fig. 2.3. The $x$-axis points from the CP to the centre of the LHC ring, and the $y$-axis points upward. Cylindrical coordinates $(r, \phi)$ are used in the transverse plane, $\phi$ being the azimuthal angle around the $z$-axis. Throughout this thesis, the word *longitudinal* indicates the positive direction of the the $z$-axis and the word *transverse* indicates the plane perpendicular to the proton direction.

In hadron collisions, it is customary to use a variable invariant under $\hat{z}$ boosts as an unit of relativistic phase-space, instead of the polar angle $\theta$. This variable is the *rapidity* defined as :

$$y = \frac{1}{2} \ln\left[\frac{E + p \cdot \cos(\theta)}{E - p \cdot \cos(\theta)}\right] \tag{2.5}$$

where $(E, \vec{p})$ is the energy-momentum four-vector of the particle. Under a $\hat{z}$ boost to an inertial frame with velocity $\beta$, the rapidity of a particle transforms linearly, according to $y \to y' \equiv y + \tanh^{-1}(\beta)$, therefore $y$ is invariant since $dy \equiv dy'$. However, a measurement of rapidity still requires a detector with accurate identification capabilities because of the mass term entering $E$. Thus, for practical reasons, it is often

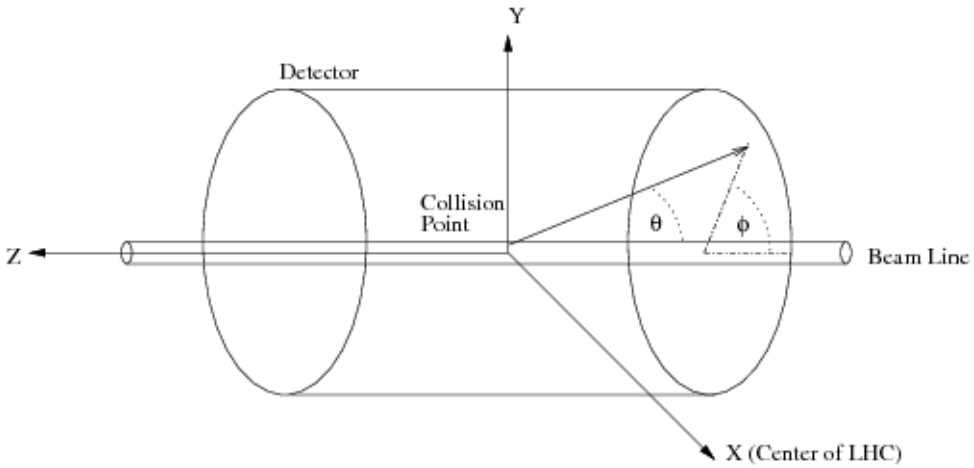


Figure 2.3: Coordinate system used by the ATLAS experiment. Figure from [84].

preferred to substitute $y$ with its approximate expression $\eta$ in the ultra-relativistic limit ($p \gg m$), usually valid for products of high-energy collisions:

$$y \xrightarrow{p \gg m} \eta + \mathcal{O}(m^2/p^2) \tag{2.6}$$

where the *pseudo-rapidity* is only function of $\theta$:

$$\eta = -\ln \tan\left(\frac{\theta}{2}\right) \tag{2.7}$$

Another commonly used variable is the transverse component of the momentum with respect to the beam axis ($p_T$), defined as:

$$\vec{p}_T \equiv (p_x, p_y) \rightarrow p_T \equiv p \cdot \sin(\theta). \tag{2.8}$$

The ATLAS detector is schematically shown in Fig. 2.4. It is conventionally divided into three regions: a central barrel with coverage $|\eta| < 1.05$ and two forward endcaps with coverage $1.05 < |\eta| < 2.4$.

Starting from the interaction point, particles generated from the $pp$ collisions encounter in sequence:

- The thin beryllium wall of the *beam vacuum pipe*.
- The high-precision tracking system, the *Inner Detector*, which provides the reconstruction of charged-particle trajectories. It consists of a silicon pixel

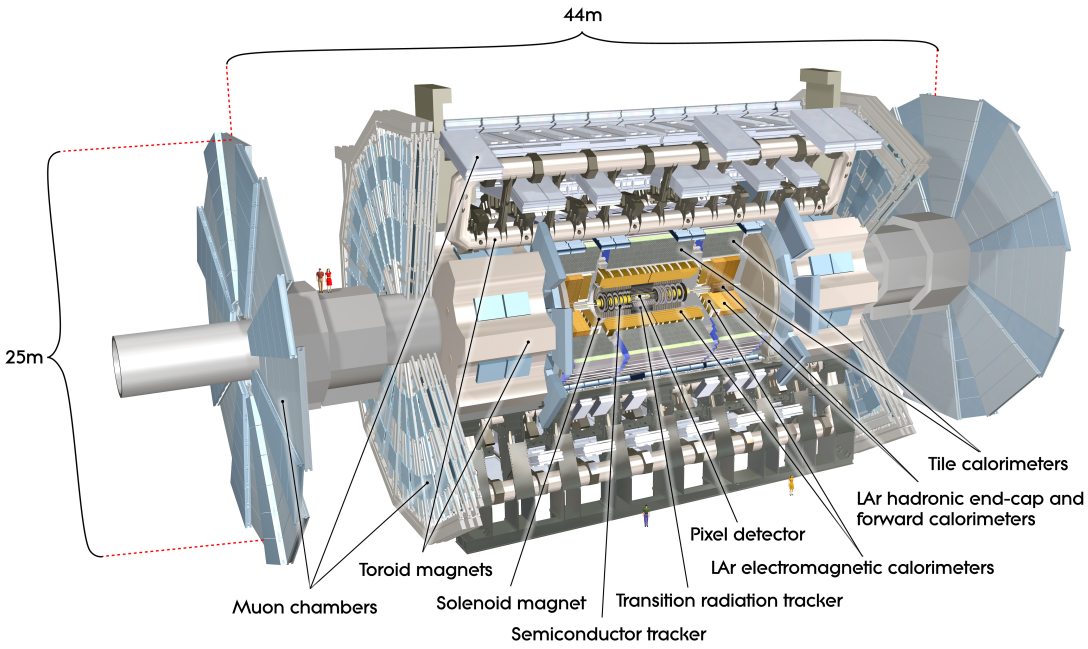


Figure 2.4: Cut-away view of the ATLAS detector. Figure from [85].

detector, a silicon microstrip detector and a transition-radiation tracker.

- A thin superconducting *solenoid*, which provides a 2 T magnetic field.
- A finely segmented *calorimeter system* including electromagnetic and hadronic calorimeters with a projective tower geometry. They measure the energy of electrons and photons and the energy of hadronic particles, respectively. The basic structures consist of alternating layers of liquid argon (LAr) as active material and lead as passive absorber for the electromagnetic calorimeter and LAr technology with a copper absorber or active scintillating tiles with steel as absorbing material for the hadronic calorimeter.
- A *muon spectrometer system* used to detect muons, which are the only charged particles able to reach this detector. The muon system incorporates large superconducting *toroidal* air-core magnets surrounding the calorimeters. There are three toroidal magnets, one in the barrel and two in the endcaps. Each of them is composed of eight coils resulting in a magnetic field with a bending integral of about 2.5 Tm in the barrel and up to 6 Tm in the endcaps.

The $pp$ interaction rate at the LHC design luminosity of $10^{34}\text{cm}^{-2}\text{s}^{-1}$ is approximately 1 GHz, while the limit on the event recording - based on the current technologies and resource limitations - is about a few hundred Hz. Therefore, an overall rejection factor of about $10^6$ against minimum-bias processes needs to be implemented. ATLAS has a sophisticated trigger system to achieve such a goal. In Run 2 the trigger system was upgraded and it is now composed of two stages. The first stage is known as *Level 1*. It is implemented with custom hardware, using information from calorimeters and muon chambers to reduce the event rate down to 100 kHz. The second stage, called the high-level trigger *HLT*, reduces the data acquisition rate to about 1 kHz on average. The HLT is software-based and runs reconstruction algorithms similar to those used in the offline reconstruction.

In the next sections, more details on each sub-detector are given. Some upgrade work performed during the long shutdown preceding Run 2 (from 2015 to 2018) is also described.

### 2.3.1 Inner Detector

The Inner Detector (ID) is the ATLAS tracker and is designed to provide accurate track reconstruction for charged particles produced in the interaction point with transverse momentum above a nominal threshold of 0.5 GeV as well vertex reconstruction for primary and secondary[1] vertices [86]. In a crowded environment, such as the LHC proton-proton collisions, a precise track reconstruction is crucial as it allows to measure both the position of the particle and its charge and momentum from the track curvature. The ID coverage is $|\eta| < 2.5$.

The ID layout is shown in Fig. 2.5. It consists of three independent but complementary sub-detectors:

- *the silicon pixel detector.* This detector is the innermost element of the ID [87]. It provides precise reconstruction of the event collision taking advantage of cutting-edge technologies. The active part of the pixel system consists of three barrel layers, at radii of 50.5 mm, 88.5 mm and 122.5 mm from the centre of the beam pipe. In addition, there are two identical endcap regions, each with three disk layers. In total, the pixel detector is made up of 1744 sensors, 250

[1]The location where unstable particles produced in the interaction point decay to lighter particles.

$\mu$m thick and with size 19 × 63 mm$^2$. Each pixel sensor is made up of 47 268 pixels of variable size. Most of them (90%) with a size 50 × 400 $\mu$m, while the remaining 10% with a size 50 × 600 $\mu$m. This results in a total area of about 1.7 m$^2$ and about 80 million readout channels.

During the shutdown preceding the LHC Run 2 (2012-2015), an additional layer was added to the pixel detector between the beam pipe and the innermost pixel - the *Insertable B Layer (IBL)* - to improve the performance in an intensive radiation environment [78]. After the Run 1 data-taking operations, in fact, in order to prevent a degradation of the precision measurement of the impact parameter from the pixel B-Layer detector, an additional layer was beneficial. The IBL is composed of cylindrical support structures around the beam pipe, known as staves, which contain 3D silicon sensors. There are 14 staves and each of them contains 32 individual chips. In total about 26 880 new pixel sensors improved the ID performance. Fig. 2.6 shows the schematic view of the ID in Run 2 where also the IBL is shown.

The pixel detector is the first sensitive material a charged particle, produced in the interaction point, enters. Here it creates electron-hole pairs which, under the the action of a bias voltage of 150 V, drift to the cathode and anode parts of the sensors. Some amplification of the signal is needed during the charge collection in order to have an observable signal. The current resolution provided by the pixel detector is 10 $\mu$m in the $r-\phi$ plane and 115 $\mu$m in the $z(R)$ plane.

- *the SemiConductor Tracker (SCT).* This silicon microstrip detector is the intermediate component of the ID [88]. It consists of 8 strip layers in the barrel and 18 strip layers in the two endcap regions to provide 3D track reconstruction of charged particles. In total there are 4088 modules of silicon strip chambers and a total number of approximately 6.3 million readout channels. The charge of the particle is determined from the direction of the track bending under the solenoidal field and the momentum is obtained from the measurement of the sagitta. Each strip module is made of two sensors chained together to provide 768 strips per side of total length ~12 cm. In the endcap region, there is a set of strips running radially and a set of stereo strips at an angle of 40 mrad with a mean pitch of approximately 80 $\mu$m. This configuration is implemented to

resolve possible ambiguities in measurements.

- *the Transition Radiation Tracker (TRT).* This gaseous drift tube detector is the outermost detector of the ID, right outside the SCT [89]. It is a collection of polymide drift (straw) tubes with a diameter of 4 mm and gold-plated tungsten wire anodes at the centre. The gas composition in the tubes is $Xe/CO_2/O_2$ (70/27/3) with 5-10 mbar. Such a composition is chosen to maximize the capture rate of the transition radiation photons which are produced every time charged particles pass through media with two different dielectric constants. The TRT provides a large number of hits (about 36) per track with a coverage up to $|\eta| < 2.0$. It is conventionally divided into a barrel region ($|\eta| < 1.0$) and two endcap regions ($1.0 < |\eta| < 2.0$). The straws in the barrel are parallel to the beam axis and are 144 cm long with wires divided into two halves, approximately at $\eta = 0$. While, in the endcaps the straws are 37 cm longer and are arranged radially in wheels. In total there are about 351 000 readout channels. The TRT drift tubes provide a detailed reconstruction of the charged particle tracks resulting in the measurement of the ($R$, $\phi$) coordinates with an intrinsic accuracy of 130 $\mu$m per straw. Additionally, it also allows for the discrimination of electrons from pions thanks to transition radiation photons. Even though the TRT provides less precise momentum measurement compared to the SCT and Pixel detectors, the contribution of the straw tubes at the outer radius is significant since they compensate the lower precision with a large number of measurements and longer measured track length.

The combination of different detectors - precision trackers at small radii and the TRT at a larger radius - provides patter recognition and high-precision in both the $R - \phi$ and $z$ coordinates.

### 2.3.2 Calorimeters

The ATLAS calorimeter system consists of two separate subsystems, the electromagnetic and the hadronic calorimeters, assembled around the beam axis with full $\phi$-symmetry and coverage up to $|\eta| < 4.9$ [90]. This system is designed to provide reconstruction and capture of particles. Over the region matched to the ID, electrons, positrons and photons are exclusively captured in a Liquid Argon (LAr)

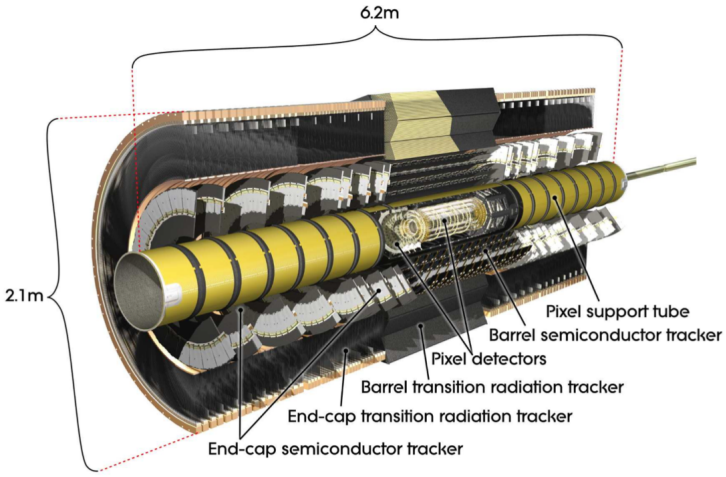


Figure 2.5: Layout of the ATLAS Inner Detector used in Run 1. Before the Run 2 data-taking operations, an additional silicon layer (IBL) was added, as explained in the text. Figure from [77].

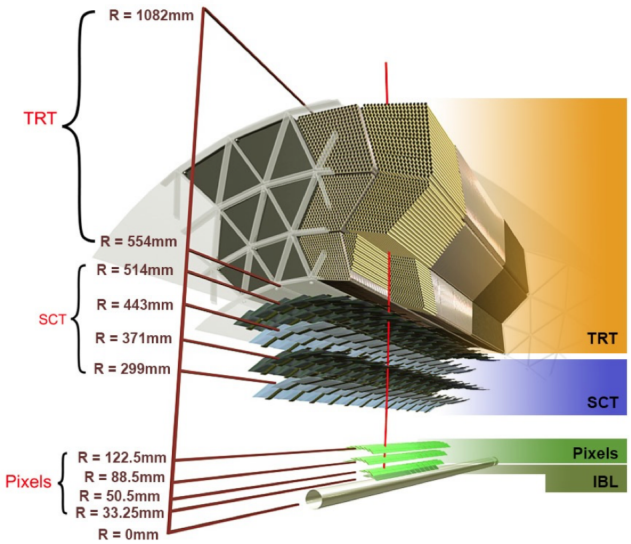


Figure 2.6: Layout of the ATLAS Inner Detector used in Run 2. Compared to the Run-1 configuration, a new pixel layer is added, the Insertable B-Layer (IBL). Figure from [78].

sampling calorimeter, also known as the electromagnetic calorimeter [91]. Hadrons, instead, are reconstructed via tile calorimeters in the central barrel regions and LAr

calorimeters in the forward endcap regions. The choice of LAr is motivated by several factors, such as its abundance, its radiation hardness and excellent energy resolution. The coarser granularity offered by the hadronic calorimeter is sufficient to satisfy the physics requirements for jet and $E_T^{miss}$ reconstruction. Electrons and photons passing through the electromagnetic calorimeter deposit their energy developing electromagnetic showers. In more detail, penetrating electrons (or positrons) emit photons through bremsstrahlung. The high energy photon produces $e^+e^-$ pairs, while the primary electrons (positrons) may emit additional photons depending on their initial energy. Secondary electrons (positrons) emit more photons which produce additional $e^+e^-$ pairs developing the shower profile. Particle multiplication continues until the mean particle energy equals roughly the critical energy. Below that value ionization and excitation losses dominate. Hadronic showers develop similar to electromagnetic showers. However, hadronic showers develop as a result of inelastic hadronic interactions of a primary particle with the nuclei of the target material. Produced secondary particles undergo further interactions and produce more particles. Among these particles, electrons and photons develop electromagnetic showers. As a result, due to the multitude of possible processes the development of a hadronic shower is considerably more complicated compared to an electromagnetic shower. Therefore, given the shower development in a calorimeter, a measurement of the initial energy of the particle requires the reconstruction and the confinement of the shower within the calorimeter, while the shower profile allows particle identification. A good calorimeter requires excellent hermeticity.

The layout of the ATLAS calorimeter system is shown in Fig. 2.7, it consists of two different calorimeters:

- LAr *Electromagnetic CALorimeter (ECAL).* The ECAL is divided into a barrel section ($|\eta| < 1.4$) and two ElectroMagnetic Endcap Calorimeter sections (EMEC with coverage $1.4 < |\eta| < 3.2$).

  The barrel is divided into three longitudinal layers which are shown in Figure 2.8. They allow for discrimination between electrons, photons and pions and provide useful information regarding the longitudinal shape of the shower. In addition, a pre-sampler sub-detector is placed before the LAr barrel, known simply as *pre-sampler*. In more detail, moving from the interaction point the longitudinal layers are structured as follows [93]:

- The *pre-sampler* which is composed of an active LAr layer of thickness 1.1 cm(0.5 cm) in the barrel(endcap) region. It doesn't contain an absorber material and is built with very high granularity in order to measure the energy lost by the particles before entering the calorimeter system [94]. The matter in front of the EMEC for the barrel cryostat and the inner detector services would degrade the energy measurement in the region $1.5 < |\eta| < 1.8$. The pre-sampler helps recover good performances in this region.
- The *front layer* which has the finest granularity in $\phi$ and is composed of $\Delta\eta = 0.0031$ strips to allow for $\gamma/\pi^0$ and $e/\pi$ separation and to provide a precise position measurement in $\eta$. Including the material in front of the active volume, this layer extends up to 6 radiation lengths ($X_0$).
- The *middle layer* which occupies most of the radial depth up to 16 $X_0$ and is segmented in towers of $\Delta\eta \times \Delta\phi = 0.025 \times 0.025$, and usually contains most of the showers initiated by electrons and photons.
- The *back layer* which provides two additional $X_0$ of $\Delta\eta \times \Delta\phi = 0.050 \times 0.025$ towers. It is added to cover for the tails of large showers initiated by high energy electrons and photons. It also acts as a presampler for the hadronic calorimeter.

Each EMEC is mechanically divided into two coaxial wheels: an outer wheel ($1.375 < |\eta| < 2.5$) and an inner wheel ($2.5 < |\eta| < 3.2$). Similar to the barrel, the EMEC has an accordion geometry, but rotated by 90 degrees to ensure complete $\phi$ symmetry with no azimuthal cracks. The LAr sampling calorimeter is made of interchangeable lead/stainless steel absorbers and sub-detectors to measure the energy deposit. These sub-detectors are electrodes submerged in LAr cooled to a temperature of 88 K. A particle passing through them in the LAr frees ions and electrons, which - under the action of the electric field - drift towards the electrodes. The collected signal is amplified and is proportional to the initial energy of the charged particle.

The transition region between the barrel and the endcaps ($1.37 < |\eta| < 1.52$) is generally excluded in physics analyses since it contains regions where detector support structures are placed and, therefore, doesn't provide accurate energy measurements.

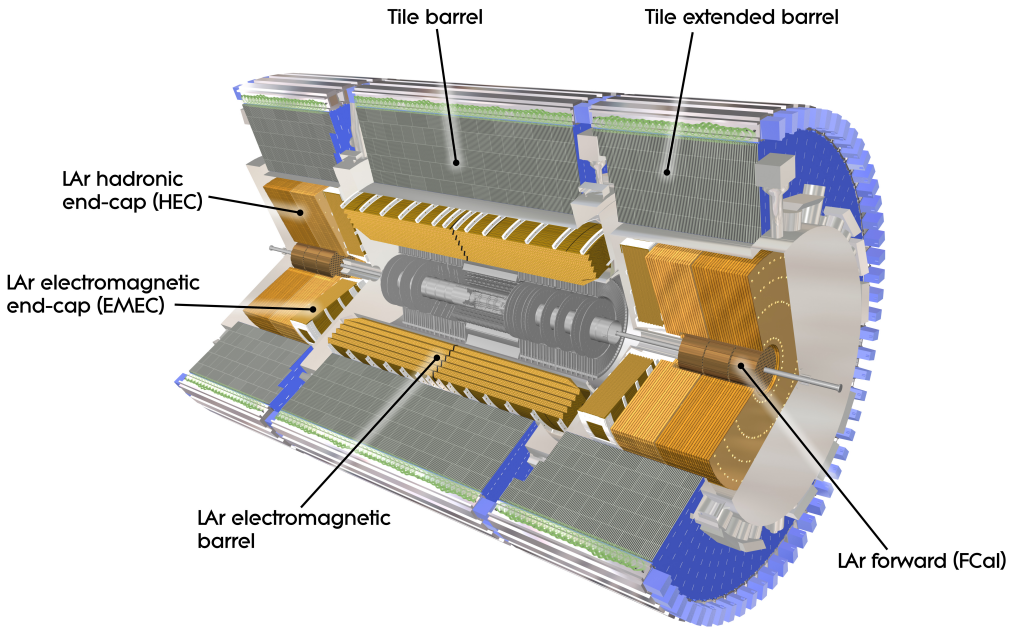


Figure 2.7: Layout of the ATLAS Calorimeter System with the various sub-detectors described in the text. Figure from [92].

- *Hadronic CALorimeter (HCAL).* The HCAL consists of three parts: the tile calorimeter [95], the LAr Hadronic Endcap Calorimeter (HEC) and the LAr Forward CALorimeter (FCAL). The tile calorimeter uses iron as the absorber and plastic scintillators as the active medium. It is located behind the LAr ECAL ($|\eta| < 1.7$) and is conventionally divided into three separate cylinders: central barrel ($|\eta| < 1.0$) and two extended barrels ($0.8 < |\eta| < 1.7$). Each barrel consists of 64 modules or wedges of size $\Delta\phi \sim 0.1$ rad and it is segmented in depth in three layers, approximately 1.5, 4.1 and 1.8 interaction lengths ($\lambda$) thick for the barrel and 1.5, 2.6, and 3.3$\lambda$ for the extended barrels.

  A particle passing through the scintillator tiles produces excitations in the atoms which result in a light-signal when the atoms de-excite. The light generated in each plastic scintillator is collected at two edges, and then transported to photomultiplier (PMT) tubes by some wavelength shifting fibers. The signal is amplified and finally detected. In more detail, the read-out cell geometry is defined by grouping the fibres from individual tiles on the corresponding PMT. Each cell is read out on each side (edge) by one PMT, each

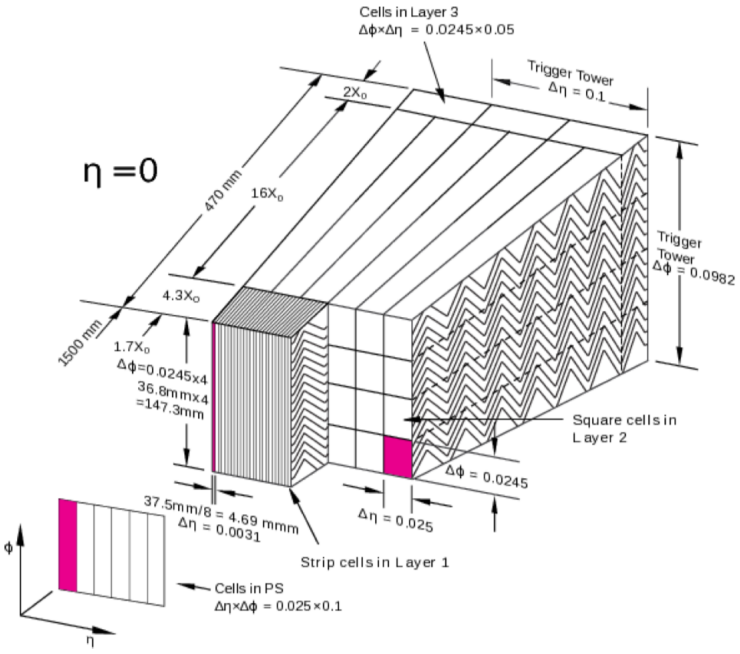


Figure 2.8: Layout and segmentation of the ATLAS Electromagnetic barrel CALorimeter (ECAL) and the pre-sampler. Figure from [91].

corresponding to one channel. The maximum height of the analogue pulse in a channel is proportional to the amount of energy deposited by the incident particle in the corresponding cell.

The HEC is located beyond the barrel ($1.5 < |\eta| < 3.2$) and consists of two wheels per endcap. The HEC extends up to $|\eta| = 3.2$ in order to reduce the drop in material density at the transition between the endcap and the forward calorimeters, thereby providing overlap with the FCAL. Each wheel uses flat parallel copper plates as the absorber material and LAr as the active material.

Finally, the FCAL is located in the same cryostat as the endcap calorimeters with coverage $3.1< |\eta| < 4.9$ and has a different design compared to the LAr calorimeters to improve the radiation robustness. The main feature is the high-density design - approximately $10\lambda$ deep - and it consists of three modules in each end-cap. The first is made of copper - it is optimized for electromagnetic measurements - the second and the third modules, instead, are made of tungsten - they are designed to measure predominantly the energy of hadronic interactions. Each FCAL module consists of an absorber matrix

with cylindrical electrodes arranged parallel to the beam pipe. Each electrode consists of a rod - the anode - inside a tube - the cathode - with a narrow annular gap between the two filled with LAr acting as the sensitive material.

### 2.3.3 Muon Spectrometer

The Muon Spectrometer (MS) [96] is the largest and outermost of the ATLAS sub-detectors. It is designed to detect muons in the pseudorapidity region up to $|\eta| = 2.7$, and to provide muon momentum measurements with a relative resolution better than 3% over a wide $p_T$ range and up to 10% at $p_T \sim 1$ TeV. It also provides (special trigger chambers) a muon trigger in the region $|\eta| < 2.7$. The design of the MS is based on the magnetic deflection of muon tracks. The spectrometer is split into three regions: a central *barrel* section with $|\eta| < 1.05$ and two *endcap* regions with $1.05 < |\eta| < 2.7$. A system of three large superconducting air-core toroid magnets provides a magnetic field with a bending integral of about 2.5 Tm in the barrel and up to 6 Tm in the end-caps. The region $1.0 < |\eta| < 1.4$ is usually referred to as the transition region, where the muon magnetic deflection is provided by a combination of barrel and end-cap fields. This magnet configuration provides a field which is mostly orthogonal to the muon trajectories. Compared to other magnet geometries which implement an iron magnet return yoke, such as the CMS detector, the ATLAS magnet geometry minimizes the degradation of the resolution due to multiple scattering in iron since there is no iron yoke instrumented. The MS layout is shown in Fig. 2.9.

Tracking, triggering and momentum measurements are provided by ~4 000 muon chambers. The MS is composed of four different types of muon chambers:

- *Monitored Drift Tubes (MDTs).* These chambers provide precision momentum measurement in the range $|\eta| < 2.7$, with the exception of the innermost endcap layer where their coverage is limited to $|\eta| < 2.0$. The MDTs are made from pressured drift tubes, with diameter ~29.970 mm, which hold a $Ar/CO_2$ gas (93/7) at 3 atmospheric bars [98]. In total there are 1 088 drift tube chambers covering an area of 5 500 $m^2$. They are arranged in three sequential layers. Ionization electrons are collected at a central tungsten-rhenium wire operating at a 3 080 V. Each MDT chamber provides six to eight $\eta$ measurements along

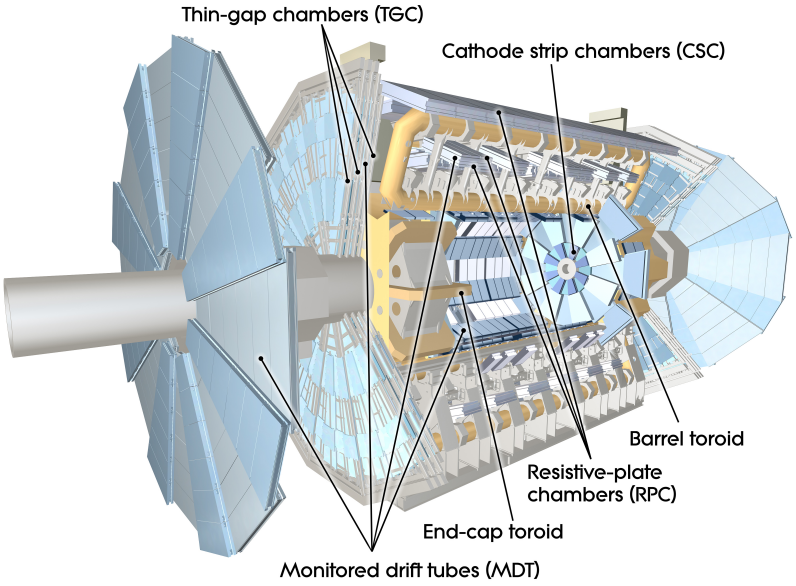


Figure 2.9: Layout of the ATLAS Muon Spectrometer and the various muon chambers described in the text. Figure from [97].

the muon track resulting in a per-hit resolution of 80 $\mu$m with an alignment precision of 30 $\mu$m.

- *Cathode Strip Chambers (CSCs).* These chambers are used in the endcap region $2.0 < |\eta| < 2.7$. In fact, due to their higher rate capability and excellent time resolution, they provide a better spatial measurement than MDTs (which instead suffer from the higher radiation flux in the forward region) [99]. The CSCs are multi-wire proportional chambers with cathodes segmented into orthogonal strips allowing for the measurement of both spatial coordinates. They are divided into two disks with eight chambers. Each chamber operates at a voltage of 1 900 V - with a gas mixtures $Ar/CO_2$ (80//20) - and has four planes resulting in four independent ($\eta$, $\phi$) readouts. Compared to the MDTs, the CSCs provide a per-hit resolution of ~60 $\mu$m, but with a worse alignment precision of ~60 $\mu$m.

- *Resistive Plate Chambers (RPCs).* Due to the good spatial and time resolution as well as excellent rate tolerance, these chambers are used as trigger detectors in the barrel region ($|\eta| < 1.05$). The RPCs are composed of three concentric cylindrical layers around the beam axis, referred to as stations. Each layer

contains parallel electrode plates with a gaseous mixture [100]. When a muon passes through the detector, an ionisation avalanche is created which is then collected at each electrode. A timing resolution of 5 ns is possible due to the electric field strength of 4.9 kV/mm. The stations are placed in a way that allows for triggering on low-$p_T$ muons (about 6 - 9 GeV) in the first two layers and on high-$p_T$ muons (about 9 - 35 GeV) in the second two layers.

- *Thin Gap Chambers (TGCs).* These chambers act as trigger detectors in the endcap region ($1.05 < |\eta| < 2.4$). They operate similarly to the multi-wire proportional chambers used for the CSCs [101]. The large voltage potential of 2 900 V results in a large electric field strength - which combined with the small wire-to-wire separation - provides a good time resolution and high rate capability. The TGCs achieve a spatial per-hit resolution of 2 - 6 mm in the radial coordinate and 3 - 7 mm in the azimuth.

During the shutdown preceding the LHC Run 2 several upgrades were implemented to improve the performance at higher rates. Additional muon chambers were added in the MS transition region between the barrel and the endcaps ($1.0 < |\eta| < 1.4$) and four RPC-equipped MDT chambers were installed inside two elevator shafts to improve the acceptance in that region compared to Run 1 [102]. As a result, the MS provides a spatial resolution of 5 - 10 mm while the timing precision is approximately 15 - 25 ns allowing for fast triggering and reliable beam-crossing identification.

### 2.3.4 Trigger System

The ATLAS trigger system is designed to reduce the flow of data to manageable levels selecting only events which are important for results. The trigger system selects approximately 1 000 of the 1.7 billion proton-proton collisions that occur each second in the centre of the ATLAS detector.

During the long shutdown preceding Run 2, the ATLAS trigger system was upgraded to cope with the large 40 MHz collision rate and the short 25 ns bunch spacing [103]. The current ATLAS trigger system carries out the selection process in two stages:

1. *the Level-1 (L1) hardware trigger with a rate limit at 100 kHz.* It consists of hardware equipment which performs a quick event selection based on a subset

of information from the calorimeter and muon detectors. The decision is made in approximately 2.5 $\mu$s. Two trigger algorithms are used, one uses calorimeter granularity information (L1 Calo) and the other gathers information from the muon detectors (L1 Muon).

The L1 Calo trigger algorithm implements a sliding window technique [104] to find local transverse energy maxima with a coverage up to $|\eta| < 4.9$ within two grids of *trigger towers*, which are groups of calorimeter cells with each tower in the barrel covering $0.1 \times 0.1$ in $\Delta\eta \times \Delta\phi$. One grid comes from the ECAL and one from the HCAL. Regions of interest (RoIs) corresponding to candidate objects are defined around the maxima.

In the L1 Muon algorithm, the RPCs and TGCs are used to trigger on muons. A muon track requires three hits in both the RPCs and the TGCs to be triggered. Exceptionally, low-$p_T$ muons in the RPCs require only two hits since their reconstruction is more challenging. As stated in Sec. 2.3.3, during the long-shutdown preceding Run 2, a fourth layer of RPCs was added to recover some trigger acceptances from losses due to support structures, services and cabling. Additional chambers were also installed to ensure improved $\eta$ coverage minimizing losses from acceptance holes.

2. *the High Level Trigger (HLT) with a rate limit at 1 kHz.* This trigger path is software based: it is a large farm of CPUs. At this level the decision is made based on either an overall examination of the whole event for specific layers of the detector (calorimeters, tracker and muon detectors) or on a subsample of data detected in smaller and isolated regions of the detector - the RoIs selected by the L1 trigger. In Run 1 the HLT consisted of a 2-level trigger path which required partial event data and event filter farms which analyzed the full detector information. After the Run 1 experience, the two levels have been merged into a single farm in order to reduce hardware and software complications and to better share resources.

The output events of the HLT are fully assembled into an event record and passed on to a data storage system for offline reconstruction calibration and physics analyses.

The ATLAS trigger menu includes dedicated triggers for electrons, muons, photons, $\tau$-leptons, jets and $E_T^{miss}$. These physics objects will be defined in Chapter 3. In addition, Minimum Bias (MB) triggers are also available. These triggers collect events using the minimum bias trigger scintillators [105] and are needed for specific studies of hadronisation, diffraction, total cross-section measurements and non-perturbative QCD. Similar to ATLAS, also the CDF experiment had a MB trigger. Since the CDF measurement reported in this thesis will be based on a kinematic region close to the regime of non-perturbative QCD, the MB trigger will be crucial. This will be described in Sec. 6.3.1.

Triggers in ATLAS are also classified into two major categories: *un-prescaled* and *prescaled* triggers. If un-prescaled, a trigger records all the events which pass the selection criteria. Prescaled triggers, on the contrary, reject a fraction of potentially interesting events to stay within the bandwidth limit. For instance, in Sec. 3.3.2.1 there will be a specific study for the dimuon trigger - which was partially prescaled - used for the $\Upsilon$ results reported in this thesis. For the ATLAS off-shell analysis in the $\ell\ell\nu\nu$ channel, single lepton triggers are used. They are described in Sec. 4.5.3.2.

## 2.4 ATLAS Data and Simulation

Every time that at least one of the ATLAS triggers fires, an *event* is labeled with an increasing number. Events are grouped into runs where a *run* is a period of continuous operation of the ATLAS Data Acquisition (DAQ) system. Several items of information, such as the position of the beam, are stored in a database on a run-averaged format. The LHC data used in this thesis were collected by the ATLAS detector in 2015 and in 2016 during the LHC Run 2 data-taking operations at a centre-of-mass energy of 13 TeV with a 25 ns bunch spacing. The total integrated luminosity delivered by the LHC was 42.7 fb$^{-1}$. However, due to reconstruction losses or periods with some ATLAS sub-detectors switched off, only 36.1 fb$^{-1}$ are used for physics analyses.

At the end of the LHC Run 2 data-taking operations, the LHC exceeded the luminosity expectation of 150 fb$^{-1}$ delivering a total integrated luminosity of 156 fb$^{-1}$. A significant fraction of it - 147 fb$^{-1}$ - was recorded by the ATLAS detector and 139 fb$^{-1}$ passed the good-physics selection criteria. This is the Run-2 sample to be scrutinized by ATLAS physicists when searching for new physics and probing

the SM. Fig. 2.10 shows the exceptional total integrated luminosity delivered by the LHC and collected by the ATLAS detector in Run 2, from 2015 to 2018. All the ATLAS results reported in this thesis will be updated in the future years using the full Run 2 dataset.

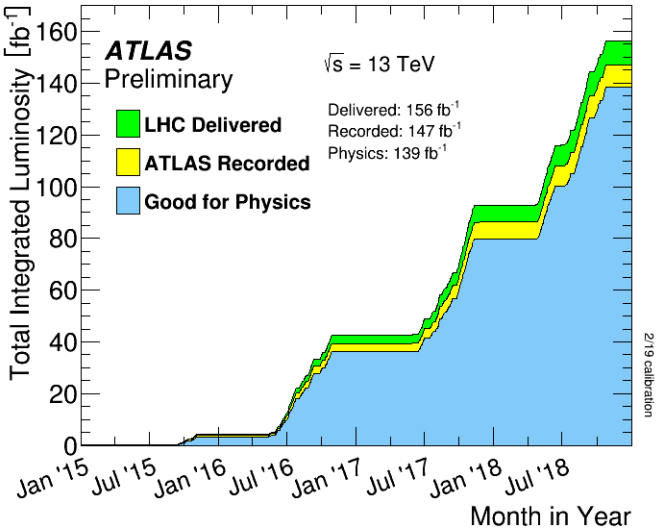


Figure 2.10: Total integrated luminosity delivered by the LHC and recorded by the ATLAS detector during the Run 2 data-taking operations, from 2015 to 2018. The sub-sample considered good for physics is also shown. Figure from [83].

During Run 2, the ATLAS collaboration redesigned its event data model (EDM) in order to reduce the complexity of the previous system used in Run 1 [106]. The common data format encouraged by the ATLAS collaboration is the xAODs format. It provides the full information of the event-level reconstruction. However, since only a small part of it is needed for physics analyses - typically $\mathcal{O}(\sim 1-2\%)$ - depending on the physics needs there are ad hoc derivations - DxAODs format - reduced in size to contain only the relevant information for the specific physics analysis.

Monte Carlo (MC) simulations of physics events and of the detector response are essential for high-energy physics experiments. They are needed for both the design and the development of the reconstruction and identification algorithms, as well as for the interpretation of physics results.

The ATLAS simulation program is integrated into the Athena framework [107] and uses the GEANT4 [108–110] simulation toolkit. The simulation software chain can be split into three main steps:

- Generation of the event;
- simulation of the detector response and physics interactions;
- digitization of the energy deposited in the sensitive regions of the detector.

The output of this chain is generally conveniently presented in a format identical to the output of the ATLAS DAQ in a way that it can be run through the ATLAS trigger and reconstruction packages similar to real data. Both data and simulation follows the xAOD file format.

MC generators mimic the interaction by calculating the matrix elements for the scattering of needed processes to a given precision. Different MC generators are used to calculate the scattering matrix amplitudes and generate the hard scatter process. Among them, POWHEG [111,112] and SHERPA [113–116] are the most widely adopted and are the ones used for the ATLAS results in this thesis. The parton kinematics of the proton-proton interactions is described by Parton Distribution Functions (PDFs) [117–119]. Parton Shower (PS) algorithms [118,120,121] provide the initial and final state parton showers. Different sets of PDFs are available depending on the physics needs. For the ATLAS results in this thesis, the CT10 [122] and NNPDF3.0 [118] sets are used, but differences due to this choice are included as systematic uncertainties. Later, MC generators are interfaced with the PYTHIA8 event generator [123–125], which simulates the PS, underlying events and the subsequent hadronisation. In order to guarantee a realistic pile-up profile, the mean number of interactions, $\mu$, is reweighted to the observed distribution preventing possible mismodelings at the initial simulation stage. Finally, $b$- and $c$-hadron decays are reproduced using the EVTGEN V1.2.0 program [126].

# Chapter 3

# Physics Objects Reconstruction

*In this chapter I describe the reconstruction of all the physics objects used for the ATLAS off-shell analysis in the $2\ell 2\nu$ channel. I first introduce charged-particle tracks and then I describe electrons, muons, jets and finally Missing Transverse Momentum ($E_T^{miss}$). In the muon section, I also report on the work I performed with the ATLAS Muon Combined Performance Group (MCP). Since my first day in ATLAS, I worked on the muon momentum corrections to be applied to the ATLAS simulation to improve the data/MC agreement. This was initially my qualification task to become an author of the ATLAS Collaboration. After completion of my task, since I liked the group and the project, I stayed in the group. I was involved in producing several Public Plots needed for International Conferences, such as ICHEP2016, LHCC2017, Moriond2017 and ICNFP2017 and finally I developed ad hoc frameworks to include the $\Upsilon(\rightarrow \mu\mu)$ resonance as a validation channel for the corrections, harmonizing them with the other frameworks developed in MCP for the $Z$ and $J/\psi$ resonances. In May 2019 I was Contact Editor and Analysis Contact for a Public Note on these activities. I wrote the publication and I was in charge of all the replies for the comments received during the ATLAS internal review. The Public Note was published during the fourth year of my DPhil. I finally presented these results in a summary talk on behalf of ATLAS and CMS at LHCP2019: "*Lepton and photon reconstruction and identification performance in ATLAS and CMS*".*

## 3.1 Introduction

The Higgs boson is not stable, it decays into products that carry the original energy of the mother Higgs particle. The focus of this thesis is the SM decay of the Higgs particle to a pair of $Z$ bosons, $H^* \to ZZ$. The $Z$ bosons themselves are also not stable particles, they quickly decay to lighter particles. In this thesis a specific final state is considered, when one of the two $Z$ bosons decays to a pair of electrons or muons - $Z \to e^+e^-$ or $Z \to \mu^+\mu^-$ - and the other decays to a pair of neutrino leptons - $Z \to \nu\bar{\nu}$ - from one of the three lepton flavours ($\nu_e$, $\nu_\mu$ and $\nu_\tau$). Even though $Z$ decays to a pair of tau leptons - $Z \to \tau^+\tau^-$ - are not considered in this analysis, in this thesis the visible decay of the $Z$ boson is referred to as $Z \to \ell\ell$ which, properly, should also include decays to a pair of $\tau$ leptons. Electrons are reconstructed using tracking and calorimeter information, while muons also use the Muon Spectrometer information. Neutrinos interact only weakly with ordinary matter and don't leave visible tracks in the ATLAS detectors. They are generally quantified by the amount of missing transverse momentum $E_T^{miss}$ measured in the ATLAS detector. Photons and $\tau$-leptons are not selected in this analysis but are reconstructed as jets. The Higgs production is studied inclusively in the jet multiplicity, i.e. there are no individual categories for cases with one, two or more jets.

To summarize, the decay channel studied in this thesis is $H \to ZZ \to \ell\ell\nu\nu$ or, equivalently[1], $H \to ZZ \to \ell\ell + E_T^{miss}$.

Since charged leptons are reconstructed as tracks in the ATLAS Inner Detector, the first section, Sec. 3.2, is dedicated to the track reconstruction and track-quality criteria implemented in ATLAS. Later, the individual physics objects of interest are described in Sec. 3.3 with a focus on electrons in Sec. 3.3.1, on muons in Sec. 3.3.2, on jets in Sec. 3.3.3 and finally on Missing Transverse Momentum $E_T^{miss}$ in Sec. 3.3.4.

## 3.2 Tracks

Tracks of charged particles are reconstructed in the ATLAS detector via two independent sub-detectors, the ID, close to the interaction point, and the MS. While the ID has to deal with high track density which imposes a large track-combinatorial

[1]Both the formalisms are used throughout this thesis.

background, the MS track reconstruction is mainly limited by the huge amount of inert material, the cavern background and the highly inhomogeneous magnetic field. Track reconstruction in the MS is mainly intended for muons and is described in Sec. 3.3.2. Track reconstruction in the ID is a three-stage procedure:

- *Pre-processing stage.* Raw data from the pixel and SCT detectors are converted into clusters and the TRT raw timing information is converted into calibrated drift circles. During this step, SCT clusters are translated into space-points.

- *Track-finding stage.* Different tracking algorithms are implemented for different applications. The ATLAS default tracking path is an *inside-out* algorithm, which exploits the high granularity of the pixel and SCT detectors to search for prompt tracks originating from the interaction region. Track seeds are initially formed from a combination of space-points in the three pixel layers and the first SCT layer. A final track candidate is formed by extending the seed throughout the SCT. Track candidates are then fitted, 'outlier' clusters and ambiguities in the cluster-to-track match are removed. The implementation of track quality criteria allows to reject fake tracks. Track candidates are later improved by including the TRT information which associates drift-circle information in a road around the extrapolation and resolves left-right ambiguities. Extended track candidates are re-fitted with information from all three detectors. Fit quality of the extended track candidates is compared to the fit quality of the initial track candidates and extension hits resulting in lower-quality candidates are labeled as 'outliers'.

  Complementary to the *inside-out* track-finding sequence, an *outside-in* approach is also implemented. Unused TRT track segments are extrapolated back to the SCT and pixel detectors to improve the tracking efficiency for secondary tracks from conversions or decays of long-lived particles.

- *Post-processing stage.* A dedicated vertex finder is used to reconstruct primary vertices. The primary vertex is defined as the point where the hard scatter interaction occurs. The reconstruction of primary vertices [127] is performed using two sequential algorithms: 1) the *primary-vertex finding* algorithm, which associates reconstructed tracks to vertex candidates. Points with the largest sum of track momenta ($\sum p_T^2$) are selected as candidates; 2) the *vertex-fitting*

algorithm, which reconstructs the vertex position and its corresponding error matrix. A single primary vertex is defined per event collision, while the other 'softer' vertices come from pile-up events. Vertices reconstructed at some distance from the primary impact point are classified as *secondary vertices*. They originate from a few sources, such as long-lived $b$-hadron decays or photon conversions. The measurement of primary vertices allows the definition of the *track impact parameters* ($d_0$,$z_0$) and their related uncertainties ($\sigma_{d_0}$,$\sigma_{z_0}$). The transverse impact parameter $d_0$ quantifies the distance of the closest approach of the track to the beam-line, while the longitudinal impact parameter $z_0$ defines the value of the coordinate $z$ (the axis along the beam-line) where the $d_0$ point is determined. They are defined with respect to the centre of the luminous region[2]. The impact-parameter resolution is sensitive to the resolution of the primary vertex, provided by the resolution of the individual measurements in the pixel detector. Such measurements are sensitive to the ID alignment, and thus, ID mis-alignments are throughly investigated to minimize any potential bias in the impact-parameter measurements [128] [129].

The overall coverage provided by all the ID components extends up to $|\eta| < 2.5$. Reconstructed tracks are used as inputs for the reconstruction of physics objects ($e^{\pm}$, $\mu^{\pm}$ etc.) which requires combination with other ATLAS sub-detectors, such as calorimeters and the MS. The loose selection criteria for tracks require a minimum track $p_T$ threshold of 400 MeV and a minimum number of 7 hits in the silicon detector. Further requirements are applied on the number of detector shared modules and holes[3].

## 3.3 Physics Objects

Track and calorimeter objects which have passed reconstruction and identification selection criteria are defined *physics objects*. Depending on their nature, they are classified as electrons, muons or - if they are composed of a shower of particles - as

[2]The ATLAS luminous region is determined during a physics run, generally every ~10 minutes, by applying an unbinned maximum likelihood fit to the distribution of primary vertices recorded in the allocated period, with no beam-spot constraints.

[3]Shared modules are either hits in the pixel detector used by more than one track candidate or shared hits in the same SCT layer. Holes are intersections of reconstructed track trajectories where the hit information from a sensitive sub-detector is missing.

jets. These physics objects are the ones used in physics analyses to reconstruct events of interest and search for new physics. In this section each of them is described.

### 3.3.1 Electrons

Many of the interesting physics processes to be measured at the LHC have a signature including one or more isolated electrons. A large background is present, though. It includes mis-identified hadrons, electrons from photon conversions and non-isolated electrons originating from heavy-flavour decays. It is thus crucial to efficiently reconstruct and identify electrons over the full ATLAS acceptance and, at the same time, reject the significant background contamination. This is done by using a combination of information from various sub-detectors. Silicon detectors and TRT hits together with the energy deposit measured by the longitudinally layered ECAL system with fine lateral segmentation are able to reconstruct and identify electron candidates. Hadronic calorimeters contribute vetoing particles which give rise to significant hadronic activity.

#### Reconstruction and Identification

When reconstructing electrons in ATLAS, in order to reject contamination by converted photons, pairs of tracks in the innermost layer of the silicon detector - the Insertable B-Layer - are not kept if they lead to a very small invariant mass. Topologically connected clusters are defined to collect calorimeter signals of a given collision event in order to extract the significant signal from a background of electronic noise and other sources of fluctuations such as pile-up. Topological clusters are also known as *topoclusters*. In practice, they are groups of calorimeter cells designed to follow the shower development taking advantage of the fine segmentation of the ATLAS calorimeters.

An initial match between tracks from the Inner Detector with energy clusters in the ECAL is performed to select electron candidates.

Electron reconstruction can be split in three steps:

- Cluster 'seeds' are formed using a sliding window algorithm with fixed size granularity of 3 × 5 elements (towers) of size $\Delta\eta \times \Delta\phi = 0.025{\times}0.025$. A clustering algorithm then reconstructs clusters around the seed [130] with an efficiency above 99% for $E_T \geq 15$ GeV.

- Track reconstruction is then performed by implementing a pattern recognition algorithm, which depends on the electron energy loss.

- Finally, the cluster seed is matched to the track candidate. It can happen that more than one track is in very close proximity to the seed cluster. In such cases, an algorithm chooses the best track candidate based on the track-cluster distance and the number of pixel hits.

The measurement of the electron energy is provided by the final calibrated cluster, while the ($\phi$, $\eta$) electron coordinates are provided by the track. Recently, a dynamic, topological cell clustering-based approach has been adopted [131] [132]. The new strategy allows for improved measurements of electron and photon energies, with a special focus on cases where an electron radiates a bremsstrahlung photon, or a photon converts to an $e^+e^-$ pair. The main reason preventing the application of the new technique in the past was the inability to apply the simultaneous calibration strategy to the dynamically-sized clusters. The advent of new multivariate techniques has made this possible allowing for a new energy calibration, where regression decision trees are trained to correct the uncalibrated energy of electrons and photons. However, for the 2015-2016 dataset used in this analysis, this technique was not available. Electrons used for the measurement described in this thesis are reconstructed with the old fixed-size algorithm.

The electron identification relies on sequential and multivariate algorithms to reject electrons from photon conversions, hadronic jets or semileptonic hadron decays. A likelihood-based (LH) identification is implemented to select prompt electrons in the central region of the ATLAS detector ($|\eta| < 2.5$). Variables used in the LH include the longitudinal and lateral shower profiles, the electron's track conditions and the track-to-cluster matching. Combining all these different variables in a LH-based identification recovers electron candidates which fail a cut-based identification because they don't satisfy a selection criterion for a single quantity. The application of a set of track- and cluster-quality criteria defines different categories targeting specific signal efficiencies and/or background rejections. They are better known as Working Points (WPs). The 'Medium' WP is used as the ATLAS default WP. It reaches 90% efficiency for electrons with $E_T \sim 40$ GeV and improves for higher energy.

### Isolation

In order to differentiate the prompt production of electrons, muons and photons in signal processes - for instance decays of heavy resonances like Higgs, $W$ and $Z$ bosons - from background processes, isolation criteria are implemented. Signal events are characterized by a specific signature, i.e. low activity (both in the calorimeter and in the tracker) in an area $\Delta\eta \times \Delta\phi$ surrounding the trajectory of the candidate object. The activity in the vicinity of the candidate object, for instance an electron, is studied by summing the transverse energy of clusters in the calorimeter (calorimeter-based isolation) or the transverse momenta of tracks (track-based isolation) in a cone of radius $\Delta R = \sqrt{(\Delta\eta)^2 + (\Delta\phi)^2}$ around the electron direction, having subtracted the contribution of the electron itself. Both calorimeter- and track-based isolation variables are used in ATLAS. A topological cluster isolation algorithm, also known as topoetcone, which includes corrections for leakage and pile-up, is used as an isolation parameter for the calorimeter information. The $E_T^{topcone20}$ algorithm has an isolation cone radius of $\Delta R = 0.2$. Thanks to the fine granularity of the tracker, it is possible to use a variable cone size. The $p_T^{varcone}$ algorithm allows the cone size to vary as a function of the $p_T$ of the electron with $\Delta R = \min(10\ \text{GeV}/p_T, R)$ and $R$ in the range 0.2 - 0.4 for different algorithms.

Some WPs are defined. They consist of cuts applied on the two isolation variables. Depending on the signal efficiency or purity one wants to achieve, the cut values can be fixed or vary as a function of $E_T$. The 'Loose' isolation WP provides a flat 99% efficiency over the full range in $\eta$ and for $p_T$ up to 80 GeV.

### Efficiency Measurements

Reconstruction, identification, isolation and trigger efficiencies are measured using the tag-and-probe method applied to $Z \to ee$ and $J/\psi \to ee$ events. The method selects unbiased samples of electrons - the probe electron - by using strict selection requirements on the other decay electron - the tag electron. Efficiencies are then measured by applying the various requirements to the probe sample (after accounting for background contamination) following the various definitions. The reconstruction efficiency is measured from the ratio of the number of reconstructed electrons to the number of electron clusters in the ECAL, the identification efficiency is defined as the ratio of the number of identified electrons to the number of recon-

structed electrons. The trigger efficiency is defined as the ratio of the number of triggered electrons to the number of all the identified electrons. For a given trigger, the trigger efficiency is determined with respect to the offline identification algorithm and isolation working point. Finally, the isolation efficiency is defined as the ratio of the number of electrons which pass the identification and isolation requirement to the number of electrons able to pass only the identification criteria. Specific information on the electron candidates used in the off-shell analysis are given in Sec. 4.5.2.1.

### 3.3.2 Muons

Similar to electrons, muons are key to some of the most important physics results published by the ATLAS collaboration. The large background to be rejected includes mostly muons originating from in-flight decays of charged hadrons in the ID.

Muon identification is performed by applying quality requirements that suppress background contamination guaranteeing, at the same time, high efficiency and robust momentum measurements for prompt muons. This is done using information from the ID, the MS, and to a lesser extent, from the calorimeter.

#### Reconstruction and Identification

Muons are initially recontructed independently in the ID and MS [133]. A combined track is then formed by combining information from individual sub-detectors. Combined tracks are used in physics analyses. In the ID, muons are reconstructed like any other charged particles, as described in Sec. 3.2. In the MS muon track segments are formed by first searching for hit patterns inside each muon chamber. A muon track candidate is reconstructed by fitting together hits from segments in different layers. At least two matching segments are required to build a track, except in the barrel-endcap transition region where a single high-quality segment with $\eta$ and $\phi$ information can be used to build a track. Since the same segment can initially be used to build multiple track candidates, an overlap removal procedure is applied to ensure the best assignment only to a single track. The hits associated with each track candidate are fit using a global $\chi^2$ fit. A track candidate is accepted if the $\chi^2$ of the fit satisfies the selection criteria.

The ID-MS combination is performed according to various algorithms based on

the information provided by the ID, MS and calorimeters defining four muon *types*: Combined (CB), Segment-tagged (ST), Calorimeter-tagged (CT) and Extrapolated (ME) muons. For the results in this thesis, almost all the muons used are CB and ME muon *types*.

CB muon track reconstruction is performed independently in the ID and MS, and a combined track is formed with a global refit that uses the hits from both the ID and MS sub-detectors. During the global fit procedure, MS hits may be added to or removed from the track to improve the fit quality. Most muons are reconstructed following an *outside-in* pattern recognition, in which muons are first reconstructed in the MS and then extrapolated inward and matched to an ID track. An *inside-out* combined reconstruction, in which ID tracks are extrapolated outward and matched to MS tracks, is used as a complementary approach.

ME muon track reconstruction is based only on the MS track and on a loose requirement on compatibility with originating from the Interaction Point (IP). The parameters of the muon track are defined at the IP, taking into account the estimated energy loss of the muon in the calorimeters. Muons are required to traverse at least two layers of MS chambers to provide a track measurement, but three layers are required in the forward region. ME muons are mainly used to extend the acceptance for muon reconstruction into the region $2.5 < |\eta| < 2.7$, which is not covered by the ID.

The reconstruction of muon tracks suffers acceptance losses at $\eta \approx 0$ due to the MS being only partially equipped with muon chambers in order to provide space for the services for the ID and the calorimeters and in the transition region, $1.0 < |\eta| < 1.4$, between the barrel and the end-caps.

CB candidates have the highest muon purity. Quality requirements are applied to identify prompt muons from $J/\psi$ decays with high efficiency guaranteeing a robust momentum measurement and suppressing background.

The main background from pion and kaon decays is often characterized by a poor fit quality of the combined track with a low compatibility of the momentum measured in the ID and MS. Several variables offering good discrimination between prompt muons and background muon candidates are studied in simulated $t\bar{t}$ events. Muons from $W$ decays are categorized as signal muons while muon candidates from light-hadron decays are categorized as background. For CB tracks, the variables used in muon identification are:

- $q/p$ *significance*, defined as the absolute value of the difference between the ratio of the charge and momentum of the muons measured in the ID and MS divided by the sum in quadrature of the corresponding uncertainties;
- $\varrho'$, defined as the absolute value of the difference between the transverse momentum measurements in the ID and MS divided by the $p_T$ of the combined track;
- normalised $\chi^2$ of the combined track fit.

A robust momentum measurement is ensured by requiring a specific number of ID and MS hits:

- at least 1 pixel hit;
- at least 5 SCT hits;
- in the region of full TRT acceptance, $0.1 < |\eta| < 1.9$, at least 10% TRT hits originally assigned to the track are included in the final fit;
- fewer than three pixel and SCT holes;

where a hole, as already defined in Sec. 3.3.1, is an active sensor traversed by the track but containing no hits. A missing hit is considered a hole only when it falls between hits successfully assigned to a given track. If the track traverses a sensor known to be inefficient, the requirements on the number of pixel and SCT hits are reduced accordingly.

Four muon identification selections (*Loose*, *Medium*, *Tight*, and *High-*$p_T$) are provided to address the specific needs of different physics analyses. *Loose*, *Medium*, and *Tight* are inclusive categories meaning that muons identified with tighter requirements are also included in the looser categories. For the results reported in this thesis mainly *Medium* muons have been used. A new identification selection, *Low-*$p_T$ muons, is now available. This is a recent performance improvement, even though it is not used for the off-shell analysis described in this thesis.

The *Loose* identification criteria are designed to maximize the reconstruction efficiency while providing good-quality muon tracks. They were specifically introduced for reconstructing Higgs boson candidates in the four-lepton final state. CB

and ME muons satisfying the Medium requirements are included in the Loose selection. CT and ST types are restricted to the $|\eta| < 0.1$ region. For $|\eta| < 2.5$, about 97.5% of Loose muons are CB, while only 1.5% are CT and the remaining 1% are ST muon types.

The *Medium* identification criteria provide the default selection for muons in ATLAS. This selection minimises the systematic uncertainties associated with muon reconstruction and calibration. Only CB and ME tracks are used. The former are required to have ≥3 hits in at least two MDT layers, except for tracks in the $\eta < 0.1$ region, where tracks with at least one MDT layer but no more than one MDT hole layer are allowed. ME muons, instead, are required to have at least three MDT/CSC layers, and are employed only in the $2.5 < |\eta| < 2.7$ region to extend the acceptance outside the ID geometrical coverage. A loose selection on the compatibility between ID and MS momentum measurements is applied to suppress the contamination due to hadrons misidentified as muons. Specifically, the $q/p\ significance$ is required to be less than seven. In the pseudorapidity region $|\eta| < 2.5$, about 0.5% of the muons classified as Medium originate from the *inside-out* combined reconstruction strategy.

**Isolation**

Unlike muons from semileptonic decays, muons from Higgs or $Z/W$ boson decays are isolated. Similar to electrons, muon isolation WPs are thus introduced by defining an isolation cone around the muon candidate. Track- and calorimeter-based variables are used. The track-based variable - $p_T^{varcone30}$ - is defined as the sum of the transverse momenta of all tracks with $p_T > 1$ GeV in a cone of size $\Delta R = \min(10\ \text{GeV}/p_T, R = 0.3)$ around the muon. The calorimeter-based variable - $E_T^{topocone20}$ - is defined as the sum of the transverse energy of topological clusters in a cone of size $\Delta R = 0.2$ around the muon candidate. The 'LooseTrackOnly' isolation WP provides a flat 99% efficiency over the full range in $\eta$ and $p_T$.

During Run-2 operations ATLAS had to deal with high-pile-up events. In order to guarantee excellent isolation efficiencies for high values of pile-up events, an ad hoc optimization of the isolation selection has been performed in ATLAS defining new pile-up WPs. High isolation efficiency is maintained even at high values of the mean number of interactions per bunch crossing.

#### Efficiency Measurements

Similar to electrons, the tag-and-probe method is used to estimate the reconstruction, identification, isolation and trigger efficiency. Muons from $J/\psi \to \mu\mu$ and $Z \to \mu\mu$ are used to cover the whole momentum spectrum. The reconstruction efficiency is found to be ~ 99% for $|\eta| < 2.5$ and $p_T > 5$ GeV. The 'Loose' isolation WP uses loose cuts on the ratios $p_T^{varcone30}/p_T$ and $E_T^{topocone20}/p_T$ to guarantee a selection efficiency better than 98% over the whole $\eta$ and $p_T$ range. An additional reconstruction efficiency, called track-to-vertex-association (TTVA) is applied. This is needed to correct for impact-parameter ($d_0$, $z_0$) mis-modeling when comparing data and MC. Specific information on the muon candidates used in the off-shell analysis are given in Sec. 4.5.2.2.

### 3.3.2.1 Muon Momentum Scale and Resolution

In this section all the work I performed in the ATLAS MCP group is described. In more detail, in 2015 I joined the 'Momentum Scale and Resolution' sub-group and I am still part of this group.

In this section I will first introduce the muon momentum corrections and I later focus on the $\Upsilon$ resonance describing the samples used, the validation strategy and the fitting modeling [134]. Results are based on data collected by the ATLAS experiment in 2015-2016. In addition, some of the results I produced for the $Z$ and $J/\psi$ resonances are reported in the Appendix A [135].

#### Muon Momentum Corrections

The ATLAS simulation includes the best knowledge of the detector geometry, material distribution, and physics model of the muon interaction at the production phase of the MC events. However, this is not enough to reproduce the muon momentum scale(resolution) of data at the needed level of permille(percent) precision. Additional corrections are applied to achieve such data/MC agreement. Geometrical and misalignment corrections are applied when reconstructing data, while ideal geometry with no misalignments is simulated. Compared to the results reported in the previous paper [133], a new ATLAS Offline Software has been released. It includes improvements in the ID alignment, in the silicon energy-loss modeling and an improved use of the MS alignment uncertainties in the muon track-combined fit.

The large sample of muons from the $J/\psi \to \mu\mu$ and $Z \to \mu\mu$ decays collected by the ATLAS detector in 2015 and 2016 has been used to derive such corrections. The procedure used to derive the corrections to the simulated muon transverse momenta reconstructed in the ID and MS subdetectors is known as "muon momentum calibration". Only CB muons are used to extract the calibration parameters. The transverse momenta of the ID and MS component of a CB track are corrected separately allowing a direct understanding of the sources of the corrections. Thus, corrections are propagated to the CB momentum reconstruction using a weighted average assuming that the relative contributions of the two subdetectors to the combined track are unchanged after the momentum corrections. Formally:

$$p_T^{Corr,CB} = f \cdot p_T^{Corr,ID} + (1-f) \cdot p_T^{Corr,MS} \tag{3.1}$$

where $f$ is the weight derived from

$$p_T^{MC,CB} = f \cdot p_T^{MC,ID} + (1-f) \cdot p_T^{MC,MS}. \tag{3.2}$$

Since the material distribution and the alignment techniques adopted depends on the sector of the ATLAS detector considered, corrections are defined in different $\eta$-$\phi$ regions. In particular, the nominal muon identification acceptance region (up to $|\eta| = 2.7$) is divided in 18 $\eta$ sectors for both the MS and the ID. In addition, the MS is divided into two types of $\phi$ sectors of approximate size of $\pi/8$, exploiting the octagonal symmetry of the magnetic system: the sectors that include the magnet coils, *small sectors*, and the sectors between two coils, *large sectors*.

The corrected transverse momentum, $p_T^{Cor,Det}$ (Det= ID, MS), is derived assuming the following parametrization:

$$p_T^{Corr,Det} = \frac{p_T^{MC,Det} + \sum_{n=0}^{1} s_n^{Det}(\eta,\phi)(p_T^{MC,Det})^n}{1 + \sum_{m=0}^{2} \Delta r_m^{Det}(\eta,\phi)(p^{MC,Det})^{m-1} g_m} \tag{3.3}$$

where $p_T^{MC,Det}$ is the uncorrected transverse momentum in simulation, $g_m$ are normally distributed random variables with zero mean and unit width, and the terms $\Delta r_m^{Det}(\eta,\phi)$ and $s_n^{Det}(\eta,\phi)$ describe the momentum resolution smearing and the scale corrections valid in that specific $(\eta,\phi)$ region of the detector. Corrections to the

muon momentum scale cover for inaccuracies:

- in the knowledge of the radial dimension of the detector, and in the description of the magnetic field integral;
- in the simulation of the energy loss in the calorimeter and other materials between the interaction point and the MS.

Corrections to the muon momentum resolution assume that the relative $p_T$ resolution can be parametrized as follows:

$$\frac{\sigma(p_T)}{p_T} = r_0/p_T \oplus r_1 \oplus r_1 \cdot p_T \tag{3.4}$$

where $\oplus$ indicates the sum in quadrature. The first term accounts mainly for fluctuations of the energy loss in the traversed material, the second term accounts mainly for multiple scattering, local magnetic field inhomogeneities and local radial displacements of the hits, and the third term mainly describes intrinsic resolution effects caused by the spatial resolution of the hit measurements and by residual misalignment of the muon spectrometer. The energy loss term is negligible in both the ID and MS measurements.

The ID and MS corrections are extracted from data. A MC template binned maximum-likelihood fit is implemented to compare the simulation to data for $J/\psi \to \mu\mu$ and $Z \to \mu\mu$ candidate events allowing a sensitivity to reconstructed muon momenta in the $p_T$ range from a few GeV to ~100 GeV. In addition, some corrections are derived from alignment studies based on special runs with the toroidal magnetic field off. To improve the precision of the corrections, the $p_T$ and $\eta$ distributions of the $Z$ and $J/\psi$ resonances in simulation are reweighted to the distributions observed in data. More details about the "muon momentum calibration" are given in [133].

### Data and MC Samples

The results presented in this section are mostly obtained from the analysis of $\sqrt{s}$ = 13 TeV $pp$ collision events corresponding to an integrated luminosity of 36.5 fb$^{-1}$ collected by the ATLAS detector in 2015-2016 during the data-taking period in which the inter-bunch crossing was 25 ns and in stable beam conditions. Events are accepted only if the ID, the MS, and the calorimeters were operational and the solenoid and toroid magnet systems were both active.

The online event selection was performed by a two-level trigger system derived from the one described in Ref. [136]. The $\Upsilon \to \mu\mu$ candidates are triggered by a dedicated dimuon trigger that requires two opposite-charge muons compatible with the same vertex, with transverse momentum $p_T > 6$ GeV, and the dimuon invariant mass in the range $[8, 12]$ GeV. Additionally, a minor sample is also selected by dimuon triggers with no invariant mass requirement and $p_T > 4$, 10, 14 and 15 GeV, respectively.

Samples of prompt $\Upsilon \to \mu\mu$ were generated using PYTHIA8, complemented with PHOTOS to simulate the effects of final state radiation. Such samples were generated requiring each muon to have $p_T > 6$ GeV. All the generated samples were passed through the simulation of the ATLAS detector based on GEANT4 [109] [110] and were reconstructed with the same programs used for the data. The ID and the MS were simulated with an ideal geometry without any misalignment.

**Validation of the muon momentum corrections**

The collected sample of $\Upsilon \to \mu\mu$ decays is used to validate the muon momentum corrections derived as described before. Since the $\Upsilon$ sample is not used to derive such corrections, it provides an independent validation.

As already reported, $\Upsilon$ candidates are selected online primarily by a dedicated dimuon trigger which includes an invariant mass cut. Depending on the pile-up conditions, this trigger was pre-scaled by a factor of four in the 2016 dataset. On the contrary, only a negligible subsample of the 2015 dataset was pre-scaled. In order to not bias the results, the pre-scale factor has been checked not to alter the mass-line shape in the 2016 dataset. Figure 3.1 shows shape consistency between the pre-scaled and the un-prescaled sample for the 2016 collected sample.

Offline both the muons are required to be reconstructed as CB muons and have $p_T > 8$ GeV. The resulting data samples consist of $2.3 \cdot 10^6$ and $20 \cdot 10^6$ $\Upsilon$ candidates in 2015 and 2016, respectively. The same corrected MC samples are used for both the 2015 and 2016 datasets. Separate MC samples for the three $\Upsilon$ resonances ($\Upsilon(1S)$, $\Upsilon(2S)$ and $\Upsilon(3S)$) are available. In order to reconstruct the full MC mass-line shape, they need to be weighted properly. A fit to data is performed to determine the $\Upsilon(2S)$ and $\Upsilon(3S)$ contributions with respect to the $\Upsilon(1S)$ number of candidates. The generated sample consists of $11.7 \cdot 10^6$ $\Upsilon$ candidates.

In Fig. 3.2 the invariant mass distributions for the 2015-2016 $\Upsilon \to \mu\mu$ candidates

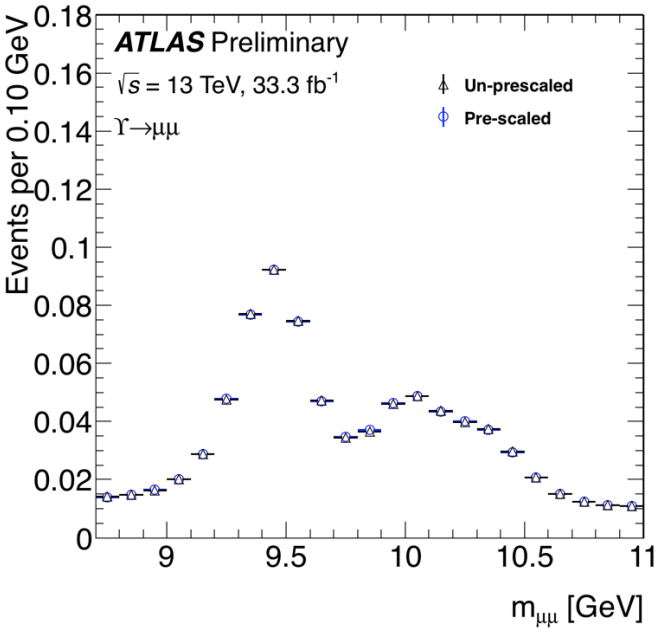


Figure 3.1: Shape comparison of the pre-scaled (blue) and un-prescaled (black) dimuon trigger in the 2016 dataset.

is compared with corrected and uncorrected simulation. In the uncorrected MC the signal peaks show a narrower width and are slightly shifted with respect to data. After correction, the lineshapes of the three resonances, $\Upsilon(1S)$, $\Upsilon(2S)$ and $\Upsilon(3S)$, agree very well with data within the systematic uncertainties, proving the effectiveness of the muon momentum corrections. For a detailed study, the position, $m_{\mu\mu}$, and the width, $\sigma(m_{\mu\mu})$, of the mass peaks are extracted in bins of $\eta$ and $p_T$ from fits of the invariant mass distributions of the three resonances. Neglecting the small contribution of the uncertainty in the opening angle of the muon pair, the relative mass resolution, $\sigma(m_{\mu\mu})/m_{\mu\mu}$, is related to the momentum resolution by:

$$\frac{\sigma(m_{\mu\mu})}{m_{\mu\mu}} = \frac{1}{2}\frac{\sigma_{p_{\mu 1}}}{p_{\mu 1}} \oplus \frac{1}{2}\frac{\sigma_{p_{\mu 2}}}{p_{\mu 2}} \tag{3.5}$$

where $p_{\mu 1}$ and $p_{\mu 2}$ are the momenta of the two muons. Assuming the two muons have similar momentum resolution, $p_\mu$, Eq. 3.5 can be written as:

$$\frac{\sigma(m_{\mu\mu})}{m_{\mu\mu}} = \frac{1}{\sqrt{2}}\frac{\sigma_{p_\mu}}{p_\mu} \tag{3.6}$$

Similarly, the dimuon mass scale, $s_{\mu\mu}$, is directly related to the muon momentum scale, $s_\mu$:

$$s_{\mu\mu} = \sqrt{s_{\mu 1} s_{\mu 2}} \tag{3.7}$$

where $s_{\mu 1}$ and $s_{\mu 2}$ are the momentum scales of the two muons defined as $s_\mu = \langle (p_\mu^{meas} - p_\mu^{true})/p_\mu^{true} \rangle$ and $s_{\mu\mu} = \langle (m_{\mu\mu}^{meas} - m_{\mu\mu}^{true})/m_{\mu\mu}^{true} \rangle$.

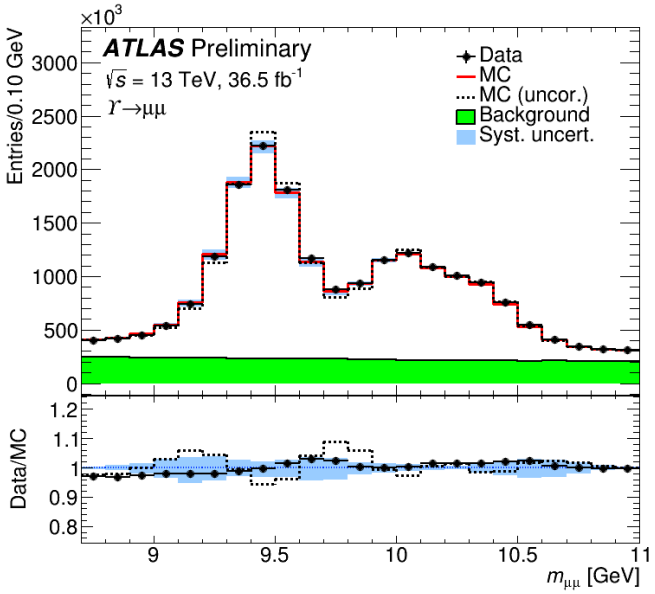


Figure 3.2: Dimuon invariant mass distribution of the 2015-2016 $\Upsilon \to \mu\mu$ candidate events reconstructed with CB muons. The upper panel shows the invariant mass distribution for data and for the signal simulation plus the background estimate. The points show the data. The continuous line corresponds to the simulation with the MC momentum corrections applied while the dashed lines show the simulation when no correction is applied. Background estimates are added to the signal simulation. The band represents the effect of the systematic uncertainties on the MC momentum corrections. The lower panel shows the data/corrected-MC and data/uncorrected-MC (dashed) ratio, respectively. The background contribution is estimated from a fit to data as described in the text. The sum of background and signal MC distributions is normalised to the data. Systematic uncertainties for the background modelling are not shown.

The dimuon mass resolution has been obtained by fitting the width of the invariant mass peaks. Since the intrinsic width of the $\Upsilon$ resonances, $\mathcal{O}(10$ keV), is

negligible with respect to the experimental resolution, $\mathcal{O}(100$ MeV), there is no need to convolve the experimental resolution function with a true line-shape. The momentum scale is obtained by comparing the mass peak position in both data and MC.

As shown in Fig. 3.2 the $\Upsilon$ resonances, $\Upsilon(1S)$, $\Upsilon(2S)$ and $\Upsilon(3S)$, partially overlap. Moreover, because of the trigger cut on the invariant mass, the size of the sidebands available for fixing the background level is considerably limited. For each bin, the whole invariant mass distribution is fitted in the range 8.2 < $m_{\mu\mu}$ <11.5 GeV. The bulk of each $\Upsilon$ peak is modeled by a Crystal Ball function [137] plus a Gaussian function centred on the Crystal Ball function in order to model the tails of the distribution, as also described in [138]. The relative mass shifts of the three signal peaks are fixed using the PDG masses of the three resonances, $\Delta_{m2S-m1S} = m_{2S,PDG} - m_{1S,PDG}$ and $\Delta_{m3S-m1S} = m_{3S,PDG} - m_{1S,PDG}$, while the widths of the three peaks, divided by the corresponding PDG masses, and the $\alpha$ and $n$ parameters defining the shape of the Crystal Ball function tails, are constrained to be equal. The non-resonant background is described by an exponential function. The remaining free parameters in the fit are the mass scale, the width $\sigma(m_{\mu\mu})$ of the $\Upsilon(1S)$, the Gaussian contribution to the fit function, the relative normalizations of the $\Upsilon(2S)$ and $\Upsilon(3S)$ distributions with respect to the $\Upsilon(1S)$ resonance, the exponential slope defining the background and the number of signal and background events. Formally, the fit function is defined as:

$$\begin{aligned} f(m;\theta) = {} & N_{1S}[(1-f)\cdot CB(m; s\cdot m_{1S}, \sigma, \alpha, n) + f\cdot \mathcal{G}(m; s\cdot m_{1S}, c\cdot\sigma)] \\ & + f_{2S}\cdot N_{1S}[(1-f)\cdot CB(m; m_{2S}, \sigma_{2S}, \alpha, n) + f\cdot \mathcal{G}(m; m_{2S}, c\cdot\sigma_{2S})] \\ & + f_{3S}\cdot N_{1S}[(1-f)\cdot CB(m; m_{3S}, \sigma_{3S}, \alpha, n) + f\cdot \mathcal{G}(m; m_{3S}, c\cdot\sigma_{3S})] \\ & + N_B\cdot \exp(m;\chi) \end{aligned} \tag{3.8}$$

where $CB(x;\bar{x},\sigma,\alpha,n)$, $\mathcal{G}(x;\bar{x},\sigma)$ and $Exp(x;\tau)$ are the Crystal Ball, the Gaussian and the Exponential functions, respectively; $f$ is the Gaussian contribution to the function; $c$ is the free parameter to model the resolution of the Gaussian function; $m_{2(3)S} = s\cdot m_{1S} + \Delta_{m2(3)S-m1S}$, and $\sigma_{2(3)S} = \frac{m_{2(3)S,PDG}}{m_{1S,PDG}}\sigma$, with $s$ and $\sigma$ the free parameters representing the momentum scale and resolution; $\tau$ is the free parameter to model the exponential slope; $N_{1S}$ and $N_B$ are the free parameter representing

the $\Upsilon(1S)$ and background normalization; $f_{2S} = \frac{N_{2S}}{N_{1S}}$ and $f_{3S} = \frac{N_{3S}}{N_{1S}}$ are the free parameters corresponding to the relative yields of the $\Upsilon(2S)$ and $\Upsilon(3S)$ resonances.

A first fit to data is performed to obtain the $\Upsilon(2S)$ and $\Upsilon(3S)$ normalizations with respect to the $\Upsilon(1S)$ and the backgroud shape. Thus, a similar fit is performed to the MC simulation with the invariant mass distribution obtained by adding the three signal peaks and a generated exponential background distribution normalized accordingly. The background distribution is generated using the fitted shape in data. The Gaussian shape is obtained from this fit to the MC simulation and fixed in a second fit to data. This is to be consistent with the fit procedure implemented for the $Z \to \mu\mu$ and $J/\psi \to \mu\mu$ reported in [133]. Finally, the peak position and width of the Crystal Ball function are used as estimators for the $m_{\mu\mu}$ and $\sigma(m_{\mu\mu})$ variables in the various $\eta$ and $p_T$ bins. They are extracted from the second fit to data and compared to the corresponding parameters extracted from the fit to the MC sample.

Some examples of fit to data and MC in central and forward $\eta$ regions are shown in Fig. 3.3. Similar fit examples for a $p_T$ bin, 25 GeV < $p_T(\mu)$ <30 GeV, are shown in Fig. 3.4. The fitted signal modeling for the three $\Upsilon$ resonances (Crystal Ball with Gaussian) and the fitted background modeling are indicated.

### Results

Figure 3.5(left) shows the position of the $\Upsilon(1S)$ peak of the invariant mass distribution, $m_{\mu\mu}$, obtained from the fits to the $\Upsilon$ samples as a function of the pseudorapidity of the highest-$p_T$ muon for CB pairs. The distributions are shown for data as well as corrected simulation, with the ratio of the two in the lower panel. The corrected MC is in very good agreement with data, within the scale systematic uncertainties of 0.05% in the barrel region and increase with $|\eta|$ to reach 0.25% in the forward region, $|\eta| \sim 2.5$. Although within systematic uncertainties, a slight bias is evident in the scale plot where the $\Upsilon(1S)$ peak estimated in the MC fits is systematically lower than the corresponding value estimated in the data fits indicating possible overcorrection effects. The systematic uncertainties shown in the plots include the effects of the uncertainties in the calibration constants and possible changes in the fit parameterization. The main contributions from the calibration procedure are from the:

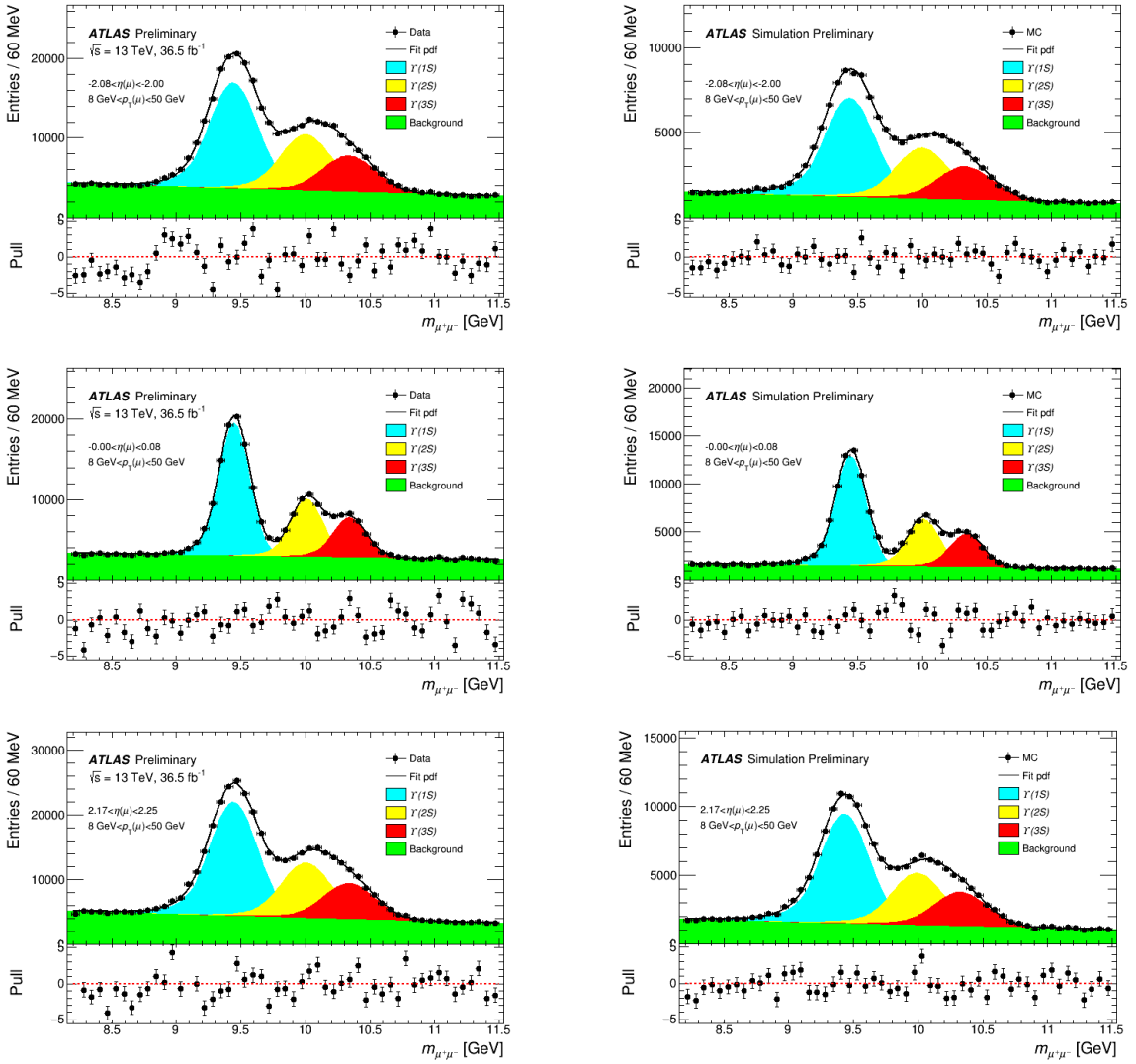


Figure 3.3: Examples of fit to data (left) and MC (right) for forward (-2.00 < $\eta$ < -2.08 and 2.17 < $\eta$ < 2.25) and for central (0.00 < $\eta$ < 0.08) detector regions. The fitted signal modeling for the three $\Upsilon$ resonances (Crystal Ball with Gaussian) and the fitted background modeling are pointed out: $\Upsilon(1S)$ (blue), $\Upsilon(2S)$ (yellow), $\Upsilon(3S)$ (red) and exponential background (green). Selected muons are required to have 8 GeV < $p_T(\mu)$ < 50 GeV.

- Variation of the mass window width for the $Z \to \mu\mu$ candidate selection used to derive the corrections. Non-Gaussian smearing effects are accounted for by varying the $m_{\mu\mu}$ selection by ±5 GeV.

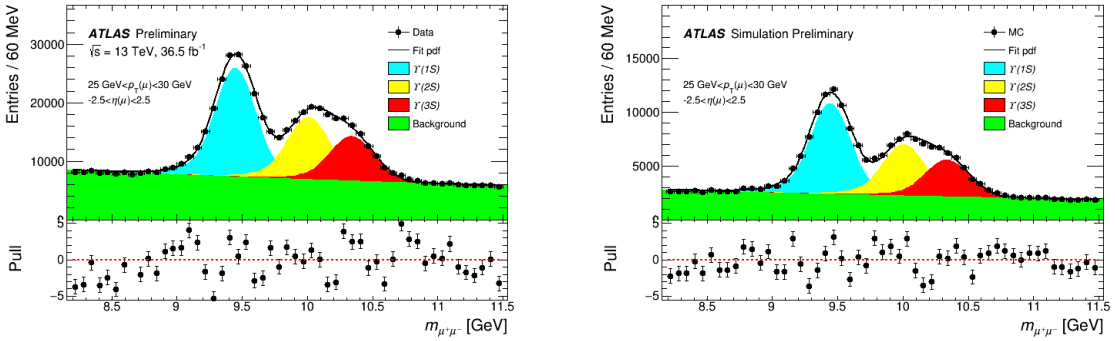


Figure 3.4: Examples of fit to data (left) and MC (right) for 25 GeV < $p_T(\mu)$ <30 GeV. The fitted signal modeling for the three $\Upsilon$ resonances (Crystal Ball with Gaussian) and the fitted background modeling are pointed out: $\Upsilon(1S)$ (blue), $\Upsilon(2S)$ (yellow), $\Upsilon(3S)$ (red) and exponential background (green).

- Background parameterization for the $J/\psi \to \mu\mu$ fit and variation in the muon $p_T$ cut (from 5 to 7 GeV) to reduce the contribution of low-$p_T$ muons.
- Scale parameter for the ID corrections obtained by fitting separately the $Z \to \mu\mu$ and the $J/\psi \to \mu\mu$ samples, to include possible non-linear scale effects.
- Alignment of the MS chambers. This systematic uncertainty is determined from alignment studies performed on special runs where the toroidal magnetic field was turned off.

In addition, some systematic uncertainties are specific for the the $\Upsilon$-fitting strategy. They have been evaluated by changing the fit range to 8.5 < $m_{\mu\mu}$ < 11.5 and 8.75 < $m_{\mu\mu}$ < 11.0 GeV, the definition range for the Crystal Ball $\alpha$ and $n$ parameters and the background modeling.

The observed level of agreement demonstrates that the $p_T$ calibration for combined muon tracks described above provides a very accurate description of the momentum scale in all $\eta$ regions, over a wide $p_T$ range. Similarly, a good data/MC agreement is observed for the ID and MS components of the combined tracks.

Figure 3.5(right) shows the dimuon mass resolution $\sigma(m_{\mu\mu})$ as a function of the leading-muon $\eta$ obtained from fits to the $\Upsilon$ samples as a function of the pseudorapidity of the highest-$p_T$ muon for CB pairs. The dimuon mass resolution is about 1.2% for central $\eta$ values and increases to 2.1% in the forward $\eta$ regions. Following Eq.

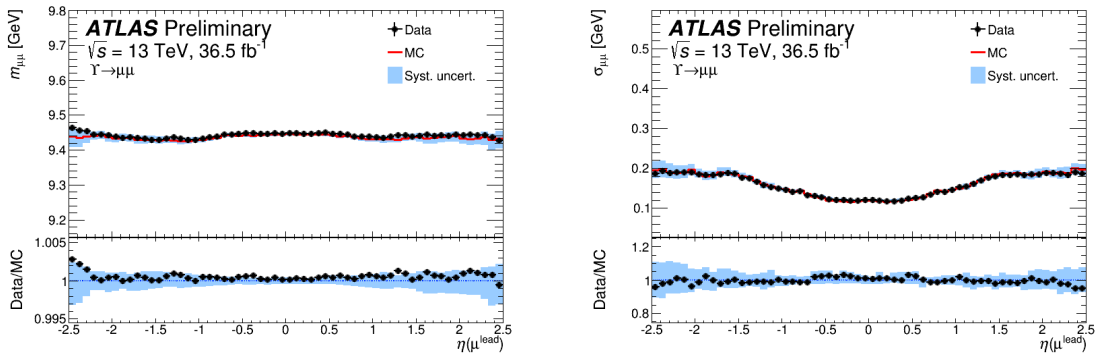


Figure 3.5: Fitted $\Upsilon(1S)$ mean mass (left) and dimuon invariant mass resolution (right) of the dimuon system for CB muons from $\Upsilon \to \mu\mu$ decays collected in 2015-2016 and for the corrected simulation as a function of the pseudorapidity of the highest-$p_T$ muon. The upper panel shows the fitted mean mass value (left) and the fitted dimuon invariant mass resolution (right) for data (black) and corrected simulation (red). The lower panel shows the data/MC ratio. The error bars represent the statistical uncertainty; the blue shaded bands represent the systematic uncertainty in the correction and the systematic uncertainty in the extraction method added in quadrature.

3.6, this corresponds to a relative muon $p_T$ resolution of 1.7% and 2.9% in the centre of the detector and in the endcaps, respectively. After applying the momentum corrections described above, this behaviour is very well reproduced by the corrected MC. Systematic uncertainties are estimated following the same procedure used for the determination of the energy scale.

Similarly, Figure 3.6(left) shows the position of the $\Upsilon(1S)$ peak of the invariant mass distribution, $m_{\mu\mu}$, and Figure 3.6(right) shows the dimuon mass resolution, $\sigma(m_{\mu\mu})$, obtained from fits to the 2015-2016 $\Upsilon$ samples as a function of the average momentum of the CB pairs, $\langle p_T \rangle$, defined as $\langle p_T \rangle = \frac{1}{2}(p_{T1}+p_{T2})$. The small variations of the invariant mass estimators as a function of pseudorapidity are due to imperfect energy loss corrections and magnetic field description in the muon reconstruction. Both effects are well reproduced in the simulation. Across the $\eta$ and $p_T$ range covered by this study, the local value of peak of the $\Upsilon(1S)$ resonances obtained from data deviates from the world average value of the $\Upsilon(1S)$ mass by less than twice the combination of systematic uncertainties in the calibration and validation procedures.

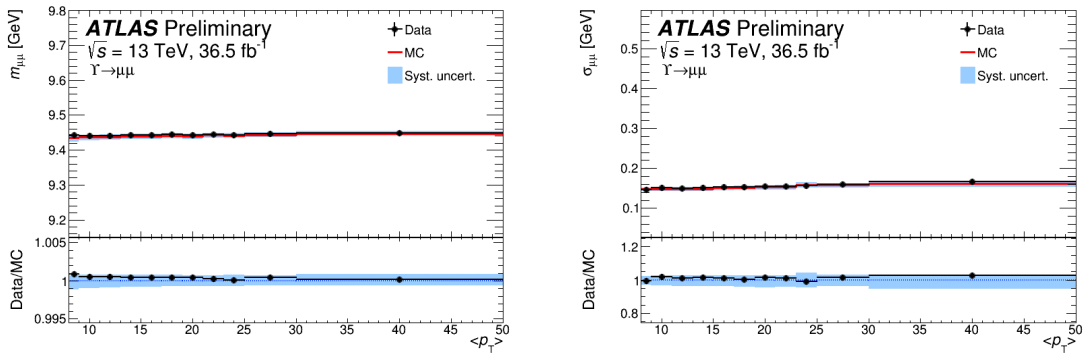


Figure 3.6: Fitted $\Upsilon(1S)$ mean mass of the dimuon system (left) and dimuon invariant mass resolution (right) for CB muons from $\Upsilon \to \mu\mu$ decays collected in 2015-2016 and for the corrected simulation as a function of the average momentum of the CB pairs, $\langle p_T \rangle$. The upper panel shows the fitted mean mass value (left) and the fitted dimuon invariant mass resolution (right) for data (black) and corrected simulation (red). The lower panel shows the data/MC ratio. The error bars represent the statistical uncertainty; the blue shaded bands represent the systematic uncertainty in the correction and the systematic uncertainty in the extraction method added in quadrature.

### 3.3.3 Jets

Quarks and gluons are the dominant interacting objects during high-energy proton-proton collisions at the LHC. As soon as they emerge from the interaction point, they quickly undergo *hadronisation*, which forms a collimated beam of particles, mostly composed of pions and kaons. These collimated collections of particle tracks are referred to as "jets".

#### Reconstruction

In ATLAS jets are observed as groups of topologically related energy deposits in the calorimeters, which can be associated with charged-particle tracks reconstructed in the ID. Topoclusters were already defined in Sec. 3.3.1, when describing the electron reconstruction in ATLAS.

Jet reconstruction is based on the anti-$k_t$ jet algorithm [139] using the *FastJet* software package [140]. This is the algorithm most widely used in ATLAS for different studies involving jets.

Topoclusters are used to feed the anti-$k_t$ algorithm. They are built starting from a *seed* calorimeter cell with a signal-to-noise level above the threshold $S/B = 4$; later, neighbouring calorimeter cells with energy sufficiently larger than noise levels ($S/B \geq 2$) are added. The topocluster algorithm efficiently suppresses the calorimeter noise. A jet must have at least a $p_T$ of 7 GeV.

The anti-$k_t$ algorithm lies in the definition of the distance parameter, $d_{ij}$, between jet constituents $i$ and $j$:

$$d_{ij} = min\left(\frac{1}{k_{t,i}^2}, \frac{1}{k_{t,j}^2}\right)\left(\frac{\Delta_{ij}}{R}\right)^2 \tag{3.9}$$

where $\Delta_{ij}^2 = (y_i - y_j)^2 + (\phi_i - \phi_j)^2$ with $k_{t,i}$, $y_i$ and $\phi_i$ representing respectively the transverse momentum, rapidity and azimuth of particle $i$ and similarly for particle $j$, and $R$ is the radius parameter of the jet algorithm - typically set to $R = 0.4$. From this definition it is clear that two soft constituents have a larger distance when compared to the separation they have with hard constituents, due to the term $\frac{1}{k_t^2}$ in the definition of the distance $d_{ij}$. As a result, soft particles tend to cluster around hard objects long before they cluster among themselves. If a hard particle has no hard neighbours within a distance $2R$, then it will simply accumulate all the soft particles within a circle of radius $R$, defining a perfectly conical jet. If other hard particles are present, then the object with the largest $p_T$ will have a conical shape and the other will be clipped. Depending on the momentum difference of the objects, it can happen that both the hard particles are clipped. The hard jets are all circular with a radius $R$, and only softer jets have more complex shapes. The total jet four-momentum is defined as the sum of the four-momenta of all jet constituents. The jet energy, mass and momentum will be derived from its four-momentum. Fig. 3.7 shows the highest-mass dijet event measured by ATLAS in Run 2 with a mass of 8.12 TeV.

Three types of jets are reconstructed in ATLAS, depending on the objects used as input for the jet algorithm

- *truth jets* with simulated particles used as input;
- *track jets* with tracks reconstructed in the ID used as input;
- *calorimeter jets* with energy deposits in the calorimeter used as input.

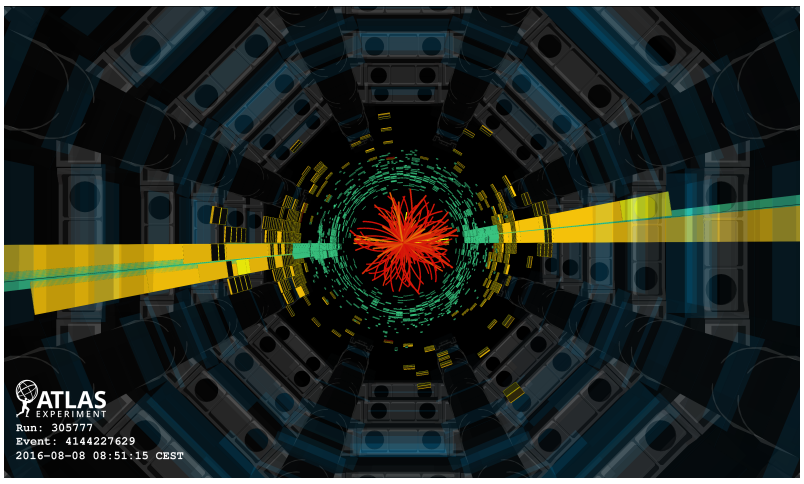


Figure 3.7: The highest-mass dijet event measured by ATLAS in Run 2 with a mass of 8.12 TeV. Event display from the ATLAS Collaboration.

The anti-$k_t$ algorithm is soft-resilient, infrared and collinear safe. It is soft-resilient since soft particles do not modify the shape of the jet, while hard particles do. This means that the jet boundary is resilient with respect to soft radiation, but flexible with respect to hard radiation. The anti-$k_t$ algorithm is also infrared and collinear safe by construction since soft perturbative objects are iteratively clustered back to the hard objects.

### Calibration

After the jet reconstruction stage, the jet calibration step follows. It consists of five different stages:

- *Pile-up corrections.* Jets formed from topoclusters are first calibrated by applying a correction to account for energy offset caused by pile-up interactions. This corrections is derived from MC simulations as a function of the number of reconstructed primary vertices and the expected average number of interactions in bins of jet $\eta$ and $p_T$;
- *Origin corrections.* This correction recalculates the jet four-momentum to make the jet point back to the primary vertex instead of the nominal centre of the ATLAS experiment;

- *Absolute MC-based calibration.* This correction is derived from the absolute MC-based Jet Energy Scale (JES) calibration needed for a better match with the truth jet in MC simulations. This first JES correction uses isolated jets from a jet MC sample including pile-up events.

- *Global sequential calibration.* This corrections is meant to improve jet energy reconstruction.

- *Residual in-situ correction.* This correction is applied to data-only samples. It uses the transverse momentum balance between the jet and well-measured reference objects - $Z/\gamma + jet$ or dijet events - to asses the data-to-MC discrepancy.

Several jet calibration schemes, with different levels of complexity and different sensitivity to systematic effects, are available in ATLAS. Each calibration scheme starts from the measured calorimeter energy at the electromagnetic (EM) energy scale, which correctly measures the energy deposited by electromagnetic showers. In the simplest scheme, which is EM+JES, the jet calibration is derived as a simple correction relating the calorimeter's response to the true jet energy [141]. Jets used for the off-shell analysis are calibrated using the EM+JES scheme which applies corrections as a function of the jet $p_T$ and $\eta$. The total number of JES systematic uncertainties is 80. They are related to the various assumptions during the calibration steps, such as the pile-up modeling, multi-jet modeling and jet composition. However, for the results shown in this thesis a powerful reduction scheme is implemented, reducing the total number to a set of five systematic uncertainties.

Further pile-up removal is crucial to improving the sensitivity of the off-shell analysis. In Run 1, a dedicated algorithm, the Jet-Vertex-Fraction (JVF) was used to reject pile-up events. After some studies, it was discovered it was dependent on the number of reconstruction vertices [142]. Thus, in Run 2 a new algorithm has been developed, the Jet-Vertex-Tagger (JVT). It is based on a multivariate technique which provides an improved rejection of pile-up events guaranteeing no dependence on the event activity. The tagging algorithm is applied only to jets with $p_T < 60$ GeV and $|\eta| < 2.4$. The output of the JVT algorithm ranges in the interval [0,1]. Values close to 0 are for soft pile-up jets, while values close to 1 are for hard-scatter jets. The ATLAS default requirements select jets with a JVT output larger than 0.49, which corresponds to a pile-up rejection efficiency of 92% and an observed

fake rate of 2%. The JVT efficiency corrections are jet-$p_T$ dependent and vary from 3.7% for the lowest jet $p_T$ bin to 0.9% for the highest jet $p_T$ bin. These corrections are estimated using a tag-and-probe method where the $Z$ boson is tagged and the leading jet recoiling from the $Z$ boson is the probe in a back-to-back topology. The tag-and-probe method was described in Sec. 3.3.1 when summarizing the strategy to measure electron reconstruction and identification efficiencies.

Finally, additional jet quality criteria are implemented. They are collectively known as *Jet Cleaning* [143]. They are needed to remove fake jets from non-collision backgrounds such as beam induced background or cosmic-ray showers and random calorimeter noise bursts [144]. The 'Loose' cleaning WP provides a selection efficiency larger than 99% for jets with $p_T > 20$ GeV.

### Jet Energy Resolution

After the jet-reconstruction and jet-calibration steps, it is possible to determine the jet energy resolution. The jet energy resolution [145] can be parametrized with three independent contributions - the *effective-noise* (N), *stochastic* (S) and *constant* (C) terms - as follows:

$$\frac{\sigma(p_T)}{p_T} = \frac{N}{p_T} \oplus \frac{S}{\sqrt{p_T}} \oplus C \tag{3.10}$$

where:

- the $N$ term is due to external noise contributions - such as electronics and pile-up noise - that are not (or only weakly) dependent on the jet $p_T$. This term is expected to dominate in the low-$p_T$ region, for $p_T < 30$ GeV.
- The $S$ term represents statistical fluctuations. It becomes the limiting factor in the jet energy resolution for intermediate $p_T$.
- The $C$ term describes fluctuations that are a constant fraction of the jet $p_T$. It is expected to dominate in the high-$p_T$ region, for $p_T > 400$ GeV.

The jet resolution is measured in dijet events from two different *in situ* methods, which are described in [145]. The resulting data/MC agreement is at the level of 10%.

### Flavour Tagging

Jets in ATLAS can be also classified based on their flavour. "Light" flavour jets originate from $u$ and $d$ quarks as opposed to "Heavy" flavour jets which originate from $c$ and $b$ quarks. In more details, $b$-quarks form long-lived $b$-hadrons which travel some distance before decaying into jets. However, their lifetimes are not so high as those of light-quark hadrons, so they decay inside the detector rather than escape. The advent of precision silicon detectors with excellent spatial resolution, such as the ATLAS ID, has made it possible to accurately reconstruct and separate the production vertex - where the $b$-hadron was produced - from the decay vertex - where the $b$-hadron decayed producing $b$-jets. This provides an effective $b$-jets identification method, known as $b$-jet tagging [146]. Several other $b$-tagging algorithms have been developed to distinguish $b$-quark jets from jets containing only lighter quarks. They exploit specific topological features of $b$-hadron decays. The list includes impact-parameter-based algorithms or semileptonic-decays-based algorithms which exploit the topology of weak $b$- and $c$-hadron decays inside the jet. In ATLAS a boosted decision tree technique combines all the $b$-tagging algorithms to obtain a $b$-tagging discriminant. Operating points are defined by assigning a single cut value on the discriminant output distribution and are chosen in order to provide a specific $b$-jet efficiency on an inclusive $t\bar{t}$ sample. The multivariate variable is called MV2c10 [147]. Correction factors are applied to the simulated event samples to compensate for data/MC differences in the $b$-tagging efficiency for $b$, $c$ and light-jets. Corrections applied to $b$-jets are derived from a $t\bar{t}$ sample with final states containing two leptons. They are all consistent with unity within uncertainties at the level of a few percent over most of the jet $p_T$ spectrum [148].

### Overlap Removal

After the object reconstruction, an *overlap-removal* procedure is applied to remove ambiguities in case the same object is reconstructed by several algorithms. The measure of the distance $\Delta R = \sqrt{(\Delta\phi)^2 + (\Delta y)^2}$, with $\Delta y$ and $\Delta\phi$ the rapidity difference and azimuthal angle between the two objects, is the metric to separate two different objects. Overlap removal is performed differently for the Missing Transverse Momentum $E_T^{miss}$ reconstruction, as discussed in Sec. 3.3.4. Specific information on the jet candidates used in the off-shell analysis are given in Sec. 4.5.2.3.

### 3.3.4 Missing Transverse Momentum $E_T^{miss}$

The missing transverse momentum $E_T^{miss}$ is defined as the momentum imbalance in the plane transverse to the beam axis, where momentum conservation is assumed. This imbalance may indicate the presence of undetectable particles, such as neutrinos or new weakly-interacting particles escaping the detector. $E_T^{miss}$ is a vector quantity in the transverse plane and is obtained from the negative vector sum of the momenta of all particles detected in a proton-proton collision event. The ATLAS detector is specifically designed to provide a $\phi$ coverage of $4\pi$ in order to reconstruct the $E_T^{miss}$ since it is a key variable in all the searches for new physics performed at the LHC [149].

#### Reconstruction and Calibration

$E_T^{miss}$ is a global detector variable and, thus, most of all of the available ATLAS sub-detectors are used for its reconstruction. Therefore all the performance studies for $E_T^{miss}$ also translate into an overall performance study of the ATLAS detector itself. Calibrated physics objects reconstructed in the detector are used to calculate the amount of missing transverse energy. An additional term is added to the $E_T^{miss}$ definition to take into account tracks unassociated with any object in the event. These two general terms lead to the $E_T^{miss}$ definition:

$$\vec{E}_T^{miss} = \vec{E}_T^{miss}(hard) + \vec{E}_T^{miss}(soft) \tag{3.11}$$

where $\vec{E}_T^{miss}(hard)$ stands for all the detector measured calibrated objects while $\vec{E}_T^{miss}(soft)$ stands for all the unused tracks present in the event.

In more detail, $\vec{E}_T^{miss}$ is calculated as the negative vector sum of the $\vec{p}_T$ of all measured objects:

$$\vec{E}_T^{miss} = -\sum_{electrons} \vec{p}_T^{e} - \sum_{photons} \vec{p}_T^{\gamma} - \sum_{\tau-leptons} \vec{p}_T^{\tau_{had}} - \sum_{muons} \vec{p}_T^{\mu} - \sum_{jets} \vec{p}_T^{jet} - \sum_{unused-tracks} \vec{p}_T^{track} \tag{3.12}$$

The $\vec{E}_T^{miss}$ reconstruction for the "hard" term associates calorimeter energy deposits with reconstructed and identified high-$p_T$ parent objects in a specific order: electrons, photons, hadronically decaying $\tau$-leptons, jets and finally muons. Any unused track in the hard term reconstruction is added to the "soft" term, the last term in

Eq. 3.12.

The magnitude of the missing transverse momentum is given by the length of the $\vec{E}_T^{miss}$ vector:

$$E_T^{miss} = |\vec{E}_T^{miss}| = \sqrt{(E_{T,x}^{miss})^2 + (E_{T,y}^{miss})^2} \tag{3.13}$$

where $E_{T,x}^{miss}$ and $E_{T,y}^{miss}$ are the $x$ and $y$ components of the $\vec{E}_T^{miss}$ vector, respectively. Its direction is given in terms of the azimuthal angle $\phi^{miss} = \tan^{-1}(E_{T,y}^{miss}/E_{T,x}^{miss})$.

Some details on the physics objects which enter the $E_T^{miss}$ calculation are listed below:

- *Electron term.* Electrons are reconstructed from energy deposits in the EM calorimeter and matched with ID tracks. They must satisfy at least the track-quality 'Medium' WP, with an applied momentum threshold of $p_T > 10$ GeV and $|\eta| < 2.5$ to be confined to the ID. The transition region $1.37 < |\eta| < 1.52$ between the barrel and end-cap calorimeters is excluded and objects detected in that region are reconstructed as jets.

- *Photon and $\tau$-lepton terms.* In the final state of interest for the off-shell analysis in the $\ell\ell\nu\nu$ channel - $\ell\ell\nu\nu + E_T^{miss}$ - photons and hadronically decaying $\tau$-leptons are not used in the $E_T^{miss}$ calculation. They are just included as jets resulting in a small contribution to the total $E_T^{miss}$.

- *Muon term.* Muons are formed from ID tracks matched with a segment or tracks reconstructed in the MS. They must satisfy the 'Medium' track-quality WP, with an applied momentum threshold of $p_T > 20$ GeV within $|\eta| < 2.5$.

- *Jet term.* Jets which enter the $E_T^{miss}$ calculation are formed from topological clusters of calorimeter cells using the anti-$k_t$ algorithm, described in Sec. 3.3.3, with a radius parameter of $\Delta R = 0.4$. Jets follow the quality criteria described in Sec. 3.3.3 (EM+JES scheme for the calibration). Generally, jets are rejected if they overlap with other physics objects. However, in some cases, a partial overlap removal is performed when overlapping with muons and electrons. When overlapping with electrons, the overlap removal is based on the ratio of the electron energy to the jet energy $k_E = E_e^{EM}/E_{jet}^{EM}$. For $k_E \leq 50\%$ jets are included as part of the jet term in Eq. 3.12, with a 1- $k_E$ scaling factor applied to their energy. On the contrary, jets are rejected for $k_E > 50\%$ and the

corresponding tracks associated to the jet are included in the "soft" term. The situation is harder when jets overlap with muon physics objects since there are more sources of overlapping. For instance, a muon can overlap with a pile-up jet, which can lead to JVT mis-tagging, and result in a pile-up jet that enters the jet term in Eq. 3.12. Additionally, stochastic process connected with large calorimeter muon energy losses can lead to an overlap of physics objects. The deposited muon energy is reconstructed as a hard jet pointing to the primary vertex. As a consequence, this results in double counting when using CB muons since reconstructed muons have already been corrected for such effect. The description of the sophisticated muon-jet overlap-removal technique is beyond the scope of this thesis. It is described in [150].

- *"soft" term.* Compared to the Run-1 $E_T^{miss}$ performance, this is the term that has changed the most. In fact, during Run 1 this term was reconstructed solely from calorimeter energy deposits not associated with any physics objects. The larger pile-up contamination observed in Run 2 has been proved to severely degrade the $E_T^{miss}$ resolution [149], when using the Run-1 definition for the "soft" term. Thus, in Run 2 the ATLAS Collaboration has introduced a term built exclusively from tracks resulting in an improved pile-up rejection and a better $E_T^{miss}$ resolution. This term is known as the Track-based soft term (TST). It is built from unidentified tracks with no applied calibration. The inclusion of this terms allows to take into account the hadronic recoil from low-energy interactions. In order to be considered for the TST term, tracks must have a minimum $p_T^{track}$ of 400 MeV and $|\eta| < 2.5$ in order to be in the fiducial volume of the ID. Also, they must satisfy the impact-parameter selections $|d_0| <$ 1.5 mm and $|z_0 sin(\theta)| < 1.5$ mm. Alternative calorimeter-based reconstruction algorithms have been considered, but the TST provides a more robust pile-up rejection being fully track-based. However, the introduction of the TST terms has two important effects, which have an impact on the $E_T^{miss}$ performance: (1) it doesn't include the contribution of neutral particles since they don't leave any visible tracks in the ID; (2) it is confined to be in the fiducial volume of the ID, $|\eta| < 2.5$ .

### $E_T^{miss}$ resolution

The $E_T^{miss}$ resolution is measured by the root-mean-square (RMS) width of the combined distributions of the differences between the measured ($E_{T,x}^{miss}$, $E_{T,y}^{miss}$) and the components of the true missing transverse momentum vector, which is referred to as $\vec{E}_T^{miss,true} = (E_{T,x}^{miss,true}, E_{T,y}^{miss,true})$. In simulated events, the genuine $\vec{E}_T^{miss,true}$ is calculated from non-interacting particles in the event, including neutrinos from heavy flavour decays. This metric provides details on the overall detector reconstructed object resolutions and on the data/MC agreement of the $E_T^{miss}$ distributions. Specific information on the $E_T^{miss}$ physics objects used in the off-shell analysis are given in Sec. 4.5.2.4.

# Chapter 4

# Measurement of the Off-Shell Higgs Boson Signal Strength and Total Width

*In this chapter I describe the ATLAS strategy for the measurement of the off-shell production of the Higgs boson, my main DPhil project. I first introduce the analysis idea, I then introduce the simulation and theoretical corrections. Finally, I report on the strategy used for the two analyses, the $4\ell$ and the $2\ell 2\nu$ analysis. I mainly focus on the $2\ell 2\nu$ result since it is the ATLAS working group I am in. I was one of the three main ATLAS members working on this analysis in a group of about 40 people. I contributed to the data analysis - MC validation, theoretical corrections, background estimation, final limits and systematic uncertainties - editorial production and review of the analysis. In addition, since I was responsible for the combination with the $4\ell$ channel to derive the final limits I briefly introduce the analysis strategy in this channel.*

## 4.1 Introduction

In the past it was proposed to constrain the Higgs boson total width using its off-shell production and decay to two $Z$ or $W$ bosons away from the resonance peak [49–52, 59,151]. In such studies it has been shown that in the leading gluon fusion production mode the off-shell production of the Higgs boson well above the measured resonance

mass of $m_H$ =125.09 ± 0.21(stat) ± 0.11(syst) GeV [33], has a substantial cross section at the LHC, due to an enhancement in the decay amplitude from the vicinity of the $Z$-boson or the $W$-boson pair production threshold and the subsequent *top*-quark pair production threshold. The zero-width approximation is inadequate and the off-shell cross section above the $2m_Z$ threshold is around 10% of the total Higgs boson production cross section [49]. This provides a unique opportunity to study the Higgs boson properties at higher energy scales. The off-shell production can provide increased sensitivity to new physics that alters the interactions between the Higgs boson and other fundamental particles in the high-mass regime [53–56]. During the LHC Run 1, both the CMS and ATLAS collaborations have set constraints of $\Gamma_H <$ 22 MeV(22.7 MeV for ATLAS) at 95% CL on the Higgs boson total width using the off-shell production method [60,61], which relies on the relative measurement of the off-shell to the on-shell production cross section. During the LHC Run 2, new results have been released by both Collaborations. In the following sections, the new ATLAS analysis will be presented.

## 4.2 Analysis Idea

This section describes the fundamental idea behind the interest in the off-shell Higgs boson production measurement, how this can be used to constrain the Higgs boson width and which assumptions need to be made.

The representative diagrams for $pp \to ZZ$ production are shown in Fig. 4.1, involving resonant Higgs boson production and non-resonant $ZZ$ continuum originating from $q\bar{q}$ and $gg$ initial states. In the dominant gluon fusion production mode for the Higgs boson at the LHC, the off-shell production cross section, away from the resonance peak, is known to be sizable. This is due to two threshold effects, one near $2M_Z$ from the enhancement of the Higgs boson decay amplitude as the two $Z$s go on-shell and the other at $2m_t$ from the $gg \to H$ production [42]. The production cross-section for $gg \to H \to ZZ$, which depends on $\Gamma_H$ through the Higgs boson propagator, can be written as:

$$\frac{\mathrm{d}\sigma_{gg\to H\to ZZ}}{\mathrm{d}M^2_{ZZ}} \sim \frac{g^2_{Hgg} g^2_{HZZ}}{(M^2_{ZZ} - m^2_H)^2 + m^2_H \Gamma^2_H}, \tag{4.1}$$

where $g_{Hgg}$, $g_{HZZ}$ are coupling constants of the Higgs boson to gluons and $Z$ bosons,

respectively. Integrating either in a small region around $m_H$, or above the mass threshold $m_{ZZ} > 2m_Z$ - where $(m_{ZZ} - m_H) >> \Gamma_H$ - the on-shell and off-shell[1] cross sections are, respectively:

$$\sigma^{gg\to H\to ZZ^*}_{on-shell} \sim \frac{g^2_{Hgg} g^2_{HZZ}}{m_H \Gamma_H}, \tag{4.2}$$

$$\sigma^{gg\to H^*\to ZZ}_{off-shell} \sim \frac{g^2_{Hgg} g^2_{HZZ}}{(M^2_{ZZ} - m^2_H)^2}. \tag{4.3}$$

A severe ambiguity is present in the on-shell regime, the so called *couplings – width* ambiguity. Indeed, all the measured on-shell cross sections can be kept fixed if one simultaneously rescales couplings of the Higgs boson to SM particles and the Higgs boson width by the appropriate factors. For instance, if $g_{Hgg} = c \cdot g^{SM}_{Hgg}$, $g_{HZZ} = c \cdot g^{SM}_{HZZ}$ and $\Gamma_H = c^4 \cdot \Gamma^{SM}_H$ the measurement of the on-shell cross sections in the various channels will be unchanged, $\sigma^{gg\to H\to ZZ^*}_{on-shell} = \sigma^{gg\to H\to ZZ^*}_{on-shell,SM}$. The LHC data are open to infinitively many possible solutions for the Higgs boson total width, its couplings to the SM particles and the branching ratio of the Higgs boson to invisible states. In 2019 the ATLAS collaboration published results on the combination of searches for invisible Higgs boson decays using 36.1 fb$^{-1}$ of $pp$ collisions at a centre-of-mass energy of $\sqrt{s}$ = 13 TeV in combination with the results at $\sqrt{s}$ = 7 and 8 TeV. Assuming the Higgs boson is produced according to the SM via vector boson fusion, $Z(\to \ell\ell)H$ and $W/Z(\to \text{had})H$, an exclusion limit on the $H \to$ invisible branching ratio of $0.26(0.17^{+0.07}_{-0.05})$ at 95% CL is observed (expected) [152]. On the contrary, the total cross-section $\sigma^{gg\to H^*\to ZZ}_{off-shell}$ for the off-shell Higgs boson production through gluon fusion with subsequent decay into vector-boson pairs, is proportional to the product of the Higgs boson couplings squared for production and decay. However, unlike the on-shell Higgs boson production, $\sigma^{gg\to H^*\to ZZ}_{off-shell}$ is independent of the total Higgs boson decay width $\Gamma_H$ [49, 50] allowing for independent measurements of the Higgs boson couplings and breaking the *couplings – width* degeneracy.

Using the framework for Higgs boson coupling deviations as described in [43], the off-shell signal strength w.r.t. the SM expectation in the high-mass region at an

[1] In the following the notation $gg \to (H^* \to)ZZ$ is used for the full signal+background process for $ZZ$ production, including the Higgs boson signal $gg \to H^* \to ZZ$ process (S), the continuum background $gg \to ZZ$ process (B) and their interference. For vector-boson fusion (VBF) production, the analogous notation VBF $(H^* \to)ZZ$ is used for the full signal plus background process, with VBF $H^* \to ZZ$ representing the Higgs boson signal and VBF $ZZ$ denoting the background.

energy scale $\hat{s}$, $\mu_{off-shell}(\hat{s})$, can be expressed as:

$$\mu_{off-shell}(\hat{s}) \equiv \frac{\sigma^{gg\to H^*\to ZZ}_{off-shell}(\hat{s})}{\sigma^{gg\to H^*\to ZZ}_{off-shell,SM}(\hat{s})} = \kappa^2_{g,off-shell}(\hat{s}) \cdot \kappa^2_{V,off-shell}(\hat{s}), \tag{4.4}$$

where $\kappa_{g,off-shell}(\hat{s})$ and $\kappa_{V,off-shell}(\hat{s})$ are the off-shell coupling scale factors associated with the $gg \to H^*$ production and the $H^* \to ZZ$ decay. The off-shell Higgs boson signal cannot be treated independently from the $gg \to ZZ$ background, Fig. 4.1(b), as sizable negative interference effects appear [49] for the $gg$ initiated processes as shown in the diagrams in Figs. 4.1(a) and 4.1(b). The interference term is proportional to $\sqrt{\mu_{off-shell}} = \kappa_{g,off-shell} \cdot \kappa_{V,off-shell}$.

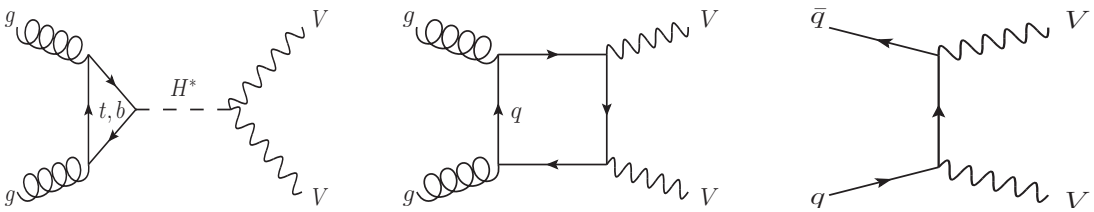


Figure 4.1: Feynman diagrams for the lowest order contributions to the main ZZ production processes: (a) Higgs-mediated $gg$ production, $gg \to H^* \to ZZ$, the signal mode; (b) the gluon-induced diboson production which involves the $gg \to ZZ$ continuum background production from the box diagrams and (c) the quark-initiated process, $q\bar{q} \to ZZ$. These diagrams are valid also for $W$ bosons.

In contrast, the cross-section for on-shell Higgs production allows a measurement of the signal strength:

$$\mu_{on-shell}(m_H) \equiv \frac{\sigma^{gg\to H\to ZZ^*}_{on-shell}(m_H)}{\sigma^{gg\to H\to ZZ^*}_{on-shell,SM}(m_H)} = \frac{\kappa^2_{g,on-shell}(m_H) \cdot \kappa^2_{V,on-shell}(m_H)}{\frac{\Gamma_H}{\Gamma^{SM}_H}}, \tag{4.5}$$

which depends on the total width $\Gamma_H$ through the Higgs boson propagator. Assuming identical on-shell and off-shell Higgs couplings, the ratio of $\mu_{off-shell}$ to $\mu_{on-shell}$ provides a measurement of the total width of the Higgs boson.

Several preliminary considerations need to be taken into account for such a strategy:

- In order to interpret the $\mu_{off-shell}/\mu_{on-shell}$ ratio as a measurement of $\Gamma_H$, the off-shell coupling scale factors must be assumed independent of the energy scale $\hat{s}$ in the high-mass region selected by the analysis and identical to the on-shell corresponding values. This assumption is particularly relevant to the running of the effective coupling $\kappa_g(\hat{s})$ for the loop-induced $gg \to H$ production process, as it is sensitive to new physics that enters at higher mass scales and could be probed in the high-mass $m_{ZZ}$ signal region of this analysis. More details are given in [53–56]. New physics can also enter in the decay of the Higgs boson, resulting in this case in a modification of the $\kappa^2_{V,on-shell}$ couplings. The study of the off-shell Higgs boson production can then add information about the coupling structure of the Higgs boson particle. In the current analysis it is assumed that there are no sizable kinematic modifications to the off-shell signal nor any new sizable signal in the search region of this analysis which are unrelated to an enhanced off-shell signal strength [57,58]. It is further assumed that any new physics which modifies the off-shell signal strength $\mu_{off-shell}$ and the off-shell couplings $\kappa_{i,off-shell}$ does not modify the predictions for the SM backgrounds. Under these assumptions, the measurement of $\mu_{off-shell}$ should be regarded as a search for a deviation from the SM expectation. The observation of a deviation is independent of any assumptions, but the interpretation of the deviation as a non-standard Higgs boson off-shell coupling is based on the assumption above.

  With the current sensitivity of the analysis, only an upper limit on the total width $\Gamma_H$ can be determined, for which the weaker assumption

$$\kappa^2_{g,on-shell} \cdot \kappa^2_{V,on-shell} \leq \kappa^2_{g,off-shell} \cdot \kappa^2_{V,off-shell}\,, \tag{4.6}$$

  that the on-shell couplings are no larger than the off-shell couplings, is sufficient. Also, events with mass > 2000 GeV are discarded, as no data events are observed above this region. Such a cutoff also avoids a phase space far away from the off-shell region, which might invalid the assumption of identical off-shell and on-shell Higgs couplings [53].

- Higher-order quantum chromodynamics (QCD) and electroweak (EW) corrections are known for the off-shell signal process $gg \to H^* \to ZZ$ [151]. During the LHC Run 1, only higher-order QCD corrections for the off-shell signal pro-

cess were known up to the next-to-next-to-leading-order (NNLO), in the form of $K$-factors $K^{H^*}(m_{ZZ}) = \sigma^{NNLO}_{gg\to H^*\to ZZ}/\sigma^{LO}_{gg\to H^*\to ZZ}$, while no higher-order QCD calculations were available for the $gg \to ZZ$ process and for the interference contribution. Thus, the result was provided in a range determined by varying the unknown $gg \to ZZ$ background $K$-factor from higher-order QCD corrections between half and twice the value of the known signal $K$-factor, formally as a function of the $K$-factor ratio $R^B_{H^*} = K(gg \to ZZ)/K(gg \to H^* \to ZZ)$ in the range [0.5, 2]. Recently, higher-order QCD corrections have become available also for the $gg \to ZZ$ background process [153, 154] making possible to provide the result without further assumptions on the higher-order QCD corrections for the background process. However, QCD corrections for the off-shell signal processes have only been calculated inclusively in the jet multiplicity or non-zero $p_T$(ZZ) values that are induced by the higher-order QCD corrections, and may no longer be accurate if event selections - which bias the jet multiplicity or transverse momentum $p_T$(ZZ) - are applied. Consequently, the impact of any direct or indirect selections in jet multiplicity or $p_T$(ZZ), must be assessed by simulating the additional QCD activity with a parton shower MC to approximate the missing higher-order matrix element contributions leading to correspondingly larger acceptance uncertainties. The experimental analyses are therefore performed inclusively in jet observables by designing the event selections in order to minimize the dependence on the boost of the $ZZ$ system, which is sensitive to the jet multiplicity.

- All the above discussion is also valid for the Higgs boson production via vector-boson-fusion (VBF), except that the gluon-Higgs ($ggH$) coupling should be replaced with the Higgs-vector-boson ($HVV$) coupling. Though the VBF Higgs production cross section is much smaller than the ggF process, the production and decay of the Higgs boson in VBF occurs at tree level, so that this process is sensitive to different theoretical systematics relative to the gluon fusion process. In particular, it is not susceptible to loop effects that decouple in the off-shell region, such as those discussed in [53]. As a consequence, the theoretical systematic uncertainties for VBF are more under control when compared to the gluon gluon fusion process. A full description of the theoretical corrections for both the processes is reported in Sec. 1.4.1. As pointed out in [155] and

shown in Figure 4.2, the tail ($m_{ZZ} > 1$ TeV) of the Higgs-mediated diagrams is relatively more important for VBF than for ggF, compared to their respective peak cross sections. The differing fall off of the purely Higgs-mediated curves is due to the growth proportional to $E^2$ ($E$) of the underlying VBF (ggF) amplitudes. For this study, the off-shell Higgs boson via VBF is also considered. Given that the analysis is performed inclusively in jet observables, no specific VBF selections - searching for well separated forward tag jets - are used.

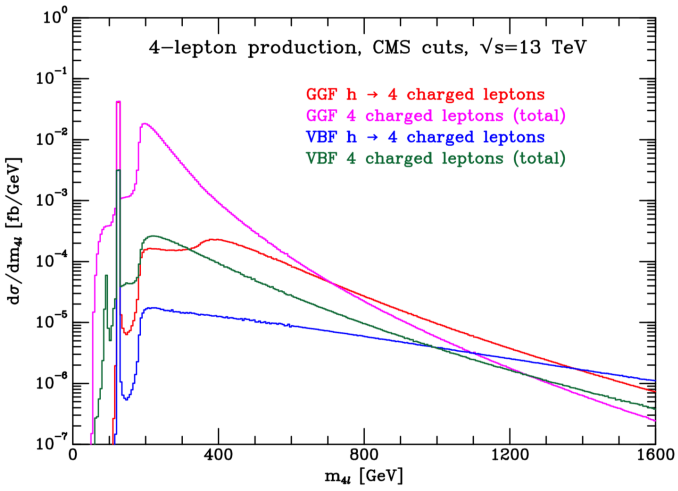


Figure 4.2: Comparison of the rates for the gluon fusion processes $gg \to e^-e^+\mu^-\mu^+$ (red and purple) and the vector boson fusion processes $qq \to e^-e^+\mu^-\mu^+qq$ (blue and green), including Higgs-mediated processes, from [155]. The rates are plotted as a function of the four-lepton mass.

Based on all the considerations described above, the primary goal of this analysis is a limit on the off-shell signal strength, $\mu_{off-shell}$, and later, under well defined assumptions, of the Higgs boson total width, $\Gamma_H$.

Figure 4.3(a) shows the size and kinematic properties of the gluon-induced signal and background processes by showing the $m_{4\ell}$ distribution for the process $gg \to (H^* \to)ZZ \to 2e2\mu$[2] on generator level quantities. For completeness, the predictions with different off-shell Higgs couplings, $\mu_{off-shell} = 5$ and 10, are shown for comparison. For low masses $m_{ZZ} < 2m_Z$ the off-shell signal is negligible, while it becomes comparable to the continuum $gg \to ZZ$ background for masses above

[2]This illustration is valid for all four lepton final states ($2e2\mu$, $4e$ and $4\mu$), as reported in [156].

the $2m_t$ threshold. The interference between the $gg \to H^* \to ZZ$ signal and the $gg \to ZZ$ background is shown in Fig. 4.3(b). The interference is always negative over the whole mass range, as predicted in the SM. Similarly, in Fig. 4.3(c) the $gg \to H^* \to ZZ \to 2\ell 2\nu$ signal is shown for the SM prediction and with different off-shell Higgs couplings, $\mu_{off-shell} = 5$ and 10.

## 4.3 Simulation and Theoretical Corrections

This section describes the Monte Carlo samples and generators used to model signal and background processes in this analysis, as well as the corrections applied to match the best available theoretical predictions.

The dominant processes contributing to the high-mass signal region in the $ZZ \to 4\ell$ and $ZZ \to 2\ell 2\nu$ final states are:

- the $gg \to H^* \to ZZ$ off-shell signal, the $gg \to ZZ$ background and the interference between them;
- the $ZZ$ production through VBF and $VH$-like production modes $pp \to ZZ+2j$ (s-, t- and u-channels)
- the dominant $q\bar{q} \to ZZ$ background (Fig. 4.1).

In the following subsections, the MC samples and the theoretical corrections for each contribution listed above are briefly described, while more details can be found in Appendix B. For all the theoretical calculations a Higgs boson mass of $m_H$ = 125 GeV is assumed for the signal processes. However, varying the Higgs mass within ± 1 GeV has been proved to have negligible effects on the off-shell mass-line shapes. The expected value for the off-shell production rate is only very weakly dependent on the Higgs boson mass value. The detector simulation for all generated Monte Carlo (MC) event samples is done with Geant4 [109, 110].

### 4.3.1 $gg \to (H^* \to)ZZ \to 4f$

Monte Carlo (MC) samples of $gg \to (H^* \to)ZZ$ events, including the $gg \to H^* \to ZZ$ signal, the continuum background $gg \to ZZ$, and the signal-background interference contribution are generated with Sherpa 2.2.2+OpenLoops [113–116]. The Sherpa

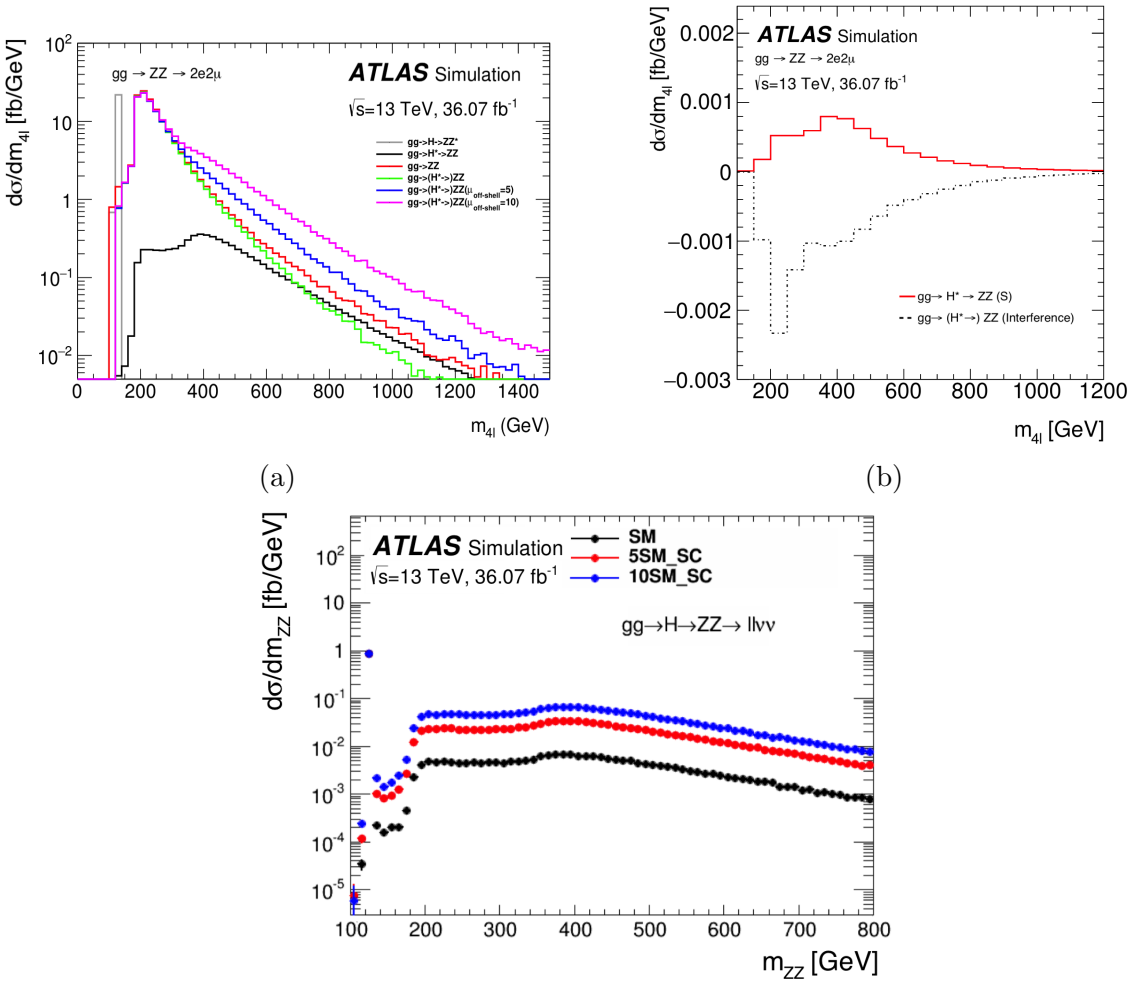


(a) (b)

(c)

Figure 4.3: (a) Differential cross-sections at parton level for the $gg \to (H^* \to)ZZ \to 2e2\mu$ channel and the on-shell Higgs: $gg \to H \to ZZ^*$ on-shell signal (grey), $gg \to H^* \to ZZ$ off-shell signal (black), $gg \to ZZ$ continuum background (red), $gg \to (H^* \to)ZZ$ with SM Higgs coupling (green), $gg \to (H^* \to)ZZ$ with $\mu_{off-shell}$ = 5 (blue) and $gg \to (H^* \to)ZZ$ with $\mu_{off-shell}$ = 10 (purple). (b) Differential cross-section at parton level for the SM $gg \to H^* \to ZZ \to 2e2\mu$ signal (solid line) and its interference with the $gg \to ZZ \to 2e2\mu$ continuum background (dashed line), as predicted in the SM. (c) Differential cross-section at parton level for the SM $gg \to H^* \to ZZ \to 2\ell 2\nu$ channel and the on-shell Higgs (black), $gg \to H^* \to ZZ \to 2\ell 2\nu$ signal with $\mu_{off-shell}$ = 5 and the on-shell Higgs (red) and $gg \to H^* \to ZZ \to 2\ell 2\nu$ signal with $\mu_{off-shell}$ = 10 and the on-shell Higgs (blue).

generator is preferable since it allows to generate $gg$ samples with up to one additional parton in the final state [116], providing a better modeling of QCD related kinematic observables than the LO samples. The core scale is set to $\mu = m_{ZZ}/2$ within the scale setting approach used by SHERPA and the `NNPDF3.0_nnlo` PDF set [119] is used.

A good theoretical control of the off-shell region requires the knowledge of higher-order QCD corrections to the signal $gg \to H^* \to ZZ$ , the background $gg \to ZZ$ and their interference. However, the state of the art for theoretical predictions of signal, background and interference is very different.

For the off-shell signal, $gg \to H^* \to ZZ$, higher-order QCD calculations are available in Ref. [151] up to the next-to-next-to-next-to-leading order (N$^3$LO[3]) [42]. However, the N$^3$LO QCD corrections are not known with exact quark mass dependence. Similarly for the NNLO and the NLO QCD corrections which are shown in Fig. 4.4. For the continuum background, $gg \to ZZ$, even the NLO calculations pose significant technical challenges, due to the complicated loop amplitudes.

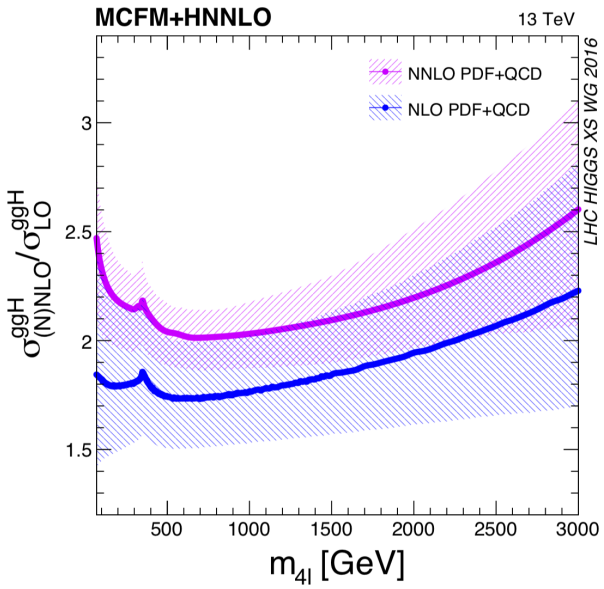


Figure 4.4: Higher-order QCD theoretical corrections for the off-shell signal process $gg \to H^* \to ZZ$ from [157]: NNLO (purple) and NLO (blue).

In 2015-2016 QCD NLO calculations for the continuum background and the

[3]Such correction was not available at the time when this analysis was performed.

signal-background interference were produced [158, 159]. Such NLO to LO corrections are incorporated through a $K$-factor correction defined as: $K(m_{ZZ}) = \sigma^{NLO}/\sigma^{LO}$ where $\sigma^{NLO}$ is the calculated NLO cross section for the $gg$ process. The corrections evolve with the Higgs boson virtuality $m_{ZZ}$ and also accounts for NLO EW corrections. The $K$-factors are calculated separately for the $gg \to H^* \to ZZ$ signal, $K^S(m_{ZZ})$, the $gg \to ZZ$ continuum background, $K^B(m_{ZZ})$, and the interference term, $K^I(m_{ZZ})$. In these calculations, the $1/m_t$ expansion is used for the $m_{ZZ} < 2m_t$ region, and for the high-mass region $m_{ZZ} > 2m_t$, the NLO calculations are available under the massless quarks assumption and $K$-factors for massive and massless contributions are assumed to be identical. Figure 4.5 shows the NLO QCD corrections as function of $m_{ZZ}$ for the different $gg \to (H^* \to)ZZ$ processes. Due to the complexity of the theoretical calculations, the $K$-factors suffer statistical fluctuations, especially in the high-mass region. A simple $2^{nd}$-order-polynomial-functional fit to the $K$-factor distributions is applied to smooth the $K$-factors.

The generator settings are summarized below and more details of this calculation can be found in [157]:

– PDF: `CT10nnlo`;

– QCD scale: $m_{ZZ}/2$;

– Fiducial cuts: lepton $p_T > 5$ GeV, $|\eta| < 3$.

The following systematic variations are included:

– QCD scale: central $m_{ZZ}/2$, $[m_{ZZ/4}, m_{ZZ}]$.

The NLO and NNLO $K$-factors for the $gg \to ZZ$ processes are calculated with respect to the pure LO calculations and thus, they cannot be applied directly to the SHERPA MC samples, which are generated with up to one hard jet from the matrix element. Therefore, the higher-order QCD theoretical corrections are applied, as a function of $m_{ZZ}$, to the LO QCD samples from MCFM (Monte Carlo for FeMtobarn processes) for the $4\ell$ analysis and from gg2VV for the $2\ell 2\nu$ channel. These samples are then used to re-weight the SHERPA samples which are needed to derive the final results in both the channels, $4\ell$ and $2\ell 2\nu$. More details on the SHERPA re-weighting procedure are given in Appendix B.

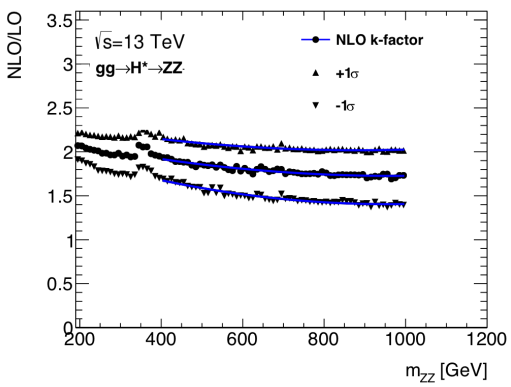


(a) $K^{S}_{NLO/LO}(m_{ZZ})$

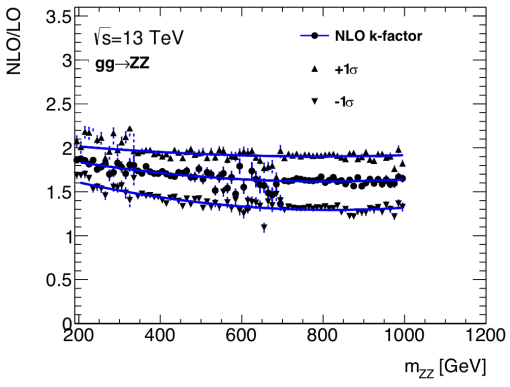


(b) $K^{B}_{NLO/LO}(m_{ZZ})$

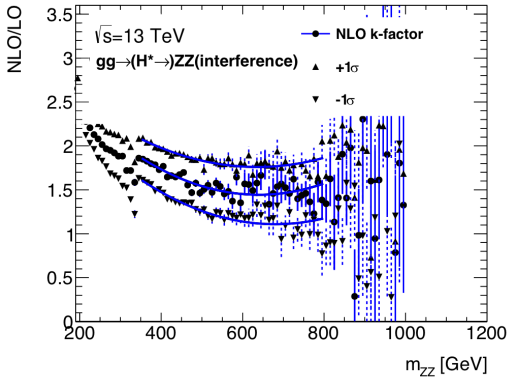


(c) $K^{I}_{NLO/LO}(m_{ZZ})$

Figure 4.5: New QCD $K_{NLO/LO}$-factors as function of $m_{ZZ}$ for the different $gg \to (H^{*} \to)ZZ$ processes, as calculated in [158, 159]. Circle markers show the central value of the $K$-factor, triangle markers show the $\pm 1\sigma$ band uncertainties due to the QCD scale variations and the blue line shows a $2^{nd}$-order-polynomial fit to the high-$m_{ZZ}$-invariant-mass distribution.

In this analysis two possible approaches for the application of the higher-order QCD corrections are considered, evaluating the impact of these corrections to the sensitivity of the $\mu_{off-shell}$ estimate:

1. **Pure NLO $K$-factors**. For this approach the NLO $K$-factors shown in Fig. 4.5 are used. For the different $gg$ processes the corresponding $K$-factors are applied as a function $m_{ZZ}$.

2. **Pure NLO $K$-factors with NNLO-NLO scale factor**. Similar to the previous approach, but on top of the NLO $K$-factors shown in Fig. 4.5, an

additional NNLO/NLO $K$-factor of 1.2 is applied to all the NLO $K$-factors: signal, background and interference. This is motivated by the fact that the NNLO corrections are available for the signal process only and this additional constant scale factor represents the constant NNLO to NLO ratio of the QCD predictions over the data region considered in the analysis, as shown in Figure 4.6. For this approach it is thus assumed that the NNLO/NLO scale factors are the same for signal, background and interference.

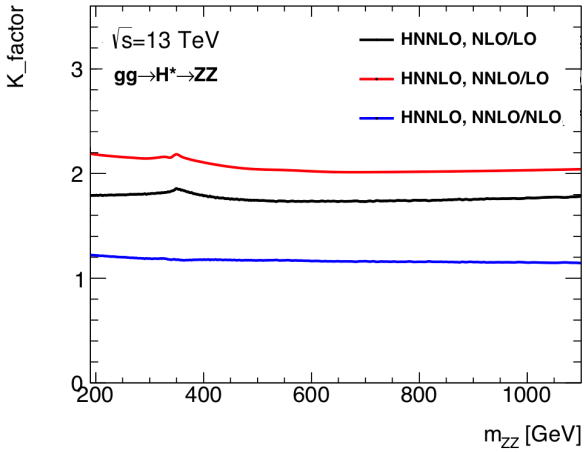


Figure 4.6: Higher-order QCD correction calculated as $K$-factors with the HNNLO generator for the $gg \to H^* \to ZZ$ process. Different $K$-factors are shown: $K_{NNLO/LO}$ (red), $K_{NNLO/NLO}$ (blue) and $K_{NLO/LO}$ (black).

In the Run-1 paper [61] for the off-shell production of the Higgs boson, the ATLAS collaboration followed the prescription in [42]. Since no higher-order QCD corrections were available for the continuum background and the signal-background interference, the signal NNLO $K$-factors were also applied to the background and interference distributions. As this is a strong assumption, results were given as a function of the $K$-factor ratio

$$R^B_{H^*} = \frac{K(gg \to ZZ)}{K(gg \to H^* \to ZZ)} = \frac{K^B(m_{ZZ})}{K^S_{gg}(m_{ZZ})}, \tag{4.7}$$

between the $gg \to ZZ$ background and the $gg \to H^* \to ZZ$ signal, in order to check the dependence of the results on the unknown NNLO $K$-factors for the background.

Since the $K$-factors $K^S_{gg}(m_{ZZ})$ was almost constant as a function of $m_{ZZ}$ in the relevant region of phase space, no mass dependence on $R^B_{H^*}$ was assumed.

In Run 2, there is no need anymore for such an approach given that a proper NLO calculation is available also for the continuum background and for the interference. For the final results, the NLO $K$-factors with the NNLO-NLO Scale Factor (SF), case (2) listed above, are used as the baseline for the application of higher-order QCD corrections to the $gg$ processes. Variations on the results using the other scenario, pure NLO $K$-factors, are also provided.

Some considerations are needed for the application of the higher-order QCD theoretical corrections described above. Because of the way they were calculated, there are some systematic uncertainties which need to be considered:

- Validity of the $K$-factors at $m_{ZZ} = 2m_t$. The top quark mass expansion does not work at the resonance threshold. To take into account the effect of the unknown $K$-factor at the threshold, the QCD scale uncertainty of the $K$-factors is increased by 50% around the $m_{ZZ} = 2m_t$-threshold, with a Gaussian-smoothed transition decreasing to the default uncertainty within $2m_t \pm 50$ GeV. This is intended to allow for possible effects on the $K$-factors which are not included in the calculation as the top quark moves on-shell.

- Jet $p_T$ cutoff at 150 GeV. As described in [159], in the NLO $K$-factors calculation, an empirical cutoff of $p_T < 150$ GeV was applied to obtain stable calculations all the way up to the top production threshold. Such a cutoff excludes only about 8% of hard jet events, but it means that for events with $m_{ZZ} < 2m_t$ and with a hard jet $p_T > 150$ GeV, the NLO corrections are missing. In the analysis, the $K$-factors are applied to all events, but for those events failing the cutoff, the QCD scale uncertainty was doubled in order to be conservative.

### 4.3.2 $ZZ$ Final States in the Electroweak Production Mode

In this section, all the details of the simulation for the $pp \to ZZ + 2j$ process are documented. The MadGraph5_aMC@NLO generator [121] is used in both the $4\ell$ and $2\ell 2\nu$ final states. The QCD renormalization and factorization scales were set to $m_W$ following the recommendations in [156] and the `NNPDF2.3_lo` PDF set [119]

was used. PYTHIA 8.186 [123] was used for parton showering and hadronisation. Since there is no dedicated VBF (or VH) category in this analysis and the inclusive ggF+VBF category is largely dominated by the gluon-gluon initiated process, no additional theoretical corrections are considered for the electroweak-production modes of the Higgs boson. The off-shell Higgs boson is simulated by applying a large Breit-Wigner cut-off (bwcutoff) value to the Higgs resonance[4]. Following recommendations in [42], $m_H$ is set at the value of 125 GeV, while its SM width value at $\Gamma_H = 4.097$ MeV.

As in the ggF production mode, various samples have been generated: the $q\bar{q} \to H^* \to ZZ + jj$ off-shell signal sample (S), with the assumption of Standard Model couplings, the $q\bar{q} \to ZZ + jj$ background-only sample (B), the sample including the S-B interference (SBI), and two additional samples with $\Gamma_H/\Gamma_H^{SM}$ = 5 or 10, named SBI5 and SBI10, respectively.

The simulated $pp \to ZZ + 2j$ process contains Higgs-signal events produced through:

- the off-shell VBF $H \to 4f$ process which scales with $k_Z^4$, but it is independent of $\Gamma_H$,
- the off-shell VH $H \to 4f$ process which also scales with $k_Z^4$ and it is $\Gamma_H$-independent,
- the on-shell VBF- and $VH$-like events which scale as $k_Z^4/\Gamma_H$.

Since the on-shell events behave differently from the off-shell events with respect to a measurement of the off-shell couplings or the Higgs boson total width, these two populations need to be separated. This is done by requiring that the generated Higgs boson mass satisfies $|m_H^{gen} - 125| < 1$ GeV which is highly efficient in selecting the on-shell events. Effectively the on-shell Higgs events behave more as a background source rather a signal for this analysis. Also, a requirement of $E_T^{miss} \geq 80$ GeV is made. The event filter is applied to the $2l2\nu$ sample to avoid generating events that will be removed by the subsequent event selection. Such a filter has an efficiency of $\sim 30\%$ on the signal sample and $\sim 60\%$ on the background sample. More details on the VBF samples are given in Appendix B.4.

[4] A resonance is considered to be on-shell if the invariant mass through the $s$-channel is within $M \pm \text{bwcutoff} * \Gamma$

Figure 4.7(a) shows the truth level $m_{4\ell}$ distribution and Fig. 4.7(b) the $m_T^{ZZ}$ distribution for the various $q\bar{q} \to ZZ + jj$ processes in both final states, $4\ell$ and $2\ell 2\nu$.

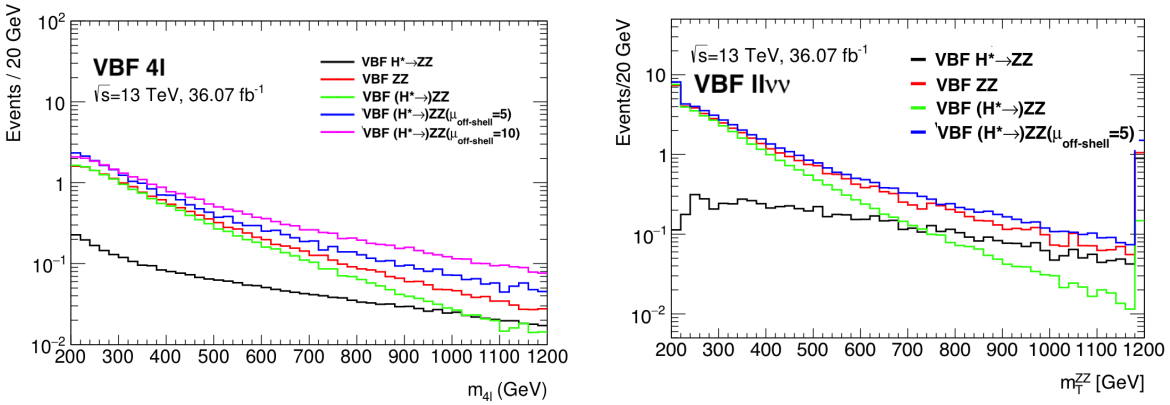


(a) $q\bar{q} \to ZZ \to 4\ell$ (b) $q\bar{q} \to ZZ \to 2\ell 2\nu$

Figure 4.7: Detector-level distribution of the $m_{4\ell}$ (a) and of the transverse mass $m_T^{ZZ}$ (b) for the various $q\bar{q} \to ZZ + jj$ processes, assuming SM couplings and for $\mu_{off-shell}$ = 5 or $\mu_{off-shell}$ = 10. The various distribution are normalized to unit area. The list of processes shown includes: Higgs signal (black), $q\bar{q}$ background (red), inclusive VBF $(H^* \to)ZZ$ (green), inclusive VBF $(H^* \to)ZZ$ with $\mu_{off-shell}$ = 5 (blue) and inclusive VBF $(H^* \to)ZZ$ with $\mu_{off-shell}$ = 10 (purple).

### 4.3.3 Parametrization for the Off-shell Regime

The known dependency of the off-shell Higgs boson signal process, the background process and the interference term on the off-shell signal strength $\mu_{off-shell}$ can be used to assemble MC samples for arbitrary values of $\mu_{off-shell}$ from three SM MC samples. An event sample $\sigma_{gg\to(H^*\to)VV}(\mu_{off-shell})$ for the $gg \to (H^* \to)VV$ process with an arbitrary value of the off-shell Higgs boson signal strength $\mu_{off-shell}$ $(SBIr)$ can be constructed from the MC sample for the SM Higgs boson signal $gg \to H^* \to VV$ $(\sigma^{SM}_{gg\to H^*\to VV})$ $(S)$, the $gg \to VV$ continuum background MC sample $(\sigma_{gg\to VV,cont})$ $(B)$ and a full SM Higgs boson signal plus background $gg \to (H^* \to)VV$ MC sample $(\sigma^{SM}_{gg\to(H^*\to)VV})$ $(SBI)$ where the last sample is required to derive the interference sample which is not directly generated.

When higher-order QCD corrections are applied, the $SBIr$ sample can be con-

structed using the following weighting function:

$$\begin{aligned}\sigma_{gg\to(H^*\to)VV}(\mu_{off-shell}) &= \mu_{off-shell}\cdot K^S(m_{VV})\cdot\sigma^{SM}_{gg\to H^*\to VV} \\ &+ \sqrt{\mu_{off-shell}}\cdot K^I(m_{VV})\cdot\sigma^{SM}_{gg\to VV,\,\text{Interference}} \\ &+ K^B(m_{VV})\cdot\sigma_{gg\to VV,\,\text{cont}}\,, \end{aligned} \tag{4.8}$$

$$\sigma^{SM}_{gg\to VV,\,\text{Interference}} = \sigma^{SM}_{gg\to(H^*\to)VV} - \sigma^{SM}_{gg\to H^*\to VV} - \sigma_{gg\to VV,\,\text{cont}}\,, \tag{4.9}$$

where the $K$-factors are calculated as described in Sec. 4.3.1 and $\sigma^{SM}_{gg\to VV,\,\text{Interference}}$ represents the MC sample for the signal-background interference.

This parametrization is validated using the generated $gg\to(H^*\to)ZZ$ samples with $\mu_{off-shell}=5$; the comparison with the reconstructed samples is shown in Fig. 4.8. The generated $SBI5$ sample and the parametrized one are consistent within statistical uncertainty.

A similar parametrization can also be used for the EW $pp\to(H^*+2j\to)ZZ+2j$ process with an arbitrary value of the off-shell Higgs boson signal strength $\mu_{off-shell}$.

### 4.3.4 $q\bar{q}\to ZZ\to 4f$

The $q\bar{q}\to ZZ$ background is simulated with the Sherpa 2.2.2 generator [113, 114, 160], with the `NNPDF3.0_nnlo` PDF set for the hard scattering process. NLO accuracy is achieved in the matrix element calculation for the 0- and 1-jet final states and LO accuracy for the 2- and 3-jet final states. The merging is performed with the Sherpa parton shower using the MePs@NLO prescription [120].

Besides QCD effects, also higher-order EW corrections need to be taken into account since they are not included in the Sherpa generator. They were calculated in [161, 162] for on-shell outgoing vector bosons and found to be sizable in the high $VV$ mass region and for high-$p_T$ observables. The NLO EW corrections are incorporated in the analysis by re-weighting the Sherpa samples. $K$-factors are calculated differentially in the transverse mass of the $ZZ$ system and in the exact fiducial volume defined in the analysis. The required quantities are derived from the initial-state quarks and the outgoing $Z$ bosons. The re-weighting method followed is taken from [163] and validated in [164]. More details on this calculation can be found in Appendix B.2.

The EW $K$-factors are shown in Fig. 4.9 as a function of the diboson mass.

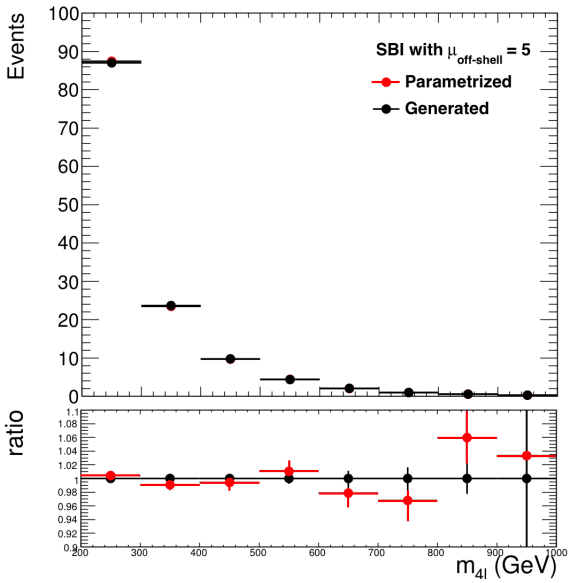


(a) $gg \to (H^* \to) ZZ \to 4\ell$

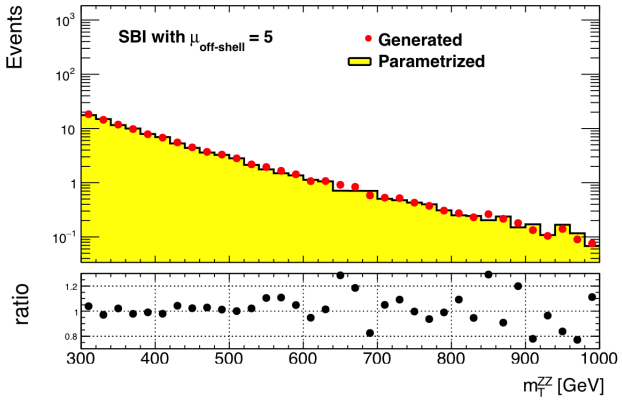


(b) $gg \to (H^* \to) ZZ \to 2\ell 2\nu$

Figure 4.8: Comparison of the distribution of the $m_{4\ell}$ (a) and of the transverse mass $m_T^{ZZ}$ (b) with $\mu_{off-shell} = 5$ for the generated $gg \to (H^* \to) ZZ$ sample [black for (a) and red for (b)] and the $gg \to (H^* \to) ZZ$ sample assembled using the parametrization discussed in the text based on the three generated samples: $gg \to H^* \to ZZ$ , $gg \to ZZ$ and $gg \to (H^* \to) ZZ$ samples [red markers for (a) and yellow histogram for (b)]. The various distribution are normalized to the same luminosity. Figure (a) produced by an ATLAS collaborator.

They are shown for the $2e2\nu$ channel, but similar results are obtained for the $2\mu 2\nu$ final state and for the $4\ell$ channel.

Some correlation studies between PDF uncertainties for the $gg \to ZZ \to 4f$ and

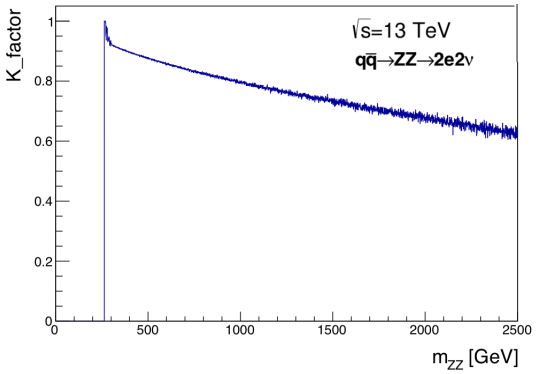


Figure 4.9: NLO EW $K$-factors applied in this analysis as a function of the diboson mass. They are shown for the $2e2\nu$ channel, but similar results are obtained for the $2\mu2\nu$ and in the $4\ell$ channel.

$q\bar{q} \to ZZ \to 4f$ processes are provided in Appendix B.3.

### 4.3.5 Other MC Samples

The $WW$ and $WZ$ backgrounds were simulated at NLO in QCD using the Powheg-Box v2 event generator [165] with the `CT10_nlo` PDF set [166] and Pythia 8.186 for parton showering and hadronisation. The non-perturbative effects were modeled with the AZNLO set of tuned parameters [167]. The interference between $q\bar{q} \to ZZ$ and $q\bar{q} \to WW$ processes for the $2\ell2\nu$ final state is found to be negligible and thus is not considered.

Events containing a single $Z$ boson with associated jets ($Z + jets$) were simulated using the Sherpa v2.2.1 event generator. Matrix elements were calculated for up to two partons at NLO and four partons at LO using the Comix [160] and OpenLoops [114] matrix-element generators and merged with the Sherpa parton shower [120] using the MePs@NLO prescription. The `NNPDF3.0_nnlo` PDF set was used in conjunction with dedicated parton-shower tuning developed by the Sherpa authors. The $Z + jets$ events are normalized using the NNLO cross sections [168].

The triboson backgrounds $ZZZ$, $WZZ$, and $WWZ$ with fully leptonic decays and at least four prompt charged leptons were modeled using Sherpa v2.1.1. The contribution from triboson backgrounds with one $W$ or $Z$ boson decaying hadronically is not included in the simulation, but the impact on the analysis is found to be negligible. For the fully leptonic $t\bar{t} + Z$ background, with four prompt

charged leptons originating from the decays of the top quarks and $Z$ boson, MadGraph5_aMC@NLO was used. The $t\bar{t}$ background, as well as the single-top and $Wt$ production, were modeled using Powheg-Box v2 interfaced to Pythia 6.428 [124] with the Perugia 2012 [169] set of tuned parameters for parton showering, hadronisation and the underlying event, and to EvtGen v1.2.0 [126] for properties of the bottom and charm hadron decays.

The ATLAS detector simulation within the Geant 4 framework [110] or the fast detector simulation package Atlfast-II [109] is used to process the particle-level events produced by the various MC event generators. The simulation also includes additional $pp$ interactions in the same and nearby bunch crossings, better known as pile-up events. The pile-up events were generated using Pythia 8 with the A2 set of tuned parameters [125] and the MSTW2008LO PDF set [117]. The simulation samples were properly weighted in order to reproduce the observed distribution of the mean number of interactions per bunch crossing observed in the data.

Table 4.1 summarizes the state of the art of theoretical corrections, generators and PDF sets used for the leading processes in the $2\ell 2\nu$ analysis.

## 4.4 Analysis in the $ZZ \to 4\ell$ Channel

This section describes the analysis strategy in the $ZZ \to 4\ell$ channel. Since I am not part of this ATLAS working group but I was responsible for the combination of the $ZZ \to 4\ell$ and $ZZ \to 2\ell 2\nu$ results, I briefly describe the overall strategy used for this decay channel.

The $H \to ZZ$ decay mode is the golden channels to explore the high-mass regime. The $ZZ \to 4\ell$ final state provides the cleanest possible channel, because of the excellent signal separation from background and the good momentum resolution measurement of the leptons which is in turn good for the invariant-mass resolution. The analysis for the $ZZ \to 4\ell$ final state closely follows the on-shell Higgs boson measurement and the high-mass search in the same final state described in [30, 170], with the same physics object definitions, trigger and event selections, and background estimation methods. Since the higher-order QCD corrections are derived inclusively in the jet multiplicity, no classification based on the number of jets is implemented. A matrix-element-based discriminant (ME-based discriminant) is constructed to enhance the separation between the $gg \to H^* \to ZZ$ signal and the $gg \to ZZ$ and

| **Process** | Theor. corrections | Generator | PDF set |
|---|---|---|---|
| $gg \to (H^* \to)ZZ$ with $gg \to H^* \to ZZ(S)$ $gg \to ZZ(B)$ and their interference (I) | NLO QCD + 1.2 NNLO/NLO SF NLO EW | SHERPA 2.2.2 + OpenLoops | `NNPDF3.0_nnlo` |
| $VBF\ (H^* \to)ZZ$ with $VBF\ H^* \to ZZ$ (S) $VBF\ ZZ(B)$ and their interference (I) | No additional corrections | MADGRAPH5 _AMC@NLO (matrix calc. at LO) | `NNPDF2.3_lo` |
| $q\bar{q} \to ZZ$ | NLO QCD (0, 1 jet) LO QCD (2, 3 jets) NLO EW | SHERPA 2.2.2 | `NNPDF3.0_nnlo` |
| $q\bar{q} \to WZ(WW)$ | NLO QCD | POWHEG-BOX | `CT10nlo` |
| $Z + jets$ | NLO QCD (2 partons) LO QCD (4 partons) | SHERPA 2.2.1 | `NNPDF3.0_nnlo` |

Table 4.1: Summary of theoretical corrections, generators and PDF sets used for the leading processes in the $2\ell 2\nu$ analysis.

$q\bar{q} \to ZZ$ backgrounds, and is subsequently used in a binned maximum-likelihood fit to derive the final result.

The analysis is split into three channels ($2\ell 2\mu$, $4\mu$ and $4e$). The off-shell region is defined as the range 220 GeV < $m_{4\ell}$ < 2000 GeV, while the on-shell region is defined as 118 GeV < $m_{4\ell}$ < 129 GeV. Events with $m_{4\ell}$ > 2000 GeV are discarded, as no data events are observed above this region and in order to avoid possible energy regimes where the assumptions of the strategy to extract the Higgs boson total width are not valid anymore [53], as largely explained in Sec. 4.2.

Each electron (muon) is required to have transverse momentum $p_T$ > 7 (5) GeV and be measured in the pseudorapidity range $|\eta| < 2.47$ ($|\eta| < 2.7$). The highest-$p_T$

lepton in the quadruplet must satisfy $p_T > 20$ GeV, and the second (third) lepton in $p_T$ order is required to have $p_T > 15$ GeV ( $p_T > 10$ GeV). Lepton pairs are formed from same-flavour opposite-charge leptons. For each channel, the quadruplet with a lepton pair whose mass is closest to the $Z$ boson mass is kept. This pair is referred to as the leading dilepton pair and its invariant mass, $m_{12}$, is required to be in the range 50 GeV $< m_{12} <$ 106 GeV. The second (subleading) pair is chosen from the remaining leptons as the pair closest in mass to the $Z$ boson and in the range 50 GeV $< m_{34} <$ 115 GeV. The Signal Region is characterized by high purity, as the cross sections for most background processes to enter this region are small. The largest contribution to the total background is the irreducible background $q\bar{q} \to ZZ$. It is modeled using MC simulation with accurate NLO QCD and NLO EW corrections, applied as explained in Sec. 4.3.4. The contribution of the reducible backgrounds, such as $Z + jets$, tri-boson production, $ttV$ and top quark production, is only about 2% of the total background in the full off-peak regime, and it is either taken from simulation or from dedicated data control regions.

The observed and expected distributions of $m_{4\ell}$ combining all lepton channels in the off-shell region are shown in Figure 4.10(a). Data are in agreement with the SM predictions, with two small excesses at $m_{4\ell}$ around 400 GeV and 650 GeV, each having a significance of less than two standard deviations ($2\sigma$). Table 5.1 in Chapter 5 shows the expected and observed numbers of events in the signal region and for comparison the equivalent expected and observed numbers of events in the signal region for the $2\ell 2\nu$ channel.

The ME-based discriminant fully exploits the event kinematics in the centre-of-mass frame of the $4\ell$ system. It is based on the following eight kinematic observables: the three masses $m_{4\ell}$, $m_{12}$ and $m_{34}$, the leading $Z$ boson production angle and four decay angles defined in [36]. The following matrix elements are calculated for each event in the off-shell regime:

- $P_{q\bar{q}}$: the matrix element squared for the $q\bar{q} \to ZZ \to 4\ell$ process;
- $P_{gg}$: the matrix element squared for the $qq \to (H^* \to)ZZ \to 4\ell$ process including the Higgs boson with SM couplings, the continuum background and their interference;
- $P_H$: the matrix element squared for the signal-only process $gg \to H^* \to ZZ \to 4\ell$.

The kinematic discriminant is defined as in [52]:

$$D_{ME} = \log_{10}\left(\frac{P_H}{P_{gg} + c \cdot P_{q\bar{q}}}\right), \tag{4.10}$$

where $c$ is an empirical constant, chosen to be 0.1. Other values for $c$ have been tested. It is found that the value of $c$ has a very small effect on the overall sensitivity compared to the other systematic uncertainties.

Figure 4.10(b) shows the shape comparisons of the ME-based discriminant combining all the lepton final states for the $q\bar{q} \to ZZ$ background, the ggF + VBF production modes for $(H^* \to)ZZ$ with SM $\mu_{off-shell}$ and $gg \to (H^* \to)ZZ$ with $\mu_{off-shell}$ = 5 and for the other backgrounds in the full off-peak region, 220 GeV < $m_{4\ell}$ < 2000 GeV, at reconstruction level. Events with ME-based discriminant values between -4.5 and 0.5 are used in the final analysis with a signal efficiency > 99%.

## 4.5 Analysis in the $ZZ \to 2\ell 2\nu$ Channel

Since the branching fraction for each $Z$ boson decaying to a charged lepton pair is low, 3.4% per lepton pair, a very low overall production cross section is expected in the $ZZ \to 4\ell$ channel. To increase the sensitivity in the Higgs off-shell production regime, the $\ell^+\ell^- + E_T^{miss}$ channel, where one of the $Z$ bosons instead decays to a pair of neutrinos, plays a leading role thanks to the higher branching fractions of $Z \to \nu\bar{\nu}$, 20.5% for the three neutrino flavours. Because of the large $Z$ branching fractions to quarks, ~ 69%, other channels like $H^* \to ZZ \to q\bar{q}\nu\bar{\nu}$ or $H^* \to ZZ \to q\bar{q}\ell\ell$ are even more sensitive. However, they are characterized by a large QCD background contaminating the signal region. Accordingly, they are useful only at large masses, $m_H$ > 1 TeV, where the jet resolution improves. For lower Higgs boson masses, the large systematics for the $E_T^{miss}$ and/or jets seriously compromise the sensitivity of these final states. The $2\ell 2\nu$ channel is the optimal choice for its sensitivity in the intermediate mass range, 300 GeV < $m_H$ < 1.5 TeV, which is the mass range of interest in this analysis.

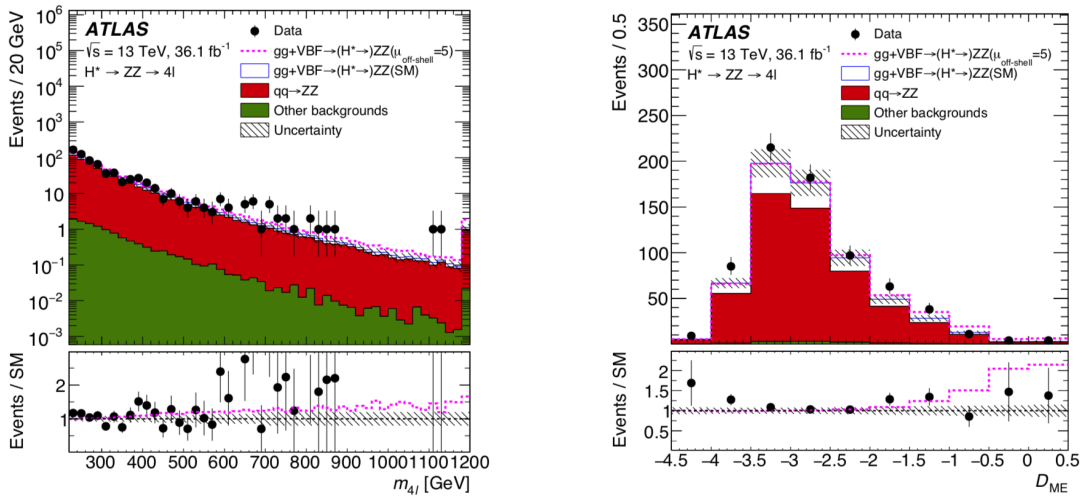


(a) $m_{4\ell}$ (b) $D_{ME}$

Figure 4.10: Observed distributions in the off-shell regime, 220 GeV < $m_{4\ell}$ < 2000 GeV, for (a) the four-lepton invariant mass, $m_{4\ell}$, and for (b) the ME-based discriminant, $D_{ME}$, combining all lepton final states. The distributions are compared to the expected contributions from the SM including the Higgs boson (stacked). Events with $m_{4\ell}$ > 1200 GeV are included in the last bin of the $m_{4\ell}$ distribution. The hatched area shows the combined statistical and systematic uncertainties. The dashed line corresponds to the total expected event yield, including all backgrounds and the Higgs boson with $\mu_{off-shell} = 5$. The ratio plot shows the observed data yield divided by the SM prediction (black points) as well as the total expected event yield with $\mu_{off-shell} = 5$ divided by the SM prediction (dashed line) in each bin. Figures from [63].

### 4.5.1 Analysis Strategy

The analysis in the $2\ell 2\nu$ final state closely follows the one performed for the search for new $ZZ$ heavy resonances at 13 TeV [30]. The reconstruction, identification and selection of physics objects (electrons, muons, jets, b-jets and missing transverse momentum) is kept identical while the event selection has been optimised to target the off-shell Higgs boson production in the gluon-gluon fusion mode. The analysis is performed inclusively by production mode, looking for both the ggF and VBF modes. A set of inclusive selections is used to isolate the ggF and VBF events from the main backgrounds. To discriminate between the signal and the background and enhance the sensitivity to off-shell Higgs boson production, the transverse mass

distribution of the $ZZ$ system ($m_T^{ZZ}$) is used, defined as:

$$(m_{\mathrm{T}}^{ZZ})^2 \equiv \left[\sqrt{m_Z^2 + |\vec{p}_T^{\,\ell\ell}|^2} + \sqrt{m_Z^2 + |\vec{E}_T^{\,miss}|^2}\right]^2 - \left[\vec{p}_T^{\,\ell\ell} + \vec{E}_T^{\,miss}\right]^2 \tag{4.11}$$

where $m_Z$ is the mass of the $Z$ boson fixed at 91.2 GeV, $\vec{p}_T^{\,\ell\ell}$ the transverse momentum of the dilepton system ($\vec{p}_T^{\,\ell\ell} = \vec{p}_T^{\,\ell_1} + \vec{p}_T^{\,\ell_2}$) and $\vec{E}_T^{\,miss}$ is the transverse momentum from the neutrino pair. The transverse mass $m_{\mathrm{T}}^{ZZ}$ is the most similar variable to the invariant mass of the system, as the latter is not accessible as the momenta of the individual neutrinos are unknown. The analysis is split in two sub-channels, $ee\nu\nu$ and $\mu\mu\nu\nu$, which are later combined to derive the final limits. The selection occurs at four levels, Object Selection described in Sec. 4.5.2, Event Pre-Selection reported in Sec. 4.5.3.1, Trigger Selection described in Sec. 4.5.3.2 and finally Event Selection reported in Sec. 4.5.3.3. Some angular variables are included in the Event Selection to better isolate the off-shell signal.

## 4.5.2 Physics Objects

Both the $ee\nu\nu$ and $\mu\mu\nu\nu$ analyses require two charged leptons in the final state, as well as large missing transverse momentum to identify neutrinos and remove backgrounds like $Z + jets$. This section describes the definitions of the physics objects used in this analysis. The details of the physics-objects reconstruction were already described in Chapter 3, here the specific treatment of the physics objects in the context of the $\ell\ell\nu\nu$ analysis is discussed.

### 4.5.2.1 Electrons

Signal electrons are selected following recommendation provided by the Egamma Combined Performance Group [171]. The 'Medium' identification criterion is chosen with the pseudorapidity of the electrons taken from the cluster when applying the fiducial cuts and from the track in all the other cases. Overlap removal is performed between electrons and jets, with jets removed if found within $\Delta R < 0.2$. Electrons are also required to have transverse energy $E_T > 20$ GeV within $|\eta| < 2.47$ and to be 'Loose' isolated, corresponding to an isolation efficiency $\geq 99\%$ for the selected electron.

To suppress the contribution of electrons from photon conversions, a cut on the

impact parameters with respect to the primary vertex ($d_0$, $z_0$) is applied. Specifically, the selection is placed on the significance of the transverse parameter, $d_0/\sigma_{d_0}$ and the product of $z_0$ with $\sin(\theta)$ where $\theta$ is the polar angle of the track with respect to the beam line axis. The $d_0$ significance is required to be less than 5 and the modulus of the longitudinal parameter, $|z_0 \cdot sin(\theta)|$, is required to be less than 0.5 mm.

#### 4.5.2.2 Muons

Signal muons are selected following recommendations provided by the Muon Combined Performance Group [172]. The 'Medium' identification criterion is chosen and the overlap removal is performed between muons and jets, with jets removed if found within $\Delta R < 0.2$ given certain $p_T$ requirements on the muon objects. Additional overlap removal is done between leptons, with electrons removed if found to have the same ID track. Muons are also required to have $p_T > 20$ GeV within $|\eta| < 2.5$ and to be 'Loose' isolated, corresponding to an isolation efficiency $\geq 99\%$ for the selected muon.

Similar to electrons, to suppress the contribution of cosmic muons and non-prompt muons a cut on the impact parameters with respect to the primary vertex is applied to the muon track in the ID. Specifically, the $d_0$ significance is required to be less than 3 and the modulus of the longitudinal parameter, $|z_0 \cdot sin(\theta)|$, is required to be less than 0.5 mm.

#### 4.5.2.3 Jets

Signal jets are selected following recommendations provided by the Jet-$E_T^{miss}$ group using the anti-$k_T$ EMTopo cluster algorithm with a radius parameter of $\Delta R = 0.4$ [173–175]. The overlap removal is performed to remove muons within $\Delta R < 0.4$ between the jet and muon. Electrons are also removed if the $\Delta R$ is found be between 0.2 and 0.4. Table 4.2 summarizes the various overlap removal criteria used for the objects in the off-shell analysis for the $\ell\ell\nu\nu$ channel.

Jets are also required to have a minimum $p_T$ threshold of 20 GeV within $|\eta| < 4.5$ and to be selected as 'Loose' for the Jet Cleaning tool [176], corresponding to an efficiency of selecting jets from proton-proton collisions above 99.5% for the selected jet. Jet cleaning is performed to remove bad quality jets due to detector inefficiencies resulting in about 10% of all jets rejected. This fraction is dominated by fake jets

| **Overlap Removal** | | |
|---|---|---|
| Object to be removed | Reference object | Criteria |
| jet | electron | $\Delta R_{e-jet} < 0.2$ |
| | muon | $\Delta R_{\mu-jet} < 0.2$ if $N_{Trk}(jet) < 3$ OR $(p_T^{jet}/p_T^{\mu} < 2$ AND $p_T^{\mu}/\sum_{Trk} p_T > 0.7)$ |
| electron | jet | $0.2 < \Delta R_{e-jet} < 0.4$ AND PU jet check |
| | muon | ID track shared |
| muon | jet | $\Delta R_{\mu-jet} < 0.4$ AND PU jet check |

Table 4.2: Overlap removal criteria used for the physics objects of the off-shell $\ell\ell\nu\nu$ analysis. "PU jet check" stands for the selection: JVT > 0.59 for jet with $p_T$ < 60 GeV and $|\eta| < 2.4$ .

seeded by sporadic noise bursts in the hadronic end-cap calorimeters.

To further reduce the effect of pile-up jets a cut on the multivariate discriminant Jet Vertex Tagger (JVT) is applied to select jets from the hard-scatter vertex [176]. The recommended threshold of 0.59 on the JVT is used leading to an efficiency of 92% and to an observed fake rate of 2%. However, if a jet passes such a JVT selection, but fails to pass the other selection requirements, then it is rejected. A veto on b-tagged jets with $p_T > 20$ GeV and $|\eta| < 2.5$ is applied to reject contributions from $t\bar{t}$ events. Jets are $b$-tagged as likely to contain $b$-hadrons using the MV2c10 algorithm.

#### 4.5.2.4 Missing Transverse Momentum

Signal $E_T^{miss}$ is calculated from the lepton and jet objects, as explained in Eq. 3.12 and following recommendations of the Jet-$E_T^{miss}$ group [177]. Since $E_T^{miss}$ is computed as the negative of the global vector sum of these identified physics objects, the lepton identified objects are passed to the $E_T^{miss}$ algorithm right before the overlap removal step. Jets are instead calibrated using the EM+JES scheme before being passed to the $E_T^{miss}$ algorithm. This is needed since the algorithm performs specific overlap removal procedures, which use detailed information for each reconstructed object. Jets follow similar $p_T$, $|\eta|$ and JVT selections as specified in the jets section above.

### 4.5.3 Analysis Selection

Based on the selections mentioned above, the physics-objects selection in the $\ell\ell\nu\nu$ analysis, harmonized with the general prescriptions of the ATLAS Collaboration, can be summarized as follows:

**MUON Selection**

- All muons must have $p_T > 7$ GeV;
- All muons must be within $|\eta| < 2.5$;
- All muons must pass the 'Loose' isolation criteria;
- All muons must be reconstructed as Combined Muon types;
- All muons must have the following ID track requirements: $|d_0/\sigma_{d_0}| < 3$ and $|z_0 \cdot sin(\theta)| < 0.5$ mm;
- Overlap removal between muons and jets and between muons and electrons;
- Signal(Veto) muons must pass the 'Medium'('Loose') identification criteria.

**ELECTRON Selection**

- All electrons must have $E_T > 7$ GeV;
- All electrons must be within $|\eta| < 2.47$;
- All electrons must pass the 'Loose' isolation criteria;
- No electrons should be classified as 'bad', i.e. electrons from a bad calorimeter cluster;
- All electrons must have the following ID track requirements: $|d_0/\sigma_{d_0}| < 5$ and $|z_0 \cdot sin(\theta)| < 0.5$ mm;
- Overlap removal between electrons and muons and between electrons and jets;
- Signal(Veto) electrons must pass the 'Medium Likelihood'('Loose Likelihood') identification criteria.

**JET Selection**

- Jets use the anti-$k_T$ EMTopo reconstruction algorithm within $\Delta R = 0.4$;
- All jets must have $p_T > 20$ GeV and must be within $|\eta| < 4.5$;
- All jets must pass the 'LooseBad' quality cleaning criteria, with the event rejected if either of the two leading jets are flagged as bad by the standard loose jet cleaning cuts;
- Overlap removal between jets and muons and between jets and electrons;
- All jets must pass JVT > 0.59 and must have $p_T < 60$ GeV and be within $|\eta| < 2.4$ for residual pile-up suppression.

$E_T^{miss}$ **Selection**

- $E_T^{miss}$ makes use of all the electrons and muons above passing all the selection requirements, except the overlap removal;
- Jets are only calibrated and processed via the $E_T^{miss}$ algorithm;
- $E_T^{miss}$ uses the soft term built from ID tracks;
- $E_T^{miss}$ uses the default jet selection: JVT > 0.59 and must have 20 GeV $< p_T <$ 60 GeV and be within $|\eta| < 2.4$.

#### 4.5.3.1 Event Pre-Selection

Before the event passes through the analysis selection, a set of quality criteria on the reconstructed events are implemented. They mostly are cleaning requirements at detector level: LAr, SCT and Tile calorimeter quality requirements. Data events must be a part of the good runs list (GRL) of data taking periods, otherwise they are discarded. The GRL used in the $\ell\ell\nu\nu$ analysis makes use of all the detector components, corresponding to a total integrated luminosity for the 2015+2016 period of 36.1 fb$^{-1}$. The presence of a hard-scattering vertex with at least two associated tracks is required, where the hard-scatter vertex is defined as the one with the highest sum of track $p_T^2$. Some jets cleaning criteria are also applied to remove jets not originating from collision events, rather from hardware problems, cosmic-ray showers or beam related backgrounds. Events containing such 'bad' jets generate fake

missing transverse momentum that manifests in a poor description of the tail of the $E_T^{miss}$ distribution. Therefore, events containing 'bad' jets are discarded.

Based on the selections mentioned above, the Pre-Selection criteria for the events used in the $\ell\ell\nu\nu$ analysis can be summarized as follows:

**EVENT Pre-Selection**

- each event must be part of the GRL;
- each event must not be flagged as incomplete;
- each event must have at least one hard-scattering vertex with at least two associated tracks;
- each event must pass the 'Loose' quality cleaning criteria;
- each event must pass the SCT-error requirement, which ensures SCT hits are recorded, and the LAr- and Tile- error requirements which provide protection against noise bursts and data corruption in the ECAL and HCAL, respectively.

#### 4.5.3.2 Trigger Selection

The full trigger menus used in the $\ell\ell\nu\nu$ analysis for the 2015-2016 periods are provided in Table 4.3. The ATLAS trigger system was described in Sec. 2.3.4. Here the single lepton triggers used for the $\ell\ell\nu\nu$ analysis are briefly described.

The lowest un-prescaled electron trigger used in 2015 is $e24\_lhmedium\_L1EM18VH$. The labels in the name have a specific meaning:

- $e24$ means that the electron must have a transverse energy of $E_T^e > 24$ GeV;
- *lhmedium* means that the electron physics object must pass the 'Medium' identification WP criteria - described in Sec. 3.3.1;
- $L1EM18VH$ means that the electron must be a L1 electromagnetic object with $E_T > 18$ GeV, hadronic veto for an excess of energy in the hadronic calorimeter behind the electromagnetic cluster and $\eta$-dependent $E_T$ threshold requirement to compensate for regions of inactive detector material. L1 stands for Level 1, the hardware trigger of the ATLAS detector described in Sec. 2.3.4.

At high $E_T$, possible losses in trigger efficiency are partially recovered by an additional trigger with 'Loose' WP identification criteria and $E_T$ > 120 GeV, as evident by the name of the $e120\_lhloose\_L1EM18VH$ trigger, reported in Table 4.3.

Similar to electrons, the lowest un-prescaled muon trigger used during the 2015 data-taking operations is $mu20\_iloose\_L1MU15$ where the labels in the name have a specific meaning:

- $mu20$ means that the muon must have a transverse momentum of $p_T^\mu$ > 20 GeV;
- *iloose* means that the muon physics object must pass the 'Loose' isolation WP criteria: $\sum_{track} \frac{p_T|_{\Delta R=0.2}}{p_T} < 12\%$, i.e. the isolation requirement on the sum of all track $p_T$ within a cone of $\Delta R = 0.2$ around the muon candidate of transverse momentum $p_T$, as described in Sec. 3.3.2;
- $L1MU15$ means that the muon must be a L1 muon object with $p_T$ > 15 GeV, where L1 stands for Level 1 - the hardware trigger of the ATLAS detector described in Sec. 2.3.4.

At high $p_T$, possible losses in trigger efficiency are partially recovered by an additional HLT trigger with a $p_T$ threshold of 50 GeV, as evident by the name of the $HLT\_mu50$ trigger, reported in Table 4.3.

For both muons and electrons, the lowest un-prescaled trigger menus changed in 2016 compared to 2015. In addition, the muon trigger $p_T$ threshold was increased to 26 GeV when the instantaneous luminosity, $\mathcal{L}$, reached $10^{34}\text{cm}^{-2}\text{s}^{-1}$, its design value. The combination of single-lepton trigger menus was studied in depth in 2015 and 2016 data and found to always exceed 95%. However, because of the sharp turn-on curve of single lepton trigger efficiencies, a $p_T$ cut on the leading lepton, $p_T^{lead}$ > 30 GeV, is implemented. This was found to be necessary to maintain high signal efficiency in the 2015 and 2016 high-mass analysis [178].

#### 4.5.3.3 Event Selection

As explained in Sec. 4.2, the event selection is designed to minimise the dependence on the $p_T$ of the $ZZ$ system, and thus performed inclusive of the number of jets. This is done in order to be able to use the higher-order QCD corrections for the

| **Trigger menus used in the $2\ell 2\nu$ analysis** | |
|---|---|
| Trigger Type | Trigger Name |
| Single Muon | mu20_ iloose_L1MU15 (2015) OR<br>HLT_mu50 (2015)<br>mu24_ ivarmedium (2016) OR<br>HLT_mu50 (2016) OR<br>mu26_ ivarmedium (2016) OR<br>HLT_mu50 (2016, after $\mathcal{L} = 10^{34} cm^{-2} s^{-1}$) |
| Single Electron | e24_ lhmedium_ L1EM18VH (2015) OR<br>e60_ lhmedium_ L1EM18VH (2015) OR<br>e120_lhloose_L1EM18VH (2015)<br>e24_ lhtight_nod0_ivarloose (2016) OR<br>e60_ lhmedium_nod0_ivarloose (2016) OR<br>e140_ lhloose_ nod0 (2016) OR<br>e26_ lhtight_nod0_ivarloose (2016) OR<br>e60_ lhmedium_nod0_ivarloose (2016, after $\mathcal{L} = 10^{34} cm^{-2} s^{-1}$)<br>e140_ lhloose_nod0 (2016, after $\mathcal{L} = 10^{34} cm^{-2} s^{-1}$) |

Table 4.3: List of Trigger menus used in the $2\ell 2\nu$ analysis in the 2015 and in 2016 data taking. All the triggers reported in this table are un-prescaled and isolated for low-$p_T$ muons. Some differences between 2015 and 2016 are due to additional trigger menus being implemented in 2016.

gg-initiated processes, computed without any selection on the number of jets in the event. As a result an inclusive ggF+VBF production category is considered. After the selections described in the previous sections, a final analysis selection is applied. As in all the $\ell\ell + E_T^{miss}$ analyses, it consists of a set of specific kinematics selections on the reconstructed $Z$ boson and the $E_T^{miss}$.

The selection for the analysis on the search for heavy $ZZ$ resonances in the $l^+l^-\nu\bar{\nu}$ final states [30] is considered as the main reference for the analysis selection. It can be summarized as follows:

- After passing the muon/electron trigger selection described in Sec. 4.5.3.2, all events are required to have exactly two same flavour and opposite charged muons or electrons with the requirement $p_T > 30(20)$ GeV for the leading(sub-leading) muon and $E_T > 20(30)$ GeV for the leading(sub-leading) electron. If more than two leptons are found, with the third lepton having a $p_T$($E_T$ for electrons) greater than 7 GeV and passing the loose ID criteria, the event

is rejected to reduce the contamination from the $WZ \to \ell\nu\ell^+\ell^-$ background, although this process can still contribute if the third lepton falls outside the analysis acceptance.

- The dilepton invariant mass is required to satisfy 76 GeV $< m_{\ell\ell} <$ 106 GeV, in order to mainly suppress the contribution from non-$Z$ backgrounds such as $t\bar{t}$ and $WW$.

- The magnitude of the $E_T^{miss}$ vector is required to be greater than 120 GeV to reduce the contribution of the $Z + jets$ background. This allows to keep the region of interest, the tail of the $E_T^{miss}$ distribution, rich in events with genuine $E_T^{miss}$.

- Given the expected large boost of each $Z$ boson from the off-shell Higgs boson decay, additional requirements are made on the angular separation between the lepton pair, $\vec{p}_T^{\,Z} = \vec{p}_T^{\,\ell_1} + \vec{p}_T^{\,\ell_2}$. The two leptons are required to be close in the space, thus the angular distance $\Delta R = \sqrt{\Delta\phi^2 + \Delta\eta^2}$ between the two leptons is required to be smaller than 1.8. This cut helps to reduce the $WW$ and top-quark background contributions.

- In the absence of initial or final state radiation, the $Z$ boson coming from a signal event is expected to be back-to-back with $E_T^{miss}$. Therefore there is a requirement that the azimuthal angle between the lepton pair system and the $E_T^{miss}$, the variable $\Delta\phi(\vec{p}_T^{\,\ell\ell}, \vec{E}_T^{miss})$, is greater than 2.7. This is not in general the case for the $Z + jets$ or the $WW$ and top-quark background contributions, which are largely suppressed by this cut.

- As stated in the previous bullet, the expected signature of signal events is that of a $Z$ boson recoiling against $E_T^{miss}$. Assuming momentum conservation in the transverse plane, the $E_T^{miss}$ plus jets are expected to be balanced against the $p_T$ of the $Z$ boson. Any possible imbalance is accounted for in the fractional $p_T$ difference variable, defined as $|\vec{p}_{\mathrm{T}}^{\,\mathrm{miss,jet}} - \vec{p}_{\mathrm{T}}^{\,\ell\ell}|/|\vec{p}_{\mathrm{T}}^{\,\ell\ell}|$ which is required to be at most 20%, where $p_{\mathrm{T}}^{\mathrm{miss,jet}} = |\vec{E}_{\mathrm{T}}^{\mathrm{miss}} + \sum_{\mathrm{jet}} \vec{p}_{\mathrm{T}}^{\,\mathrm{jet}}|$. The fractional $p_T$ difference gives an indication of the presence of fake $E_T^{miss}$ in the event.

- In order to further suppress the Drell-Yan background contamination, additional cleaning criteria are implemented. A minimum $\Delta\phi(\vec{p}_T^{\,jet} >$ 100 GeV,

$\vec{E}_T^{miss}$) distance of 0.4 is required for a mis-measured jet to contribute to the $E_T^{miss}$. In fact, high-$m_T^{ZZ}$ Drell-Yan events that pass the the previous selections, usually have high-$p_T$ jets, boosted $Z$ bosons and large $E_T^{miss}$ correlated with mis-measurement of high-$p_T$ jets. Therefore, a minimum azimuthal angle separation turns out to be a helpful cut. In addition, the $E_T^{miss}$ is required to be a large fraction of $H_T$, defined as the scalar sum of the momenta of leptons and jets (with $p_T > 30$ GeV) in the event. In background events with fake $E_T^{miss}$, like $Z + jets$, events tend to have a large contribution to $H_T$ coming from jets rather from the $E_T^{miss}$. The minimum threshold value of 0.4 for $E_T^{miss}/H_T$ is found to be satisfactory.

- Lastly, to decrease the contamination from the $t\bar{t}$ background, a veto on any $b$-tagged jets is implemented. For the jets to be $b$-tagged, the multivariate MV2c10 [147] algorithm output, is required to be greater than 0.1785 fixing at 85% the tagging efficiency working point.

**Selection Optimization**

With respect to the selection described above which is used in [30], for the off-shell analysis some changes are needed. The main change with respect to the selection implemented in Run 1 for the corresponding analysis, is the introduction of the $E_T^{miss}/H_T$ cut. It was motivated by the increased pile-up activity observed during the Run 2 of the LHC. The $Z + jets$ can be a serious threat to the sensitivity of the $2\ell 2\nu$ analysis if not properly treated. The $E_T^{miss}$ cut, while greatly reducing the core of the $Z + jets$ background, can also significantly reduce the signal efficiency. The Run 1 cleaning cuts were found to be insufficient when looking at the $Z + jets$ contamination. Several variables used in other analyses were studied and the $E_T^{miss}/H_T$ variable was selected since is able to further reduce this background. Events with non-negligible $E_T^{miss}$ values caused by mis-reconstructed or mis-calibrated objects result in small values of $E_T^{miss}$ when compared to $H_T$ , while events with genuine missing transverse momentum tend to have large $E_T^{miss}$ values with respect to $H_T$.

To find the proper balance between these crucial cuts, $E_T^{miss}$ and $E_T^{miss}/H_T$, a new optimization for the off-shell Higgs production is performed. As a result the $E_T^{miss}$ and the $E_T^{miss}/H_T$ selections are moved to tighter cuts (175 GeV and 0.33, respectively). The optimal cut thresholds for the above selections are chosen in

order to maximise the signal significance:

$$Z_2 = \sqrt{2\left((S+B)\ln\left[1+\frac{S}{B}\right]-S\right)} \tag{4.12}$$

where $S$ is the signal yield and $B$ is the total background yield. For regions of high statistics and large background, $B >> S$, the figure of merit becomes the approximated version of the signal significance:

$$Z_1 = S/\sqrt{B} \tag{4.13}$$

Keeping all the selection cuts, but $E_T^{miss}$ and $E_T^{miss}/H_T$, at the optimised values, it is possible to scan simultaneously the optimal values for $E_T^{miss}$ and $E_T^{miss}/H_T$ in a two-dimensional approach. In particular, the variable $E_T^{miss}$ is scanned in the interval [50 GeV - 1 TeV] in steps of 10 GeV, while the variable $E_T^{miss}/H_T$ is scanned in the interval [0.2 - 1.2] in 50 steps. As an example of the optimisation, Figure 4.11 shows the scan of the signal significance curves for the sample with the SM couplings.

As an additional check, a third definition of the signal significance is also used which, unlike the $Z_1$ and $Z_2$ formulas, takes also into account the background statistical uncertainty. $Z_3$ is defined through the 'BinomialExpZ' function of the RooStats class, and corresponds to the output of a hypothesis test between background only and signal-plus-background. The optimal cut on the above selections is chosen by looking at the $Z_2$ figure of merit, but then compared with that obtained using $Z_1$ and $Z_3$ definitions for completeness, as shown in Table 4.4. Using different definitions of the significance leads to the same results.

| | Max Significance | $E_T^{miss}$ [GeV] | $E_T^{miss}/H_T$ |
|---|---|---|---|
| $Z_1$ | 0.984676 | 175 | 0.33 |
| $Z_2$ | 0.994535 | 175 | 0.33 |
| $Z_3$ | 0.930532 | 175 | 0.33 |

Table 4.4: Comparison between different definitions of signal significance used to select the optimal cut on the $E_T^{miss}$ and the $E_T^{miss}/H_T$ variables used in the $ZZ \to 2\ell 2\nu$ event selection. The significance is calculated for the $gg \to H^* \to ZZ \to 2\ell 2\nu$ signal sample with SM couplings. Comparable results are evident for the three definitions.

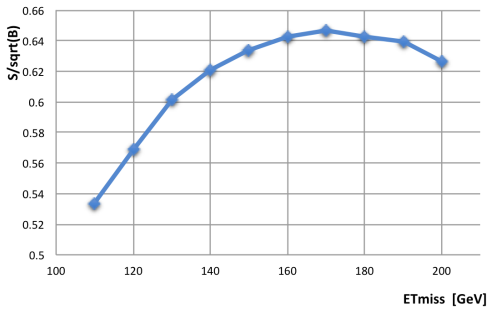


(a) 1D Significance scan for $E_T^{miss}$

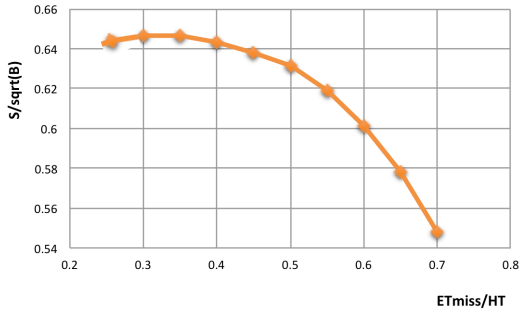


(b) 1D Significance scan for $E_T^{miss}/H_T$

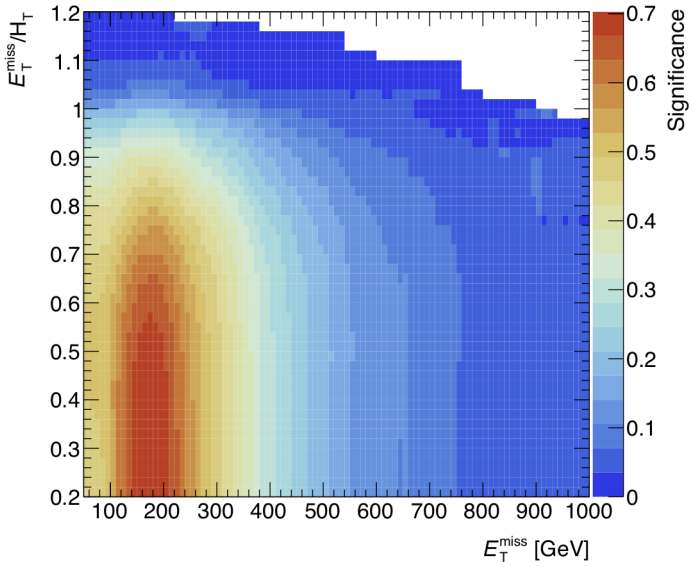


(c) 2D Significance scan for $Z_2$

Figure 4.11: 1D Significance scan for $E_T^{miss}$ (a), $E_T^{miss}/H_T$ (b) and the 2D Significance scan of the $Z_2$ Figure of Merit (c), based on the samples with SM couplings.

The final $\ell\ell\nu\nu$ off-shell Signal Region (SR) is defined in Table 4.5, where for each selection the corresponding optimal cut is given as well.

The $E_T^{miss}$ and $E_T^{miss}/H_T$ distributions after the event optimisation are shown in Figure 4.12.

The expected and observed signal yields for the $2\ell 2\nu$ off-shell SR are given in Table 5.1 along with the expected background contributions, while in Figure 5.2 the expected $ZZ$-transverse-mass distribution in the SR for both the channels, $ee\nu\nu$ and $\mu\mu\nu\nu$, is shown.

| **Event Pre-Selection and Trigger Selection** |
|---|
| All_Good GRL events |
| Vertex with $\geq 2$ tracks with $p_T > 1$ GeV |
| Single lepton trigger ($e$ or $\mu$) |
| **Event Selection** |
| Two same flavour opposite-sign leptons ($e^+e^-$ OR $\mu^+\mu^-$) |
| Veto of any additional lepton with Loose ID and $p_T > 7$ GeV |
| $76 < m_{\ell\ell} < 106$ GeV |
| $E_T^{miss} > 175$ GeV |
| $\Delta R_{\ell\ell} < 1.8$ |
| $\Delta\phi(\vec{p}_T^{\ell\ell}, \vec{E}_T^{miss}) > 2.7$ |
| Fractional $p_T$ difference $< 0.2$ |
| $\Delta\phi(\text{jet}(\vec{p}_T > 100GeV), \vec{E}_T^{miss}) > 0.4$ |
| $E_T^{miss}/H_T > 0.33$ |
| b-jet veto |

Table 4.5: List of selections applied at the event selection level for the off-shell $ZZ \to 2\ell\,2\nu$ analysis.

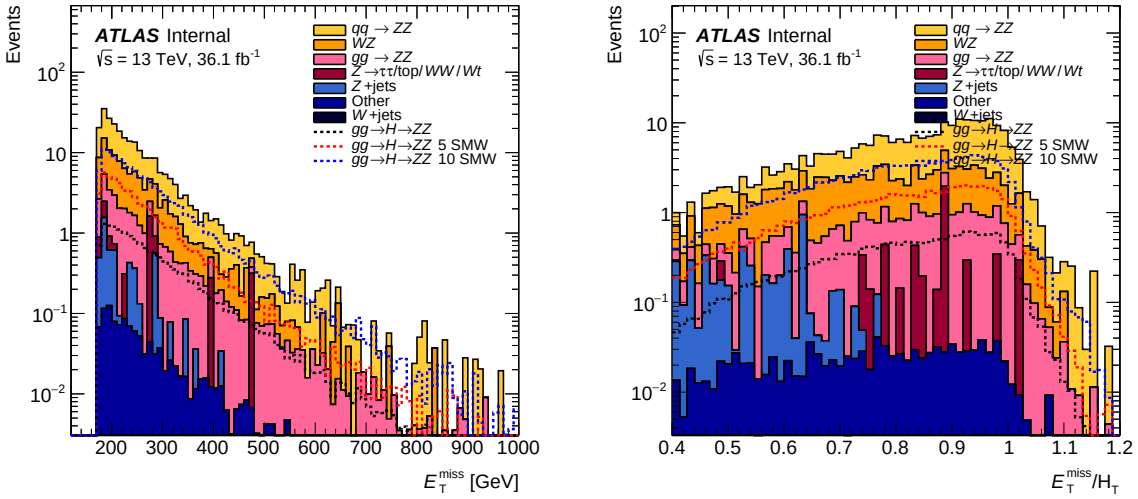


(a) $E_T^{miss}$ (b) $E_T^{miss}/H_T$

Figure 4.12: Expected $E_T^{miss}$ (a) and $E_T^{miss}/H_T$ (b) distributions in the off-shell $\ell\ell\nu\nu$ final state with 36.1 fb$^{-1}$ after the event optimization. Backgrounds are derived as described in Sec. 4.5.4.

A detailed breakdown of the background composition is given in the next section.

### 4.5.4 Backgrounds Estimation

This section describes the background estimation strategy adopted in the $ZZ \to 2\ell 2\nu$ final state. Strategies are very similar to the ones followed in the search of new $ZZ$ heavy resonances at 13 TeV [30].

The various background contributions and the techniques used to derive them are summarized below:

- The dominant background in the $H^* \to ZZ \to 2\ell 2\nu$ channel is composed of $ZZ \to 2\ell 2\nu$ events produced via both $q\bar{q}$ and $gg$ processes. This estimate is purely MC-based. Higher-order QCD and EW corrections are applied.

- The second leading background source is originating from $WZ$ events where the lepton from the $W$ boson is either not reconstructed or falls outside the fiducial volume. A data-driven $3\ell$ Control Region is defined with the application of a data/MC Scale Factor.

- The third background contribution to the off-shell $2\ell 2\nu$ signal region comes from $Z + jets$ with poorly reconstructed $E_T^{miss}$. A data-driven Control Region is defined to obtain the estimate.

- The fourth background contribution is from two genuine leptons not originating from a $Z$ decay, but from $WW$, $t\bar{t}$, $Wt$ production and leptonic $Z \to \tau\tau$ decays. The latter contribute only marginally due to the softer $p_T$ spectrum of the corresponding leptons. An enriched data-driven $e\mu$ Control Region is defined exploiting the flavour proportion $ee : \mu\mu : e\mu = 1 : 1 : 2$. Differences in the muon and electron reconstruction performance are taken into account.

- The least significant background contributions are from $W$+jets events with at least one misidentified electron or muon and from tri-boson processes, semileptonic top decays and multi-jet events. They are all estimated from simulation.

#### 4.5.4.1 $ZZ$ Background

The non-resonant continuum $ZZ$ background is produced via quark-quark and gluon-gluon initiated processes. It is irreducible since it is able to pass our signal selection containing the same final state particles ($ee\nu\nu$) and ($\mu\mu\nu\nu$). Data measurements of $ZZ$ background in ATLAS and CMS suffer from large experimental uncertainty. The $q\bar{q} \to ZZ$ background is modeled in the same manner as for the $ZZ \to 4l$ channel. It is the largest background contribution. Both the $q\bar{q} \to ZZ$ and the $gg \to ZZ$ processes are entirely estimated from MC. A better prediction is achieved by applying higher-order EW and QCD corrections to both correct the predicted normalization and to take into account any possible variation of the $m_T^{ZZ}$ shape. As explained in Section 4.3.1 and Section 4.3.4, the SHERPA generator is used to model both processes, the only difference being the application of higher-order theoretical corrections. Following this procedure, the $ZZ$ background represents 68% of the total background in the signal region for the $\ell\ell\nu\nu$ analysis with $q\bar{q} \to ZZ$ being 54% and $gg + VBF \to ZZ$ 14%, respectively.

#### 4.5.4.2 $WZ$ Background

The second largest contribution to the total background is the $WZ$, $W \to \ell\nu$, $Z \to \ell\ell$ process. The third lepton veto requirement reduces the $WZ$ background, but $WZ$

events can still enter the off-shell signal region either if one lepton is not reconstructed, almost exclusively the lepton from the $W$ boson decay, or if it falls outside the acceptance. A dedicated Control Region (CR) is used in order to estimate the normalisation of the $WZ$ background from data. This Control Region is referred to as $3\ell$ CR.

The $3\ell$ CR is defined by relaxing the third lepton veto requirement, in order to populate the region with $WZ$ events. However, this is not the sole requirement. To better isolate the $WZ$ topology from other backgrounds, further selections are implemented. The third lepton is required to pass the same set of selections as the two leptons, including a $p_T$ cut of 20 GeV. Additionally, a constraint on the $Z$-mass selects events containing a $Z$ boson. A transverse mass variable, $m_T^W$, is defined from the $E_T^{miss}$ and the $p_T$ of the third lepton and a cut of $m_T^W > 60$ GeV is made to reduce the $Z + jets$ background. To reduce the $t\bar{t}$ contamination, a veto on $b$-jets is also implemented. Applying this selection, the $WZ$ purity[5] in the control region is ~ 90%. The $3\ell$ CR definition is summarized in Table 4.6.

| **Three-Lepton CR definition** |
|---|
| Two same flavour opposite-sign leptons ($e^+e^-$ OR $\mu^+\mu^-$) |
| Require one additional lepton with $p_T^{3\ell} > 20$ GeV |
| $76 < m_{\ell\ell} < 106$ GeV |
| $m_T^W > 60$ GeV |
| $b$-jet Veto |

Table 4.6: Definition of the $3\ell$ CR.

The $WZ$ background in the SR is then normalized to data through a Scale Factor (SF) correction. From the $3\ell$ CR, the $WZ$ yield in the SR is:

[5]The selection purity for a background contribution in a CR is defined as the ratio of the expected background for the specific process under investigation to the total expected background in the same region.

$$\mathrm{N}_{2\ell SR}^{Data} = \mathrm{N}_{2\ell SR}^{MC} \times \frac{\mathrm{N}_{3\ell CR}^{Data}}{\mathrm{N}_{3\ell CR}^{MC}} = \mathrm{N}_{3\ell CR}^{Data} \times \frac{\mathrm{N}_{2\ell SR}^{MC}}{\mathrm{N}_{3\ell CR}^{MC}} \tag{4.14}$$

where $\mathrm{N}_{2\ell SR}^{Data}$ is the number of events in data in the $\ell\ell\nu\nu$ SR with the SF defined as $\mathrm{SF} = \frac{\mathrm{N}_{3\ell CR}^{Data}}{\mathrm{N}_{3\ell CR}^{MC}}$. A simulation-based Transfer Factor (TF) is defined between the $2\ell$ SR and the $3\ell$ CR as $N_{2\ell,SR}^{MC}/N_{3\ell,CR}^{MC}$. The $3\ell$ CR is split into 4 categories based on the lepton flavour: $ee$+$e$, $ee$+$\mu$, $\mu\mu$+$e$, $\mu\mu$+$\mu$. The SFs are estimated in each category by subtracting the non-$WZ$ backgrounds (estimated in MC) from the observed yields in data and taking the ratio between this and the expected number of events from the $WZ$ MC. An inclusive SF is finally derived as the average of the SFs from all four categories. The combined SF, which is used to normalize the $WZ$ events, is found to be 1.29 ± 0.03(stat.) ± 0.07(sys.). The data/MC modeling of the $E_T^{miss}$ distribution in the $3\ell$ CR is shown in Figure 4.13 for the inclusive category.

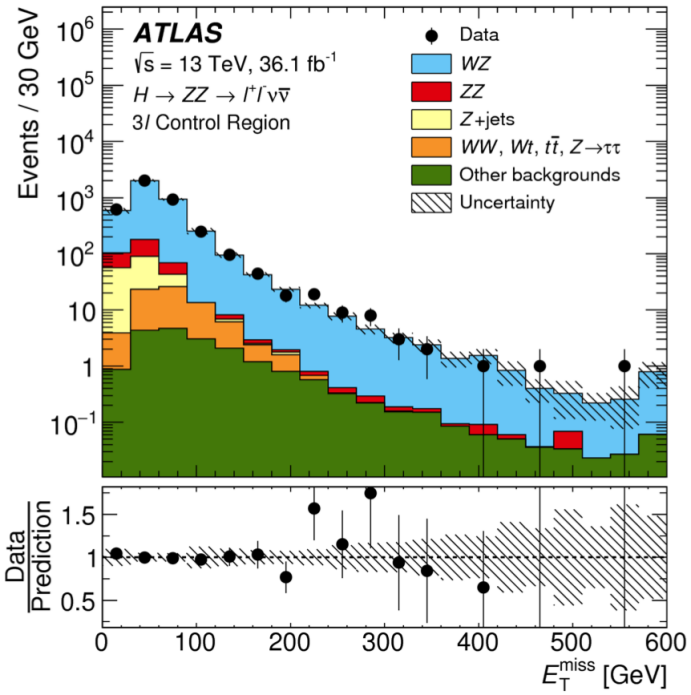


Figure 4.13: Data/MC modeling of the $E_T^{miss}$ in the $3\ell$ Control Region. Figure produced by an ATLAS collaborator.

### Systematic Uncertainties

The main sources of systematic uncertainties are listed below.

**Theoretical uncertainties.** The uncertainty on the $WZ$ contribution is assessed by considering theoretical and experimental systematic uncertainties on the TF. Theoretical systematic uncertainties are evaluated using the MC-driven TF. The $m_T^{ZZ}$ distribution is taken from simulation as predicted by the POWHEG generator, with variations due to uncertainty in QCD factorization and the renormalization scales and PDFs which combined amount to less than ~ 2.5% as shown in Fig. 4.14.

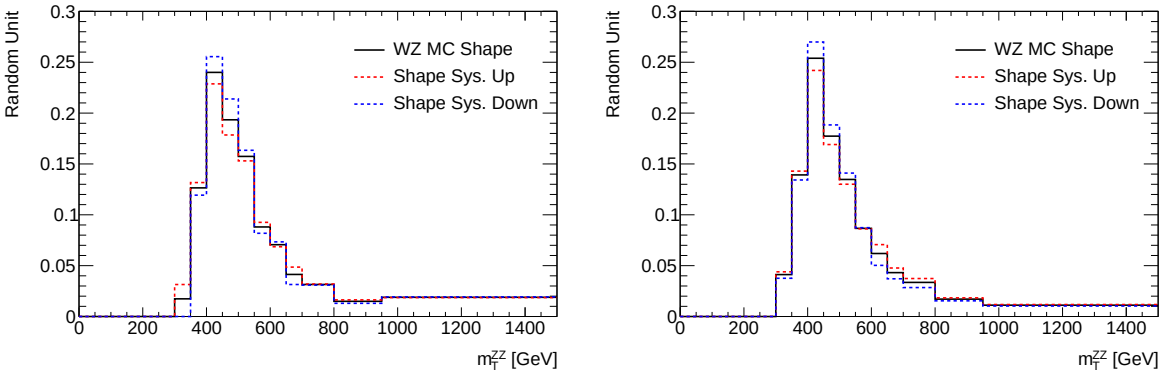


(a) $ee + \ell$ channel (b) $\mu\mu + \ell$ channel

Figure 4.14: Impact of the total theoretical systematic uncertainties (QCD factorization and renormalization scales and PDFs) on the $m_T^{ZZ}$ distribution in the $ee + \ell$ channel (a) and in the $\mu\mu + \ell$ channel (b). In both figures the nominal WZ MC shape (black), the up systematic uncertainty (dashed red) and the down systematic uncertainty (dashed blue) on the shape are shown.

**Experimental Uncertainties.** Experimentally, the detector uncertainties were evaluated and found to be ~ 4.2%. This estimate also includes the contribution to the experimental uncertainty on the TFs. An additional SF is applied to the $WZ$ background. This is needed to take into account the inefficiency of the third lepton in the $WZ$ background because only two leptons are kept in the SR. To get the inefficiency of the third lepton two main conditions are imposed on the third lepton: 1) it should be a genuine mis-identified or not reconstructed electron or muon; 2) it is within the boundary of the ATLAS Inner Detector as dictated by our object

selection criteria. The inefficiency SF is calculated by using the efficiencies in data and simulation of the third lepton for each of the four possible leptonic combinations, following the formula:

$$SF^{inefficiency} = \frac{1 - \epsilon^{Data}}{1 - \epsilon^{MC}} \tag{4.15}$$

where $\epsilon^{Data}$ and $\epsilon^{MC}$ refers to the efficiency in Data and MC, respectively. The impact of such a SF on the number of $WZ$ events is estimated to be ~ 4% (~ 1%) for the third lepton being a muon (electron). This is found by multiplying the largest inefficiency SF by the percent yield from the channel $W \to \mu\nu$ (20%) and $W \to e\nu$ (15%). The larger impact observed for a muon third lepton is due to the slightly higher efficiencies which makes the data/MC discrepancy more evident. To be conservative the larger 4% is added as an experimental systematic uncertainty in the $WZ$ background estimation to take into account the inefficiency SF for both muons and electrons.

In Table 4.7 a summary of the different systematic uncertainties considered in both the $ee$ and $\mu\mu$ channels is reported. The total systematic uncertainty on the estimate is found by summing in quadrature all the various contributions.

| Channel | Theoretical unc. | Experimental unc. | Total |
|---|---|---|---|
| $ee$ or $\mu\mu$ | 2.5% | 5.8% | 6.3% |

Table 4.7: Contributions to the systematic uncertainties for the $WZ$ background in both the $ee\nu\nu$ and the $\mu\mu\nu\nu$ channels.

The $WZ$ background contribution in the $ee$ and $\mu\mu$ final state is reported in Table 4.8.

#### 4.5.4.3 $Z + jets$ Background

The third largest background contribution is given by the $Z + jets$ process. The $Z + jets$ background appears in the $\ell\ell\nu\nu$ final state due to mis-reconstructed jets. Before any analysis selections are applied, it represents the largest contribution because of the large production cross section of the $Z \to \ell\ell$ process. However, the $Z + jets$ background is well-known to contribute the most at low $E_T^{miss}$, as low energy jets are easier to miss than highly energetic ones which would correspond to

| Channel | $WZ$ estimate |
|---|---|
| $ee$ | 32.8±1.3±2.1 |
| $\mu\mu$ | 34.9±1.4±2.2 |

Table 4.8: Number of $WZ$ events estimated in the $ZZ \to 2\ell\,2\nu$ off-shell signal region per flavour channel.

the $E_T^{miss}$ tail. This means that a first effective reduction is achieved by imposing a sufficiently hard $E_T^{miss}$ cut. Additional selections are applied to further reduce the $Z + jets$ contribution, such as fractional $p_T$ difference, $\Delta\phi(\text{jet}(\vec{p}_T), \vec{E}_T^{miss})$ $E_T^{miss}/H_T$ and the other cuts defining the SR. However, given that this background is able to enter the SR due to the presence of fake $E_T^{miss}$ in the event, which is known to not be well modeled in the simulation, a data-driven technique is used for its estimation. The chosen strategy consists of a CR definition, built in a similar way as the SR, shown in Table 4.5, but reversing the $E_T^{miss}/H_T$ cut in order to populate this newly defined CR with $Z + jets$ events, as shown in Fig. 4.15. In Fig. 4.16 the $m_T^{ZZ}$ modeling in the SR and in the CR is shown, after reverting the $E_T^{miss}/H_T$ cut and applying solely the $Z$ mass requirement. This demonstrates that the definition of the CR is sufficient to populate the $Z + jets$ background in both the electron and muon channels.

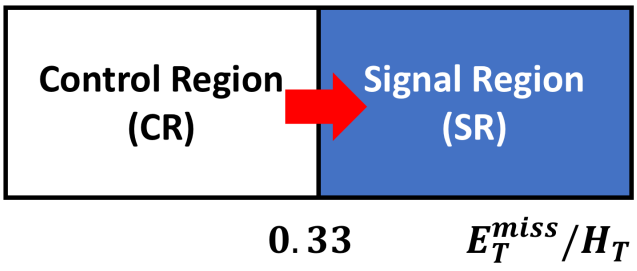


Figure 4.15: Pictorial representation of the $Z + jets$ Control Region. The $E_T^{miss}/H_T$ cut is reversed to construct the Control Region.

.

Unfortunately, the first attempt to estimate the $Z + jets$ background from this

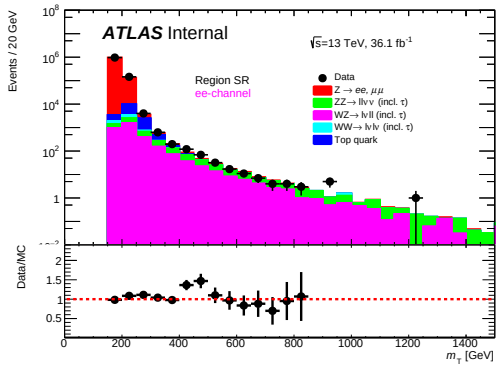


(a) SR in the $ee$ channel

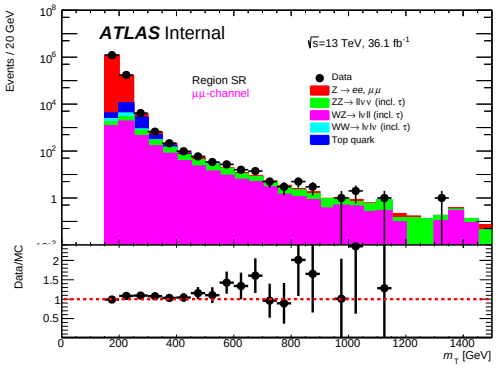


(b) SR in the $\mu\mu$ channel

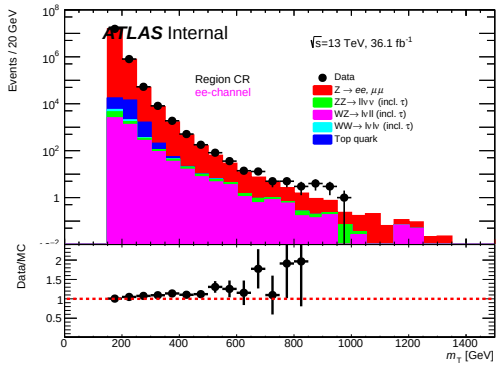


(c) CR in the $ee$ channel

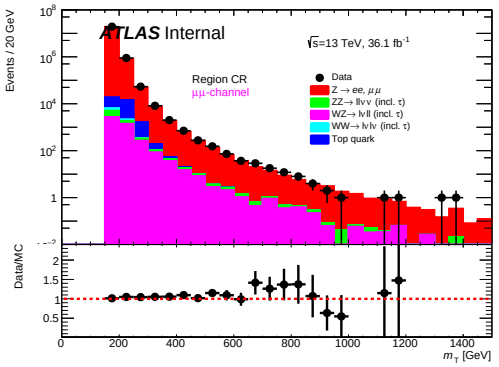


(d) CR in the $\mu\mu$ channel

Figure 4.16: $m_T^{ZZ}$ data/MC comparison in the Signal Region (SR) for the $ee$ channel (a) and the $\mu\mu$ channel (b), and in the Control Region (CR) obtained by reversing the $E_T^{miss}/H_T > 0.33$ cut for the $ee$ channel (c) and the $\mu\mu$ channel (d) after the $Z$ mass requirement has been applied. All the backgrounds shown here are normalised to their expectations from simulation. The plots demonstrate that the CR definition is suitable to enhance the $Z+jets$ background. In all figures data (black) and different background contaminations - $Z \to ee, \mu\mu$ (red), $ZZ \to \ell\ell\nu\nu$ including $\tau$-leptons (green), $WZ \to \ell\nu\ell\ell$ including $\tau$-leptons (purple), $WW \to \ell\nu\ell\nu$ including $\tau$-leptons (light blue) and top quark contribution (blue) - are shown. Figures produced by an ATLAS collaborator.

CR showed that the region suffered from being poorly populated. To overcome such an issue, a looser event selection is applied defining the CR with $\Delta\phi(\text{jet}(\vec{p}_T), \vec{E}_T^{miss})$ and the $b$-jet veto cuts removed. This makes the CR less pure in $Z+jets$ events allowing for possible $t\bar{t}$ contaminations, but provides enough statistics to estimate

the $Z + jets$ number of events in the SR. To demonstrate the effectiveness of the selection change, in Table 4.9 the yields in the CR as a function of the different cuts applied is shown. If only the $Z$ mass cut is applied, abundant statistics are available, but the selection doesn't favor purity for the $Z + jets$ process. If all the cuts in Table 4.5 up to the Fractional-$p_T$-difference cut are applied, enough statistics is still available. The implementation of the $\Delta\phi(\text{jet}(\vec{p}_T), \vec{E}_T^{miss})$ and the $b$-jets veto cut can dramatically reduce the number of events.

| $ee$-channel | $N_{CR}^{data}$ |
|---|---|
| $Z$ mass | $(1.6411 \pm 0.0004) \times 10^7$ |
| $E_T^{miss}$, $\Delta R_{\ell\ell}$, $\Delta\phi(\vec{p}_T^{\ell\ell}, \vec{E}_T^{miss})$, Fract. $p_T$ diff. | $34 \pm 6$ |
| $\Delta\phi(\text{jet}(\vec{p}_T), \vec{E}_T^{miss})$ | $1.5 \pm 1.8$ |
| $b$-jets veto | $1.1 \pm 1.4$ |
| $\mu\mu$-channel | $N_{CR}^{data}$ |
| $Z$ mass | $(2.0189 \pm 0.0004) \times 10^7$ |
| $E_T^{miss}$, $\Delta R_{\ell\ell}$, $\Delta\phi(\vec{p}_T^{\ell\ell}, \vec{E}_T^{miss})$, Fract. $p_T$ diff. | $41 \pm 7$ |
| $\Delta\phi((\vec{p}_T^{\ell\ell}), \vec{E}_T^{miss})$ | $0.6 \pm 1.4$ |
| $b$-jets veto | $-0.2 \pm 1.0$ |

Table 4.9: Yields in the $Z + jets$ data CR with the application of solely the $Z$ mass cut, the selection in Table 4.5 but the $\Delta\phi(\text{jet}(\vec{p}_T), \vec{E}_T^{miss})$ and the $b$-jets veto cut or with the inclusion of these further cuts. Uncertainties are statistical only.

By removing the last two cuts discussed above, sufficient statistics are still available in the CR. However, the $m_T^{ZZ}$ shape needs to be checked. Distortions are possible because of the cuts removed. This check is shown in Fig. 4.17. No biases are evident.

The extrapolation of the data-driven estimate from the $Z + jets$ CR to the off-

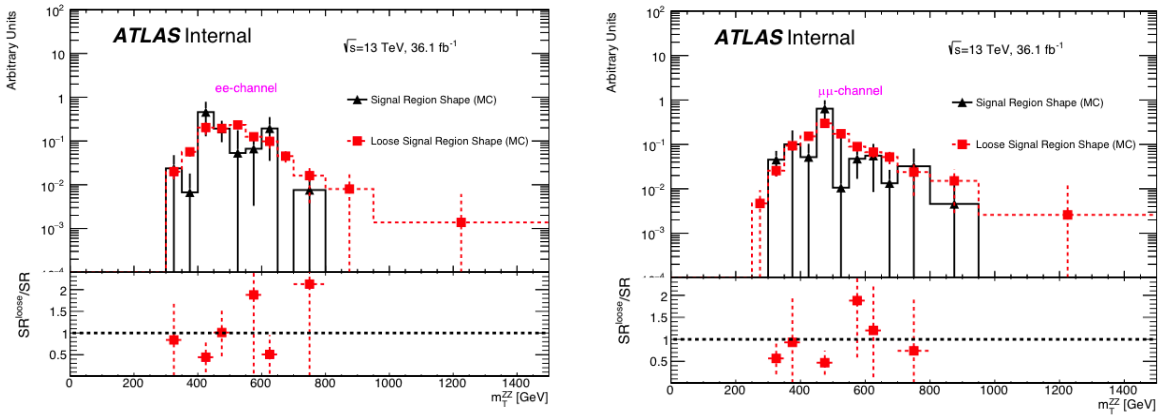


(a) $ee$ channel (b) $\mu\mu$ channel

Figure 4.17: Comparison of the $m_T^{ZZ}$ shape for the $Z + jets$ background in the $ee$ channel (a) and in the $\mu\mu$ channel (b), as expected in the off-shell Signal Region (black) and in a looser Signal Region (red), obtained by removing the cut on the $\Delta\phi(\text{jet}(\vec{p}_T), \vec{E}_T^{miss})$ and the $b$-jet veto variable. Figures produced by an ATLAS collaborator.

shell SR happens through the Transfer Factor:

$$N^{Data}_{Z+jets,SR} = N^{Data,sub}_{Z+jets,CR} \times \frac{N^{MC}_{SR}}{N^{MC}_{Z+jets,CR}} \tag{4.16}$$

where $N^{Data,sub}_{CR}$ is the number of data events in the CR from which non-$Z$+$jets$ background is subtracted based on its expectation. The method is based on simulation of the CR → SR Transfer Factor, defined as $\frac{N^{MC}_{SR}}{N^{MC}_{Z+jets,CR}}$.

### Systematic Uncertainties

The main sources of systematic uncertainties come from:

**Transfer Factor.** The systematic uncertainty associated with the MC-based Transfer Factor $\frac{N^{MC}_{SR}}{N^{MC}_{Z+jets,CR}}$ amounts to ~ 35% and ~ 65% for the $ee$ and $\mu\mu$ channels, respectively. Experimentally, a small contribution is due to the the Jet Energy Scale and the Jet response, but it is less relevant than the TF systematic uncertainty.

**Non-$Z$ background.** The systematic uncertainty associated with the non-$Z$ background, which is subtracted in the CR to get $N^{Data,sub}_{Z+jets,CR}$, amounts to ~ 2% for both channels. It is a small contribution since the selection applied to define the CR ensures excellent $Z + jets$ purity.

**Shape.** The $m_T^{ZZ}$ shape. As for the normalization, if all the SR cuts are applied insufficient events remain. As explained, to derive the shape systematic the CR is defined removing the $\Delta\phi(\text{jet}(\vec{p}_T), \vec{E}_T^{miss})$ and the $b$-jet-veto cuts. The shape comparison between the loose SR and the proper SR in MC is shown in Fig. 4.17. Since the shapes are quite consistent within the statistical uncertainty, loosening the selection to extract the shape of $m_T^{ZZ}$ seems justifiable. In addition to this shape comparison, the expected $m_T^{ZZ}$ shape is compared between the SR and data-CR (after non-$Z$+$jets$ background are subtracted) or the MC-based CR with results shown in Fig. 4.18. A significant shape difference is observed by comparing the SR and the CR. This has been taken into account by deriving a MC-based re-weighting function when comparing the $m_T^{ZZ}$ shape in the MC CR and the MC SR. A MC-based re-weighting function is applied to the data $m_T^{ZZ}$ shape in the CR. The MC-based re-weighting function is shown in Fig. 4.19 for both the $ee$ and $\mu\mu$ channels. Additionally, experimental systematics such as the jet energy scale etc. are also considered by looking at the change in the re-weighting function due to $\pm 1\sigma$ variation of each of them. This contribution has been taken into account when providing the estimate due to the MC-based Transfer Factor described before. The final $m_T^{ZZ}$ shape in the SR is taken from the MC, but a systematic uncertainty associated with the shape variation is taken from the difference with respect to the data-driven shape described above.

In Table 4.10 a summary of the different systematic uncertainties considered in both the $ee$ and $\mu\mu$ channels is reported. The total systematic uncertainty on the estimate is found by summing in quadrature all the various contributions.

The estimate of the $Z + jets$ background in the $ee$ and $\mu\mu$ channel can be found in Table 4.11. Uncertainties on the yield include both statistical and systematic sources. In the $ee$ channel a larger observed/expected discrepancy is observed, but the estimate is compatible with the MC expectation within the large uncertainties.

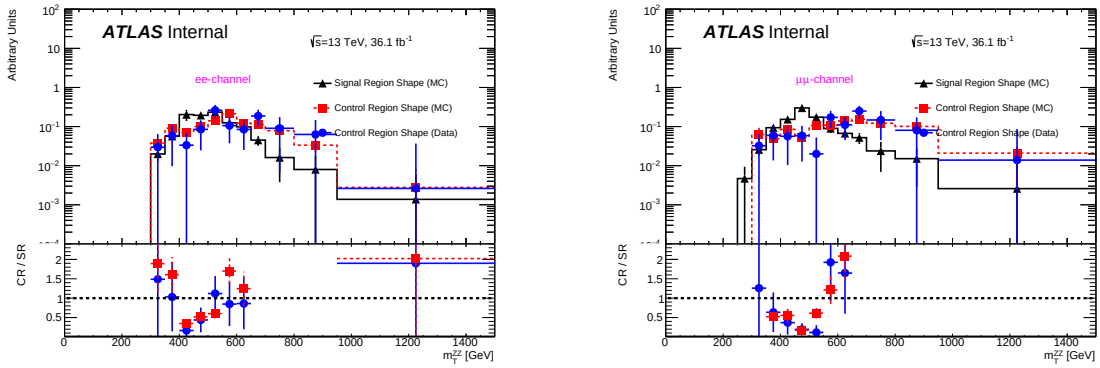


(a) $ee$ channel (b) $\mu\mu$ channel

Figure 4.18: Comparison of the $m_T^{ZZ}$ shape for the $Z + jets$ background in the $ee$ channel (a) and in the $\mu\mu$ channel (b), as expected in the off-shell Signal Region (black) and in the MC-based CR (red) and in the data-based CR (blue). Figures produced by an ATLAS collaborator.

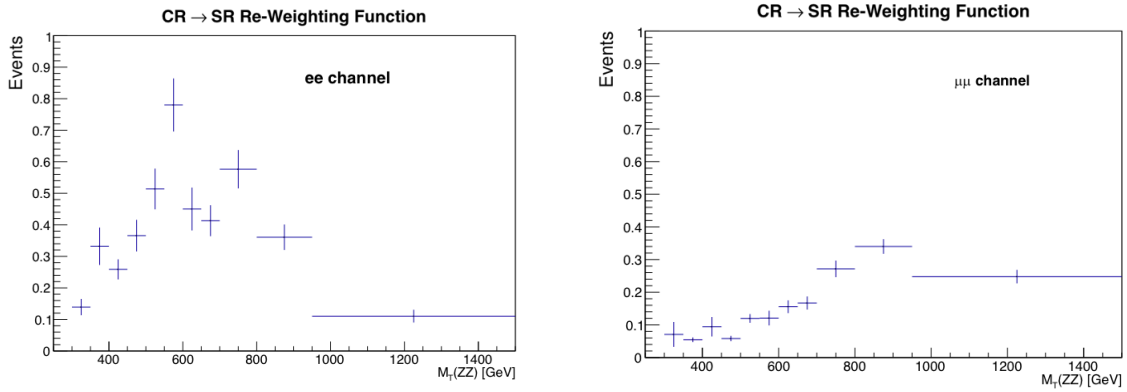


(a) $ee$ channel (b) $\mu\mu$ channel

Figure 4.19: Re-weighting function derived from the bin-by-bin $m_T^{ZZ}$ shape comparison between the MC-based SR and MC-based CR for the $Z + jets$ background in the $ee$ channel (a) and in the $\mu\mu$ channel (b). This function is applied to the CR data-driven shape to extrapolate the shape systematic uncertainty in the off-shell SR.

| Channel | Transfer Factor/Shape | non-$Z$ background | Total |
|---|---|---|---|
| $ee$ | 35% | 2% | 35% |
| $\mu\mu$ | 65% | 2% | 65% |

Table 4.10: Contributions to the systematic uncertainties for the $Z$+$jets$ background in both the $ee\nu\nu$ and the $\mu\mu\nu\nu$ channels.

| Channel | $Z + jets$ estimate | MC expectation |
|---|---|---|
| $ee$ | 4.3 ± 1.9(stat.) ± 1.5(sys.) | 3.0 ± 1.2(stat.) ± 0.9(sys.) |
| $\mu\mu$ | 1.7 ± 0.8(stat.) ± 1.1(sys.) | 1.8 ± 0.7(stat.) ± 0.9(sys.) |

Table 4.11: $Z + jets$ estimate in the off-shell Signal Region, as extracted from the Control Region. A comparison with the expectation from MC is also reported. Uncertainties on the estimate include both the statistical and the systematic components.

#### 4.5.4.4 $WW$, $t\bar{t}$, $Wt$, $Z \to \tau\tau$ Background

The fourth largest contribution, ~ 1% of the total background, comes from a collection of different sources:

- the $WW$ process. This is largely removed by the $Z$-mass window requirement and the large $E_T^{miss}$ cut;
- the $t\bar{t}$ production faking the $\ell\ell\nu\nu$ final state and largely removed by the $b$-jet veto;
- the $Wt$ production which has a small production cross section and doesn't have a large impact;
- the $Z \to \tau\tau$ decay, easily reduced by the $Z$-mass cut and other cuts in the SR definition.

All these non-resonant processes are in the same category since they can be estimated in data by exploiting the lepton flavour symmetry defining a dedicated $e\mu$ CR. In

fact, a useful feature of all four backgrounds in the lepton decay modes is that they all decay in a 1 : 1 : 2 proportion in the $ee$ : $\mu\mu$ : $e\mu$ channels. This motivates the use of an $e\mu$ CR to estimate the number of events in the corresponding $\ell\ell + E_T^{miss}$ final state. This dedicated CR contains opposite-sign and opposite-flavour leptons which are enriched in backgrounds of interest since processes with $Z$ bosons are suppressed. Additional leptons with loose identification and $p_T > 7$ GeV, able to enter the $e\mu$ CR, are removed to suppress the $WZ$ production. Because of the CR definition these background sources are referred to as $e\mu$ background in the following description.

A first attempt to define the $e\mu$ CR is made by applying all the cuts in the SR except for the requirement of two opposite-flavour leptons. However, with this selection the $e\mu$ CR defined is lacking of sufficient events. For this reason, the variation of the number of data and MC events is studied as a function of the cuts on $E_T^{miss}$, $E_T^{miss}/H_T$ and the fractional $p_T$ difference, as these cuts have the largest impact on the number of events in data and MC. Keeping all the other selection cuts at their optimized values, the $E_T^{miss}$ variable is scanned in the range [70-190] GeV with steps of 30 GeV, the $E_T^{miss}/H_T$ variable is scanned in the range [0.2, 1.0] with steps of 0.2 and the fractional $p_T$ difference in the range [0.1, 0.9] with steps of 0.2. Lower $E_T^{miss}$ cuts are preferable to increase statistics. Thus the $E_T^{miss}$ cut is moved to 120 GeV in the $e\mu$ CR with respect to the nominal 175 GeV adopted in the off-shell SR. In the following description this relaxed CR is called "Loose CR", and the analogous relaxed SR is called "Loose SR". The exact CR definition is detailed in Table 4.12.

Using the $e\mu$ number of events estimated in the CR, the number of $ee$ and $\mu\mu$ events in the SR, $N_{SRee}^{e\mu}$ and $N_{SR\mu\mu}^{e\mu}$, can be derived as:

$$N_{SRee}^{e\mu} = \frac{1}{2} \times \epsilon \times N_{e\mu}^{Data,sub}, \quad N_{SR\mu\mu}^{e\mu} = \frac{1}{2} \times \frac{1}{\epsilon} \times N_{e\mu}^{Data,sub} \tag{4.17}$$

where $N_{e\mu}^{Data,sub} = N_{e\mu}^{Data} - N_{Other}$ is the number of data events in the $e\mu$ CR after subtracting the non-$e\mu$ background ($N_{Other} = \sum_i^{non-e\mu} N_i$). Since electrons and muons are different objects with different reconstruction efficiencies, an additional factor, $\epsilon$, needs to be included in the estimation to reflect the different reconstruction efficiencies. This is defined as:

$$\epsilon^2 = \frac{N_{ee}}{N_{\mu\mu}} \tag{4.18}$$

| **e$\mu$ CR definition** |
|---|
| Vertex with $\geq 2$ tracks with $p_T > 1$ GeV |
| Single lepton trigger ($e$ or $\mu$) |
| Two opposite-flavour opposite-sign leptons ($e^{\pm}\mu^{\mp}$) |
| Veto of any additional lepton with Loose ID and $p_T > 7$ GeV |
| $76 < m_{e\mu} < 106$ GeV |
| $E_T^{miss}$ >120 GeV |
| $\Delta R_{e\mu} < 1.8$ |
| $\Delta\phi(Z, E_T^{miss}) > 2.7$ |
| Fractional $p_T$ difference < 0.2 |
| $\Delta\phi(\text{jet}(p_T > 100\text{GeV}), E_T^{miss}) > 0.4$ |
| $E_T^{miss}/H_T > 0.33$ |
| b-jet veto |

Table 4.12: Event selection applied to define the $e\mu$ "Loose" Control Region. The Control Region definition is the same as the SR definition but for the requirement of two opposite-flavour leptons and a lower $E_T^{miss}$ cut at 120 GeV.

where $N_{ee}$ and $N_{\mu\mu}$ is the number of events in the $ee$ and $\mu\mu$ channels after the $Z$ mass window cut. For a first rough estimate the $\epsilon$ factor is integrated in $\eta$ and $p_T$. However, muon and electron reconstruction performances generally depend on the region of the detectors and on the momentum of the lepton. Thus, a 'binned' efficiency factor is introduced for a more accurate background estimate. The 'binned' efficiency factor is defined as:

$$\epsilon^2 = \frac{N_{e^1_{(p_T,\eta)}e^2_{(p_T,\eta)}}}{N_{\mu^1_{(p_T,\eta)}\mu^2_{(p_T,\eta)}}} \tag{4.19}$$

The number of events is taken from a 2D-binned-($p_T$, $\eta$) distribution which consists of 24 bins, with:

- six $p_T$ bins:

  [30 GeV < $p_T^{lead}$ < 44 GeV & 20 GeV < $p_T^{sublead}$ < 44 GeV],

  [44 GeV < $p_T^{lead}$ < 52 GeV & 20 GeV < $p_T^{sublead}$ < 44 GeV],

  [44 GeV < $p_T^{lead}$ < 52 GeV & 44 GeV < $p_T^{sublead}$ < 52 GeV],

  [52 GeV < $p_T^{lead}$ < 2 TeV & 20 GeV < $p_T^{sublead}$ < 44 GeV],

  [52 GeV < $p_T^{lead}$ < 2 TeV & 44 GeV < $p_T^{sublead}$ < 52 GeV] and

  [52 GeV < $p_T^{lead}$ < 2 TeV & 52 GeV < $p_T^{sublead}$ < 2 TeV]

  where *lead* and *sublead* stands for $p_T$-leading and $p_T$-sub-leading lepton, respectively.

- four $\eta$ regions: $BB$, $BE$, $EB$ and $EE$ where $E$ and and $B$ stands for end-cap and barrel, respectively. The ordering of the regions is also used for the $p_T$ ordering of the leptons, for instance $BE$ means that the leading lepton is in the barrel and the sub-leading lepton is in the end-cap.

The binning choice was optimized in order to ensure sufficient statistics in each $(p_T, \eta)$-bin.

**Transfer Function**

In order to obtain the background estimate in the SR it is necessary to extrapolate the $m_T^{ZZ}$ shape derived in the "Loose CR" by using a MC-based Transfer Factor, TF, defined as:

$$TF = \frac{N^{SR}_{ee(\mu\mu)}}{N^{LooseSR}_{ee(\mu\mu)}} \tag{4.20}$$

where $N^{SR}_{ee(\mu\mu)}$ is the number of $ee(\mu\mu)$-MC events in the nominal off-shell SR and $N^{LooseSR}_{ee(\mu\mu)}$ is the number of $ee(\mu\mu)$-MC events in the "Loose SR", where a looser $E_T^{miss}$ cut at 120 GeV is applied.

Since the TF depends only on the definition of the "Loose" and final SR, there is no need to derive it separately for electron and muons. As a first attempt, it is derived inclusively, by comparing the total number of events in the nominal SR with

those in the "Loose SR". However, this TF shows strong dependence on $m_T^{ZZ}$. Due to this, a Transfer Function is preferable. It is defined as:

$$\begin{aligned} TFunction &= C - a \cdot m_T^{ZZ} \quad for \quad m_T^{ZZ} \leq 520 \\ &= 1 \qquad\qquad\quad for \quad m_T^{ZZ} > 520 \end{aligned} \tag{4.21}$$

where $C$ and $a$ are the free parameters. In Figure 4.20 the TFactors as a function of the $m_T^{ZZ}$ with the fitted Transfer Function overlaid are shown. The goodness of fit is $\chi^2/NDF$ = 1.7/2. Each charged lepton pair in the "Loose CR" is moved to the "Loose SR" via Eq. 4.17 and then weighted by the Transfer Function for the extrapolation to the proper off-shell SR.

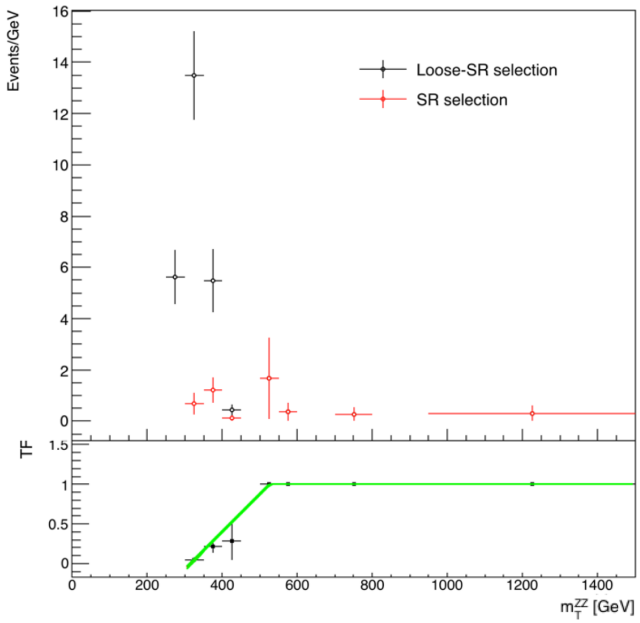


Figure 4.20: The $m_T^{ZZ}$ shape for MC $ee + \mu\mu$ events in both the SR (red) and the "Loose SR" (black). Their ratio is shown in the bottom plot with the Transfer Function fit overlaid.

### Systematic Uncertainties

Systematic uncertainties are assessed on both the $e\mu$ background normalization and the shape of the transverse mass for $e\mu$ events. The contribution to the systematic

uncertainty on the estimated $e\mu$ yield in the SR comes from the non-closure of the method. Both the systematic contributions are detailed below.

**MC closure.** Before the application of the method to data to extract the $e\mu$ contribution, a MC closure test is performed. This is done by applying the same strategy to the MC sample to test its validity. The estimation obtained through the $e\mu$ Control Region method is then compared with the effective number of events found in the SR for the entire $e\mu$ background. The comparison, which shows agreement within the statistical errors, is given in Table 4.13, after all numbers are normalized to 36.1 fb$^{-1}$. The non-closure of the method, a 12% effect, has been considered as a source of systematic uncertainty.

| $Ne\mu^{est.}$ | $Ne\mu^{MC}$ |
|---|---|
| 5.2 ± 1.0 | 4.6 ± 1.8 |

Table 4.13: Closure of the $e\mu$ backgrounds estimation. $Ne\mu^{est}$ is the number of $e\mu$ events in the SR estimated through the $e\mu$ Control Region, while $Ne\mu^{MC}$ is the expected event yields for the $e\mu$ background. Numbers are normalized to a data sample of 36.1 fb$^{-1}$. Errors contain statistical uncertainty only.

**Shape Variation.** The shape of the final discriminant variable for the $e\mu$ background is extracted from data in the $e\mu$ "Loose CR", and it is then extrapolated to the "Loose SR" by correcting for the binned efficiency factor to take into account the differences in reconstruction/identification efficiency between electrons and muons. To obtain the $m_T^{ZZ}$ shape for the $e\mu$ background in the final SR, it is however necessary to further extrapolate this shape by using a MC-based Transfer Function defined as explained above. The Data Driven (DD) shapes in the $ee$ and $\mu\mu$ channels are given in Figure 4.21 for the $m_T^{ZZ}$. The $m_T^{ZZ}$ shape shows good agreement between MC and data. Since the data tail lacks sufficient events, unlike MC, a conservative MC upper tail systematic uncertainty is taken as the shape systematic on the core of the distribution. The up/down systematic uncertainties are derived varying by $\pm 1\sigma$ the binned efficiency factors and extracting every time the shape. The final impact on the background estimation is 8% for both electrons and muons,

averaging over all the bins. The overall up/down systematics is then normalized to the DD estimate (nominal shape) in the corresponding SR. The nominal shape along with the up/down systematic uncertainties is shown in Figure 4.22. Additionally, a systematic uncertainty for the shape of the Transfer Function is evaluated by using a different definition and looking for the difference in the final estimate:

$$TFunction = 1 - a \cdot e^{-b \cdot m_T^{ZZ}} \tag{4.22}$$

where $a$ and $b$ are the free parameters. In Figure 4.23 the TFactors as a function of the $m_T^{ZZ}$ with the fitted alternative Transfer Function overlaid are shown. The final effect is a systematic uncertainty of 38%.

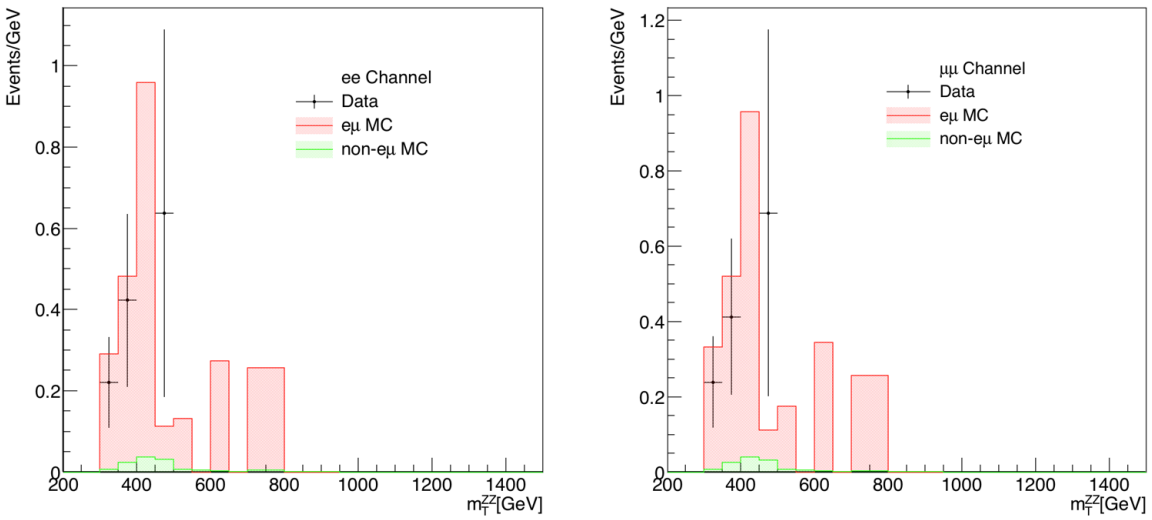


(a) $ee\nu\nu$ final state (b) $\mu\mu\nu\nu$ final state

Figure 4.21: The $m_T^{ZZ}$ shape in the $e\mu$ CR for the $ee\nu\nu$ channel (a) and $\mu\mu\nu\nu$ channel (b) with 36.1 fb$^{-1}$.

In Table 4.14 a summary of the different systematic uncertainties considered in both the $ee$ and $\mu\mu$ channels is reported. The MC closure refers to systematic uncertainty assessed from the non-closure method, as in Table 4.13. The shape uncertainty has been evaluated on the transverse mass distribution by varying the efficiency factors, as explained above, while the Transfer Function uncertainty is assessed by comparing the $e\mu$ estimate obtained in MC with the two different defi-

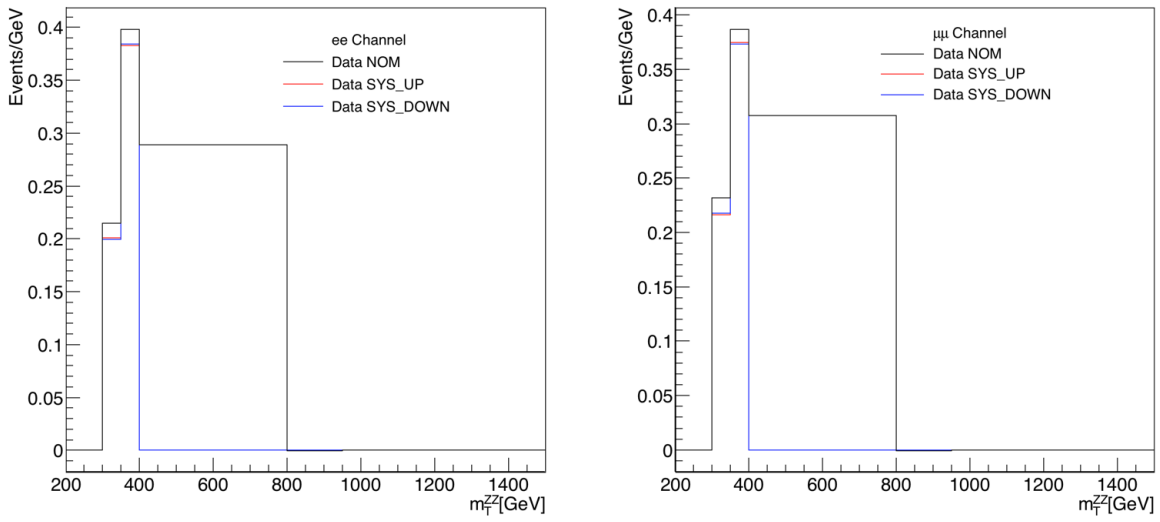


(a) $ee\nu\nu$ final state

(b) $\mu\mu\nu\nu$ final state

Figure 4.22: The $m_T^{ZZ}$ shape systematic uncertainties in the SR for the $ee\nu\nu$ channel (a) and $\mu\mu\nu\nu$ channel (b) with 36.1 fb$^{-1}$: up systematic (red), down systematic (blue) and nominal (grey).

nitions of this function. The total systematic uncertainty on the estimate is found by summing in quadrature all of these contributions.

| Channel | MC Closure | Shape | Transfer Function | Total |
|---|---|---|---|---|
| $ee$ | 12% | 10% | 38% | 41% |
| $\mu\mu$ | 12% | 10% | 38% | 41% |

Table 4.14: Contributions to the systematic uncertainties for the $e\mu$ background in both the $ee\nu\nu$ and the $\mu\mu\nu\nu$ channels.

The final estimates are evaluated event-by-event taking into account the binned efficiency factors. They are reported in Table 4.15.

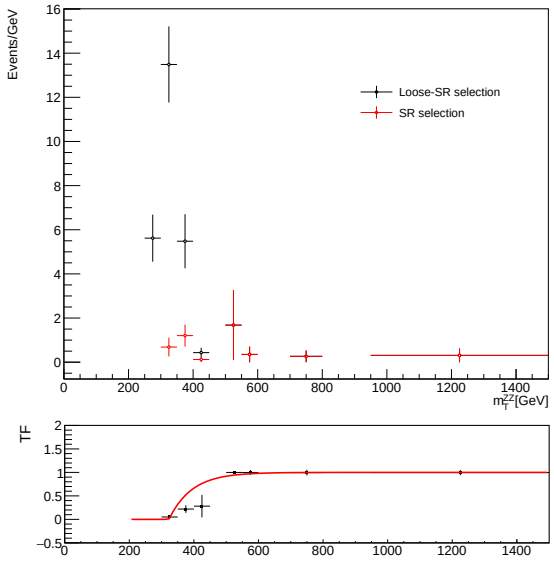


Figure 4.23: The $m_T^{ZZ}$ shape for MC $ee + \mu\mu$ events in both the SR (red) and the "Loose SR" (black). Their ratio is shown in the bottom plot with the alternative Transfer Function fit overlaid.

| Data Estimate | Binned ($p_T$, $\eta$) $\epsilon$ |
|---|---|
| $N_{ee}$ | 1.3 ± 0.5 ± 0.5 |
| $N_{\mu\mu}$ | 1.3 ± 0.5 ± 0.5 |

Table 4.15: Data-driven results in the SR for the $WW$, $t\bar{t}$, $Wt$, $Z \to \tau\tau$ background after applying the binned efficiency factors for both the $ee\nu\nu$ and the $\mu\mu\nu\nu$ channels. Errors contain both statistical and systematic uncertainties.

#### 4.5.4.5 Other Backgrounds

Other backgrounds, such as tri-boson production, $ttV$, single-top and $W + jets$, constitute only a tiny fraction of the total background in the off-shell signal region, ~ 0.5%, and are taken from simulation.

In Table 4.17 the various background contributions described in the previous sub-sections are summarized.

| Process | Number of events in the SR |
|---|---|
| $q\bar{q} \to ZZ$ | 132 ± 7(stat.) ± 13(sys.) |
| $WZ$ | 67.7 ± 2.0(stat.) ± 3.0(sys.) |
| $Z + jets$ | 6.0 ± 2.0(stat.) ± 2.0(sys.) |
| $t\bar{t}$, $WW$, $Wt$ and $Z \to \tau\tau$ | 2.6 ± 0.7(stat.) ± 0.7 (sys.) |
| Other | 1.14 ± 0.08 (no sys.) |

Table 4.16: Background contributions in the $\ell\ell\nu\nu$ analysis including the statistical and systematic uncertainties. The $ee\nu\nu$ and the $\mu\mu\nu\nu$ channels are merged together.

### 4.5.5 Systematic Uncertainties

This section describes all the systematic uncertainties that can impact the $\ell\ell\nu\nu$ analysis. They originate from theory calculations, data-driven estimate of background contributions, luminosity and pile-up. The largest contribution arise from theoretical uncertainties on the $gg \to H^* \to ZZ$ signal process, the $q\bar{q}/gg \to ZZ$ background and the signal/background interference in the $gg \to ZZ$ process. For the signal process, the reconstruction, acceptance and theory uncertainties have a significant impact on the determination of the $m_T^{ZZ}$ shape. Similarly for the background contributions, if the estimate is MC based. While for a data-driven background estimate, the yields are generally taken from data, while the shapes are taken from data when possible. In the subsections below both the theoretical and experimental uncertainties are described. A detailed description of the systematic uncertainties for the various background sources was given in the previous sections for each individual contribution. In Table 4.17 the various contributions in the different physics processes in the $\ell\ell\nu\nu$ analysis are summarized.

#### 4.5.5.1 Experimental Uncertainties

Compared to the theoretical uncertainties, the experimental systematic uncertainties are small in the $ZZ \to 2\ell 2\nu$ analysis and they have a small impact on the analysis sensitivity. They correspond to uncertainties on the luminosity, pile-up and efficiency

| Process | Luminosity | Experimental unc. | Theoretical unc. |
|---|---|---|---|
| $q\bar{q}/gg \to ZZ$ | Yield | - | Yield, Shape |
| $WZ$ | - | Yield | Shape |
| $Z + jets$ | - | Yield, Shape | - |
| $t\bar{t}$, $WW$, $Wt$ and $Z \to \tau\tau$ | - | Yield, Shape | Shape |
| Other | Yield | - | Yield, Shape |

Table 4.17: Impact of the sources of systematic uncertainty to the different background processes in the $\ell\ell\nu\nu$ analysis. The experimental source includes systematic uncertainties due to the data-driven strategy used to evaluate it.

corrections and/or calibrations of simulated objects. The latter have been provided by the combined performance groups for the relevant physics objects.

**Luminosity uncertainties.** The number of signal events via a specific Higgs boson production mode $i$ and decay mode $f$ is derived from:

$$n_{signal} = \mathcal{L} \times \mu_i \mu_f \times \sigma_{i,SM} \times A^f_{i,SM} \times \epsilon^f_i \times BR^f_{SM} \tag{4.23}$$

where $\mathcal{L}$ is the integrated luminosity, $A^f_{i,SM}$ is the detector acceptance and $\epsilon^f_i$ is the overall selection efficiency assuming the SM Higgs boson production and decay. A variation on the luminosity has then an impact on the production and decay signal strength $\mu_i$ and $\mu_f$ ( in this analysis on the off-shell signal strength). The luminosity uncertainty is ± 2.1% for the combined 2015 and 2016 dataset. It is derived following a methodology similar to that used in Run 1 [179]. Data collected in August 2015 and May 2016 are used. This uncertainty is applied to the normalization of the signal and also to background contributions whose normalizations are derived from MC simulations.

**Pile-up uncertainties.** Pile-up uncertainties are derived from variations of $< \mu >$ which change the pile-up re-weighting scheme. This is needed to cover the uncertainty in the ratio of the predicted and measured inelastic cross sections, as reported

in [180]. Differences between the up and down variations with respect to the nominal values are assigned as systematic uncertainties.

**Electron uncertainties.** In Sec. 3.3.1 a description of the electron reconstruction, calibration and derivation of efficiency corrections was given. The uncertainties on the electron objects are estimated from the energy scale and the electron efficiency factors. The uncertainties on the resolution and scale are provided by the official ATLAS $e/\gamma$ group [181]. The $\ell\ell\nu\nu$ analysis is weakly sensitive to the energy scale of electrons, thus a special simplified correlation model is applied. All effects are considered fully correlated in $\eta$ and consequently summed in quadrature. Based on this simplification only two systematic variations are provided, the first for the scale and the second for the resolution.

Additionally, uncertainties are also assigned to the reconstruction, identification, isolation and trigger efficiency factors [182]. Systematic uncertainties for electrons are at the percent level.

**Muon Uncertainties.** Similar to electrons, a description of the muon reconstruction, calibration and derivation of efficiency corrections was given in Sec. 3.3.2. The uncertainties on the muon objects are estimated from the muon momentum scale, the muon sagitta bias, possible detectors mis-alignments and the muon momentum resolution. The various systematic uncertainties are provided by the official ATLAS Muon Combined Performance (MCP) group [183]. In more detail, systematics are added to the resolution smearing of the muon track in the ID and MS chambers, due to small mis-alignments present between them. A scale systematic is assigned from variation of the muon momentum scale. Two additional scale systematic variations are added, due to the muon sagitta bias [184].

Additionally, uncertainties are also assigned on the reconstruction, identification, isolation and trigger efficiency factors. For muons, a systematic uncertainty is also attached to the track-to-vertex-association efficiency. Two different components of the systematics variations are used for each correction, the statistical and systematic error on the scale factors. For the low-$p_T$ component of the scale factors extra systematics are needed [185]. Systematic uncertainties for muons are at the percent level.

**Jet Uncertainties.** A description of the reconstruction, calibration and derivation of the Jet Vertex Tagger (JVT) efficiency corrections was given in Sec. 3.3.3. Jet systematic uncertainties are the largest contribution from the physics objects to the systematic uncertainty on the results. The jet systematic uncertainties are provided by the official ATLAS Jet/$E_T^{miss}$ group [175]. The derivation of the Jet Energy Scale, JES, uncertainty is described in [186]. Following a recommendation for most of ATLAS analyses, the JES uncertainty is derived from a highly reduced model of nuisance parameters. An extra uncertainty is added, due to an observed non-closure in the $2.4 < |\eta| < 2.5$ region. Additionally, a one sided systematic is provided for the jet resolution and energy smearing and a systematic uncertainty is provided for the JVT selection efficiency. Jet energy scale and resolution systematics are 1%-3% depending on the jet $p_T$.

$E_T^{miss}$ **Uncertainties.** Following recommendations of the official ATLAS Jet/$E_T^{miss}$ group [187], only the systematic uncertainty coming from the Track Soft Term (TST) is provided. All the other contributions are propagated from their respective object uncertainties. Three uncertainties on the soft terms are provided, two for the resolution and one for the scale [188]. The resolution uncertainties are taken from the data/MC differences of the variances of the projections parallel and perpendicular to $p_T^{hard}$, while for the scale systematic only data/MC differences of the variances of projections of the parallel component of $p_T^{hard}$ are considered. Systematic uncertainties for the soft term of $E_T^{miss}$ have $\sim 1\%$ of impact on the analysis.

**Flavor-tagging Uncertainties.** Three uncertainties for the heavy $b$, $c$ and light-flavour jets are included, based on the envelope method. They correspond to the uncertainties on the tagging efficiencies for the three jet types. Additionally MC-based systematic uncertainties are added for high-$p_T$ jets (> 300 GeV) [189].

#### 4.5.5.2 Theoretical Uncertainties

Theoretical uncertainties originate from the particular choice of various parameters such as PDFs, higher-order corrections and parton-shower modeling. Theoretical uncertainties are added to the signal and to the $ZZ$ and $WZ$ backgrounds. In the sub-sections below each contribution is described.

The theoretical uncertainties due to the missing higher-order corrections and PDF variations are small for $VH$-like and $VBF$-like processes $pp \to ZZ + 2j$; therefore, they are not included in the analysis.

**PDF uncertainties.** The PDF uncertainty covers the 68% CL variations of the nominal PDF `NNPDF3.0_nnlo` for both $q\bar{q} \to ZZ$ and $gg \to (H^* \to)ZZ$, as well as the difference from alternative PDF sets. The alternative PDF sets used are `CT10_nnlo` [122] and `MMHT2014_nnlo` [118]. For the $WZ$ background, normalization is taken from data using the $3\ell$ CR, as described in Section 4.5.4.2, thus only shape uncertainties from the variation of PDF sets need to be considered. The impact of the PDF systematic uncertainties on the $m_T^{ZZ}$ shape uncertainty is shown in Figure 4.24(a). Similarly, the impact of the PDF systematic uncertainties on the $m_T^{ZZ}$ shape uncertainty for the $q\bar{q} \to ZZ$ background is shown in Figure 4.24(b).

Given that the $ZZ$ background is normalized from simulation, the PDF variations also contribute to the normalization uncertainty. The PDF normalization uncertainty is found to be at the percent level.

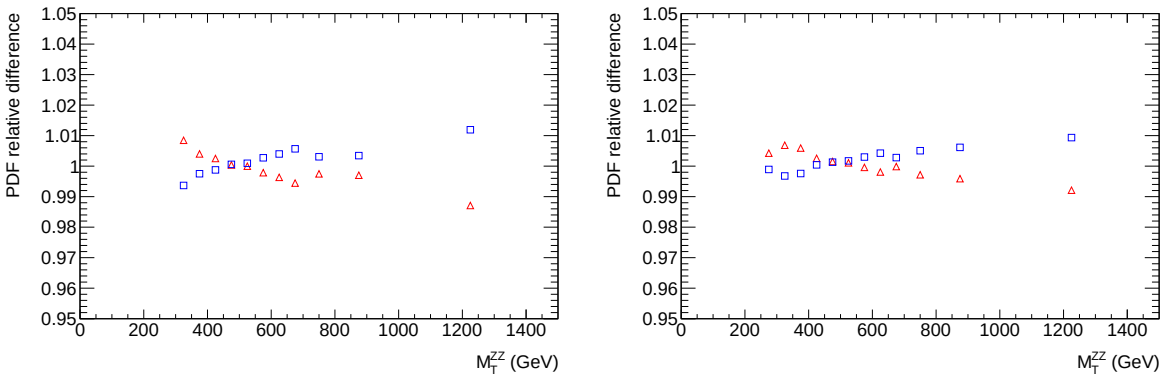


(a) $WZ$ background

(b) $q\bar{q} \to ZZ$ background

Figure 4.24: PDF shape uncertainties as a function of the transverse mass for the $WZ$ process (a) and the $q\bar{q} \to ZZ$ process (b) for the $\ell\ell\nu\nu$ analysis. The y-axis values indicate how much the uncertainty affects the $WZ$ or the $ZZ$ yield - the uncertainty is shown as up systematic uncertainty (blue) and down systematic uncertainty (red) - with a value of unity corresponding to the nominal yield. Figures produced by an ATLAS collaborator.

**Higher-order Uncertainties.** The uncertainty due to higher-order QCD corrections is estimated by varying the factorization scale, $\mu_F$ and the renormalization scale, $\mu_R$, from the nominal value independently, ranging from a factor of 0.5 to a factor of 2. For $ZZ$ backgrounds predicted by POWHEG, the uncertainty on NNLO QCD correction to the $q\bar{q} \to ZZ$ cross section and NLO EW corrections are also taken into account. However, the NLO EW correction uncertainty is found to be small, ~ 1%, given the tight event selection used in the analysis. Given that the $ZZ$ background is taken from simulation, the QCD scales variations also contribute to the normalization uncertainty. For the $ZZ$ modeling from SHERPA, only NLO EW corrections are applied. As stated above, systematics related to NLO EW are small. On the contrary, a 10% normalization uncertainty is assigned to account for the QCD scale systematics for the $q\bar{q} \to ZZ$ process and a few percents are assigned for the normalization uncertainty due to the QCD scale systematics for the $WZ$. The $gg \to ZZ$ process is characterized by the dominant systematic uncertainty from the $K$-factor uncertainty, forming about 10-20% normalization uncertainty in the $\ell\ell\nu\nu$ channel. The QCD scale uncertainties in the higher-order $K$-factor corrections are taken into account and propagated to extract the final results. Details on how higher-order corrections are applied in the various processes were given in Sec. 4.3. The QCD scale uncertainties are treated as uncorrelated between the $gg$ and the $q\bar{q}$ initiated $ZZ$ processes. There are a few additional normalization uncertainties associated with the NLO $K$-factors discussed in Sec. 4.3.1. In the region below $2m_t$, the higher-order corrections are computed with a maximum jet transverse momentum of 150 GeV to ensure a good description by the $1/m_t$ expansion. The default scale uncertainty is therefore doubled for events which have a jet with $p_T > 150$ GeV, corresponding to about 8% of the events in this region. The scale uncertainty is also increased by 50% around the $2m_t$ threshold, with a Gaussian-smoothed transition decreasing to the default uncertainty within 50 GeV of the threshold. This is intended to allow for possible effects on the $K$-factor which have not been estimated as the top quark moves on-shell. It is assumed that the 10-20% NLO QCD scale uncertainty for the $gg$-initiated $ZZ$ processes covers the assumption of massless loops above the $2m_t$ threshold, and as well the uncertainties in the 1.2 scale factor estimated only for the NNLO/NLO signal correction but also applied to the background and interference components. These NLO QCD scale uncertainties are larger than those associated with the NNLO QCD signal uncertainties.

**Parton-shower Uncertainties.** The showering systematics are evaluated for both the $ZZ$ and $WZ$ processes by varying the resummation scale by a factor of 4, changing the $CKKW$ setting and using different showering options [125, 167]. It is found to be 2-3% in normalization.

# Chapter 5

# Results and Interpretations

*In this chapter I describe the results obtained for the ATLAS off-shell strategy, my main DPhil project. After applying the strategy described in Chapter 4, it is possible to examine the data sample 'un-blinding' the results in the $\ell\ell\nu\nu$ Signal Region. I first introduce the $\ell\ell\nu\nu$ yields obtained. I later focus on the statistical framework used to perform the data fit for the signal hypothesis for the off-shell signal strength of the Higgs boson production. Results are combined with those from the $4\ell$ channel to increase sensitivity deriving the ATLAS Run-2 estimate of the off-shell signal strength. After combining with the results of the on-shell signal strength based on the same dataset, a limit on the Higgs boson total width is derived. Alternative interpretations of these results are possible and they are described in this chapter along with the corresponding assumptions. It was also proposed to use this dataset to search for new interactions beyond the SM (BSM) parameterizing new physics interactions with the effective field theory formalism. In the final section I will present this novel study I produced for the $\ell\ell\nu\nu$ channel. The results summarized in this chapter were published at the end of my third year of DPhil and I presented them in a summary talk on behalf of the ATLAS and CMS collaborations at* HiggsHunting2018 *with a talk titled* "Higgs width at LHC and ILC" *and on behalf of the ATLAS collaboration at* LISHEP2018 *with a talk titled* "Measurement of cross sections and properties of the Higgs boson using the ATLAS detector"*. I also gave more than ten seminars on the topic in Europe and in the USA (Heidelberg, Zurich, Princeton, Harvard, Scuola Normale di Pisa, FERMILAB, SLAC, Imperial College, CALTECH etc.)*

## 5.1 Yields

The signal modeling and background estimation for the extraction of the off-shell signal strength in the $\ell\ell\nu\nu$ channel were provided in Chapter 4. The definition of the Signal Region was given in Sec. 4.5.3.3, while the various techniques to extract the background estimate were given in Sec. 4.5.4. After all the needed checks on these estimates are completed, it is possible to *un-blind* the results. Figure 5.1 shows a pie chart summarizing the individual background contributions with respect to the total background in the $\ell\ell\nu\nu$ channel.

The discriminant for the $\ell\ell\nu\nu$ channel is the transverse mass, $m_T^{ZZ}$, defined in Eq. 4.11. Its distribution after the un-blinding in the Signal Region is shown in Fig. 5.2. The $ee\nu\nu$ channel is shown in Fig. 5.2(a) and the $\mu\mu\nu\nu$ channel is shown in Fig. 5.2(b). All the background contributions are shown along with the SM expectation for the off-shell signal strength. In addition, the SM expectations for $\mu_{off-shell} = 5$ are also shown. The Signal Region yield is summarized in Table 5.1, along with the corresponding yields for the $4\ell$ analysis which was described in Sec. 4.4.

## 5.2 Statistical Analysis

This section brifely focuses on the general procedure and formalism used to search for new phenomena in the context of a frequentist statistical test[1]. When looking for a new signal process, one generally defines (at least) two hypotheses, the null hypothesis, $H_0$, as describing only known processes, better known as background hypothesis, and the alternative hypothesis, $H_1$, including the new signal+background. When settings limits for new physics, the signal+background hypothesis is the one to be tested against the background-only hypothesis. In the context of hypothesis testing and confidence intervals theory, it is convenient to define the signal strengths as the ratios of cross section and branching fractions to the corresponding SM predictions such that:

$$\mu_i^f = \frac{\sigma_i \times BR^f}{(\sigma_i)_{SM} \times (BR^f)_{SM}} = \mu_i \times \mu^f \tag{5.1}$$

where the subscript $i$ and $f$ stands for the production mode and decay channel, respectively. By definition all $\mu_i^f$ are equal to 1 in the assumption of a SM Higgs

[1]The description and the formalism used in this section closely follows [190].

| **Process** | $4\ell$ $m_{4\ell} > 220$ GeV | $\ell\ell\nu\nu$ $m_T^{ZZ} > 250$ GeV |
|---|---|---|
| $\boldsymbol{gg \to (H^* \to) ZZ}$ | **96 ± 15** | **22 ± 4** |
| with | | |
| $gg \to H^* \to ZZ(S)$ | 9.8 ± 1.5 | 20.1 ± 3.3 |
| $gg \to ZZ(B)$ | 101 ± 16 | 28 ± 6 |
| $\boldsymbol{VBF\ (H^* \to) ZZ}$ | **8.29 ± 0.34** | **2.83 ± 0.14** |
| with | | |
| $VBF\ H^* \to ZZ$ (S) | 1.67 ± 0.08 | 5.45 ± 0.30 |
| $VBF\ ZZ(B)$ | 9.9 ± 0.4 | 6.92 ± 0.35 |
| $q\bar{q} \to ZZ$ | 520 ± 42 | 132 ± 15 |
| $q\bar{q} \to WZ$ | - | 68 ± 4 |
| $WW$, $t\bar{t}$, $Wt$ and $Z \to \tau\tau$ | - | 2.6 ± 1.0 |
| $Z + jets$ | - | 6.0 ± 2.8 |
| Other backgrounds | 14.6 ± 0.7 | 1.14 ± 0.08 |
| Total Expected (SM) | 639 ± 60 | 234 ± 16 |
| Observed | 704 | 261 |
| Alternative signal hypothesis | | |
| $gg \to (H^* \to) ZZ$ ($\mu_{off-shell} = 5$) | 117 ± 18 | 61 ± 12 |
| $VBF (H^* \to) ZZ$ ($\mu_{off-shell} = 5$) | 11.0 ± 0.5 | 8.8 ± 0.4 |

Table 5.1: Expected and observed yields in the off-shell Signal Region for both the final states, $ZZ \to 4\ell$ and $ZZ \to \ell\ell\nu\nu$. The Signal Region is defined as 220 GeV $< m_{4\ell} <$ 2 TeV for the $4\ell$ channel and as 250 GeV $< m_T^{ZZ} <$ 2 TeV for the $\ell\ell\nu\nu$ channel, respectively. The expected background contributions are also reported. They are derived as described in Sec. 4.5.4. The uncertainties on the number of expected events include both the statistical and systematic uncertainties, summed in quadrature. Empty entries correspond to contributions with event yields smaller than 0.1 events. The expected number of events for the $gg \to (H^* \to) ZZ$ and $VBF\ (H^* \to) ZZ$ processes, including the Higgs boson signal, background and interference are reported for both the SM predictions (in bold) and for the alternative signal hypothesis $\mu_{off-shell} = 5$. (S) and (B) stands for the signal and background-only yields with no interference contribution.

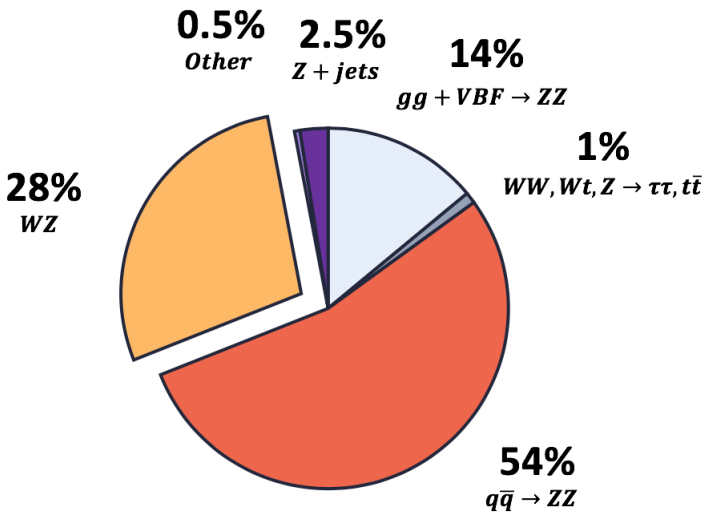


Figure 5.1: Pie chart summarizing the individual background contributions with respect to the total background in the $\ell\ell\nu\nu$ analysis. Background estimates are derived following strategies described in Sec. 4.5.4. As only background is considered, contributions from the signal-background interference in the ggF and VBF production modes are not included in the estimate.

boson. The simplest and most popular parameterization for the signal strength is to assume that the $\mu_i$ and $\mu^f$ values are the same for all the production modes and decays channels. With that assumption, SM predictions of signal yields are all scaled by a global signal strength $\mu$. This is a very special case of the kappa-framework [43] and provides the simplest test of compatibility of the observed data with the SM predictions. In the off-shell analysis the signal strength under consideration is:

$$\mu_{off-shell} = \frac{\sigma \times BR(H^* \to ZZ)}{\sigma_{SM} \times BR_{SM}(H^* \to ZZ)} \tag{5.2}$$

as shown in Eq. 4.4.

In the $\ell\ell\nu\nu$ analysis, the SM hypothesis of $\mu_{off-shell} = 1$ is the one to be tested against a different hypothesized value for $\mu_{off-shell}$.

A robust formalism has been developed to study most of the cases of interest at the LHC. Consider an experiment where for each selected event of $N$ total events

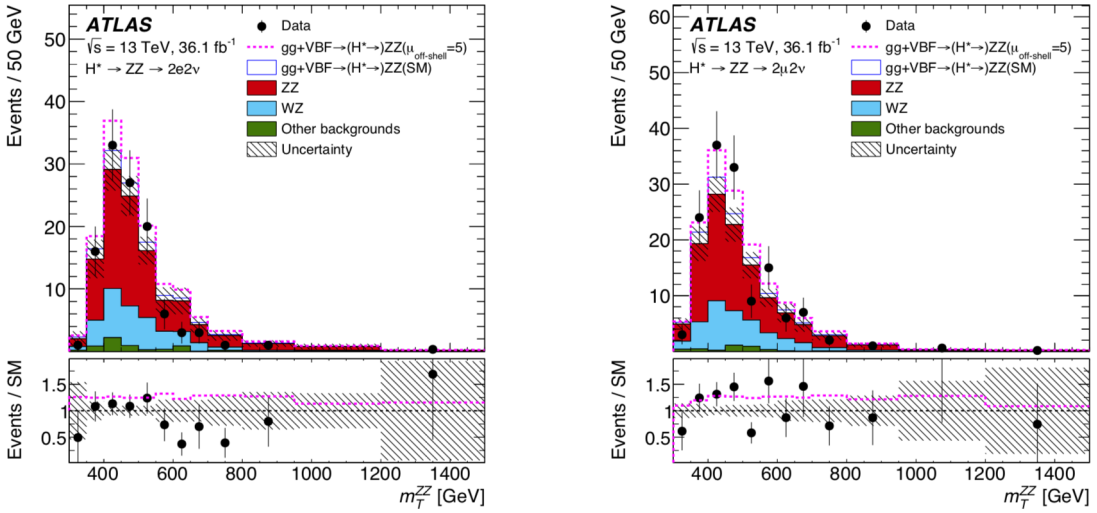


(a) $ee\nu\nu$ final state (b) $\mu\mu\nu\nu$ final state

Figure 5.2: Observed and expected transverse mass $m_T^{ZZ}$ distribution in the off-shell Signal Region for the $ee\nu\nu$ channel (a) and $\mu\mu\nu\nu$ channel (b) with 36.1 fb$^{-1}$. The hatched area shows the combined statistical and systematic uncertainties. The dashed line corresponds to the total expected event yield including all backgrounds and the Higgs boson with $\mu_{off-shell} = 5$. Backgrounds are derived as described in Sec. 4.5.4.

in the signal sample one measures a variable $x$ (e.g. the transverse mass, $m_T^{ZZ}$, in the $\ell\ell\nu\nu$ analysis) and constructs a histogram of the variable $x$, with $N$ bins $\boldsymbol{n} \equiv (n_1, n_2, \ldots \quad n_N)$[2]. The expectation value of the total number of events in the $i^{th}$ bin can be written as:

$$E[n_i] = \mu \cdot S_i + B_i \tag{5.3}$$

where the mean number of signal and background entries are defined as:

$$S_i = S_{tot} \int_{bin_i} f_S(x;\boldsymbol{\theta_S})dx \quad \text{and} \quad B_i = B_{tot} \int_{bin_i} f_B(x;\boldsymbol{\theta_B})dx \tag{5.4}$$

where the functions $f_S(x;\boldsymbol{\theta_S})$ and $f_B(x;\boldsymbol{\theta_B})$ are the Probability Density Functions (PDFs) of the variable $x$ for signal and background events, respectively. The vectors $\boldsymbol{\theta_S}$ and $\boldsymbol{\theta_B}$ stand for all the signal and background parameters that model the shapes of the PDFs. The two integrals determine the probability for an event to be found in

[2]The generalization to an unbinned analysis strategy is straightforward.

the $i^{th}$ bin with $S_{tot}$ and $B_{tot}$ being the total mean numbers of signal and background events. The signal normalization, $S_{tot}$, is fixed to the value predicted by the nominal signal model, while the background normalization, $B_{tot}$, is an adjustable parameter. Traditionally, in literature one indicates all the parameters as $\boldsymbol{\theta} \equiv (\boldsymbol{\theta_S}, \boldsymbol{\theta_B}, B_{tot})$. They constitute the *nuisance parameters*, NPs. In addition to the parameter to be determined - the cross section of the signal process - signal and background models often contain *nuisance parameters*, whose values must be derived from the data fit. These parameters are needed to take into account systematic uncertainties of the analysis (theoretical model, detector effects, background estimation ...). However, the additional flexibility required to parameterize systematic uncertainties results in a loss of sensitivity. In a way, the degree to which the fit can modify the background estimate is determined by the features of the nuisance parameters affecting the background itself: these nuisance parameters can be either freely floating normalization parameters or constrained parameters on the shape and normalization of the background prediction.

Often, subsidiary measurements are helpful to constrain the *nuisance parameters*. In practice, this is often achieved by introducing a Control Region which should be mostly populated by background events. From this Control Sample it is possible to construct a histogram of some chosen kinematic variables, $\boldsymbol{m} \equiv (m_1, m_2, ... \quad m_M)$ where $M$ is the total number of bins for the histogram in the Control Region. Similar to Eq. 5.3, one can write the expectation value of $m_i$:

$$E[m_i] = u_i(\boldsymbol{\theta}) \tag{5.5}$$

where the functions $u_i$ express the dependence on the parameters $\boldsymbol{\theta}$. The Control Regions and so the functions $u_i$ are often constructed in a way to obtain greater information on the background normalization parameter, $B_{tot}$, and also on the corresponding shapes. Control Regions can be considered as additional bins depending on the *nuisance parameters*, but not on the signal strength. A clear example is what was done in the $\ell\ell\nu\nu$ analysis when defining the $3\ell$ CR for the estimate of the $WZ$ background normalization and shape (Sec. 4.5.4.2) or when defining the $Z + jets$ CR for the estimate of the $WZ$ background normalization and shape (Sec. 4.5.4.3).

The test statistics can be written as a Maximum Likelihood Function. The likelihood approach allows the determination of the parameters of interest by searching

for values which maximize the likelihood function. In more detail, the likelihood function is the product of Poisson probabilities for the expected number of events over all the bins:

$$\mathcal{L}(\mu, \boldsymbol{\theta}) = \prod_{j=1}^{N} \frac{(\mu \cdot S_j + B_j)^{n_j}}{n_j!} e^{-(\mu \cdot S_j + B_j)} \prod_{l=1}^{M} \frac{u_l^{m_l}}{m_l!} e^{-u_l} \tag{5.6}$$

where possible CRs for background estimates are included. The likelihood function is just the conditional probability of a certain observed variable $x$, given some unknown parameters $(\mu, \boldsymbol{\theta})$.

The formalism is slightly different if one includes also systematic uncertainties via the set of *nuisance parameters*. Generally, systematic uncertainties are split into two categories: normalization uncertainties and shape uncertainties. NPs for normalization uncertainties are parametrized using Gaussian functions centred on their nominal expectation values, $\widetilde{\boldsymbol{\theta}}$:

$$\mathcal{G}(\theta|\widetilde{\theta}, \sigma_\theta) = \frac{1}{\sigma_\theta \sqrt{2\pi}} e^{-\frac{(\theta-\widetilde{\theta})^2}{2\sigma_\theta^2}} \tag{5.7}$$

NPs are then constrained to their assigned values within their uncertainties. As an example, it has been shown (sec. 4.5.5.1) that the measured integrated luminosity for this analysis results in a 2.1% uncertainty. Thus, the correct method to take into account such a systematic uncertainty is to rewrite the likelihood as:

$$\mathcal{L}(\mu, \boldsymbol{\theta}) = \prod_{j=1}^{N} \frac{(\mu \cdot S_j + B_j)^{n_j}}{n_j!} e^{-(\mu \cdot S_j + B_j)} \times \mathcal{G}(L|\widetilde{L}, \sigma_L) \tag{5.8}$$

where $\mathcal{G}$ is a normalized Gaussian of mean $\widetilde{L}$[3] and width $\sigma_\mathcal{L}$ for the measured value $\widetilde{L} \pm \sigma_\mathcal{L}$. The Gaussian function serves to constrain the value of the luminosity nuisance parameter $L$ to its measured value. Any normalization uncertainty can be introduced in the likelihood this way, including uncertainties on cross sections, overall efficiencies etc. In many cases, however, the allowed physical bound on a multiplicative nuisance parameter is that it remains positive which is not always possible when representing a constraint by a Gaussian. In such cases one might also consider constraining the parameter with a log-normal or other probability density

[3]To avoid confusion with the Likelihood function, in this section the luminosity is written as $L$ rather $\mathcal{L}$, which is the formalism used in the previous chapters.

which does not allow the parameter to become negative. In the $\ell\ell\nu\nu$ analysis, both Gaussian and log-normal probability density functions are used, based on external studies.

Many systematic uncertainties result in a shape distortion of the distributions of interest. For instance, this is the case for the $m_T^{ZZ}$ shape variation studied for the $Z + jets$ background, Sec. 4.5.4.3. This is taken into account using a 'vertical morphing' technique [191]. It involves producing multiple templates from the variation of the nominal estimate by $\pm 1\sigma$ and deriving the yield every time. These three measurements of the spectral shape are turned into a continuous estimate by using the morphing technique, which allows for a quadratic interpolation among the three measurements, later smoothly converted into a new NP used to parametrize the yield variation.

**Test statistic** When performing a hypothesis test between two simple hypotheses, $H_0$ and $H_1$, the likelihood-ratio which rejects $H_0$ in favour of $H_1$ at a significance level $\alpha$, is proven to be the most powerful test statistic by the Neyman-Pearson lemma [191].

Thus, to test a hypothesized value of $\mu$ the profile likelihood ratio is considered:

$$\lambda(\mu) = \frac{\mathcal{L}(\mu, \hat{\hat{\theta}})}{\mathcal{L}(\hat{\mu}, \hat{\theta})} \tag{5.9}$$

where $\hat{\hat{\theta}}$ in the numerator denotes the value of the parameter $\theta$ that maximizes the likelihood $\mathcal{L}$ for the specific $\mu$ under consideration. In the literature it is better known as the conditional maximum-likelihood (ML) estimator of $\boldsymbol{\theta}$ and as a consequence is a function of $\mu$. The denominator is the maximized and unconditional likelihood function, with $\hat{\mu}$ and $\hat{\boldsymbol{\theta}}$ being the corresponding unconditional ML estimators. Since the likelihood involves products, it is preferable to work with the logarithm likelihood function in a way that products are turned into a sum of terms. Also, it is more practical to look for the minimum of the log-likelihood function rather for its maximum since all software routines already implemented for the $\chi^2$ minimize the function rather maximizing it. Thus, the test statistic is:

$$q_\mu = -2 \cdot \ln \lambda(\mu) \tag{5.10}$$

Since the logarithm is a monotonic function, the maximum/minimum of the function is unchanged. The likelihood ratio tests the compatibility between the observed value of the parameter of interest, POI, $\hat{\mu}$ and the one given by a certain hypothesis $\mu$. The likelihood ratio value, once plotted as a function of $\mu$ shows the behaviour of the likelihood for different possibile values of the hypothesized $\mu$.

As anticipated, the presence of NPs broadens the profile likelihood ratio as a function of $\mu$ compared to if their values were fixed. This is how the loss of information due to systematic uncertainties propagates to the estimate of $\mu$. From Eq. 5.9 $0 \leq \lambda \leq 1$. If the likelihood ratio approaches one and thus $q_\mu \to 0$, good agreement is found between data and the hypothesis under test. On the contrary, $q_\mu > 0$, implies poor agreement is found with the tested hypothesis on $\mu$.

Since the presence of a new signal means an increased mean event rate beyond what is expected from the background-only hypothesis, one would naturally expect $\mu \geq 0$. Also, when setting superior limits the additional constraint $\hat{\mu} \leq \mu$ holds. The test statistic $q_\mu$ follows a probability density function, $f(q_\mu|\mu)$, for a given assumption on the signal strength $\mu$. The probability density function can be computed using toy MC pseudo-datasets, but because of the computational power required, generally a useful asymptotic limit approximation is used to derive a proper formula [190]. To quantify the level of disagreement it is helpful to compute the $p$-value:

$$p_\mu = \int_{q_{\mu,obs}}^{\infty} f(q_\mu|\mu) dq_\mu \tag{5.11}$$

where $q_{\mu,obs}$ is the value of the statistic $q_\mu$ observed in data. The $p$-value is the probability, under a given hypothesis on $\mu$, of finding data of equal or greater incompatibility with the predictions of $\mu$. The hypothesis can be excluded if its $p$-value is observed below a specific threshold. To exclude a signal hypothesis, a threshold $p$-value of 0.05 is generally considered a common standard in particle physics. This corresponds to 95% Confidence Level, CL.

In particle physics it is conventional to convert the $p$-value into an equivalent significance, $Z$, defined such that a Gaussian distributed variable found $Z$ standard deviations above its mean has an upper-tail probability equal to $p$. Formally:

$$Z = \Phi^{-1}(1 - p) \tag{5.12}$$

where $\Phi^{-1}$ is the inverse of the cumulative distribution, i.e. the quantile of the

standard Gaussian. For signal observation purposes it has been decided to reject the background hypothesis with a significance of at least $Z = 5$ which corresponds to $p = 2.87 \times 10^{-7}$. As noted above, for signal exclusion the $p$-value threshold is 0.05, which corresponds to $Z = 1.64$.

When setting upper limits on a production process, one is setting a maximum production rate supported by observation at a certain statistical level of confidence. At the LHC this is achieved using the frequentist Confidence Interval ($\mathrm{CL}_s$) method [192], which is currently the most popular approach. In the $\mathrm{CL}_s$ method one tests the compatibility of the Background-only hypothesis ($\mu = 0$), given the outcome in data, against the Signal+Background hypothesis for different values of $\mu$. For the Signal+Background hypothesis one can write the $p$-value:

$$p_\mu = \mathcal{P}(q_\mu \geq q_{\mu,obs}|\mu) = CL_{S+B} = \int_{q_{\mu,obs}}^{\infty} f(q_\mu|\mu)dq_\mu \tag{5.13}$$

and for the Background-only hypothesis, one can write the $p$-value:

$$1 - p_b = \mathcal{P}(q_\mu \geq q_{\mu,obs}|\mu = 0) = CL_B = \int_{q_{\mu,obs}}^{\infty} f(q_\mu|\mu = 0)dq_\mu \tag{5.14}$$

The $CL_S$ is defined as:

$$CL_S = \frac{CL_{S+B}}{CL_B} = \frac{p_\mu}{1 - p_b} \tag{5.15}$$

If $CL_S \leq \alpha$, then the hypothesized $\mu$ is rejected with (1- $\alpha$) Confidence Level. The conventional choice for signal exclusion purposes is $\alpha = 0.05$. Thus, the 95% $CL_S$ upper limits are obtained by finding the value of $\mu$ which gives $CL_S(\mu) = 0.05$.

**Sensitivity of an experiment** Before doing the measurement, it is often useful to determine the sensitivity of the experiment for the specific analysis under consideration. Based on the simulation, it is possible to calculate at which CL we can exclude the hypothesized $\mu$. This expected exclusion of the signal is an important parameter in the design of the experiment itself. Generally one provides two upper limits based on two kinds of test statistics, the observed $q_\mu$ and the expected $q_\mu^A$. Upper limits are similarly calculated from the $CL_S$ method described before for both samples. A special, artificial data set is used, called the 'Asimov dataset'. It is defined such that when one uses it to evaluate the estimators for all parameters, one obtains the true parameter values. In practice, these are the values estimable from

the MC model using a very large data sample. The likelihood ratio for the Asimov data set can be defined as:

$$\lambda_A(\mu) = \frac{\mathcal{L}_{\mathcal{A}}(\mu, \hat{\hat{\theta}})}{\mathcal{L}_{\mathcal{A}}(\hat{\mu}, \hat{\theta})} = \frac{\mathcal{L}_{\mathcal{A}}(\mu, \hat{\hat{\theta}})}{\mathcal{L}_{\mathcal{A}}(\mu', \hat{\theta})} \tag{5.16}$$

where the last equality exploits the fact that the estimators for the parameters are equal to their hypothesized values when the likelihood is evaluated with the Asimov dataset. It is assumed that the estimator $\hat{\mu}$ follows a Gaussian distribution with a mean of $\mu'$. The Asimov dataset is a sample in which all the statistical fluctuations are suppressed. This automatically leads to the estimate of the experimental sensitivity.

**Combining multiple channels** For several searches, it might be convenient to combine several channels. For the off-shell analysis, for instance there will a combination between the $\ell\ell\nu\nu$ and the $4\ell$ channel. For each channel there is a likelihood function $\mathcal{L}_i(\mu, \boldsymbol{\theta_i})$ where $\boldsymbol{\theta_i}$ represents the set of nuisance parameters for the $i^{th}$ channel. The signal strength parameter $\mu$ is the same for all the channels. For statistically-independent channels, the full likelihood and thus the likelihood ratio can be factorized as:

$$\lambda(\mu) = \frac{\prod_{i=1}^{N} \mathcal{L}_i(\mu, \hat{\hat{\theta}}_i)}{\prod_{i=1}^{N} \mathcal{L}_i(\hat{\mu}, \hat{\theta}_i)} \tag{5.17}$$

Since Asimov datasets contain no statistical fluctuation, one has $\hat{\mu} = \mu'$ and the same components of $\theta_i$ for all channels, thus for a strength parameter $\mu'$ the formalism simplifies:

$$\lambda_A(\mu) = \frac{\prod_{i=1}^{N} \mathcal{L}_i(\mu, \hat{\hat{\theta}}_i)}{\prod_{i=1}^{N} \mathcal{L}_i(\mu', \hat{\theta}_i)} = \prod_{i=1}^{N} \lambda_{A,i}(\mu) \tag{5.18}$$

where $\lambda_{A,i}(\mu)$ is the profile likelihood ratio for the $i^{th}$ channel. For the Asimov dataset it is possible to obtain the sensitivity of the experiment separately for each channel deriving later the combined result, simplifying greatly the task rather deriving it from the full combination.

## 5.3 Experimental Results

In this section experimental results for the estimate of $\mu_{off-shell}$ and $\Gamma_H$ are presented. They are based on the yield extraction described in Sec. 5.1 and on the statistical approach introduced in Sec. 5.2. The extraction of the off-shell couplings in the $\ell\ell\nu\nu$ channels is presented in Sec. 5.3.1. A similar extraction in the $4\ell$ channel is introduced in Sec. 5.3.2. The combination of the two channels is presented in Sec. 5.3.3. A subsequent combination with the on-shell couplings allows for the extraction of the limit on the Higgs boson total width, shown in Sec. 5.3.4. Finally, an alternative interpretation leads to consistency tests on gluon couplings between the off-shell and on-shell regime, the $R_{gg}$ *interpretation*, reported in Sec. 5.3.5.

It is useful to briefly describe the formalism used for the various combinations, in order to understand the different interpretations that have been considered.

**Formalism and Interpretations.** The off-shell analysis can be schematically summarized in a two-step strategy:

1. In a first step, the off-shell signal strength is extracted in both channels, $4\ell$ and $\ell\ell\nu\nu$, and finally combined in a limit on the $\mu_{off-shell}$ signal strength;

2. In a second step, the off-shell analyses are combined with the on-shell $H \to ZZ^* \to 4\ell$ [193] analysis based on the 13 TeV data taken in 2015 and 2016 to derive the final estimate on the Higgs boson total width, $\Gamma_H$.

For each step, some assumptions are needed which lead to different interpretations. It is useful to summarize the definitions of signal strength used in the on-shell and off-shell analyses. For the on-shell analysis, the signal strength for the ggF and VBF[4] production can be written as:

$$\mu^{ggF}_{on-shell} = \frac{\sigma^{gg\to H\to ZZ}_{on-shell}}{\sigma^{gg\to H\to ZZ}_{on-shell,SM}} = \frac{\kappa^2_{g,on-shell}\cdot\kappa^2_{V,on-shell}}{\Gamma_H/\Gamma^{SM}_H}, \tag{5.19}$$

$$\mu^{VBF}_{on-shell} \equiv \frac{\sigma^{VBFH\to ZZ}_{on-shell}}{\sigma^{VBFH\to ZZ}_{on-shell,SM}} = \frac{\kappa^4_{V,on-shell}}{\Gamma_H/\Gamma^{SM}_H} \tag{5.20}$$

[4]In all results the signal strength for the $VH$ associated production is assumed to scale with the VBF production while the $b\bar{b}H$ and $t\bar{t}H$ processes scale with the $gg \to H$ process. These additional production modes are expected to give negligible contributions to the off-shell measurements, but have small contributions to the on-shell signal yields.

For the off-shell analysis, the signal strength for the ggF and VBF production can be written as:

$$\mu^{ggF}_{off-shell} = \frac{\sigma^{gg\to H\to ZZ}_{off-shell}}{\sigma^{gg\to H\to ZZ}_{off-shell,SM}} = \kappa^2_{g,off-shell}\cdot\kappa^2_{V,off-shell}, \tag{5.21}$$

$$\mu^{VBF}_{off-shell} = \frac{\sigma^{VBFH\to ZZ}_{off-shell}}{\sigma^{VBFH\to ZZ}_{off-shell,SM}} = \kappa^4_{V,off-shell} \tag{5.22}$$

If the following coupling ratios are defined:

$$R_{gg} = \kappa^2_{g,off-shell}/\kappa^2_{g,on-shell}, \tag{5.23}$$

$$R_{VV} = \kappa^2_{V,off-shell}/\kappa^2_{V,on-shell} \tag{5.24}$$

it is then possible to relate the on-shell and off-shell signal strengths in the following way:

$$\mu^{ggF}_{off-shell} = R_{gg}\cdot R_{VV}\cdot\mu^{ggF}_{on-shell}\cdot\Gamma_H/\Gamma^{SM}_H \tag{5.25}$$

$$\mu^{VBF}_{off-shell} = R^2_{VV}\cdot\mu^{VBF}_{on-shell}\cdot\Gamma_H/\Gamma^{SM}_H \tag{5.26}$$

Since the off-shell analysis is performed inclusively in jet multiplicity, i.e. no event categorization for the ggF and VBF production modes separately, there is insufficient sensitivity to individually constrain the off-shell signal strength for the ggF and VBF production modes. Thus, in the first step described above, a single off-shell signal strength parameter is applied for all the production modes, assuming that the ratio of the off-shell production rates via the process $gg \to H^*$ to those via VBF processes is as predicted in the SM, which means $\mu^{ggF}_{off-shell}/\mu^{VBF}_{off-shell} = 1$.

Later, when moving to the second step described above, the combination with the on-shell analysis is performed under two different assumptions which correspond to different interpretations of the results:

- $\Gamma_H$ *interpretation*: The Parameter Of Interest (POI) is the ratio of off-shell to on-shell signal strengths, which can be interpreted as the ratio of the Higgs boson total width to the SM expectation, $\mu_{off-shell}/\mu_{on-shell} = \Gamma_H/\Gamma^{SM}_H$. This interpretation assumes that the off- and on-shell coupling modifiers are the same for both the ggF and VBF production modes, $k_{g,on-shell} = k_{g,off-shell}$

$= k_{V,off-shell} = k_{V,on-shell}$ with $V = W, Z$. The common coupling modifier $k = k_g = k_V$ is profiled (i.e. fit to data).

- $R_{gg}$ *interpretation*: The POI is the ratio of off-shell to on-shell signal strengths for the ggF production only, $R_{gg} = \mu^{ggF}_{off-shell}/\mu^{ggF}_{on-shell}$ which can be interpreted as the ratio of off-shell to on-shell gluon couplings, Eq. 5.23. In this case the coupling scale factors $k_V = k_{V,on-shell} = k_{V,off-shell}$ associated with the on- and off-shell VBF production modes are assumed to be the same and profiled (i.e. fit to data). Also, the width ratio $\Gamma_H/\Gamma_H^{SM}$ is fixed to the SM expectation: $\Gamma_H/\Gamma_H^{SM} = 1$.

In principle, other interpretations are possible. For instance the $R_{VV}$ interpretation, mirroring the $R_{gg}$ interpretation with $k_V$ replacing $k_g$. This interpretation would test variations of couplings to vector bosons between the on- and off-shell regime. I have produced limits assuming this interpretation and an alternative interpretation, but more studies were needed to consolidate them and it was decided to not include them in this first Run-2 paper. The current plan is to include them in the next paper, based on the full Run-2 data set. Therefore, the $R_{VV}$ and the alternative interpretation will not be discussed here.

The on-shell and off-shell combined-fit assumptions used for the results reported in this thesis are summarized in Table 5.2.

| POI | Profiling | Assumptions |
|---|---|---|
| $\Gamma_H/\Gamma_H^{SM}$ | $\mu_{on-shell}$ | $\kappa_{g,on-shell} = \kappa_{g,off-shell} = \kappa_{V,on-shell} = \kappa_{V,off-shell}$, thus $R_{gg}$=1, $R_{VV}$=1, single $\mu_{off-shell}$ and $\mu_{on-shell}$ for both ggF and VBF |
| $R_{gg}$ | $\mu^{ggF}_{on-shell}$, $\mu^{VBF}_{on-shell}$ | $R_{VV}$=1, $\Gamma_H/\Gamma_H^{SM}$=1 |

Table 5.2: Assumptions for the various interpretations considered when combining the on- and off-shell results from the $4\ell$ and $\ell\ell\nu\nu$ channels.

### 5.3.1 Extraction of Off-shell Couplings in the $\ell\ell\nu\nu$ Analysis

To extract constraints on the off-shell Higgs couplings a binned maximum likelihood fit is performed. The transverse mass, $m_T^{ZZ}$, shown in Fig. 5.2, is used as a final

discriminant in the binned fit. The likelihood fit model accounts for signal and background processes, including $gg \to (H^* \to) ZZ$, VBF $(H^* \to) ZZ$, $q\bar{q} \to ZZ$ and all the other backgrounds reported in the $\ell\ell\nu\nu$ column of Table 5.1. The $gg \to (H^* \to) ZZ$ process includes the signal $gg \to H^* \to ZZ$, the continuum background $gg \to ZZ$ and the interference between the two. The probability density function of $gg \to ZZ$ and VBF $ZZ$ can be parametrized as a function of $\mu_{off-shell}$, as described in Sec. 4.3.3. In more detail, a binned likelihood function is constructed as a product of Poisson probability terms over all the bins of the fit templates considered. This function depends on the off-shell signal strength parameter $\mu_{off-shell}$, the multiplicative factor applied to the theoretical signal production cross section, and $\hat{\theta}$, a set of nuisance parameters that encode the effects of systematic uncertainties on the expected signal and background contributions, described in Sec. 4.5.5. Nuisance parameters are constrained using either Gaussian or log-normal terms, based on independent studies.

Figure 5.3 shows the likelihood scan for $\mu_{off-shell}$ for the $\ell\ell\nu\nu$ channel, with and without systematic uncertainties. NLO QCD $m^{ZZ}$ dependent $K$-factors are applied to each individual $gg \to ZZ$ process and an additional NNLO/NLO QCD $K$-factor of 1.2 is also applied, as described in Sec. 4.3.1. The corresponding Observed(Expected) 95% CL upper limit is 5.7(4.5).

**Nuisance parameter pulls and rankings** As mentioned in Sec. 5.2 the impact of systematic uncertainties on the result is performed through the study of the effects of NPs, $\hat{\theta}$, on the fit. All the various systematic uncertainties in the $\ell\ell\nu\nu$ analysis are listed in Table 5.3 including a short description of the various contributions.

A critical test to check the stability and the behaviour of the fit is represented by the pull studies of the NPs. The pull of a NP is defined as the difference between the estimator value, $\hat{\theta}$, and the nominal NP value, $\theta_0$, normalized by the constraint on the nominal NP, $\Delta\theta$, which is calculated in the fit. The pull distribution is expected to follow a standard Gaussian centred in 0 with unit width. Departures from the expected behaviour need to be investigated. Pulls and constraints for the $\ell\ell\nu\nu$ analysis are shown in Fig. 5.4 as black dots for the top ranked parametrized NPs. All the top ranked NPs have pulls which are compatible with the expected value within the fitted uncertainties. The lower $x$-axis shows the NP pulls.

Another powerful test ranks the systematic uncertainties according to their im-

| Description | Systematic uncertainty name |
|---|---|
| Electron identification and reconstruction | ATLAS_EG_RESOLUTION_ALL<br>alpha_EG_SCALE_ALL<br>alpha_EL_EFF_ID_TOTAL_1NPCOR_PLUS_UNCOR<br>alpha_EL_EFF_ISO_TOTAL_1NPCOR_PLUS_UNCOR<br>alpha_EL_EFF_RECO_TOTAL_1NPCOR_PLUS_UNCOR<br>alpha_EL_EFF_Trigger_TOTAL_1NPCOR_PLUS_UNCOR |
| Muon identification and reconstruction | ATLAS_MUON_EFF_STAT<br>alpha_MUON_EFF_SYS<br>alpha_MUON_ID<br>alpha_MUON_ISO_STAT<br>alpha_MUON_ISO_SYS<br>alpha_MUON_MS<br>alpha_MUON_SAGITTA_RESBIAS<br>alpha_MUON_SAGITTA_RHO<br>alpha_MUON_SCALE<br>alpha_MUON_TTVA_STAT<br>alpha_MUON_TTVA_SYS<br>alpha_MUON_EFF_TrigStatUncertainty<br>alpha_MUON_EFF_TrigSystUncertainty |
| $b$-jet reconstruction | alpha_FT_EFF_B_systematics<br>alpha_FT_EFF_C_systematics<br>alpha_FT_EFF_Light_systematics<br>alpha_FT_EFF_extrapolation__1<br>alpha_FT_EFF_extrapolation_from_charm |
| jet reconstruction | alpha_JET_EtaIntercalibration_NonClosure<br>alpha_JET_GroupedNP_1<br>alpha_JET_GroupedNP_2<br>alpha_JET_GroupedNP_3<br>alpha_JET_JER_SINGLE_NP<br>alpha_JET_JvtEfficiency |
| $E_T^{miss}$ reconstruction | alpha_MET_SoftTrk_ResoPara<br>alpha_MET_SoftTrk_ResoPerp<br>alpha_MET_SoftTrk_Scale |
| Pile-up reconstruction | alpha_ATLAS_PRW_DATASF |
| Luminosity | ATLAS_LUMI |
| Theoretical corrections and PDFs | alpha_HOEW_QCD<br>alpha_PDF_gg_syst<br>alpha_NLOZZPDF<br>alpha_HOQCD_scale_gg_syst<br>alpha_NLOZZQCD<br>alpha_PS_qq_syst |
| $Z + jets$-background strategy | alpha_ATLAS_Norm_llee_Zjet_OffShell<br>alpha_ATLAS_Norm_llmumu_Zjet_OffShell<br>alpha_ZjetsShape<br>alpha_ZjetsStat<br>alpha_ZjetsSys |
| $e\mu$-background strategy | alpha_EMUShape<br>alpha_EMUStat<br>alpha_EMUSys |
| $WZ$-background strategy | alpha_WZScaleStat<br>alpha_WZScaleSys |

Table 5.3: List of systematic uncertainties in the $\ell\ell\nu\nu$ analysis, as from the $\ell\ell\nu\nu$ workspace.

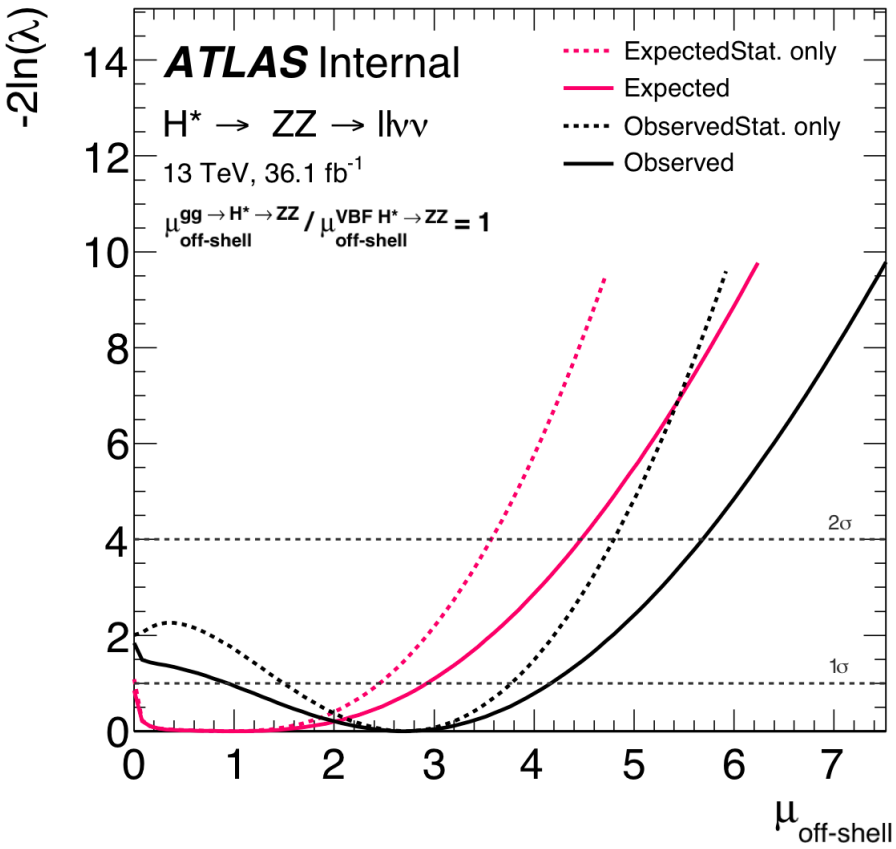


Figure 5.3: Scan of the negative log-likelihood, $-2ln(\lambda)$, as function of $\mu_{off-shell}$ for the $\ell\ell\nu\nu$ channel in both data (black) and simulation (red) with NLO QCD $m^{ZZ}$ dependent $K$-factors applied to each individual $gg \to ZZ$ process and an additional NNLO/NLO QCD $K$-factor of 1.2, as described in Sec. 4.3.1. The cross point of the $2\sigma$ line with the likelihood scan curve gives the 95% CL upper limit on $\mu_{off-shell}$. The dotted line shows the scan when only the statistical uncertainty is considered, while the solid line shows the impact of the systematic uncertainties on the result. The ratio of the ggF and VBF processes is assumed to have the SM value.

pact on the final result, the fitted value of the signal strength $\hat{\mu}$. This NP ranking is obtained by performing an iteration of the fit for each systematic uncertainty, fixing the corresponding NP to the fitted value $\hat{\theta}$ from the baseline fit, shifted up or down by its fitted uncertainty, $\pm\sigma$. All the remaining parameters are allowed to vary, in order to properly account for correlations between the systematic uncertainties. The magnitude of the fitted signal strength $\hat{\mu}$ is then compared to the baseline Likelihood fit giving a measurement of the impact of the NP (held fixed

or under consideration) on the signal strength. This is reported in Fig. 5.4 for the $\ell\ell\nu\nu$ analysis, in the the upper $x$-axis. Systematics are neglected if their effect is smaller than 1%. The leading systematic uncertainties are mainly from theoretical predictions: the QCD scale uncertainties for the $q\bar{q} \to ZZ$ and $gg \to ZZ$ processes. When fitting to the observed data, the $q\bar{q} \to ZZ$ QCD scale uncertainty nuisance parameter (`NLOZZQCD`) is pulled positive, due to an insignificant excess in data in the $2\mu 2\nu$ channel at about $m_T^{ZZ} = 500$ GeV, as shown in Fig. 5.2(b). This excess is not confirmed by the $2e2\nu$ search.

### 5.3.2 Extraction of Off-shell Couplings in the $4\ell$ Analysis

The Higgs off-shell analysis is also performed in the $H^* \to ZZ \to 4\ell$ channel. In this channel, a binned maximum-likelihood fit to the Matrix-Element-Based discriminant (ME) is performed to extract the limits on $\mu_{off-shell}$. The analysis strategy was described in Sec. 4.4, along with the observed and expected distributions of $m_{4\ell}$ and of the ME-discriminant, both shown in Figure 4.10. The Signal Region yield is reported in Table 5.1, along with the corresponding yields for the $\ell\ell\nu\nu$ analysis. The likelihood fit model accounts for signal and background processes, including $gg \to (H^* \to) ZZ$, VBF $(H^* \to)ZZ$, $q\bar{q} \to ZZ$ and all the other backgrounds reported in the $4\ell$ column of Table 5.1. The $gg \to (H^* \to) ZZ$ process includes the signal $gg \to H^* \to ZZ$, the continuum background $gg \to ZZ$ and the interference between the two. The probability density function of $gg \to ZZ$ and VBF $ZZ$ can be parametrized as a function of $\mu_{off-shell}$, as described in Sec. 4.3.3 and a binned likelihood function is constructed as a product of Poisson probability terms over all the bins of the fit templates considered.

Figure 5.5 shows the likelihood scan on $\mu_{off-shell}$ for the $4\ell$ channel, with and without systematic uncertainties. NLO QCD $m^{ZZ}$ dependent $K$-factors are applied to each individual $gg \to ZZ$ process and an additional NNLO/NLO QCD $K$-factor of 1.2 is also applied, as described in Sec. 4.3.1. The corresponding Observed(Expected) 95% CL upper limit is 4.7(4.3).

**Nuisance parameter pulls and rankings** Similar to the $\ell\ell\nu\nu$ channel, pull studies for the $4\ell$ channel are shown in Fig. 5.6. All the top ranked NPs have pulls which are compatible with the expected value within the fitted uncertainties.

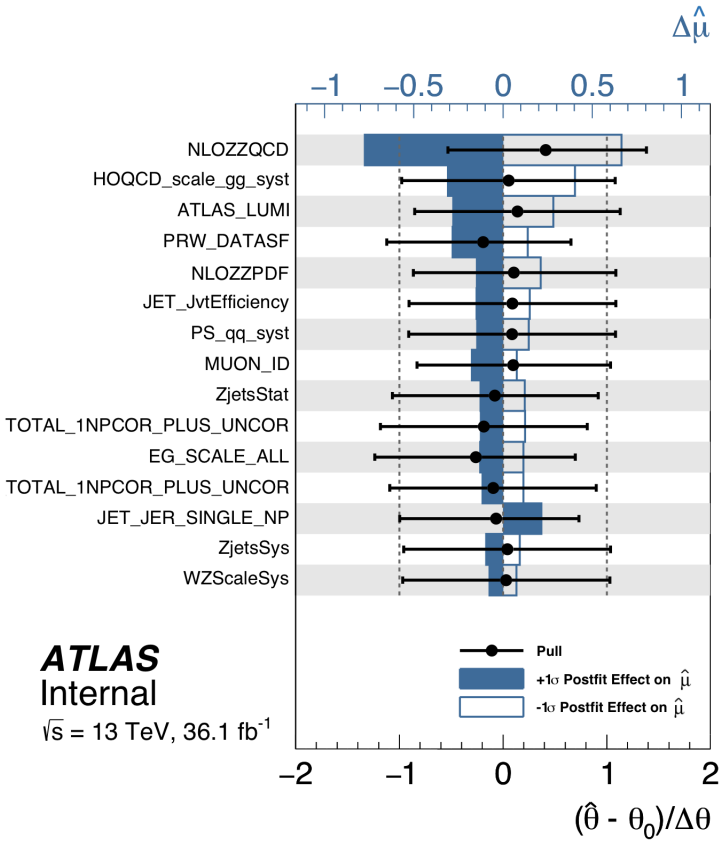


Figure 5.4: Impact of systematic uncertainties on the fitted signal-strength parameter $\hat{\mu}$ in the $\ell\ell\nu\nu$ channel. The systematic uncertainties are ranked in descending order of their impact on $\hat{\mu}$ on the $y$-axis. The boxes show the variations of $\hat{\mu}$ - they refer to the upper $x$-axis - when fixing the corresponding individual nuisance parameter $\theta$ to its post-fit value $\hat{\theta}$ modified upwards or downwards by its post-fit uncertainty, and repeating the fit. The blue and uncoloured boxes correspond to the upwards and downwards variations, respectively. Dots with error bars refer to the lower $x$-axis and show the deviations of the fitted nuisance parameters $\hat{\theta}$ from their nominal values $\theta_0$, expressed in terms of standard deviations with respect to their nominal uncertainties $\Delta\theta$. The associated error bars show the post-fit uncertainties of the nuisance parameters, relative to their nominal uncertainties. Systematics are neglected if their effect is smaller than 1%.

The leading systematic uncertainties are mainly from theoretical predictions: the QCD scale uncertainties for the $q\bar{q} \to ZZ$ and $gg \to ZZ$ processes. When fitting to the observed data, the $q\bar{q} \to ZZ$ QCD scale uncertainty nuisance parameter (`HOQCD_scale_syst`) is pulled positive, due to a couple of insignificant excesses in

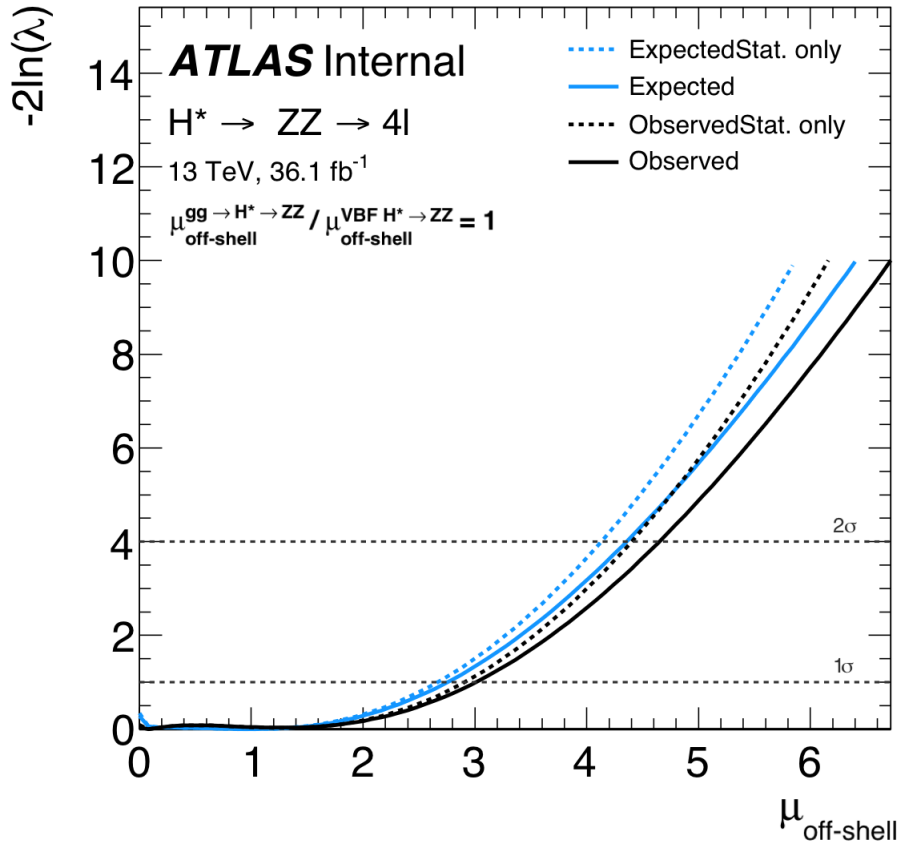


Figure 5.5: Scan of the negative log-likelihood, $-2ln(\lambda)$, as function of $\mu_{off-shell}$ for the $4\ell$ channel in both data (black) and simulation (blue) with NLO QCD $m^{ZZ}$ dependent $K$-factors applied to each individual $gg \to ZZ$ process and an additional NNLO/NLO QCD $K$-factor of 1.2, as described in Sec. 4.3.1. The cross point of the $2\sigma$ line with the likelihood scan curve gives the 95% CL upper limit on $\mu_{off-shell}$. The dotted line shows the scan when only the statistical uncertainty is considered, while the solid line shows the impact of the systematic uncertainties on the result. The ratio of the ggF and VBF processes is assumed to have the SM value.

data in the $4\ell$ channel at about $m_{4\ell} = 400$ GeV and $m_{4\ell} = 650$ GeV, as shown in Fig. 4.10(a). They are both excluded at 95% CL by the $\ell\ell\nu\nu$ analysis which is more sensitive in this mass range.

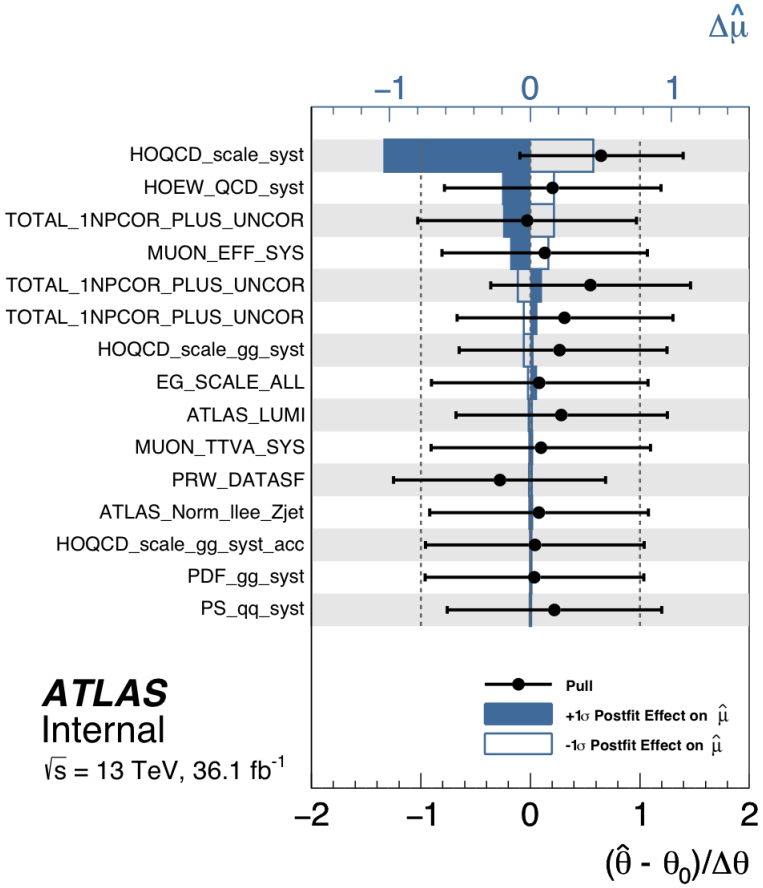


Figure 5.6: Impact of systematic uncertainties on the fitted signal-strength parameter $\hat{\mu}$ in the $4\ell$ channel. The systematic uncertainties are ranked in descending order of their impact on $\hat{\mu}$ on the $y$-axis. The boxes show the variations of $\hat{\mu}$ - they refer to the upper $x$-axis - when fixing the corresponding individual nuisance parameter $\theta$ to its post-fit value $\hat{\theta}$ modified upwards or downwards by its post-fit uncertainty, and repeating the fit. The blue and uncoloured boxes correspond to the upwards and downwards variations, respectively. Dots with error bars refer to the lower $x$-axis and show the deviations of the fitted nuisance parameters $\hat{\theta}$ from their nominal values $\theta_0$, expressed in terms of standard deviations with respect to their nominal uncertainties $\Delta\theta$. The associated error bars show the post-fit uncertainties of the nuisance parameters, relative to their nominal uncertainties. Systematics are neglected if their effect is smaller than 1%.

### 5.3.3 Combination with the $4\ell$ Channel

By combining the two analyses, $4\ell$ and $2\ell 2\nu$, the sensitivity to $\mu_{off-shell}$ can be improved. The combination procedure requires a simultaneous fit between the Signal

Regions of both channels. The likelihood function for the combination is the product of the Poisson likelihoods of the individual channels. Technically, the procedure for the channel combination is implemented with RooFit [194] and RooStats [195]. The combination must account for the correlation of systematic uncertainties. Uncorrelated uncertainties are applied as in Eq. 5.8 for each channel. A correlated uncertainty is modeled in the combined fit by using a common NP. These correlated NPs are thus assumed to have a 100% correlation. Because of the large number of systematic uncertainties to be considered, certain NPs with very small impact on the normalization are neglected in the final combination. A complete description of the systematic uncertainties was given in Sec. 4.5.5.2. Here, just the major ones are repeated focusing more on the correlation among the channels. The main systematic uncertainties originate from the theory uncertainties on the $gg \to (H^* \to)ZZ$ (including signal and interference contributions) and $q\bar{q} \to ZZ$ processes. The uncertainty in the $K$-factors due to the NLO QCD scale uncertainty is 10-20% as a function of $m_{ZZ}$ for the $gg$-initiated $ZZ$ processes in the high-mass region under study, and ranges from 5% to 10% as a function of $m_{ZZ}$ for the $q\bar{q} \to ZZ$ background. The QCD scale uncertainties and the PDF uncertainties are treated as correlated among the $gg$-initiated $ZZ$ processes, and uncorrelated with the $q\bar{q}$-initiated $ZZ$ processes. Where appropriate, the experimental systematic uncertainties are also treated as correlated. However, they are found to have a very small impact on the final combined limit. The detailed nuisance parameter correlation scheme can be found in Table 5.4.

The likelihood scan as a function of $\mu_{off-shell}$ for the combined $4\ell{+}\ell\ell\nu\nu$ channel is shown in Fig. 5.7 with and without the contribution of systematic uncertainties. NLO QCD $m^{ZZ}$ dependent $K$-factors are applied to each individual $gg \to ZZ$ process and an additional NNLO/NLO QCD $K$-factor of 1.2 is also applied, as described in Sec. 4.3.1. The corresponding Observed(Expected) 95% CL upper limit is 4.0(3.5). As a result of the small data excesses observed in the off-shell region, the observed limits on $\mu_{off-shell}$ are less stringent than the expected ones.

**Nuisance parameter pulls and rankings** Similar to the individual channels, pull studies for the combined $4\ell{+}\ell\ell\nu\nu$ channel are shown in Fig. 5.8. All the top ranked NPs have pulls which are compatible with the expected value within the fitted uncertainties. Consistent with the individual channels, the leading systematic

| Systematic name - Combined | Systematic name - $4\ell$ | Systematic name - $\ell\ell\nu\nu$ |
|---|---|---|
| ATLAS_EG_RESOLUTION_ALL | alpha_EG_RESOLUTION_ALL | alpha_EG_RESOLUTION_ALL |
| ATLAS_EG_SCALE_ALL | alpha_EG_SCALE_ALL | alpha_EG_SCALE_ALL |
| ATLAS_EL_EFF_ID_TOTAL_1NPCOR_PLUS_UNCOR | alpha_EL_EFF_ID_TOTAL_1NPCOR_PLUS_UNCOR | alpha_EL_EFF_ID_TOTAL_1NPCOR_PLUS_UNCOR |
| ATLAS_EL_EFF_ISO_TOTAL_1NPCOR_PLUS_UNCOR | alpha_EL_EFF_Iso_TOTAL_1NPCOR_PLUS_UNCOR | alpha_EL_EFF_Iso_TOTAL_1NPCOR_PLUS_UNCOR |
| ATLAS_EL_EFF_RECO_TOTAL_1NPCOR_PLUS_UNCOR | alpha_EL_EFF_Reco_TOTAL_1NPCOR_PLUS_UNCOR | alpha_EL_EFF_Reco_TOTAL_1NPCOR_PLUS_UNCOR |
| ATLAS_HOEW_QCD | alpha_HOEW_QCD_syst | |
| ATLAS_LUMI | alpha_ATLAS_LUMI | alpha_ATLAS_LUMI |
| ATLAS_MUON_EFF_STAT | alpha_MUON_EFF_STAT | alpha_MUON_EFF_STAT |
| ATLAS_MUON_EFF_SYS | alpha_MUON_EFF_SYS | alpha_MUON_EFF_SYS |
| ATLAS_MUON_ID | alpha_MUON_ID | alpha_MUON_ID |
| ATLAS_MUON_ISO_STAT | | alpha_MUON_ISO_STAT |
| ATLAS_MUON_ISO_SYS | alpha_MUON_ISO_SYS | alpha_MUON_ISO_SYS |
| ATLAS_MUON_MS | alpha_MUON_MS | alpha_MUON_MS |
| ATLAS_MUON_SAGITTA_RESBIAS | alpha_MUON_SAGITTA_RESBIAS | |
| ATLAS_MUON_SAGITTA_RHO | alpha_MUON_SAGITTA_RHO | |
| ATLAS_MUON_SCALE | alpha_MUON_SCALE | alpha_MUON_SCALE |
| ATLAS_MUON_TTVA_STAT | alpha_MUON_TTVA_STAT | alpha_MUON_TTVA_STAT |
| ATLAS_MUON_TTVA_SYS | alpha_MUON_TTVA_SYS | alpha_MUON_TTVA_SYS |
| ATLAS_PRW_DATASF | alpha_PRW_DATASF | alpha_PRW_DATASF |
| ATLAS_pdf_ggZZ | alpha_PDF_gg_syst | |
| ATLAS_pdf_qqZZ | alpha_PDF_qq_syst | alpha_NLOZZPDF |
| ATLAS_scale_ggZZ_offShell | alpha_HOQCD_scale_gg_syst | alpha_HOQCD_scale_gg_syst |
| ATLAS_scale_qqZZ | alpha_HOQCD_scale_syst | alpha_NLOZZQCD |
| ATLAS_shower_qqZZ | alpha_PS_qq_syst | alpha_PS_qq_syst |
| auto_alpha_ATLAS_Norm_llee_Zjet_OffShell | alpha_ATLAS_Norm_llee_Zjet | |
| auto_alpha_ATLAS_Norm_llmumu_Zjet_OffShell | alpha_ATLAS_Norm_llmumu_Zjet | |
| auto_alpha_EL_EFF_Trigger_TOTAL_1NPCOR_PLUS_UNCOR_llvv | | alpha_EL_EFF_Trigger_TOTAL_1NPCOR_PLUS_UNCOR |
| auto_alpha_EMUShape_llvv | | alpha_EMUShape |
| auto_alpha_EMUStat_llvv | | alpha_EMUStat |
| auto_alpha_EMUSys_llvv | | alpha_EMUSys |
| auto_alpha_FT_EFF_B_systematics_llvv | | alpha_FT_EFF_B_systematics |
| auto_alpha_FT_EFF_C_systematics_llvv | | alpha_FT_EFF_C_systematics |
| auto_alpha_FT_EFF_Light_systematics_llvv | | alpha_FT_EFF_Light_systematics |
| auto_alpha_FT_EFF_extrapolation__1_llvv | | alpha_FT_EFF_extrapolation__1 |
| auto_alpha_FT_EFF_extrapolation_from_charm_llvv | | alpha_FT_EFF_extrapolation_from_charm |
| auto_alpha_JET_EtaIntercalibration_NonClosure_llvv | | alpha_JET_EtaIntercalibration_NonClosure |
| auto_alpha_JET_GroupedNP_1_llvv | | alpha_JET_GroupedNP_1 |
| auto_alpha_JET_GroupedNP_2_llvv | | alpha_JET_GroupedNP_2 |
| auto_alpha_JET_GroupedNP_3_llvv | | alpha_JET_GroupedNP_3 |
| auto_alpha_JET_JER_SINGLE_NP_llvv | | alpha_JET_JER_SINGLE_NP |
| auto_alpha_JET_JvtEfficiency_llvv | | alpha_JET_JvtEfficiency |
| auto_alpha_MET_SoftTrk_ResoPara_llvv | | alpha_MET_SoftTrk_ResoPara |
| auto_alpha_MET_SoftTrk_ResoPerp_llvv | | alpha_MET_SoftTrk_ResoPerp |
| auto_alpha_MET_SoftTrk_Scale_llvv | | alpha_MET_SoftTrk_Scale |
| auto_alpha_MUON_EFF_TrigStatUncertainty_llvv | | alpha_MUON_EFF_TrigStatUncertainty |
| auto_alpha_MUON_EFF_TrigSystUncertainty_llvv | | alpha_MUON_EFF_TrigSystUncertainty |
| auto_alpha_WZScaleStat_llvv | | alpha_WZScaleStat |
| auto_alpha_WZScaleSys_llvv | | alpha_WZScaleSys |
| auto_alpha_ZjetsShape_llvv | | alpha_ZjetsShape |
| auto_alpha_ZjetsStat_llvv | | alpha_ZjetsStat |
| auto_alpha_ZjetsSys_llvv | | alpha_ZjetsSys |

Table 5.4: Systematic correlation scheme for the workspace of the combined $4\ell$+$\ell\ell\nu\nu$ channel. The list includes the names for systematic uncertainties used in the individual $4\ell$ and $\ell\ell\nu\nu$ workspaces and in the combined $4\ell$+$\ell\ell\nu\nu$ workspace.

uncertainties are mainly from theoretical predictions, i.e. the QCD scale uncertainties for the $q\bar{q} \to ZZ$ process.

### 5.3.4 Constraints on the Higgs Boson Total Width

To extract the final result on the Higgs boson total width constraint, the off-shell analyses of both the $ZZ \to 4\ell$ and $ZZ \to \ell\ell\nu\nu$ final states are combined with the on-shell $ZZ^* \to 4\ell$ analysis. The combination assumptions were described at the beginning of this section in the context of the $\Gamma_H$ *interpretation*. When combining with the on-shell results, the experimental and theoretical uncertainties are properly considered. The PDF uncertainties and uncertainties from higher-order QCD corrections applied to the $q\bar{q} \to ZZ$ process are considered correlated between the

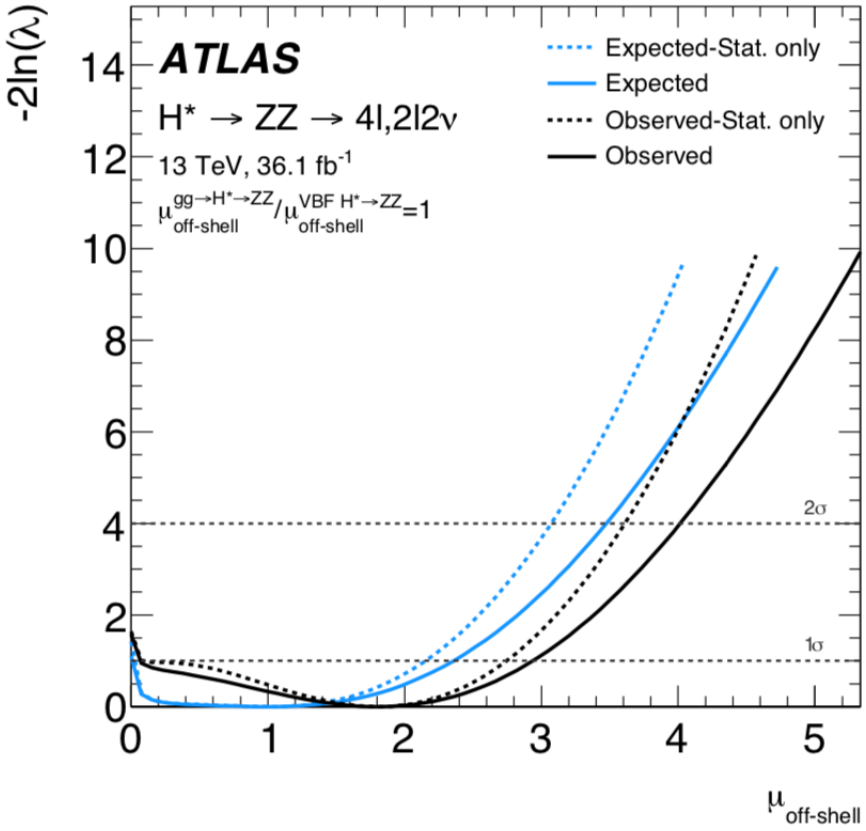


Figure 5.7: Scan of the negative log-likelihood, $-2ln(\lambda)$, as function of $\mu_{off-shell}$ for the combined $4\ell+\ell\ell\nu\nu$ channel in both data (black) and simulation (blue) with NLO QCD $m^{ZZ}$ dependent $K$-factors applied to each individual $gg \to ZZ$ process and an additional NNLO/NLO QCD $K$-factor of 1.2, as described in Sec. 4.3.1. The cross point of the $2\sigma$ line with the likelihood scan curve gives the 95% CL upper limit on $\mu_{off-shell}$. The dotted line shows the scan when only the statistical uncertainty is considered, while the solid line shows the impact of the systematic uncertainties on the result. The ratio of the ggF and VBF processes is assumed to have the SM value.

on-shell and off-shell measurements. Given the different theoretical computations, the corresponding uncertainties are considered uncorrelated for the $gg$-initiated $ZZ$ processes between the on-shell and off-shell measurements, and the impact of such a correlation effect is found to be small. In addition to the main theoretical uncertainties, the common experimental systematic uncertainties are treated as correlated between the on-shell and off-shell measurements. However, they are found to have

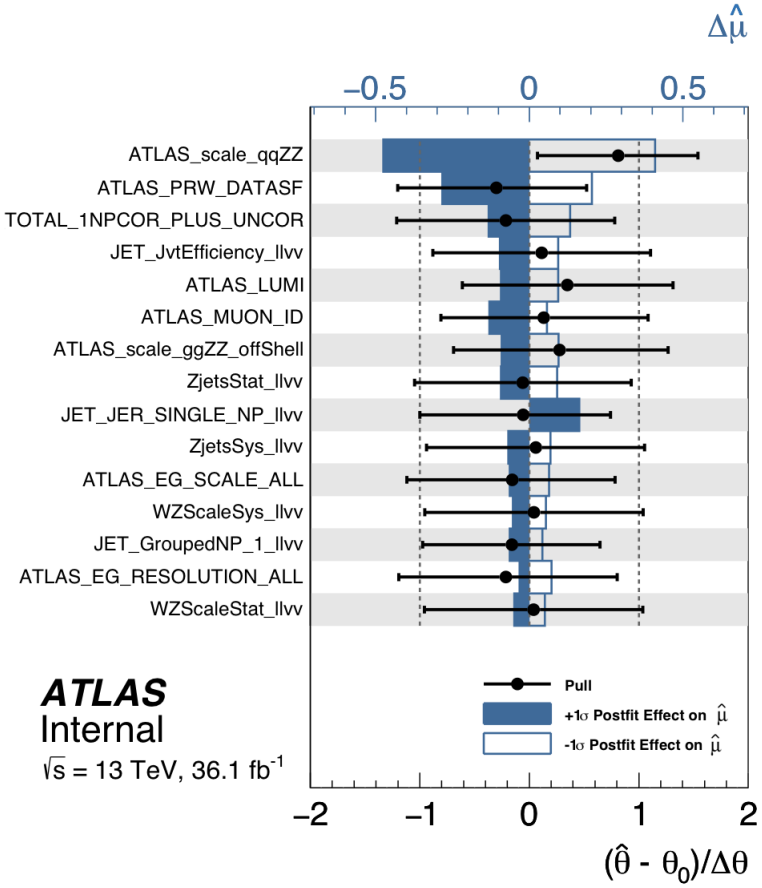


Figure 5.8: Impact of systematic uncertainties on the fitted signal-strength parameter $\hat{\mu}$ in the combined $4\ell$+$\ell\ell\nu\nu$ channel. The systematic uncertainties are ranked in descending order of their impact on $\hat{\mu}$ on the $y$-axis. The boxes show the variations of $\hat{\mu}$ - they refer to the upper $x$-axis - when fixing the corresponding individual nuisance parameter $\theta$ to its post-fit value $\hat{\theta}$ modified upwards or downwards by its post-fit uncertainty, and repeating the fit. The blue and uncoloured boxes correspond to the upwards and downwards variations, respectively. Dots with error bars refer to the lower $x$-axis and show the deviations of the fitted nuisance parameters $\hat{\theta}$ from their nominal values $\theta_0$, expressed in terms of standard deviations with respect to their nominal uncertainties $\Delta\theta$. The associated error bars show the post-fit uncertainties of the nuisance parameters, relative to their nominal uncertainties. Systematics are neglected if their effect is smaller than 1%.

a very small impact on the final combined limit on $\Gamma_H$. The detailed nuisance parameter correlation scheme between the on- and off-shell analyses can be found in Table 5.5.

| Systematic name - On- and Off-shell Combined | Systematic name - $4\ell$ Off-shell | Systematic name - $4\ell$ On-shell | Systematic name - $\ell\ell\nu\nu$ Off-shell |
|---|---|---|---|
| ATLAS_EG_RESOLUTION_ALL | alpha_EG_RESOLUTION_ALL | ATLAS_EG_RESOLUTION_ALL | alpha_EG_RESOLUTION_ALL |
| ATLAS_EG_SCALE_ALL | alpha_EG_SCALE_ALL | ATLAS_EG_SCALE_ALLCORR | alpha_EG_SCALE_ALL |
| ATLAS_EL_EFF_ID_TOTAL_1NPCOR_PLUS_UNCOR | alpha_EL_EFF_ID_TOTAL_1NPCOR_PLUS_UNCOR | | alpha_EL_EFF_ID_TOTAL_1NPCOR_PLUS_UNCOR |
| ATLAS_EL_EFF_ISO_TOTAL_1NPCOR_PLUS_UNCOR | alpha_EL_EFF_Iso_TOTAL_1NPCOR_PLUS_UNCOR | ATLAS_EL_EFF_ISO_TOTAL_1NPCOR_PLUS_UNCOR | alpha_EL_EFF_Iso_TOTAL_1NPCOR_PLUS_UNCOR |
| ATLAS_EL_EFF_RECO_TOTAL_1NPCOR_PLUS_UNCOR | alpha_EL_EFF_Reco_TOTAL_1NPCOR_PLUS_UNCOR | ATLAS_EL_EFF_RECO_TOTAL_1NPCOR_PLUS_UNCOR | alpha_EL_EFF_Reco_TOTAL_1NPCOR_PLUS_UNCOR |
| ATLAS_HOEW | | ATLAS_HOEW | |
| ATLAS_HOEW_QCD | alpha_HOEW_QCD_syst | ATLAS_HOEW_QCD | |
| ATLAS_LUMI | alpha_ATLAS_LUMI | Luminosity | alpha_ATLAS_LUMI |
| ATLAS_MUON_EFF_STAT | alpha_MUON_EFF_STAT | ATLAS_MUON_EFF_STAT | alpha_MUON_EFF_STAT |
| ATLAS_MUON_EFF_SYS | alpha_MUON_EFF_SYS | ATLAS_MUON_EFF_SYS | alpha_MUON_EFF_SYS |
| ATLAS_MUON_EFF_SYS_LOWPT | | ATLAS_MUON_EFF_SYS_LOWPT | |
| ATLAS_MUON_ID | alpha_MUON_ID | ATLAS_MUON_ID | alpha_MUON_ID |
| ATLAS_MUON_ISO_STAT | | ATLAS_MUON_ISO_STAT | alpha_MUON_ISO_STAT |
| ATLAS_MUON_ISO_SYS | alpha_MUON_ISO_SYS | ATLAS_MUON_ISO_SYS | alpha_MUON_ISO_SYS |
| ATLAS_MUON_MS | alpha_MUON_MS | ATLAS_MUON_MS | alpha_MUON_MS |
| ATLAS_MUON_SAGITTA_RESBIAS | alpha_MUON_SAGITTA_RESBIAS | ATLAS_MUON_SAGITTA_RESBIAS | |
| ATLAS_MUON_SAGITTA_RHO | alpha_MUON_SAGITTA_RHO | ATLAS_MUON_SAGITTA_RHO | |
| ATLAS_MUON_SCALE | alpha_MUON_SCALE | ATLAS_MUON_SCALE | alpha_MUON_SCALE |
| ATLAS_MUON_TTVA_STAT | alpha_MUON_TTVA_STAT | ATLAS_MUON_TTVA_STAT | alpha_MUON_TTVA_STAT |
| ATLAS_MUON_TTVA_SYS | alpha_MUON_TTVA_SYS | | alpha_MUON_TTVA_SYS |
| ATLAS_PRW_DATASF | alpha_PRW_DATASF | ATLAS_PRW_DATASF | alpha_PRW_DATASF |
| ATLAS_pdf_ggZZ | alpha_PDF_gg_syst | ATLAS_pdf_ggZZ | |
| ATLAS_pdf_qqZZ | alpha_PDF_qq_syst | ATLAS_pdf_qqZZ | alpha_NLOZZPDF |
| ATLAS_scale_ggZZ | | ATLAS_scale_ggZZ | |
| ATLAS_scale_ggZZ_offShell | alpha_HOQCD_scale_gg_syst | | alpha_HOQCD_scale_gg_syst |
| ATLAS_scale_qqZZ | alpha_HOQCD_scale_syst | ATLAS_scale_qqZZ | alpha_NLOZZQCD |
| ATLAS_shower_qqZZ | alpha_PS_qq_syst | | alpha_PS_qq_syst |
| auto_ATLAS_BR_HZZSig_XS | | ATLAS_BR_HZZSig | |
| auto_ATLAS_EG_SCALE_E4SCINTILLATOR_XS | | ATLAS_EG_SCALE_E4SCINTILLATOR | |
| auto_ATLAS_EG_SCALE_LARCALIB_EXTRA2015PRE_XS | | ATLAS_EG_SCALE_LARCALIB_EXTRA2015PRE | |
| auto_ATLAS_EL_EFF_ID_CorrUncertaintyNP11_XS | | ATLAS_EL_EFF_ID_CorrUncertaintyNP11 | |
| auto_ATLAS_EL_EFF_ID_CorrUncertaintyNP12_XS | | ATLAS_EL_EFF_ID_CorrUncertaintyNP12 | |
| auto_ATLAS_EL_EFF_ID_CorrUncertaintyNP13_XS | | ATLAS_EL_EFF_ID_CorrUncertaintyNP13 | |
| auto_ATLAS_EL_EFF_ID_CorrUncertaintyNP14_XS | | ATLAS_EL_EFF_ID_CorrUncertaintyNP14 | |
| auto_ATLAS_EL_EFF_ID_CorrUncertaintyNP9_XS | | ATLAS_EL_EFF_ID_CorrUncertaintyNP9 | |
| auto_ATLAS_EL_EFF_ID_SIMPLIFIED_UncorrUncertaintyNP10_XS | | ATLAS_EL_EFF_ID_SIMPLIFIED_UncorrUncertaintyNP10 | |
| auto_ATLAS_EL_EFF_ID_SIMPLIFIED_UncorrUncertaintyNP11_XS | | ATLAS_EL_EFF_ID_SIMPLIFIED_UncorrUncertaintyNP11 | |
| auto_ATLAS_EL_EFF_ID_SIMPLIFIED_UncorrUncertaintyNP1_XS | | ATLAS_EL_EFF_ID_SIMPLIFIED_UncorrUncertaintyNP1 | |
| auto_ATLAS_EL_EFF_ID_SIMPLIFIED_UncorrUncertaintyNP2_XS | | ATLAS_EL_EFF_ID_SIMPLIFIED_UncorrUncertaintyNP2 | |
| auto_ATLAS_FT_EFF_Eigen_C_0_XS | | ATLAS_FT_EFF_Eigen_C_0 | |
| auto_ATLAS_HiggsMassVariation_XS | | ATLAS_HiggsMassVariation | |
| auto_ATLAS_ShowerCKKW_qqZZ_XS | | ATLAS_ShowerCKKW_qqZZ | |
| auto_ATLAS_ShowerQSF_qqZZ_XS | | ATLAS_ShowerQSF_qqZZ | |
| auto_ATLAS_Shower_Sig_XS | | ATLAS_Shower_Sig | |
| auto_ATLAS_SignalComposition_VBF_XS | | ATLAS_SignalComposition_VBF | |
| auto_ATLAS_SignalComposition_WH_XS | | ATLAS_SignalComposition_WH | |
| auto_ATLAS_SignalComposition_ZH_XS | | ATLAS_SignalComposition_ZH | |
| auto_ATLAS_SignalComposition_bbH_XS | | ATLAS_SignalComposition_bbH | |
| auto_ATLAS_SignalComposition_ggH_XS | | ATLAS_SignalComposition_ggH | |
| auto_ATLAS_SignalComposition_ttH_XS | | ATLAS_SignalComposition_ttH | |
| auto_ATLAS_ZJET_llee_sys_XS | | ATLAS_ZJET_llee_sys | |
| auto_ATLAS_ZJET_llmumu_sys_XS | | ATLAS_ZJET_llmumu_sys | |
| auto_ATLAS_pdf_sig_gg_XS | | ATLAS_pdf_sig_gg | |
| auto_ATLAS_pdf_sig_qq_XS | | ATLAS_pdf_sig_qq | |
| auto_ATLAS_scale_sig_VBF_XS | | ATLAS_scale_sig_VBF | |
| auto_ATLAS_scale_sig_WH_XS | | ATLAS_scale_sig_WH | |
| auto_ATLAS_scale_sig_ZH_XS | | ATLAS_scale_sig_ZH | |
| auto_ATLAS_scale_sig_bbH_XS | | ATLAS_scale_sig_bbH | |
| auto_ATLAS_scale_sig_ggH_XS | | ATLAS_scale_sig_ggH | |
| auto_ATLAS_scale_sig_ttH_XS | | ATLAS_scale_sig_ttH | |
| auto_alpha_ATLAS_Norm_llee_Zjet_OffShell | alpha_ATLAS_Norm_llee_Zjet | | |
| auto_alpha_ATLAS_Norm_llmumu_Zjet_OffShell | alpha_ATLAS_Norm_llmumu_Zjet | | |
| auto_alpha_EL_EFF_Trigger_TOTAL_1NPCOR_PLUS_UNCOR_llvv | | | alpha_EL_EFF_Trigger_TOTAL_1NPCOR_PLUS_UNCOR |
| auto_alpha_EMUShape_llvv | | | alpha_EMUShape |
| auto_alpha_EMUStat_llvv | | | alpha_EMUStat |
| auto_alpha_EMUSys_llvv | | | alpha_EMUSys |
| auto_alpha_FT_EFF_B_systematics_llvv | | | alpha_FT_EFF_B_systematics |
| auto_alpha_FT_EFF_C_systematics_llvv | | | alpha_FT_EFF_C_systematics |
| auto_alpha_FT_EFF_Light_systematics_llvv | | | alpha_FT_EFF_Light_systematics |
| auto_alpha_FT_EFF_extrapolation_1_llvv | | | alpha_FT_EFF_extrapolation_1 |
| auto_alpha_FT_EFF_extrapolation_from_charm_llvv | | | alpha_FT_EFF_extrapolation_from_charm |
| auto_alpha_JET_EtaIntercalibration_NonClosure_llvv | | | alpha_JET_EtaIntercalibration_NonClosure |
| auto_alpha_JET_GroupedNP_1_llvv | | | alpha_JET_GroupedNP_1 |
| auto_alpha_JET_GroupedNP_2_llvv | | | alpha_JET_GroupedNP_2 |
| auto_alpha_JET_GroupedNP_3_llvv | | | alpha_JET_GroupedNP_3 |
| auto_alpha_JET_JER_SINGLE_NP_llvv | | | alpha_JET_JER_SINGLE_NP |
| auto_alpha_JET_JvtEfficiency_llvv | | | alpha_JET_JvtEfficiency |
| auto_alpha_MET_SoftTrk_ResoPara_llvv | | | alpha_MET_SoftTrk_ResoPara |
| auto_alpha_MET_SoftTrk_ResoPerp_llvv | | | alpha_MET_SoftTrk_ResoPerp |
| auto_alpha_MET_SoftTrk_Scale_llvv | | | alpha_MET_SoftTrk_Scale |
| auto_alpha_MUON_EFF_TrigStatUncertainty_llvv | | | alpha_MUON_EFF_TrigStatUncertainty |
| auto_alpha_MUON_EFF_TrigSystUncertainty_llvv | | | alpha_MUON_EFF_TrigSystUncertainty |
| auto_alpha_WZScaleStat_llvv | | | alpha_WZScaleStat |
| auto_alpha_WZScaleSys_llvv | | | alpha_WZScaleSys |
| auto_alpha_ZjetsShape_llvv | | | alpha_ZjetsShape |
| auto_alpha_ZjetsStat_llvv | | | alpha_ZjetsStat |
| auto_alpha_ZjetsSys_llvv | | | alpha_ZjetsSys |

Table 5.5: Systematic correlation scheme for the workspace of the on- and off-shell combination. The list includes the names for systematic uncertainties used in the individual off-shell $4\ell$ and $\ell\ell\nu\nu$ workspaces, the on-shell $4\ell$ workspace and the combined on- and off-shell workspace.

The likelihood scan as a function of the on-shell signal strength, $\mu_{on-shell}$, and of the $\Gamma_H/\Gamma_H^{SM}$ ratio when combining the on- and off-shell channels with and without the contribution of systematic uncertainties is shown in Fig. 5.9(a) and Fig. 5.9(b), respectively. Solid lines indicate the scan including systematic uncertainties, whereas dotted lines indicate the scan without systematic uncertainties. In the off-shell

production, NLO QCD $m^{ZZ}$ dependent $K$-factors are applied to each individual $gg \to ZZ$ process and an additional NNLO/NLO QCD $K$-factor of 1.2 is also applied, as described in Sec. 4.3.1. The best fit signal strength for the on-shell Higgs, $\mu_{on-shell}$ is found to be 1.25, slightly different from the measurement in the couplings analysis [193], which is $\mu_{on-shell} = 1.28^{+0.21}_{-0.19}$. The difference is due to the correlation of the NPs in the on- and off-shell combined fit. Due to the fact that the measured on-shell signal strength $\mu_{on-shell}$ is larger than one, the observed limit on $\Gamma_H/\Gamma_H^{SM}$ is smaller than the expected limit. The corresponding Observed(Expected) 95% CL upper limit is 3.5(3.7). The limit on $\Gamma_H/\Gamma_H^{SM}$ can be translated into a limit on the total width of the Higgs boson, leading to an Observed(Expected) 95% CL upper limit on the Higgs boson total width of 14.4(15.2) MeV[5].

**Nuisance parameter pulls and rankings** Similar to the $\mu_{off-shell}$ extraction, pull studies for the combined on-shell $4\ell$ channel and the off-shell $4\ell$ and $\ell\ell\nu\nu$ channels are shown in Fig. 5.10. All the top ranked NPs have pulls which are compatible with the expected value within the uncertainties. Consistent with what is observed in the individual channels, the leading systematic uncertainties are mainly from theoretical predictions, i.e. the QCD scale uncertainties for the off-shell $q\bar{q} \to ZZ$ and $gg \to ZZ$ processes. Theoretical uncertainties from the $\mu_{on-shell}$ analysis also play an important role, though.

### 5.3.5 $R_{gg}$ Interpretation

Similar to the $\Gamma_H$ *interpretation*, the off-shell analyses of both the $ZZ \to 4\ell$ and $ZZ \to \ell\ell\nu\nu$ final states are combined with the on-shell $ZZ^* \to 4\ell$ analysis to extract limits on $R_{gg}$. The combination assumptions were described at the beginning of this section when mentioning the $R_{gg}$ *interpretation*. When combining with the on-shell results, the experimental and theoretical uncertainties are properly correlated, as done in the $\Gamma_H$ *interpretation*.

The likelihood scan as a function of $R_{gg}$ when combining the on- and off-shell channels with and without the contribution of systematic uncertainties is shown in Fig. 5.11. In the off-shell production, NLO QCD $m^{ZZ}$ dependent $K$-factors are applied to each individual $gg \to ZZ$ process and an additional NNLO/NLO

[5]The value of the SM Higgs boson total width of 4.1 MeV at a mass of 125.1 GeV [43] is used to convert the limit $\Gamma_H/\Gamma_H^{SM}$ into the total width limit.

QCD $K$-factor of 1.2 is also applied, as described in Sec. 4.3.1. The corresponding Observed(Expected) 95% CL upper limit is 4.5(4.3).

### 5.3.6 $CL_s$ Limits

As an alternative to the likelihood scan, 95% CL upper limits can be derived using the $CL_s$ method described in Sec. 5.2 for all the parameters of interest, $\mu_{off-shell}$, $\Gamma_H/\Gamma_H^{SM}$ and $R_{gg}$. In more detail, one needs to evaluate the ratio of one-sided $p$-values: $CL_s\ (\mu) = p_\mu/(1\text{-}p_1)$ where $p_\mu$ is the $p$-value for testing a given $\mu = \mu_{off-shell}$ or $\mu = \Gamma_H/\Gamma_H^{SM}$ or $R_{gg}$ (the non-SM hypothesis) and $p_1$ is the $p$-value derived from the same test statistic under the SM hypothesis of $\mu_{off-shell} = 1$ in the first case and $\Gamma_H/\Gamma_H^{SM} = 1$ or $R_{gg} = 1$ in the other cases.

Results for the two individual analyses and their combination are reported in Table 5.6. These results are significantly improved compared to the Run-1 publication [61], the expected limit being about a factor two better.

Given the slight excess in data and the capability of the ME-based discriminant to differentiate the $q\bar{q} \to ZZ$ background and the $gg \to ZZ$ signal in the $4\ell$ channel, it is possible to leave free the normalization of the $q\bar{q} \to ZZ$ background in the profile likelihood fit rather than constraining it to the theoretical expectation degrading the upper limit by about 4% in the $4\ell$ channel.

If only the NLO $K$-factors are applied to the SM prediction of the $gg$-initiated $ZZ$ processes, without the additional NNLO/NLO $K$-factor of 1.2 (Sec. 4.3.1), the upper limits on $\mu_{off-shell}$ and $\Gamma_H/\Gamma_H^{SM}$ are about 10% less restrictive.

| Parameter of Interest | Channel | Observed | Expected | | |
|---|---|---|---|---|---|
| | | | Median | $\pm1\sigma$ | $\pm2\sigma$ |
| $\mu_{off-shell}$ | $4\ell$ | 4.5 | 4.3 | [3.3, 5.4] | [2.7, 7.1] |
| | $2\ell2\nu$ | 5.3 | 4.4 | [3.4, 5.5] | [2.8, 7.0] |
| | Combined | 3.8 | 3.4 | [2.7, 4.2] | [2.3, 5.3] |
| $\Gamma_H/\Gamma_H^{SM}$ | Combined | 3.5 | 3.7 | [2.9, 4.8] | [2.4, 6.5] |
| $R_{gg}$ | Combined | 4.3 | 4.1 | [3.3, 5.6] | [2.7, 8.2] |

Table 5.6: Summary of the 95% CL upper limits on $\mu_{off-shell}$, $\Gamma_H/\Gamma_H^{SM}$ and $R_{gg}$. Upper limits are evaluated using the $CL_s$ method. These results are obtained by applying the NLO QCD $K$-factors and an additional NNLO/NLO QCD $K$-factor of 1.2 to the off-shell Higgs production.

The impact of the various systematic uncertainties on the expected limit in the $\mu_{off-shell}$ fit are listed in Table 5.7. The values in this table were derived by fixing all the nuisance parameters associated with the systematic uncertainties to the values derived from the SM-conditional fit to the data, with the exception of the one under study. The uncertainties with the largest impact on the sensitivity of $\mu_{off-shell}$ are the theoretical uncertainties of the $gg$- and $q\bar{q}$-initiated $ZZ$ processes. Limits are derived using the $CL_s$ method.

| Systematic uncertainty | 95% CL upper limit on $\mu_{off-shell}$ | | |
|---|---|---|---|
| | $4\ell$ | $2\ell 2\nu$ | Combined |
| QCD scale $q\bar{q} \to ZZ$ | 4.2 | 3.9 | 3.2 |
| QCD scale $gg \to (H^* \to)ZZ$ | 4.2 | 3.6 | 3.1 |
| Luminosity | 4.1 | 3.5 | 3.1 |
| Remaining systematic uncertainties | 4.1 | 3.5 | 3.0 |
| All systematic uncertainties | 4.3 | 4.4 | 3.4 |
| No systematic uncertainties | 4.0 | 3.4 | 3.0 |

Table 5.7: The expected 95% CL upper limit on $\mu_{off-shell}$ with a ranked listing of the impact of the leading systematic uncertainty individually, comparing with no systematic uncertainty or all systematic uncertainties. The upper limits are evaluated using the $CL_s$ method. These results are obtained by applying the NLO QCD $K$-factors and an additional NNLO/NLO QCD $K$-factor of 1.2 to the off-shell Higgs production.

## 5.4 EFT Approach

In the previous sections of this Chapter the derivation of the limits on the Higgs boson total width exploiting the off-shell Higgs production have been described. However, it has been shown in [55] that the same off-shell dataset for the ggF production mode can be used to constrain new physics effects in the context of Effective Field Theory (EFT)[6]. In the absence of any indication of new light degrees of freedom below the TeV scale, the EFT approach claims that the effect of new physics can be easily parametrized in terms of higher dimensional operators for the SM fields. This approach provides a powerful and systematic way for controlling

[6]The description and the formalism used in this section closely follows [55].

deviations from SM expectations, organizing them as an expansion in powers of the ratio of the momentum over the new physics scale. Since the ggF off-shell production mode allows to probe the EFT at large momenta, it could help reveal the energy-dependence of the Higgs couplings controlled by higher-dimensional operators with extra derivatives. As explained in Sec. 4.2, this is one of the strongest assumptions when using the Higgs off-shell production to constrain the Higgs boson total width, i.e. the same couplings are assumed in the off-shell and on-shell regime even though the energies are different.

Historically, this is not the first time the off-shell production of a resonance is used to constrain effects of new physics. The off-shell production of the $Z$ boson at LEP2 complemented the on-shell $Z$-boson physics program of LEP1 bounding the $\mathcal{O}(p^4)$ dimension-6 operators [196], in addition to the $\mathcal{O}(p^2)$ dimension-6 operators already excluded at LEP1. Returning to the off-shell Higgs production, out of the eight $CP$-even dimension-6 operators uniquely testable by Higgs physics, five have already been bounded by the on-shell Higgs program at the LHC. The $H \to Z\gamma$ and the $pp \to t\bar{t}H$ channels are the golden channels to bound two extra dimension-6 operators that are still unconstrained. Since the $Z\gamma$ channel is currently out-of-reach at the LHC, additional and complementary ways to separate the long- and short-distance contributions to the $ggH$ vertex can be explored, as the off-shell Higgs production in ggF is able to break the couplings degeneracy enriching the current knowledge on the top Yukawa coupling.

The Higgs boson total width interpretation and the EFT approach applied to the off-shell dataset are mutually exclusive. In fact, in order to use the off-shell dataset to constrain the Higgs boson total width one needs to assume that there are no higher dimensional operators affecting either Higgs decays or production. Only under this assumption, it is possible to set a limit on the Higgs boson total width using the off-shell Higgs production. On the contrary, if one assumes that there is new physics affecting Higgs decays or production, then the off-shell dataset allows for bounding these additional dimension-6 operators, but not $\Gamma_H$. Also, for the $\Gamma_H$ interpretation it is assumed that variations of all the Higgs couplings are universal making the strategy model-dependent. The latter assumption is released in the context of the EFT approach, making the strategy model-independent.

**Formalism.** Assuming the Higgs boson to be part of a doublet of $SU(2)_L$, there are three relevant dimension-6 operators that should be tested at the LHC since they can affect the ggF production of the Higgs boson:

$$\mathcal{L}^{dim-6} = c_y \frac{y_t |H|^2 \bar{Q}_L \tilde{H} t_R}{v^2} + h.c. + \frac{c_g g_s^2 |H|^2 G_{\mu\nu} G^{\mu\nu}}{48\pi^2 v^2} + \frac{\tilde{c}_g g_s^2 |H|^2 G_{\mu\nu} \tilde{G}^{\mu\nu}}{32\pi^2 v^2} \tag{5.27}$$

$$with \quad \tilde{G}_{\mu\nu} = \frac{1}{2} \epsilon^{\mu\nu\lambda\rho} G_{\lambda\rho} \tag{5.28}$$

where $v \sim 246$ GeV is the Higgs vacuum expectation value. Because of the adopted theoretical normalization, the parametrization of new physics in terms of an EFT expansion must satisfy the condition $c_i << 1$ for the Wilson coefficients.

After the EW symmetry breaking, if one ignores the $CP$-odd contributions, Eq. 5.28 simplifies as:

$$\mathcal{L} = -c_t \frac{m_t}{v} \bar{t}tH + \frac{g_s^2}{48\pi^2} c_g \frac{h}{v} G_{\mu\nu} G^{\mu\nu} \tag{5.29}$$

where $c_t = 1 - \mathcal{R}e(c_y)$.

Due to the Higgs low-energy theorem[7], it is expected that the current Higgs measurements of the Higgs couplings exhibit a strongly degenerate solution along the line $c_t + c_g = constant$ [198]. Thus:

- In the on-shell regime, i.e. at the scale $m_H < m_t$, the Higgs on-shell cross section is proportional to:

$$\sigma_{on-shell,H} \sim |c_t + c_g|^2 \tag{5.30}$$

- In the off-shell regime, since the partonic center-of-mass energy of the process $\sqrt{\hat{s}}$ becomes higher than $m_t$, it is not possible to integrate out the top quark and so the on-shell cross section given in Eq. 5.30 is not valid.

Thus, if one compares the on- and off-shell Higgs production it is possible to disentangle the effects of the $c_t$ and $c_g$ couplings. This is how the off-shell dataset in

[7] The Higgs low-energy theorem gives an elegant way to estimate the couplings of the Higgs boson to massless gluons and photons induced by loops of heavy particles. According to this theorem, the interactions of the Higgs boson with gluons, mediated by loops of heavy coloured particles, can be calculated by treating the Higgs field as a background field and taking the field-dependent mass of each heavy particle as a threshold for the running of the QCD gauge couplings. Under these assumptions is possible to write the effective Lagrangian and expand the field-dependent masses around the VEV obtaining the couplings of the Higgs boson to gluons mediated by loops of heavy fermions [197]. Similarly for photons.

the ggF production mode can help when searching for BSM physics in the context of the EFT approach.

To summarize, the diagrams of the processes contributing to $gg \to ZZ$ are shown in Fig. 5.12. The final amplitude for the process can be written as:

$$\mathcal{M}_{gg\to ZZ} = \mathcal{M}_H + \mathcal{M}_{Bkg} = c_t\mathcal{M}_{c_t} + c_g\mathcal{M}_{c_g} + \mathcal{M}_{Bkg} \tag{5.31}$$

where $\mathcal{M}_H$ is the Higgs-mediated amplitude and $\mathcal{M}_{Bkg}$ is the amplitude for the $gg \to ZZ$ background interfering with the signal process. In the SM it is expected to have no contribution from $c_g$ and all the signal contribution coming from $c_t$: $c_g = 0$ and $c_t = 1$. By exploring the ggF production mode in the off-shell regime for the Higgs boson it is possible to constrain two dimension-6 operators parameterizing modifications of the top Yukawa coupling and the effective interactions between the Higgs boson and gluons mediated by heavy new physics.

In order to find constraints on the Higgs couplings $c_t$ and $c_g$, a proper parametrization for the differential cross section as a function of the invariant mass is required. In [55] a calculation is available for the $4\ell$ channel:

$$\frac{d\sigma}{dm_{4\ell}} = F_0(m_{4l}) + F_1(m_{4l})c_R^2 + F_2(m_{4l})c_I^2 + F_3(m_{4l})c_R + F_4(m_{4l})c_I \tag{5.32}$$

where $c_I$ and $c_R$ are the ratios of the Higgs-mediated amplitudes compared to the SM values:

$$c_R = \frac{\mathcal{R}e\mathcal{M}_\Delta^{NP+SM}}{\mathcal{R}e\mathcal{M}_\Delta^{SM}}, \quad c_I = \frac{\mathcal{I}m\mathcal{M}_\Delta^{NP+SM}}{\mathcal{I}m\mathcal{M}_\Delta^{SM}} \tag{5.33}$$

where NP means New Physics contribution. By varying the mass of the particle running in the triangle diagram, $M$, it is possible to extract the functions $F_0$ ...$F_4$ from the following constraining equations:

1. Signal-only constraint: $|\mathcal{M}_H|^2 \sim F_1 + F_2$
2. Background-only constraint: $|\mathcal{M}_{Bkg}|^2 \sim F_0$
3. Interference-only constraint: $|\mathcal{M}_{Bkg} + \mathcal{M}_H|^2 - |\mathcal{M}_H|^2 - |\mathcal{M}_{Bkg}|^2 \sim F_3 + F_4$
4. Signal-only with $m_t = M$ constraint: $|\mathcal{M}_H|^2_{m_t=M} \sim F_1c_R(M)^2 + F_2c_I(M)^2$
5. Interference-only with $m_t = M$ constraint: $|\mathcal{M}_{H,m_t=M} + \mathcal{M}_{Bkg}|^2 - |\mathcal{M}_{H,m_t=M}|^2 - |\mathcal{M}_{Bkg}|^2 \sim F_3c_R(M) + F_4c_I(M)$

Finally, one can easily write $d\sigma/dm_{4\ell}$ as a function of the coefficients of physics interest ($c_t$, $c_g$) rather than ($c_R$, $c_I$) by using the well-known expression for the triangle amplitude:

$$\frac{d\sigma(c_t, c_g)}{dm_{4\ell}} = 2F_1 c_A \cdot c_t c_g + F_1 c_A^2 \cdot c_g^2 + F_3 c_A \cdot c_g + (F_1 + F_2) \cdot c_t^2 + (F_3 + F_4) + F_0 \quad (5.34)$$

with a multiplicative factor $c_{com}$ included in all the terms as a normalization parameter which is needed to take into account the integrated luminosity $\mathcal{L}$ and the acceptance of the sample used and $c_A$ given by:

$$c_A = \frac{F_\Delta(\infty)}{\mathcal{R}eF_\Delta(m_t)} \quad (5.35)$$

where $F_\Delta$ is the fermionic leading order loop function for single Higgs production.

The parametrization I obtained in Eq. 5.34 was checked with the authors of the paper [55] since an inconsistency was found. The authors confirmed they had made an error - $F_3$ was switched with $F_4$ - and my parametrization was correct.

The parametrization in Eq. 5.34 is for the $H^* \to 4\ell$ final state, while in the $H^* \to \ell\ell\nu\nu$ final state only the transverse mass, $m_T^{ZZ}$ defined in Eq. 4.11, is available due to the presence of neutrinos in the final state. It has not been demonstrated that the parametrization for $H^* \to \ell\ell\nu\nu$ can be obtained from the parametrization for $H^* \to 4\ell$ with the substitution $m_T^{ZZ}$ for $m_{4\ell}$. An appropriate calculation for this specific final state is not available yet. This is the main reason why it was decided to not include this EFT study in the current ATLAS paper [63] on the off-shell production of the Higgs boson in Run 2. Nevertheless, some assumptions can be made to apply the same parametrization in the $\ell\ell\nu\nu$ channel. If we use truth level information where it is known what is a neutrino and what is a lepton the parametrization is properly usable as a function of $m^{ZZ}$, i.e. $m_{4\ell}$ for the $\ell\ell\nu\nu$ final state. One can think to derive the various coefficients based on the parametrization given in Eq. 5.34 for three different cases, truth $m^{ZZ}$, truth $m_T^{ZZ}$ and reconstructed $m_T^{ZZ}$. When moving from truth level to reconstructed level, acceptance factors are applied. If significant variations are observed, it is not possible to proceed with the $m_{4\ell}$ parametrization. If consistency is observed, it is possible to set preliminary limits on $c_t$ and $c_g$ based on this parametrization. To check the parametrization reported in Eq. 5.34, MCFM samples have been produced with a different value of the

mass of the particle running in the triangle diagram, for example $M = 500m_t$. Another MCFM sample with $M = 1000m_t$ has later been used to derive the coefficients following such a parametrization. In Fig. 5.13 and Fig. 5.14 the various coefficients for $d\sigma(c_t, c_g)/dm_{ZZ}$ are shown for the $2e2\nu$ channel and for the $2\mu2\nu$ channel, respectively. A colour code is shown to easily identify the different coefficients for the couplings contributions. In the three cases, the coefficients calculation shows consistent results within systematic uncertainties. The coefficients in the reconstructed $m_T^{ZZ}$ scenario are used as the nominal reference.

After the derivation of the coefficients, it is possible to test the sensitivity of ATLAS on ($c_t$, $c_g$) based on the same dataset used in the other interpretations presented in this thesis, 36.1 fb$^{-1}$ . The same statistical analysis (signal selection and background estimation) performed for the $\Gamma_H$ and $R_{gg}$ interpretations is used including $c_t$ and $c_g$ as parameters of interest. The only difference being the parametrization for the ggF production mode. In the context of the EFT approach for ggF a polynomial function is used, based on the coefficients derived before and shown in Figures 5.13 and 5.14. The SM hypothesis of $c_t = 1$ and $c_g = 0$ is tested. Systematic uncertainties are not included for this preliminary study. The expected exclusion contour plots for ($c_t$, $c_g$) is shown in Fig. 5.15. No significant deviations from the SM predictions are observed. This is a preliminary result assuming the $4\ell$ parametrization is valid also in the $2\ell2\nu$ channel. A more accurate study will be possible once a proper theoretical parametrization for the off-shell cross section as a function of $m_T^{ZZ}$ will be available.

## 5.5 Future Improvements and Sensitivity at LHC

The results reported in the previous sections are based on an integrated luminosity of 36.1 fb$^{-1}$. This dataset was collected by the ATLAS detector in 2015 and in 2016. In April 2018, at the ATLAS HZZ workshop [199] I provided the experimental sensitivity for $\mu_{off-shell}$ when exploiting the full Run-2 dataset of 140 fb$^{-1}$. These predictions, which are based on the state of the art of the analysis reported in this thesis (signal selection, background estimation and systematic uncertainties) scaled to 140 fb$^{-1}$, are reported in Fig. 5.16. The combined $4\ell$+$2\ell2\nu$ 95% CL limit on $\mu_{off-shell}$ is estimated to be 2.5 .

In addition, in 2015 ATLAS published prospects on the sensitivity to off-shell

Higgs production in the High-Luminosity LHC (HL-LHC) scenario, assuming 3000 fb$^{-1}$ of collision data collected at $\sqrt{s} = 14$ TeV [200]. These prospects are based on the Run-1 analysis [61] when less information on the QCD theoretical corrections for the $gg \to ZZ$ background and the signal-background interference resulted in large systematic uncertainties, as explained in Sec. 4.2. Furthermore, they are based on the $4\ell$ channel only, excluding the $2\ell 2\nu$ channel which is equally or even more sensitive in the high-mass regime. Results in this thesis show already improvements with respect to the Run-1 scenario. Therefore, these prospects should be considered as a pessimistic scenario. The expected signal and background yields at 14 TeV are obtained by scaling the cross sections for each process to 14 TeV with 3000 fb$^{-1}$. It is predicted that the off-shell signal strength will be determined with an accuracy of approximately 50% at the $1\sigma$ level. Under the same assumptions reported in this thesis, the projected determination of the Higgs boson total width is $\Gamma_H = 4.2^{+1.5}_{-2.1}$ MeV when the systematic uncertainty on the $K$-factor ratio $R^B_{H^*} = K(gg \to ZZ)/K(gg \to H^* \to ZZ)$[8] is set to 10%.

In 2018 some future improvements to the current strategy were discussed. New discriminants could be tested in the $2\ell 2\nu$ channel. The transverse mass, $m_T^{ZZ}$, is the current discriminant in the $2l2\nu$ analysis, but it is not optimal. In the $4l$ channel a Boosted Decision Tree (BDT) is implemented. This technique could be explored in the $2l2\nu$ analysis as well. The $E_T^{miss}$ contribution makes the BDT less powerful, since its discriminating power mostly relies on the kinematic variables which are degraded in the $2l2\nu$ channel. Some other helpful variables, such as $\eta_{Z,visible}$ or $\Delta R_{\ell\ell}$, can be studied to feed the BDT. Very preliminary studies were discussed at the ATLAS HZZ workshop in 2018 [199] showing promising results.

Furthermore, ATLAS could try to fully exploit the VBF potential for the next public result. The VBF process exhibits a striking signature (forward/backward jets and large dijet invariant mass) allowing a better signal-background separation. In the current result an inclusive ggF-VBF category was considered. As discussed in Sec. 4.2, theoretical uncertainties in VBF are more under control than ggF theoretical uncertainties, which are still the leading systematic uncertainties. The ATLAS ITk upgrade will open a new window into VBF processes. The forward

[8] In 2017 an ad hoc calculation for the QCD theoretical corrections to the $gg \to ZZ$ background and the signal-background interference was produced and, therefore, the $R^B_{H^*}$ factor and its systematic uncertainties are not needed anymore.

extension of the inner tracker will be crucial to tag forward jets from the hard-scattering interaction. VBF cross section measurements represent a sensitive metric against which to evaluate the impact of forward tracking detectors in ATLAS for the HL-LHC era. It has been shown that the precision achievable on the VBF $H \to ZZ^* \to 4l$ cross section will be 12% with a tracking coverage up to $|\eta| < 4.0$ [201]. Also, the ITk Pixel Detector TDR [202] shows that a precision of 12% on the VBF $H \to WW^* \to \ell\nu\ell\nu$ cross section is achievable. Similar improvements can be expected in the off-shell regime of the Higgs boson allowing exploitation of also the $H \to WW^* \to \ell\nu\ell\nu$ channel for the Higgs width strategy described in this thesis. In Run 1 this channel provided a less stringent limit on $\Gamma_H$ because of the hard background rejection; this can improve in the ATLAS ITk era.

Finally, in the clean environment of an $e^+e^-$ machine, it is possible to measure the Higgs boson total width at higher accuracy. In 2018 both the International Linear Collider (ILC) and Future Circular Collider (FCC) collaborations published prospects showing that the accuracy achievable on $\Gamma_H$, when combining with some information from the HL-LHC, will be 1.7%[9] [203] and 1.3%[10] [204,205], respectively.

[9]This prediction assumes a total integrated luminosity of 2 ab$^{-1}$ at $\sqrt{s} = 250$ GeV and a total integrated luminosity of 4 ab$^{-1}$ at $\sqrt{s} = 500$ GeV at the ILC.

[10]This prediction assumes a total integrated luminosity of 5 ab$^{-1}$ at $\sqrt{s} = 240$ GeV and a total integrated luminosity of 1.5 ab$^{-1}$ at $\sqrt{s} = 365$ GeV at the FCC-ee.

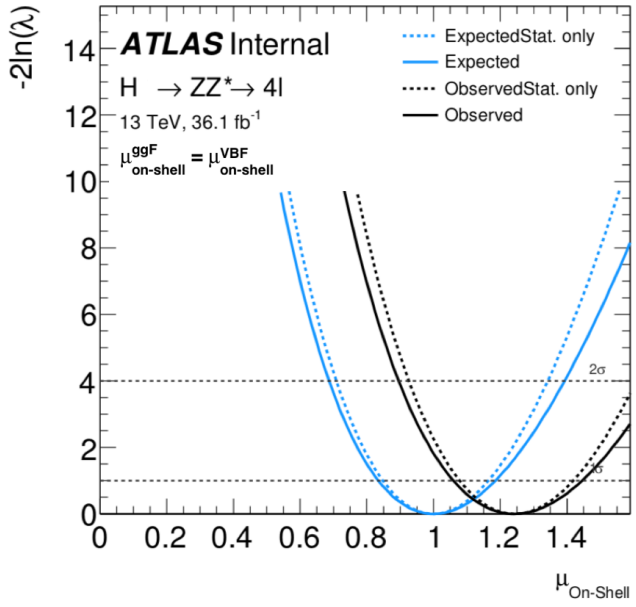


(a) On-shell signal strength, $\mu_{on-shell}$

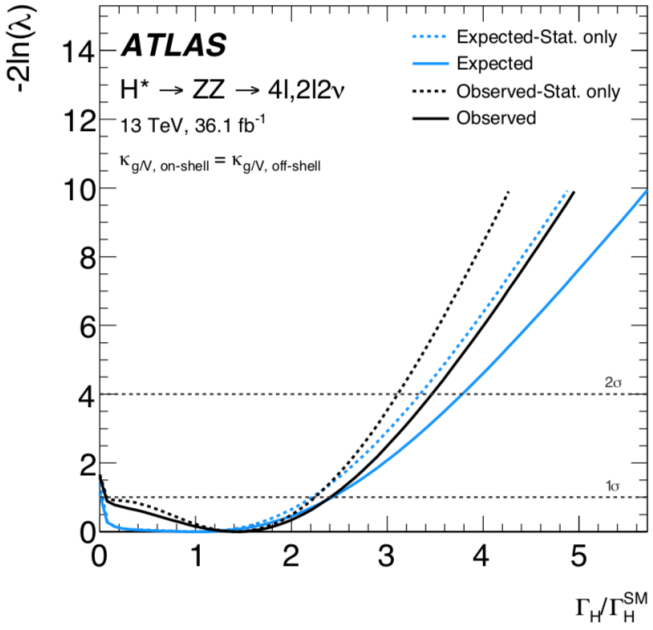


(b) $\Gamma_H/\Gamma_H^{SM}$ ratio

Figure 5.9: Scan of the negative log-likelihood, $-2ln(\lambda)$, as function of the on-shell signal strength $\mu_{on-shell}$ (a) and of the $\Gamma_H/\Gamma_H^{SM}$ ratio (b) after the combination of the on-shell $4\ell$ channel and the off-shell $4\ell$ and $\ell\ell\nu\nu$ channels in both data (black) and simulation (blue). For the off-shell channels, NLO QCD $m^{ZZ}$ dependent $K$-factors and an additional NNLO/NLO QCD $K$-factor of 1.2 are applied to each individual $gg \to ZZ$ process, as described in Sec. 4.3.1. The cross point of the $2\sigma$ line with the likelihood scan curve gives the 95% CL upper limit on $\mu_{off-shell}$. The dotted line shows the scan when only the statistical uncertainty is considered, while the solid line shows the impact of the systematic uncertainties on the result. The ratio of the ggF and VBF processes is assumed to have the SM value for both the on- and off-shell production.

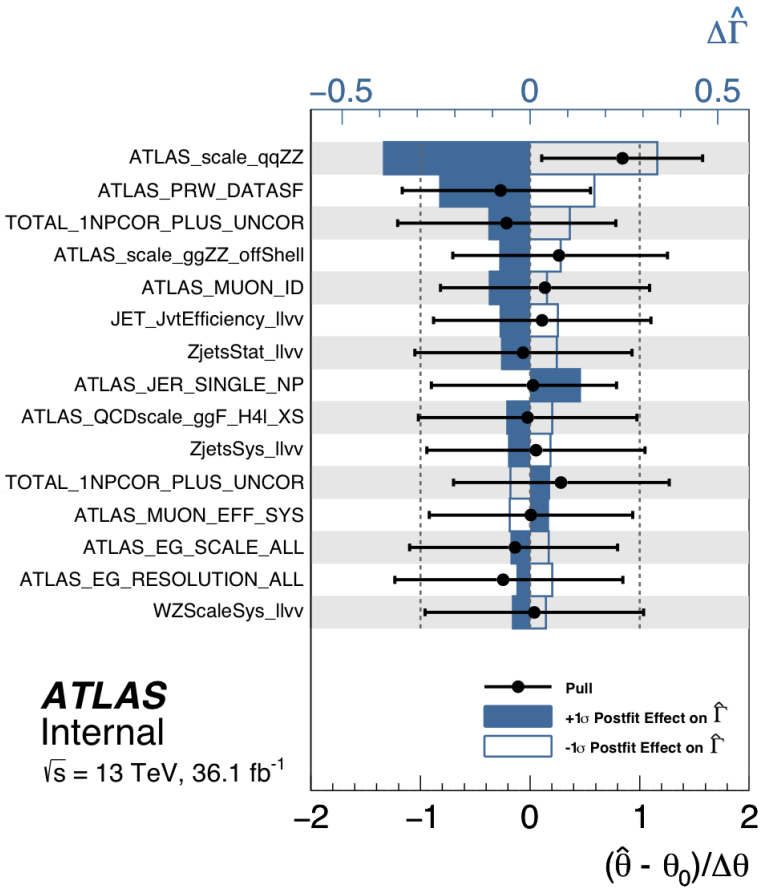


Figure 5.10: Impact of systematic uncertainties on the fitted $\Gamma_H/\Gamma_H^{SM}$-ratio parameter $\hat{\Gamma}$ in the combination of the on-shell $4\ell$ channel with the off-shell $4\ell$ and $\ell\ell\nu\nu$ channels. The systematic uncertainties are ranked in descending order of their impact on $\hat{\Gamma}$ on the $y$-axis. The boxes show the variations of $\hat{\Gamma}$ - they refer to the upper $x$-axis - when fixing the corresponding individual nuisance parameter $\theta$ to its post-fit value $\hat{\theta}$ modified upwards or downwards by its post-fit uncertainty, and repeating the fit. The blue and uncoloured boxes correspond to the upwards and downwards variations, respectively. Dots with error bars refer to the lower $x$-axis and show the deviations of the fitted nuisance parameters $\hat{\theta}$ from their nominal values $\theta_0$, expressed in terms of standard deviations with respect to their nominal uncertainties $\Delta\theta$. The associated error bars show the post-fit uncertainties of the nuisance parameters, relative to their nominal uncertainties. Systematics are neglected if their effect is smaller than 1%.

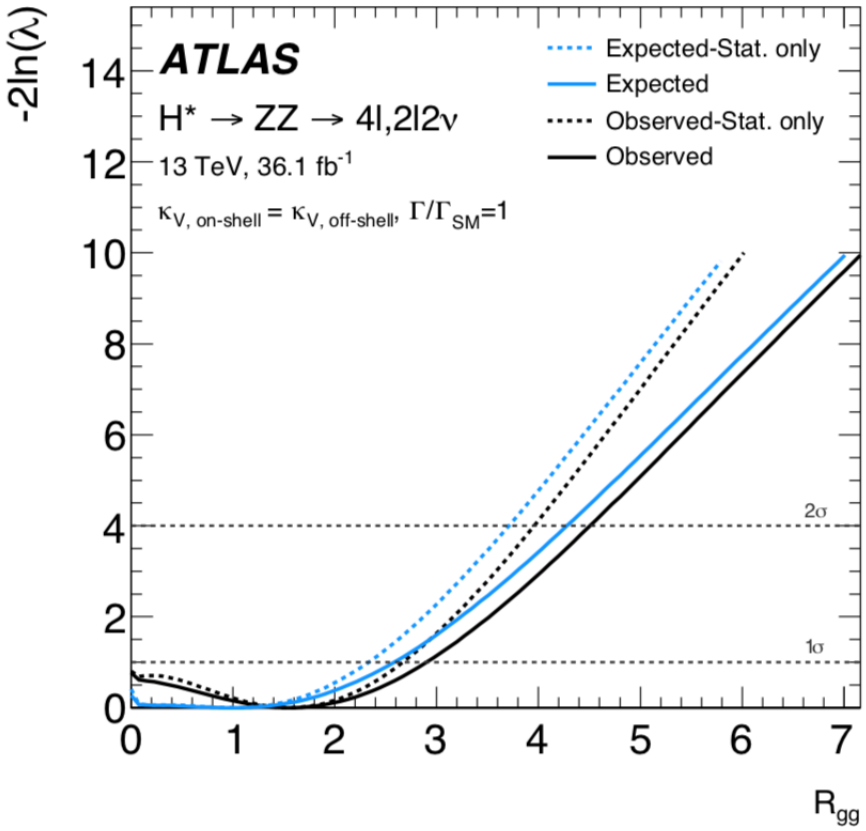


Figure 5.11: Scan of the negative log-likelihood, $-2ln(\lambda)$, as function of $R_{gg}$ after the combination of the on-shell $4\ell$ channel and the off-shell $4\ell$ and $\ell\ell\nu\nu$ channels in both data (black line) and simulation (blue line). For the off-shell channels, NLO QCD $m^{ZZ}$ dependent $K$-factors and an additional NNLO/NLO QCD $K$-factor of 1.2 are applied to each individual $gg \to ZZ$ process, as described in Sec. 4.3.1. The cross point of the $2\sigma$ line with the likelihood scan curve gives the 95% CL upper limit on $\mu_{off-shell}$. The dotted line shows the scan when only the statistical uncertainty is considered, while the solid line shows the impact of the systematic uncertainties on the result. The ratio of the off-shell ggF and VBF processes is assumed to have the SM value.

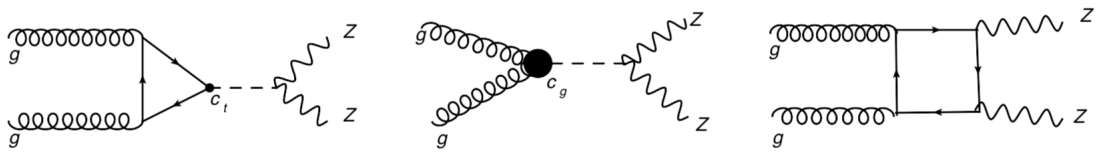


Figure 5.12: Feynman diagrams for the various processes contributing to $gg \to ZZ$.

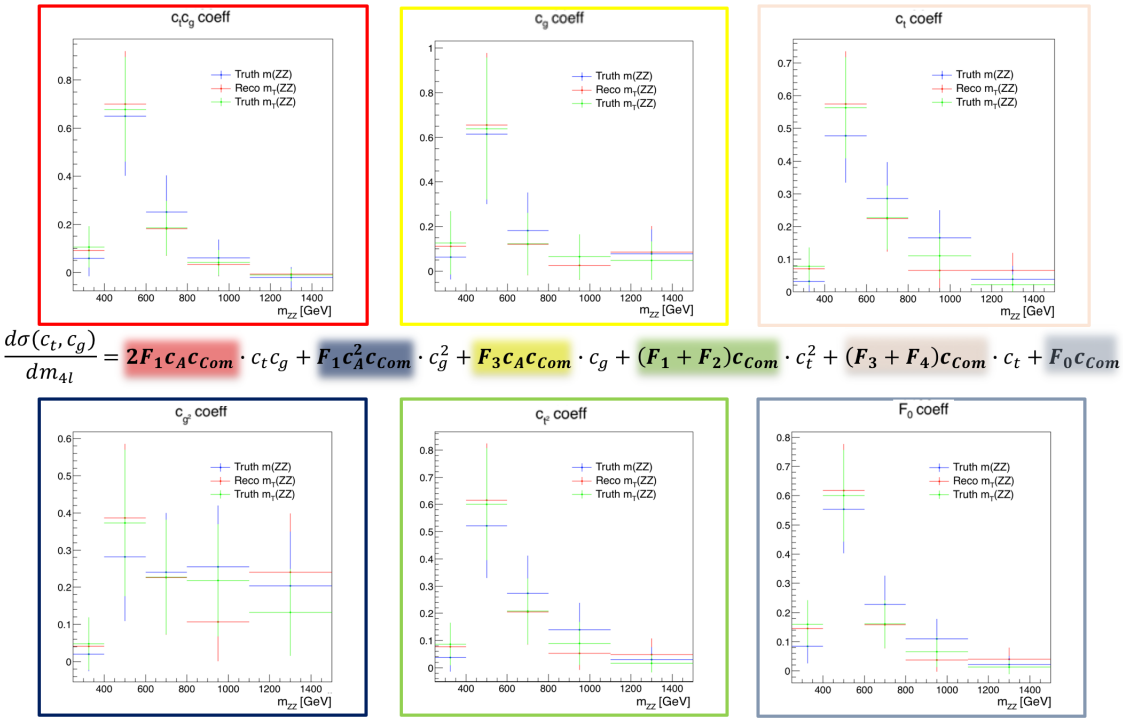


Figure 5.13: Coefficients for $d\sigma(c_t, c_g)/dm_{ZZ}$ in the $2e2\nu$ channels based on the parametrization given in Eq. 5.34 for truth $m_{ZZ}$, truth $m_T^{ZZ}$ and reconstructed $m_T^{ZZ}$. The parametrization is properly calculated only for the $4\ell$ channel, $d\sigma(c_t, c_g)/dm_{4\ell}$. The $x$-axis reports only $m^{ZZ}$ for practical reasons, but in the legend it is clear when it refers to $m_T^{ZZ}$ and when to $m_{ZZ}$. A colour code is used to easily identify the different coefficients for the couplings contributions. Systematic uncertainties are not included.

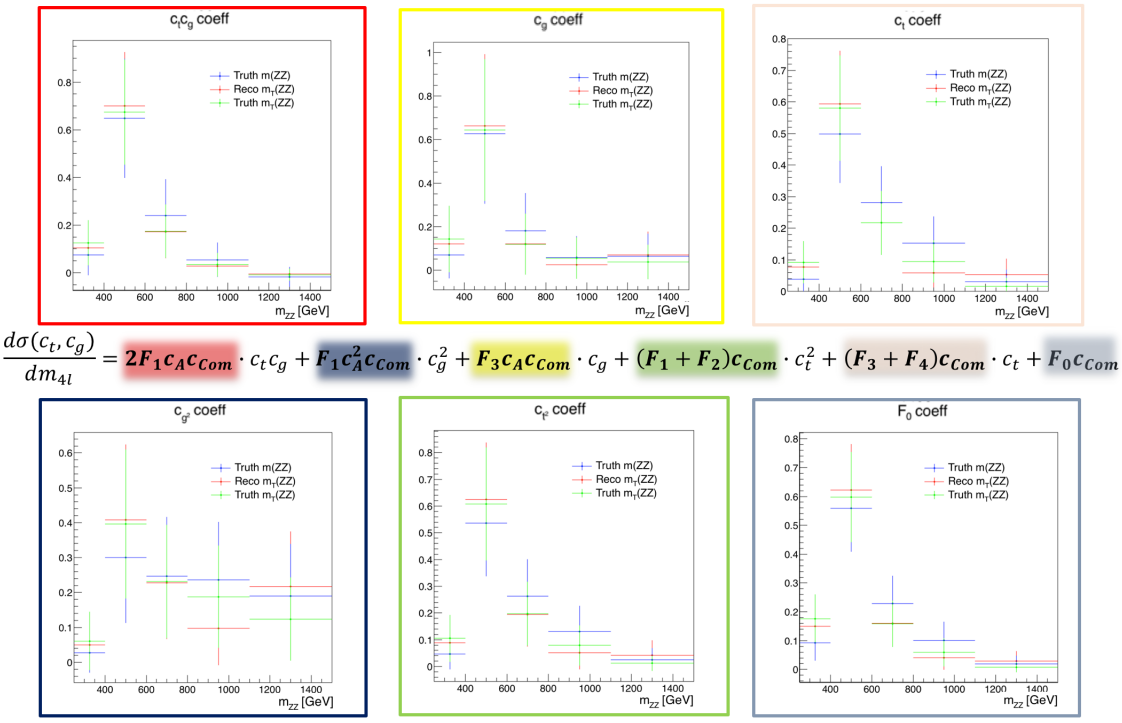


Figure 5.14: Coefficients for $d\sigma(c_t, c_g)/dm_{ZZ}$ in the $2\mu 2\nu$ channels based on the parametrization given in Eq. 5.34 for truth $m_{ZZ}$, truth $m_T^{ZZ}$ and reconstructed $m_T^{ZZ}$. The parametrization is properly calculated only for the $4\ell$ channel, $d\sigma(c_t, c_g)/dm_{4\ell}$. The $x$-axis reports only $m^{ZZ}$ for practical reasons, but in the legend it is clear when it refers to $m_T^{ZZ}$ and when to $m_{ZZ}$. A colour code is used to easily identify the different coefficients for the couplings contributions. Systematic uncertainties are not included.

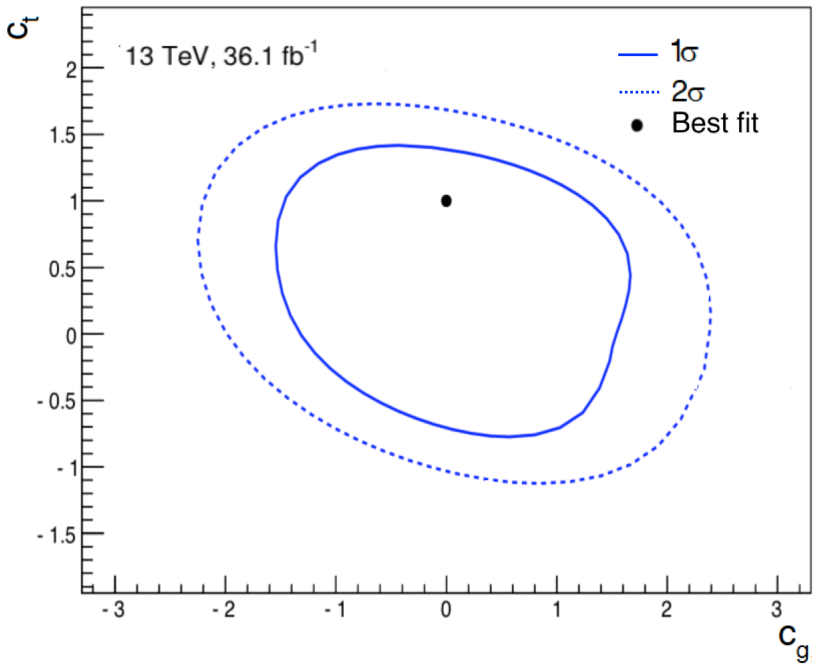


Figure 5.15: Expected 68% and 95% CL exclusion contour plot for the coefficients ($c_t$, $c_g$) based on an integrated luminosity of 36.1 fb$^{-1}$. Systematic uncertainties are not included. This is a preliminary result assuming the $4\ell$ parametrization from [55] is valid also in the $2\ell 2\nu$ channel. A more accurate study will be possible once a proper theoretical parametrization for the off-shell cross section as a function of $m_T^{ZZ}$ will be available.

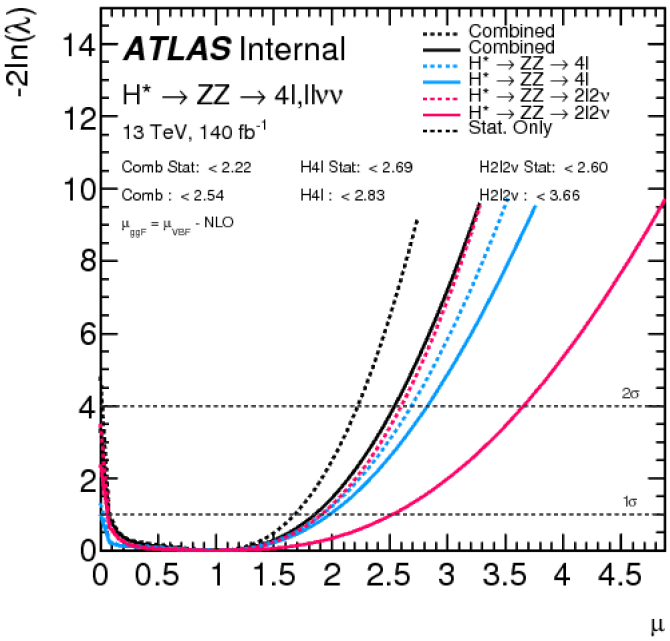


Figure 5.16: Expected sensitivity for the Higgs off-shell signal strength with the full Run-2 dataset of 140 fb$^{-1}$. Scan of the negative log-likelihood, $-2ln(\lambda)$, as function of $\mu_{off-shell}$ for the combined $4\ell$+$2\ell2\nu$ channel (black) and the individual channels $4\ell$ (blue) and $2\ell2\nu$ (red) with NLO QCD $m^{ZZ}$ dependent $K$-factors applied to each individual $gg \to ZZ$ process and an additional NNLO/NLO QCD $K$-factor of 1.2, as described in Sec. 4.3.1. The cross point of the $2\sigma$ line with the likelihood scan curve gives the 95% CL upper limit on $\mu_{off-shell}$. The dotted line shows the scan when only the statistical uncertainty is considered, while the solid line shows the impact of the systematic uncertainties on the result. The ratio of the ggF and VBF processes is assumed to have the SM value.

# Chapter 6

# $D^+$-meson Production Cross Section

*In this chapter I describe the CDF strategy for the measurement of the $D^+$-meson production cross-section at low transverse momentum. I first introduce the measurement and the motivation for it, then I briefly describe the Tevatron collider and the CDF experiment. Secondly, I introduce the samples used for this analysis and the yield extraction. Thirdly, I describe the efficiency measurement and the systematic uncertainties and, finally, I report on the results, the comparison with the previous CDF result in the high-$p_T$ regime and the theoretical model. For this measurement I was the Contact Editor and the Analysis Contact. I performed all the steps of the analysis: signal selection, optimization, background estimation, systematic uncertainties and comparisons with the theoretical model and the previous high-$p_T$ CDF measurement. I was also responsible for all the replies to the journal referees. The results summarized in this chapter were published in 2017 at the end of my second DPhil year. This is the 700$^{th}$ paper of the CDF Collaboration. I presented this measurement in a summary talk on behalf of the CDF collaboration at* Charm2016, QCD16 *and* ichep2016 *with a talk titled* "Measurement of low-$p_T$ $D^+$-meson production cross section at CDF II"*. In addition, I gave three seminars on the topic in Europe and in the USA (Siena, Bologna and Harvard).*

## 6.1 Introduction

Measurements of production cross sections of heavy mesons in hadron collisions offer important information to test and refine phenomenological QCD models of the strong interaction at small momentum transfer, a regime in which standard perturbative calculations fail and colour confinement is poorly known. In Run I, the CDF experiment has been pioneering the exploration of heavy-meson production in hadron collisions, with measurements of bottom-quark cross sections. In Run II, CDF continued this program with the world's first measurements of charm-meson production cross sections in hadron collisions. Theoretically, the cross section for the inclusive production of mesons containing net charm flavour ($X_c$) is modeled by the convolution of universal parton distribution functions (PDFs) and universal fragmentation functions (FFs) with calculable hard-scattering cross sections via a perturbative approach. Early CDF results on $D$ mesons did not agree with theory [72] [73]. Today, the predictions have been improved and calculations with the FONLL (fixed-order combined with next-to-leading-log) [206] expansion are available. Since 2010, the LHC proton-proton collider has replaced the Tevatron as one of the most prolific $c$-factories allowing the ALICE and LHCb experiments to report on measurements of charm production cross-sections at centre-of-mass energies $\sqrt{s}$ = 2.76, 7, 8 and 13 TeV [65–68]. However, since differing admixtures of quark-level processes contribute at different energy scales and with different initial states, proton-antiproton collision measurements at lower-energies remain crucial to extend our understanding in a regime in which QCD perturbative expansions are challenging. In addition, in searches for astrophysical neutrinos, knowledge of charm production cross-sections may improve estimations of background rates from neutrinos produced in decays of charm hadrons from cosmic-ray interactions with atmospheric nuclei [64].

In 2003, CDF [74] reported the first charm-production cross section in hadron collisions. That measurement used charm mesons reconstructed down to minimum transverse momenta of 6.0 GeV[1], because it was based on data selected by a trigger that imposed 2-GeV thresholds on the $D$ meson decay products. In this thesis a new

[1]Since the CDF Collaboration publishes plots and tables expressly writing $c$ when reporting GeV/$c$ (or similar) results in public plots and public tables, in this Chapter this notation is used. On the contrary, the ATLAS Collaboration prefers the notation with $c = 1$ for public plots and tables.

measurement of the $D^+$-meson production cross-section as a function of meson transverse momentum is reported. Samples of $D^+ \to K^-\pi^+\pi^+$ decays are reconstructed using the full CDF Run II dataset in the transverse-momentum range down to 1.5 GeV, still unexplored in $p\bar{p}$ collisions. The event sample is selected online using minimally biasing requirements and a data-driven optimization for each $p_T$ bin is used to determine the offline selection. A two-dimensional simultaneous fit of the $K^-\pi^+\pi^+$-mass and $D^+$ Impact-Parameter (IP) distributions allows to determine, in each transverse-momentum bin, the number of $D^+$ decays produced directly in the hard scattering. These are combined with reconstruction and selection efficiencies derived from simulation, but validated with data, to determine the differential cross section. The low-$p_T$ extension of the previous measurement strengthens significantly the experimental leverage to refine the current knowledge. To achieve a measurement down to $p_T(D^+)$ as low as 1.5 GeV, $D^+$ mesons reconstructed in the minimum-bias (MB) and zero-bias (ZB) data samples are used. ZB and the MB triggers impose minimal generic requirements on the events to reduce selection-induced biases to the physics properties of the collected data. The price is a reduced fraction of heavy-flavour events compared to the large light-quark background. However, in the full 10 fb$^{-1}$ sample of Run II data, the size of these minimally-biased samples is such that a significant number of charm decays is present and allows the reconstruction of visible exclusive signals. The differential production cross section $d\sigma/dp_T$ is integrated over the rapidity, $y$, between $-1$ and $+1$ and averaged over each $p_T$ bin:

$$\frac{d\sigma_{D^+\to K^-\pi^+\pi^+}}{dp_T}(p_T; |y| \le 1) = \left.\frac{N_{D^+}(p_T)}{\Delta p_T \cdot\ L \cdot \varepsilon_{\rm trig} \cdot \varepsilon_{\rm rec}(p_T) \cdot \mathcal{B}(D^+ \to K^-\pi^+\pi^+)}\right|_{|y|\le 1} \tag{6.1}$$

where

- $N_{D^+}$ are the yields of $D^+$ decays in each $p_T$ bin. Since the total number of $D^+$ and $D^-$ - $N_D$ - is measured, but only the cross section for $D^+$ mesons is reported, $N_D$ needs to be divided by a factor of 2, $N_{D^+} = N_D/2$. This is assuming charge invariance in the strong-interaction production. The yield extraction is reported in Sec. 6.5.
- $\Delta p_T$ is the bin width.
- $L$ is the integrated luminosity of the data sample. This is reported in Sec. 6.3.2.

- $\varepsilon_{\text{trig}}$ is the efficiency associated with the trigger selection. This is reported in Sec. 6.6.1.
- $\varepsilon_{\text{rec}}$ is the global reconstruction efficiency of the candidates including geometrical and kinematical acceptances as well as the detector reconstruction efficiency of the signal. The reconstruction efficiency measurement is reported in Sec. 6.6.2.
- $\mathcal{B}(D^+ \to K^-\pi^+\pi^+)$ is the *CP*-averaged decay branching ratio of the channel used in this analysis.
- $|y| \leq 1$ is the rapidity range considered.

The average value of the cross section in the $i^{th}$ bin, $\sigma/\Delta p_{T,i}$, differs from the value corresponding to the $p_T$ value of the centre of the bin. In this thesis the differential cross section $d\sigma/dp_T$ integrated over the width of each bin is reported.

## 6.2 Accelerator and Detector

Results presented in this Chapter are based on the dataset collected by the CDF experiment of the Tevatron accelerator during the Run II data-taking operations.

Since both, the Tevatron accelerator and the CDF detector, were decommissioned in 2011, past tenses are used in this Section. Later, when describing the analysis, the present tense is used.

### 6.2.1 Tevatron

The Tevatron, located at the Fermi National Accelerator Laboratory (FNAL or FERMILAB) in Batavia (Illinois, USA), was a proton-antiproton ($p\bar{p}$) collider. It produced collisions at centre-of-mass energy of $\sqrt{s}$ = 1.96 TeV during Run II. It was a superconducting synchrotron 6.3 km in circumference that took advantage of the higher magnetic-field strengths produced by 1 000 superconducting magnets. It started operating in 1975, producing its first $p\bar{p}$ collision in 1985 followed by extensive upgrades and improvements until it was shut down on September $30^{th}$, 2011. The machine collided $36 \times 36$ bunches every 396 ns. In order to reach $p\bar{p}$ interactions at this energy, several preparation and acceleration steps were needed.

Figure 6.1 shows the arrangement in the laboratory area of all the machines involved. The acceleration cycle started with the production of protons from ionized hydrogen atoms, $H^-$, which were accelerated to 750 keV by a *Cockroft-Walton* electrostatic accelerator. Pre-accelerated $H^-$ ions were then injected into the *LINAC* (LINear ACcelerator), where they were accelerated up to 400 MeV by passing through a 150 m long chain of radio-frequency (RF) accelerator cavities. To obtain protons, the $H^-$ ions were passed through a carbon foil which stripped their electrons off. The resulting protons were then injected to the *Booster*, a rapid cycling synchrotron (with a radius of 75.5 m) that accelerated the protons up to 8 GeV and compacted them into bunches. Each turn around the Booster, the protons accrued about 500 keV of kinetic energy. The protons were then transfered to a synchrotron, called the *Main Injector*, which brought their energy to 150 GeV: this was the beginning of the final injection process into the Tevatron, known as a "shot". Inside the Main Injector several bunches were coalesced into one for the Tevatron injection.

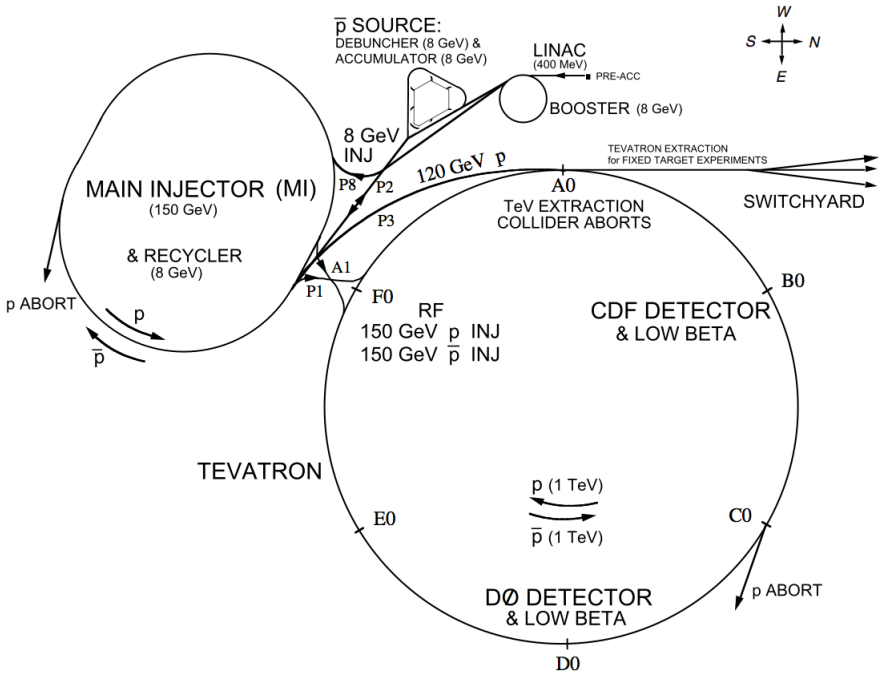


Figure 6.1: The Tevatron Collider chain at FERMILAB.

The production of the antiproton beam was significantly more complicated. The cycle started with extracting a 120 GeV proton beam from the Main Injector onto a stainless steel target. This process produced a variety of different particles, including

antiprotons. The particles came off the target at many different angles and they were focused into a beam line with a lithium lens. In order to select only the antiprotons, the beam was sent through a pulsed magnet which acted as a charge-mass spectrometer. The emerging antiprotons had a bunch structure similar to that of the incident protons and were stored in a *Debuncher*. It was a storage ring where the momentum spread of the antiprotons was reduced while maintaining a constant energy of 8 GeV, via stochastic cooling stations. Many cycles of the Debuncher caused the destruction of the bunch structure which resulted in a continuous beam of antiprotons. At the end of the process the monochromatic antiprotons were stored in the *Accumulator*, which was a triangle-shaped storage ring where they were further cooled and stored until the cycles of the Debuncher were completed. After the accumulator had collected sufficient antiprotons ($6 \cdot 10^{11}$), they were transferred to the *Recycler*, which was an 8 GeV storage ring made of permanent magnets and further cooled using stochastic cooling and accumulated. When a current sufficient to create 36 bunches with the required density was available, the antiprotons were injected into the Main Injector. Here their energy was raised to 150 GeV and they were transferred to the Tevatron, the last stage of the process.

The Tevatron kept both protons and antiprotons in the same beam-pipe, revolving in opposite directions. When 36 bunches of both protons and antiprotons were circulating in the Tevatron, the energy of the machine was increased in about 10 seconds from 150 to 980 GeV and the collisions began at the two interaction points: DØ (where the eponymous detector was located) and BØ (home for CDF II). Special quadrupole magnets (*low-$\beta$ squeezers*) located at both extremities of the detectors along the beam pipe "squeezed" the beam to maximize the luminosity inside the detectors. A roughly Gaussian distribution of the interaction region along the beam axis was achieved ($\sigma_z \approx 28$ cm) and its centre was shifted on the nominal interaction point by the fine tuning of the squeezers. Only when the beam profile was narrow enough and the conditions were safely stable, the detectors were turned on and the data acquisition started. This was the end of the shot.

The inter-bunch crossing was 396 ns and this defined an overall time constant which influenced the whole detector design: on this parameter depended the choice of the active parts, the design of the readout electronics, the structure of the trigger, etc. The average pile up was approximately 10 when the luminosity was at Tevatron's peak of $\mathcal{L} \approx 4 \times 10^{32}$ cm$^{-2}$s$^{-1}$. Each time that at least one of the CDF II triggers

fired, an *event* was labeled with an increasing number. Events were grouped into *Runs*. A Run was a period of continuous operation of the CDF II Data Acquisition (DAQ).

As stated in the proposal of Tevatron Run II, the goal was the accumulation of 2 $fb^{-1}$ at $\sqrt{s}$ = 2 TeV with instantaneous luminosity peaks up to 2 × $10^{32}$ $cm^{-2}s^{-1}$. The performance was always well beyond these expectations. Even though the maximum centre-of-mass energy achieved was 1.96 TeV, the peak luminosity was almost regularly > 2 × $10^{32}$ $cm^{-2}s^{-1}$ after 2006 (with usual peaks at 4 × $10^{32}$ $cm^{-2}s^{-1}$ in the last years of operations) and the crossing time was equal to 396 ns. The total luminosity delivered by the Tevatron during its activity was about 12 $fb^{-1}$, but only 10 $fb^{-1}$ of data were "acquired" on tape: these are the data used for the CDF analysis reported in this thesis.

### 6.2.2 The CDF Experiment

The CDF II detector was a large multi purpose solenoidal magnetic spectrometer surrounded by $4\pi$, fast, projective calorimeters and fine-grained muon detectors. It was installed at the BØ interaction point of the Tevatron and it was designed to study 1.96-TeV $p\bar{p}$ collisions. The original facility, commissioned in 1985, was subjected to several upgrades; the most extensive one started in 1995 and led to the detector configuration whose operation, begun in 2001, was generally referred to as CDF II. An isometric view of the CDF II detector is shown in Fig. 6.2.

The CDF II detector was composed of several specialized subsystems arranged in concentric layers, each one aimed at performing a specific task. CDF II was a 5 000-ton approximately cylindric assembly of sub-detectors, ~15 m in length and ~15 m in diameter. An accurate description of the particle's final state in energetic hadronic collisions was quantitatively well obtained by the use of the (pseudo)rapidity, transverse component of the momentum and azimuthal-angle coordinates around the longitudinal axis, described later. This motivates the CDF II cylindrical symmetry both in the azimuthal plane and in the *forward* ($z > 0$) – *backward* ($z < 0$) directions with spatial segmentation of its subcomponents roughly uniform in pseudorapidity and azimuth.

Starting from the interaction point, particles generated from the $p\bar{p}$ collisions encountered in sequence:

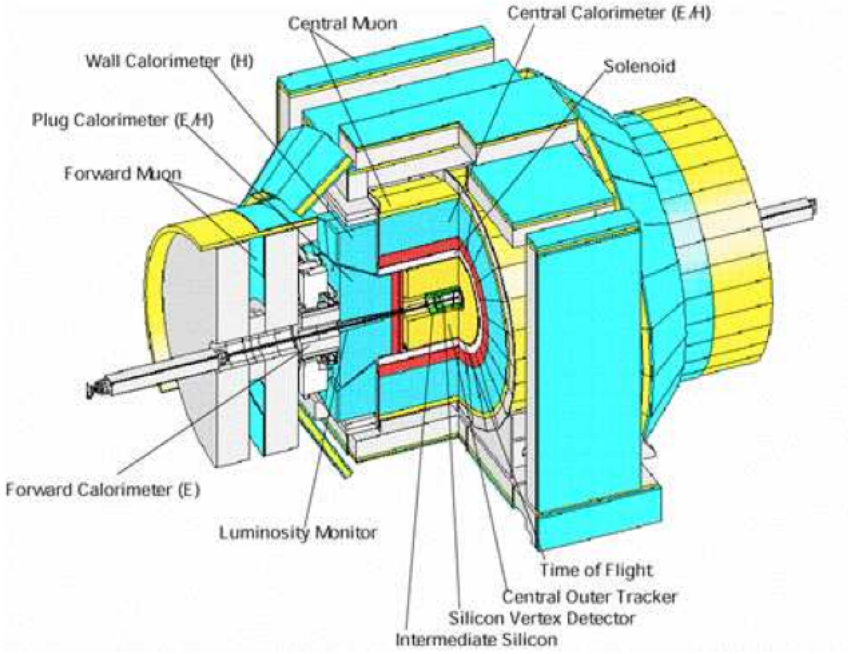


Figure 6.2: Isometric view of the CDF II detector.

- The thin beryllium wall of the beam vacuum pipe.
- A high-precision tracking system - that provided charged-particle trajectory reconstruction - composed of an inner set of silicon microstrip detectors and an outer drift chamber.
- A Time Of Flight (TOF) detector for particle identification. It was a cylindrical array made of scintillating bars that allowed particle identification via the time of flight method. The TOF was also inside the solenoid;
- A solenoidal magnet and its return steel yoke to avoid having the field interfere with the proper operation of the following calorimeter's PMTs.
- A set of electromagnetic and hadronic calorimeters segmented with a projective tower geometry. They measured respectively the energy of photons and electrons and the energy of hadronic particles. The basic structure consisted of alternating layers of passive absorber and plastic scintillator.
- A set of drift chambers and scintillators counters, used to detect muons.

The set of all of these components enabled CDF II to perform a wide range of measurements, including high resolution tracking of charged particles, electron and muon identification, low momentum $\pi/K$ separation, precise secondary-vertex measurements, finely segmented sampling of energy flow coming from final state hadrons, electrons or photons and identification of neutrinos via transverse energy imbalance. Another fundamental feature of CDF II was the capability to monitor the instantaneous luminosity. This was achieved by the use of Cherenkov Luminosity Counters (CLC), described later in this section.

A 1.4 T solenoidal magnetic field was maintained in the region with $r \leq 150$ cm and $|z| \leq 250$ cm by circulating a 4 650 A current through 1 164 turns of a Nb-Ti/Cu superconducting coil. The field was oriented along the positive $\hat{z}$ direction and was uniform at the 0.1% level in the $|z| \leq 150$ cm volume, where tracking measurements were made.

The detector was divided conventionally into two main polar regions. In the following, if not otherwise stated, the *central region* of the detector stands for the volume contained in $|\eta| < 1$, while the *forward region* indicates the detector volume satisfying $1 < |\eta| < 3.6$.

Since the main physical objects used in the analysis reported in this Chapter are *tracks*, the description of the CDF detector is limited to the tracking and triggering system. More details on the CDF II sub-detectors not used in this analysis (TOF system, calorimeters and muon system) can be found in the CDF Technical Design Report [207].

#### 6.2.2.1 The CDF Coordinate System

Similar to ATLAS, a coordinate system was defined at CDF. Figure 6.3, shows the right-handed Cartesian coordinate system employed at CDF II.

The origin of the frame was assumed to coincide with the BØ nominal interaction point and with the centre of the drift chamber. The proton direction (East) defined the positive $z$-axis which lay along the nominal beam line. The $(x, y)$ plane was therefore perpendicular to both proton and antiproton beams. The positive *y-axis* pointed vertically upward and the positive $x$-axis pointed radially outward with respect to the centre of the ring, in the horizontal plane of the Tevatron. Neither the protons beam nor the antiprotons beam was polarized. As a consequence, the resulting physical observations were invariant under rotations around the z-axis and,

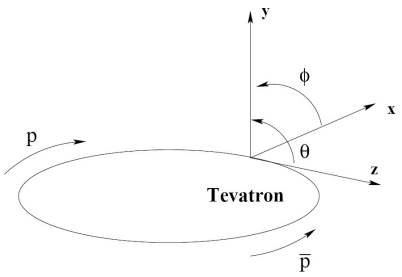


Figure 6.3: CDF II coordinate system.

thus, the description of the detector geometry in cylindrical coordinates $(r, \phi, z)$ was convenient. As for the ATLAS result, in this chapter the word *longitudinal* is used to indicate the positive direction of the the $z$-axis and the word *transverse* to indicate the plane perpendicular to the proton direction.

#### 6.2.2.2 Tracking System

An integrated cylindrical system consisting of three silicon inner sub-detectors (LØØ, SVX II and ISL) and an outer drift chamber (COT), immersed in a B = 1.4 T solenoidal magnetic field parallel to the beam axis, provided an excellent three-dimensional charged particle tracking with the trajectories of particles described by helices. A diagram of the CDF tracking volume in the $(r, z)$ plane is shown in Figure 6.4.

The vertex detector contained seven concentric layers of single- and double-sided silicon sensors at radii between 1.5 and 22 cm, each providing a position measurement with up to 15 (70) $\mu$m resolution in the azimuthal (longitudinal) direction. In more detail:

- The LayerØØ (LØØ) was the innermost layer of the microvertex silicon detector. It was a single sided silicon microstrip detector directly mounted on the 80 cm long beryllium beam pipe, at an alternating radius of 1.35 cm or 1.62 cm. The LØØ strips were located parallel to the beam axis and provided the first sampling of tracks in the $r - \phi$ plane; the inter-strip pitch was 25 $\mu$m but the read-out strips were alternated with floating ones resulting in a 50 $\mu$m readout pitch and a resolution of the $r - \phi$ charged particle's impact point of about 10 $\mu$m.

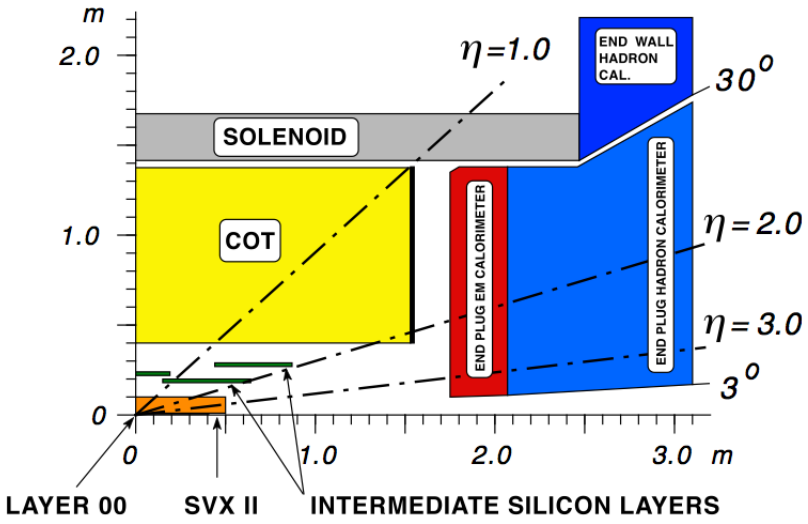


Figure 6.4: Elevation view of one quadrant of the inner portion of the CDF detector: the tracking volume inside the solenoid and the forward calorimeters are shown.

- Located outside LØØ, the Silicon VerteX detector II (SVX II) consisted of a fine resolution silicon microstrip vertex detector which provided five 3D samplings of a track in the transversal region between 2.4 and 10.7 cm from the beam. The detector cylindrical geometry coaxial with the beam was segmented along $z$ into three 32 cm long *mechanical barrels* for a total length of 96 cm which assured a complete geometrical coverage within $|\eta| < 2$. The impact parameter resolutions for central high momentum tracks were $\sigma_\phi < 35$ $\mu$m and $\sigma_z < 60$ $\mu$m.

- Outside the SVX II sub-detector, the Intermediate Silicon Layer (ISL) detector was placed. It was another silicon tracker placed at intermediate radial distance between the SVX II and the drift chamber. The polar coverage extended to $|\eta| < 2$. ISL could be roughly divided into three regions: a central region and two forward regions. The central region consisted of a single layer of silicon installed over a cylindrical barrel at radius of 22 cm, while the forward regions consisted of two layers of silicon installed on concentric barrels at radii of 20 and 28 cm.

A radial view of the three silicon sub-detectors and their coverage is shown in Figure 6.5.

The outermost tracking volume of CDF II was a large open cell drift chamber

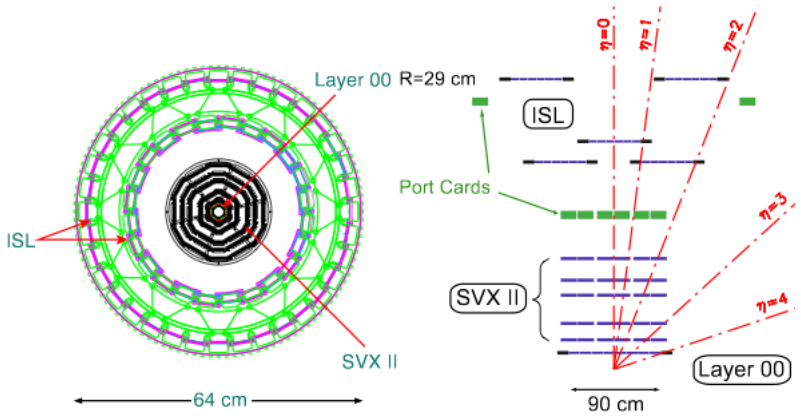


Figure 6.5: A radial view of the three silicon sub-detectors (left) and their coverage in the $r-z$ plane (right).

called the Central Outer Tracker (COT) - a cylindrical detector, coaxial with the beam. It extended radially, within the central region, between a radius of 40 cm and 138 cm along the $z$-axis. The gas composition of the chamber was Argon (50%), Ethane (35%) and $CF_4$ (15%). The chamber contained 96 radial layers of wires arranged into 8 *superlayers* (SL). In order to reconstruct the path of a charged particle in the $r-z$ volume, the wires of the 8 SL were not oriented all in the same way: four SL had wires oriented parallel to the beam axis (*axial* SL) and the wires of the remaining four SL were oriented either +3° or -3° with respect to the beamline (*stereo* SL). The axial SLs were radially interleaved with the stereo SL. Combined readout of stereo and axial SLs allowed the measurement of the $r-z$ hit coordinates. The COT efficiency for tracks was typically 99% and all the COT channels worked properly until the last Tevatron Run. Cosmic rays were exploited to maintain the internal alignments of the COT cells within 10 $\mu$m. The single-hit resolution was about 140 $\mu$m, including a 75 $\mu$m contribution from the uncertainty on the measurement of the proton-anitproton interaction time. The typical resolutions on track parameters for track fits with no silicon information or beam constraint were: $\sigma_{p_T}/p_T^2 \approx 0.07\%$ GeV, $\sigma_{\varphi_0} \approx 0.035°$, $\sigma_{d_0} \approx 250$ $\mu$m, $\sigma_\theta \approx 0.17°$ and $\sigma_{z_0} \approx 0.3$ cm.

**Tracking Performances.** For the analysis reported in this Chapter only tracks reconstructed with both silicon and COT hits have been used (*SVX+COT* tracks) for three reasons:

- Silicon stand-alone tracking (*SVX-only* tracks) becomes important in the region $1 \leq |\eta| \leq 2$ where the COT coverage was incomplete. This region of acceptance is excluded in the analysis, since the reconstruction efficiency and the momentum resolution outside of this region are too low);
- In the central region only tracks with $p_T < 0.28$ GeV have SVX-only information and this value is well below the minimum requested in the analysis;
- COT stand-alone tracking (*COT-only* tracks) had an insufficient impact parameter resolution for this analysis;

All SVX+COT tracks were first fit as COT-only tracks and then extrapolated inward to the silicon and refit with the additional points. In the COT the track density was lower than in the silicon, because of its greater radial dimension, consequently the probability of accidental hit combination in the track reconstruction was smaller. This way of performing the fit was fast and efficient; the resulting tracks had high purity.

The reconstruction of the hits in the silicon detector was fundamental to improve the impact parameter resolution of tracks. In fact, with the additional information provided by the silicon detectors, the resolution could reach $\sigma_{d_0} \approx 20$ $\mu$m (not including the transverse beam size). This value, combined with the $\sigma_{\mathrm{T}} \approx 30$ $\mu$m transverse beam size, was sufficiently small with respect to the typical transverse decay-lengths of heavy flavours hadrons (a few hundred microns) to allow separation of their decay vertices from production vertices. The silicon tracker improved also the stereo resolutions up to $\sigma_\theta \approx 0.06°$ and $\sigma_{z_0} \approx 70$ $\mu$m, while the transverse momentum and the azimuthal resolutions remained approximately the same as COT-only tracks, 0.07% GeV, which corresponds to a typical mass resolution of 6.0 MeV for the $D^+$ decays studied in this analysis.

#### 6.2.2.3 Cherenkov Luminosity Counters and Measurement of the Luminosity

Absolute luminosity measurements by the machine based on measurements of beam had uncertainties of the order of 15 - 20%. For this reason, at CDF the beam luminosity was determined using gas Cherenkov counters (CLC) located in the

pseudorapidity region $3.7 < |\eta| < 4.7$, which measured the average number of inelastic interactions per bunch crossing. Each module consisted of 48 thin, gas-filled, Cherenkov counters. The counters were arranged around the beam pipe in three concentric layers, with 16 counters each, and pointing to the centre of the interaction region. The cones in the two outer layers were about 180 cm long and the inner layer counters, closer to the beam pipe, had a length of 110 cm.

The Cherenkov light was detected with photomultiplier tubes and the momentum threshold for light emission was 9.3 MeV for electrons and 2.6 GeV for pions. The number of $p\bar{p}$ interactions in a bunch crossing followed a Poisson distribution with mean $\mu$, where the probability of empty crossing was given by:

$$P_0(\mu) = e^{-\mu} \tag{6.2}$$

This formula was correct if the acceptance of the detector and its efficiency were 100%. Therefore, detector acceptances were taken into account to describe a realistic situation. From the measurement of $\mu$ the luminosity could be extracted. Since the CLCs were not sensitive at all to the elastic component of the $p\bar{p}$ scattering, the rate of inelastic $p\bar{p}$ interactions was given by:

$$\mu \cdot f_{\text{b.c.}} = \sigma_{\text{p}\bar{\text{p}}\text{-in.}} \cdot \mathcal{L} \tag{6.3}$$

where the bunch-crossing frequency ($f_{\text{b.c.}}$) was known from the Tevatron RF, $\sigma_{\text{p}\bar{\text{p}}\text{-in.}} = 59.3 \pm 2.3$ mb was the inelastic $p\bar{p}$ cross-section resulting from the averaged CDF and E811 luminosity-independent measurements at $\sqrt{s} = 1.8$ TeV [208] [209] and extrapolated to $\sqrt{s} = 1.96$ TeV .

#### 6.2.2.4 Trigger System

The average interaction rate at the Tevatron was 1.7 MHz for 36 × 36 bunches. In fact, the interaction rate was higher because the bunches circulated in three trains of 12 bunches in each group spaced 396 ns apart, which led to a crossing rate of 2.53 MHz. The interaction rate was orders of magnitude higher than the maximum rate that the mass storage system could handle (f ~ 100 Hz). This led to the implementation of a trigger system that preselected events online and decided if the corresponding event information was written to tape or discarded. The CDF

trigger system consisted of three trigger levels. The first two levels were hardware based and the third one was processed by a farm of computers. The decisions taken by the system were based on increasingly more complex event information. Each level received the data event accepted by the previous one and, provided with more accurate detector information and more time for processing, chose to discard it or to send it to the following level. Level-1 and Level-2 received data directly from the detector front end electronics; events passing the Level-3 were stored to permanent memory.

Since the read-out of the entire detector needed about 2 ms on average, without a triggering system, after the acquisition of one event, another ~ 5 000 interactions could occur and they remained unrecorded. The percentage of events rejected solely because the trigger was busy processing previous events was referred to as trigger *deadtime* and at the final luminosity its typical value was approximately 5%.

In more detail:

- The Level 1 (L1) trigger was a synchronous system with an event read and a decision made every beam crossing. The depth of the L1 decision pipeline was approximately 4 $\mu$s (L1 latency). The Level 1 reduced the event rates from 2.53 MHz to about 18 KHz.

- The Level-2 (L2) trigger fulfilled two subsequent tasks, the *Event building* and the *Decision*. L2 detector information was more complex than L1 detector information; thus, the EVent Builder (EVB) reconstructed the event with L2 information. The EVB processed in parallel the calorimetric and the tracking information. It combined outputs from L1 and L2 in order to decide whether or not an event was sent to Level 3. The maximum decision time of L2 was 20 $\mu s$ for each event and the output rate was about 300 Hz.

- The Level 3 (L3) was exclusively software-based. About 400 commercial processors running in parallel reconstructed the event provided by L2 at full detector resolution. L3 codes were very similar to the offline reconstruction codes. After the full reconstruction of the event was completed and the integrity of its data was checked in less than 10 ms, the L3 decision to write on tape was taken. The typical size for an event was 150 kbytes and the maximum storage rate was about 20 Mbyte/s. The event output rate was finally ~ 75 Hz: the

relative fractions of high level objects was about 40% for the tracking, 30% for jets and photons and 30% for leptons.

## 6.3 Data Selection

The decay channel $D^+ \to K^-\pi^+\pi^+$ offers a convenient final state for a straightforward reconstruction of charged $D$ mesons[2]. The 9.5% branching fraction guarantees a significant signal yield, and the presence of three charged particles benefits from the excellent CDF tracking performance. In addition, no ambiguity is possible in the assignment of the masses to the tracks since the two tracks with the same sign curvature are pions for genuine signal decays. The 1 ps average lifetime of the $D^+$ meson corresponds to flight distances of about 300 $\mu$m, which are measured with good precision by the SVX II, as described in Sec. 6.2.2.2. In Figure 6.6 the topology of the $D^+$ decaying to $K^-\pi^+\pi^+$ is sketched out focusing on the relevant variables used in this analysis:

- the **transverse plane** is the plane perpendicular to the proton beam direction $(0xy)$;
- $\vec{x}_{pri}$ - the **primary vertex** - is the point where the $p\bar{p}$ collision takes place. It is located within the beam pipe and it represents the point where the meson is produced: $D^+$ **origin vertex**;
- $\vec{x}_{sec}$ - the **secondary vertex** - is the decaying point of the $D^+$;
- $\vec{p}_T$ - the **transverse momentum of the particle** - is the projection of the momentum vector to the transverse plane (writing $p_T$ we refer to its magnitude);
- $L_{xy}$ - the **transverse decay length** - is the signed distance between the primary and the secondary vertices projected to the $\vec{p}_T$ direction. It is defined as follows:
$$L_{xy} = \frac{(\vec{x}_{sec} - \vec{x}_{pri}) \cdot \vec{p}_T}{p_T}; \tag{6.4}$$
- $d_0$ - the **impact parameter** - is the signed distance between the origin vertex and the helix of a track at their closest approach.

[2]Charge conjugate processes are implied throughout.

These variables are used to extract the $D^+$-meson signal from the background of light particles, mainly pions, that is several orders of magnitude larger.

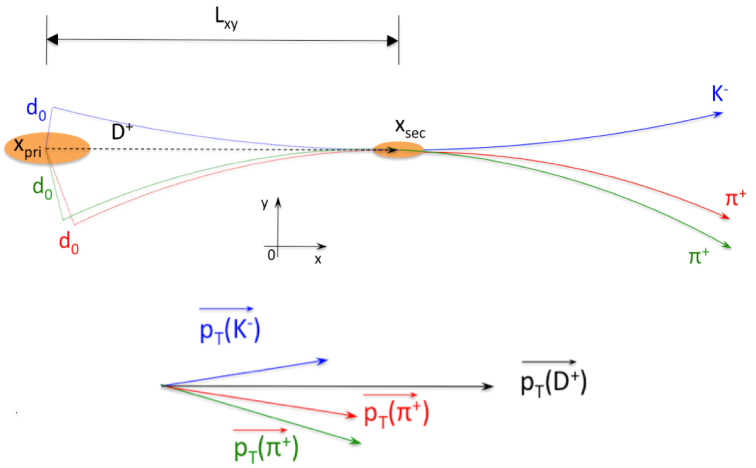


Figure 6.6: Graphical representation in the transverse plane of the decay channel $D^+ \to K^-\pi^+\pi^+$ with some kinematics variables indicated.

The CDF detector was not specifically designed to study charm physics. It was mostly conceived for high-$p_T$ searches such as the Higgs or $Z$ bosons etc. Thanks to the tracker, CDF was also able to collect huge samples of $D$-mesons decays, becoming competitive in terms of sensitivity to previous charm factories. However, some limitations to charm physics at CDF are due to physics and detector constraints:

- **Limited particle identification.** The Time-Of-Flight detector provides $\pi/K$ separation $\geq 2\sigma$ for $p_T \leq 1.6$ GeV, with some help also from the $dE/dx$ separation. CDF had no powerful PID over the full momentum-spectrum of interest, though.

- **Secondary charm production.** $B$ mesons preferentially decay into charm hadrons. Due to the long $B$ lifetime, charm hadrons could be produced at a significant distance from the Primary Vertex (PV). As a result, this can bias the measurement of charm production at the $p\bar{p}$ interaction point, if the $B$ decay vertex is not reconstructed. The impact-parameter distribution of the candidate is key to the separation of prompt and secondary charm production. In Figure 6.7, a *prompt or primary* $D^+$ meson - produced directly in the $p\bar{p}$ interaction - and a *secondary* $D^+$ - produced from a $B^-$ decay - are shown.

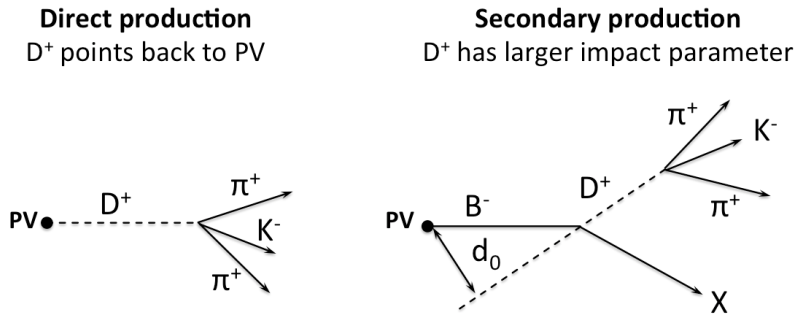


Figure 6.7: The impact parameter for prompt and secondary $D^+$ mesons in the $r$-$\phi$ plane.

In the following sections the limitations listed above are resolved to measure the $D^+$-meson production cross section at CDF II.

### 6.3.1 Online

The previous CDF measurement of the $D^+$ production cross section [74] could not use charged $D$ mesons with transverse momenta lower than 6.0 GeV because it was based on data selected by a trigger that imposed 2 GeV thresholds on the $D$ meson decay products. For this result, the minimally-biased data samples collected by the `ZEROBIAS` and `MINBIAS` trigger paths are used, extending the reach to $p_T(D^+)$ down to 1.5 GeV. The samples are collected during the whole Run II (February 2002 to September 2011) and correspond to a total luminosity recorded on tape of 10 fb$^{-1}$.

#### 6.3.1.1 Zero Bias Trigger

The `ZB` trigger decision is not based on any information associated with the detector. The trigger randomly samples $p\bar{p}$ crossings independently of whether they produced a hard scattering or not. To limit the acceptance rate within the bandwidth constraints compatible with all other triggers, the rate is prescaled at L1. The ZB requirements are the following:

**Level 1:** any bunch crossing fires L1. Prescale factor: $10^6$.

**Level 2:** no restrictions on L1-accepted events.

**Level 3:** no restrictions on L2-accepted events.

About 214 million of events are collected by the ZB trigger.

#### 6.3.1.2 Minimum Bias Trigger

The `MB` trigger aims at selecting only crossings resulting in at least an inelastic $p\bar{p}$ collision. The main restrictions exploit the CLC subdetectors: L1 accepts an event if one or more East CLC signals is in coincidence with a signal in one or more West CLCs. Given the typical Tevatron initial luminosities, nearly all crossings resulted in a hard collision. To limit the acceptance rate, a prescale is applied. Further rate limitations are imposed at L2 and L3 that reduce the acceptance rate to one event per second. The MB requirements to trigger an event are the following:

**Level 1:** CLC signals coincidence. Prescale factor: $10^5$.

**Level 2:** no restrictions on L1-accepted events. Rate limit: 3 Hz.

**Level 3:** no restrictions on L2-accepted events. Rate limit: 1 Hz.

About 154 million of events are collected by this path.

#### 6.3.1.3 Overlap Between ZB and MB Samples

During data acquisition, the ZB and MB trigger selections operate at the same time. Events might be collected by both triggers and appear twice in the sample. Without prescales, the MB sample would be a subset of the ZB sample. Prescale factors and rate limits reduce by a factor of approximately $10^6$ the number of overlapping events: only 409 events are common to both samples. Such events are used only once, with a negligible impact on the estimated integrated luminosity.

### 6.3.2 Data Quality and Luminosity

The CDF collaboration has defined a list of standard data-quality requirements a Run has to satisfy to be considered "good". Such Runs are collected in the so-called `Good Run List` (GRL). All CDF analysis must conform to it. Several specific good runs lists - dedicated to analyses based on different sub-detectors status - have been developed by different groups. Which list is the most suitable for a certain

analysis depends on the sub-detectors it uses. That is why low $p_T$ analyses that are not related to the muon systems can include runs where the muon systems is not working properly, but not runs were the COT is excluded or not working. In the case of interest for the results in this thesis, a good list is made up only by Runs where SVX II and the COT are working properly without further requirements on the other sub-detectors. After applying the GRL selection, the ZB sample is reduced to about 183 million events, while the MB sample is reduced to about 133 million events.

The measured rate of the inelastic $p\bar{p}$ events, $R_{p\bar{p}}$, allows for an estimation of the CDF II instantaneous luminosity according to $\mathcal{L} = R_{p\bar{p}}/(\sigma_{\text{in}} \cdot \epsilon_{\text{CLC}})$, where $\sigma_{\text{in}}$ is the inelastic $p\bar{p}$ cross section at $\sqrt{s}$ = 1.96 TeV and $\epsilon_{\text{CLC}}$ is the CLCs acceptance. The only direct measurement of $\sigma_{in}$ at the Tevatron has been performed at the beginning of Run I, at 1.8 TeV energy [208]. The instantaneous luminosity used in the online and offline calculations at CDF is obtained by extrapolating the combination of CDF and E811 measurements at $\sqrt{s}$ = 1.8 TeV to the projected energy of 2 TeV. This overestimates the total $p\bar{p}$ cross section by about 1.9%; hence, the raw integrated luminosity stored in the data base is corrected by this factor, as listed in Table 6.1 to derive the trigger luminosity of the sample. In [209] the systematic uncertainty on the luminosity is assessed to be approximately 6%.

| | $L_{\text{raw}}$ | $L_{\text{raw}} \times$ 1.019 |
|---|---|---|
| ZB | 8.90 | 9.07 |
| MB | 6.83 | 6.96 |
| Tot | 15.73 | 16.03 |

Table 6.1: Luminosity corrections for ZB, MB and total samples in $(\text{nb})^{-1}$.

### 6.3.3 Candidate Selection

In each event, $D^+$ candidates are reconstructed offline by combining all the possible triplets of tracks consistent with the decay of a charge-one particle into a kinematic fit. Only tracks in the $\eta$ and $p_T$ ranges where the reconstruction of the tracking system is efficient are selected. The base-quality requirements for each track are as follows:

- SVX II hits: SAS $\geq 1$, $r - z \geq 2$; and $r - \phi \geq 3$;

- COT hits: stereo $\geq 25$ and axial $\geq 25$;
- $|\eta| \leq 1.2$;
- $p_T \geq 0.4$ GeV;
- $0 \leq |d_0| \leq 1$ mm.

The hit requirements follow the standard prescriptions in heavy flavour analyses. Fiducial requirements that ensure that each track is reconstructed in the portion of the tracking volume where the COT and SVX detectors have optimal performance [210] are also introduced:

- $|z| \leq 155(47.25)$ cm at radius R = 133(10.645) cm;

A triplet of good tracks satisfy the following criteria:

- $|\sum_{i=1}^{3} q_i| = 1$;
- $d_{0,max} \cdot d_{0,min} < 0$;
- $\Delta\varphi_{0,min} = |\varphi_{0,i} - \varphi_{0,j}| \geq 2°$;
- $\Delta z_{0,max} = |z_{0,max} - z_{0,min}| \leq 3$ cm;

where the index `i` and `j` refer to the tracks of the triplet; $q_i$ is the charge of the particle `i`; $d_{0,max}$, $d_{0,min}$, $z_{0,max}$, $z_{0,min}$ represent the maximum or the minimum value of the impact parameter $d_0$ or of the $z_0$ coordinate of the three tracks; $\Delta z_{0,max}$ and $\Delta\varphi_{0,min}$ represent the maximum and minimum variation of the $z_0$ coordinate and $\varphi_0$ among the tracks of the triplet. The requirement $\Delta\varphi_{0,min} \geq 2°$ is needed to avoid ghost tracks: in the course of track-reconstruction, different pattern recognition algorithms work independently, so it can occur that the trajectory of the same charged particle is reconstructed more than once with slightly different parameters and identified as multiple tracks. The three tracks are fit together looking for a common point of interaction (vertex) displaced from the primary vertex. The fit converges only if the reconstructed track-helices are within a certain longitudinal range. Track steering is implemented: for each event, the track fit is performed again using the primary vertex as an additional point for each of the three tracks. A successful fit returns the coordinates of the candidate's decay vertex, the resulting

global $\chi^2$ of the fit and the parameters of refitted tracks. A candidate is selected if it meets the following base requirements:

- $L_{xy} \geq 0$ cm;
- $|y(D^+)| \leq 1$;
- $\chi^2_{\text{red}} \leq 10$;

where $y(D^+)$ is the candidate's rapidity and $\chi^2_{\text{red}}$ is the $\chi^2$ of the fit divided by the number of degrees of freedom. Figure 6.8 shows the $K^-\pi^+\pi^+$ mass distribution of the resulting candidates. No signal is observed with the application of the base-selection only. Thus, an optimization of the selection is required.

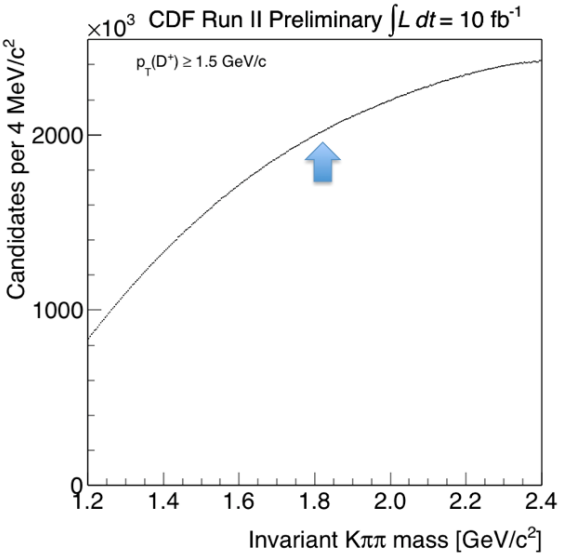


Figure 6.8: $K^-\pi^+\pi^+$ mass distribution of the candidates obtained using the selection described in Sec. 6.3.3. The arrow indicates where the $D^+$ peak is expected.

### 6.3.4 Selection Optimization

One of the main challenges of the present work is the optimization of the candidate selection, which aims at reducing the light-meson background, initially about $10^4$ times more abundant than the signal.

A data-driven optimization, that achieves an unbiased final selection [211], is used. The optimization strategy of the selection is performed *independently* in each

$p_T(D^+)$ bin. The sample size available is sufficient to probe the $p_T(D^+)$ range 1.5 - 14.5 GeV in a few variable-size bins. Before proceeding to the optimization, secondary decays are suppressed. Because of the additional energy release in the $B \to D$ decay, secondary $D^+$ mesons originating from $B$-meson decays are less likely to point back to the beam-line, and therefore feature a wider impact-parameter distribution than that of the prompt component. Therefore, secondary decays are suppressed simply by restricting the samples to candidates whose impact parameter does not exceed 100 $\mu$m. While this requirement is removed in the analysis sample, where the impact-parameter distribution is fit to infer the fraction of secondaries, here an upper threshold on impact parameter helps target the optimization toward the primary signal. Let $\mathcal{M}$ be the data sample on which the selection is optimized, following the formalism used in Fig. 6.9:

1. The event number is used as a random criterion to divide the sample $\mathcal{M}$ into two statistically independent subsamples with approximately the same size, even- and odd-numbered events.

2. A configuration space is built from three optimization variables. After studying several variables, a subset of three that offer the most discriminating power against background events is selected: the transverse momenta of the final-state particles, $p_T$(TRK)[3], the fit $\chi^2_{red}$, and $L_{xy}$. Ten possible thresholds for the selection criteria of each variable are considered, resulting in 1000 samples of the configuration space. The $i^{th}$ element of the configuration space is a possible combination of criteria applied to the three variables:

| Variable | Range | Step |
|---|---|---|
| Two $p_T$(TRK) [GeV/$c$] | 0.4–1.3 | $p_{T,j}$ [0.1] |
| $\chi^2_{\rm red}$ | 10–0 | $\chi^2_{\rm red,m}$ [1] |
| $L_{xy}$ | 0–1450 $\mu$m | $L_{xy,n}$ [150 ] |

Table 6.2: Optimization variables.

Table 2 lists the optimization variables along with the steps and ranges used for the optimization procedure.

- Two $p_T$(TRK) $\geq$ $\rm p_{T,j}$ ;

[3]TRK is used to signify one of the $D^+$ products to avoid confusion with the $p_T(D^+)$.

- $\chi^2_{\rm red} \leq \chi^2_{\rm red,m}$;
- $L_{xy} \geq L_{xy,n}$.

3. For each $i^{th}$ configuration, signal ($\mathcal{S}_i$) and background ($\mathcal{B}_i$) are obtained through a likelihood fit of the binned $K^-\pi^+\pi^+$ mass distribution, by integrating the yield of each class of event over a range of $2\sigma$ around the $D^+$ peak (*signal region*). The figure of merit used in the optimization is

$$f(\mathcal{S}_i, \mathcal{B}_i) = \mathcal{S}_i/\sqrt{\mathcal{S}_i + \mathcal{B}_i}. \tag{6.5}$$

   which is roughly proportional to the inverse of the expected average statistical uncertainty on the measured signal yield.

4. The configuration space is scanned using the Even ($E$) sample to find the criteria that maximize the figure of merit, $f(\mathcal{S}^E, \mathcal{B}^E)$.

5. The last two steps are repeated using the Odd sample ($O$) to obtain the criteria that optimize the sample $O$. Due to statistical fluctuations, the two sets of optimized criteria can differ, in general. They are not so different for the optimization presented in this thesis, however.

6. The final analysis sample is obtained by applying the requirements optimized in the subsample $O$ to the subsample $E$ and viceversa.

Splitting the sample $\mathcal{M}$ avoids biases in the selection and makes maximal use of the available statistics.

Table 6.3 lists the optimized criteria as functions of $p_T(D^+)$ for the even and odd subsamples.

In Figure 6.10 the invariant-mass distribution after the application of the optimization criteria is shown for both the Even and Odd subsamples for $p_T(D^+) \geq 1.5$ GeV.

## 6.4 Simulated Samples

Simulated Monte Carlo (MC) samples are used for the following purposes:

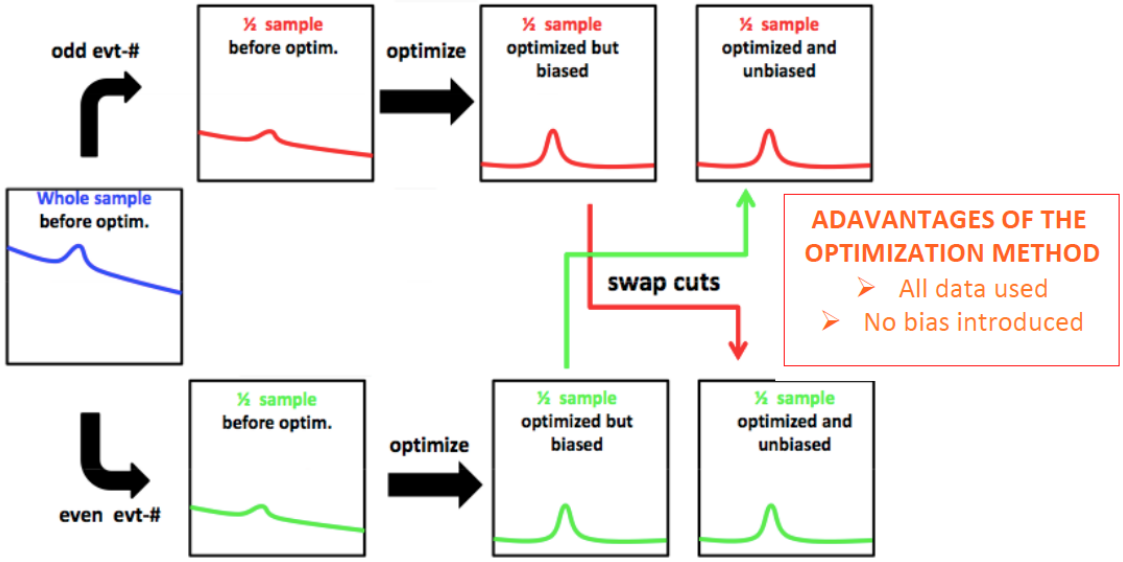


Figure 6.9: Graphical scheme of the optimization. The optimization strategy is derived from [211].

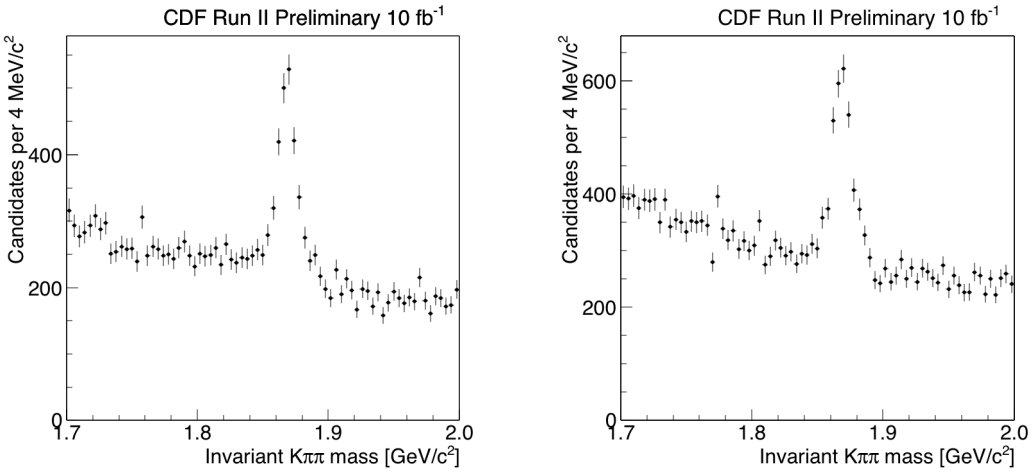


(a) Even-numbered events (b) Odd-numbered events

Figure 6.10: Invariant-mass distribution after the application of the optimization criteria for both the Even (a) and Odd (b) subsamples for $p_T(D^+) \geq 1.5$ GeV.

| $p_T(D^+)$ [GeV/$c$] | Subsample | $p_{T,j}$ [GeV/$c$] | $\chi^2_m$ | $L_{xy,n}$ [$\mu$m] |
|---|---|---|---|---|
| 1.5–2.5 | Even | 0.7 | 4 | 600 |
| | Odd | 0.6 | 4 | 600 |
| 2.5–3.5 | Even | 0.6 | 2 | 600 |
| | Odd | 0.6 | 3 | 600 |
| 3.5–4.5 | Even | 0.7 | 5 | 750 |
| | Odd | 0.7 | 6 | 750 |
| 4.5–6.5 | Even | 0.9 | 6 | 750 |
| | Odd | 0.9 | 6 | 750 |
| 6.5–14.5 | Even | 1.1 | 7 | 750 |
| | Odd | 1.1 | 7 | 750 |

Table 6.3: Optimized criteria for each $p_T(D^+)$ bin for the even and odd subsamples.

- derivation of the invariant-mass template and shape of the $D^+$-mesons produced. It is needed to perform the fit to extract the yields in each bin of $p_T$.
- derivation of the impact-parameter templates and shapes of the prompt and secondary $D^+$-mesons produced. They will be needed to separate the prompt fraction from the secondary contribution.
- estimate of the reconstruction efficiency of the selection.

The Bgenerator is used, consistently with the official simulated samples of CDF's flavour group. The Bgenerator is explicity designed for beauty and charm physics [212]. It simulates the production and fragmentation of $b$ and $c$ quarks and the resulting hadron decays according to QQ, the CLEO Monte Carlo generator adapted for CDF. The Bgenerator algorithm needs the joint distribution of transverse momentum and rapidity for the generated input quark. Realistic input distributions that sample the $y$–$p_T$ domain in $[-1.3,\ 1.3]\times[0,\ 15]$ GeV are used. In addition, for a more detailed simulation of the actual experimental conditions, the offline database is used to tune the simulation. After the decay particles are generated, they are propagated towards the detector volume. Interactions with detectors materials are reproduced. Also, the responses of the different sub-detectors are simulated. To model the detector geometry and materials, the standard CDF II simulation uses version 3 of the Geant package [108]. It is tuned by data from test-beams and collision data. Position and four-momentum of each particle produced by the simulated

collisions and able to pass through the beam pipe, are requested by Geant as input. Later, their passage through the detector and all the interactions that take place are reproduced: ionization, bremsstrahlung losses, multiple scattering, pairs production etc ...

Many sub-detectors are simulated by specific packages rather than Geant. For instance, GFLASH [213] replaces Geant to mimic the calorimeter response. It is a parametric shower-simulator tuned from single particle response and shower shape using test beam data (8-230 GeV electrons and charged pions) and collision data (0.5-40 GeV single isolated tracks). For the silicon detector, a parametric charge deposition model, tuned on data, is exploited. It accounts for restricted Landau distribution, production of $\delta$ rays, capacitive charge sharing between neighboring strips, noise, etc., while the GARFIELD standard package [214], tuned on data, mimics the drift time within the COT.

Between the data acquisition periods, the detector and trigger configuration underwent several changes. For instance, after major hardware improvements, large modifications occurred. At the same time, relative mis-alignments between subdetectors, local or temporary inefficiencies of the silicon tracker (active coverage, noisy channels, etc ... ) must be considered. In order to have a more detailed simulation of the actual experimental conditions, the off-line database is used to tune the simulation. On a run-by-run basis, all known variations in configuration are taken into account. So, a detailed simulation of real runs is available, allowing to match, in any given sample, the distribution of data and MC. In order to analyze simulated data with the same reconstruction programs used for data, the two samples share the same output format.

MC events follow the same reconstruction chain as in data and, after the detector simulation, the same candidate selection applied to data is used. Finally, MC events are distributed across data-taking-time periods *P0–P38* in proportions that approximate the actual integrated luminosity collected in each period.

#### 6.4.0.1 $D^+ \to K^-\pi^+\pi^+$

A sample of about 75 million $D^{\pm}$-mesons, forced to decay into the $K^{\mp}\pi^{\pm}\pi^{\pm}$ final state, is generated in equal proportions for the $D^+$ and $D^-$ mesons. This sample is used to derive mass and impact-parameter templates to be used in the yield fits. The top-left panel of Fig. 6.11 shows the resulting $K^-\pi^+\pi^+$ mass distribution. A

long tail at lower masses is evident, due to final state radiation.

Previous studies [215] have shown that the MC does not correctly reproduce the COT occupancy and thus the number of hits associated with each track. This results in an incorrect simulation of the single-track *absolute* reconstruction efficiency of the COT. Thus, the samples are generated by adding additional MB interactions as underlying events to the $D^+$ signal as suggested in [215]. Nevertheless, the distribution of primary-vertex multiplicity of this simulation does not match perfectly that of experimental data in each data-taking-time period. Hence, the primary-vertex multiplicity distribution of simulated events is reweighted to reproduce the actual distribution observed in data. The data sample is divided into five subsamples according to data-taking-time periods. Figure 6.11 shows the simulated mass distribution and the simulated primary-vertex distribution for each data-taking-time period before the reweighting. This sample is used to measure the $D^+$ reconstruction efficiency, as reported in Sec. 6.6.2.

#### 6.4.0.2 $B^{\pm,0} \to D^+ X$

In addition to the prompt $D^+$-mesons generated, 36 million $B^0$ and 36 million $B^\pm$ decays are generated. $B$-mesons are forced to decay only into final states involving at least one $D^\pm$ meson, which is in turn forced to decay into the $K^\mp\pi^\pm\pi^\pm$ final state. This sample is used to define the templates that describe the secondary $D^+$ sample coming from $B$-meson decays.

## 6.5 Signal Yield

For events restricted to each transverse-momentum bin, the $D^+$ signal yield is determined by performing a two-dimensional maximum likelihood fit to the unbinned $K^-\pi^+\pi^+$-invariant-mass and candidate-impact-parameter distributions.

It is assumed that three components contribute in the signal region: primary signal, secondary $D^+$ decays originating from $B$-meson decays, and combinatorial candidates composed of three unrelated tracks that combine, yielding signal-like values of invariant mass.

Using only the $D$-mass information, it is not possible to distinguish between primary and secondary $D^+$ components. The impact-parameter distribution helps

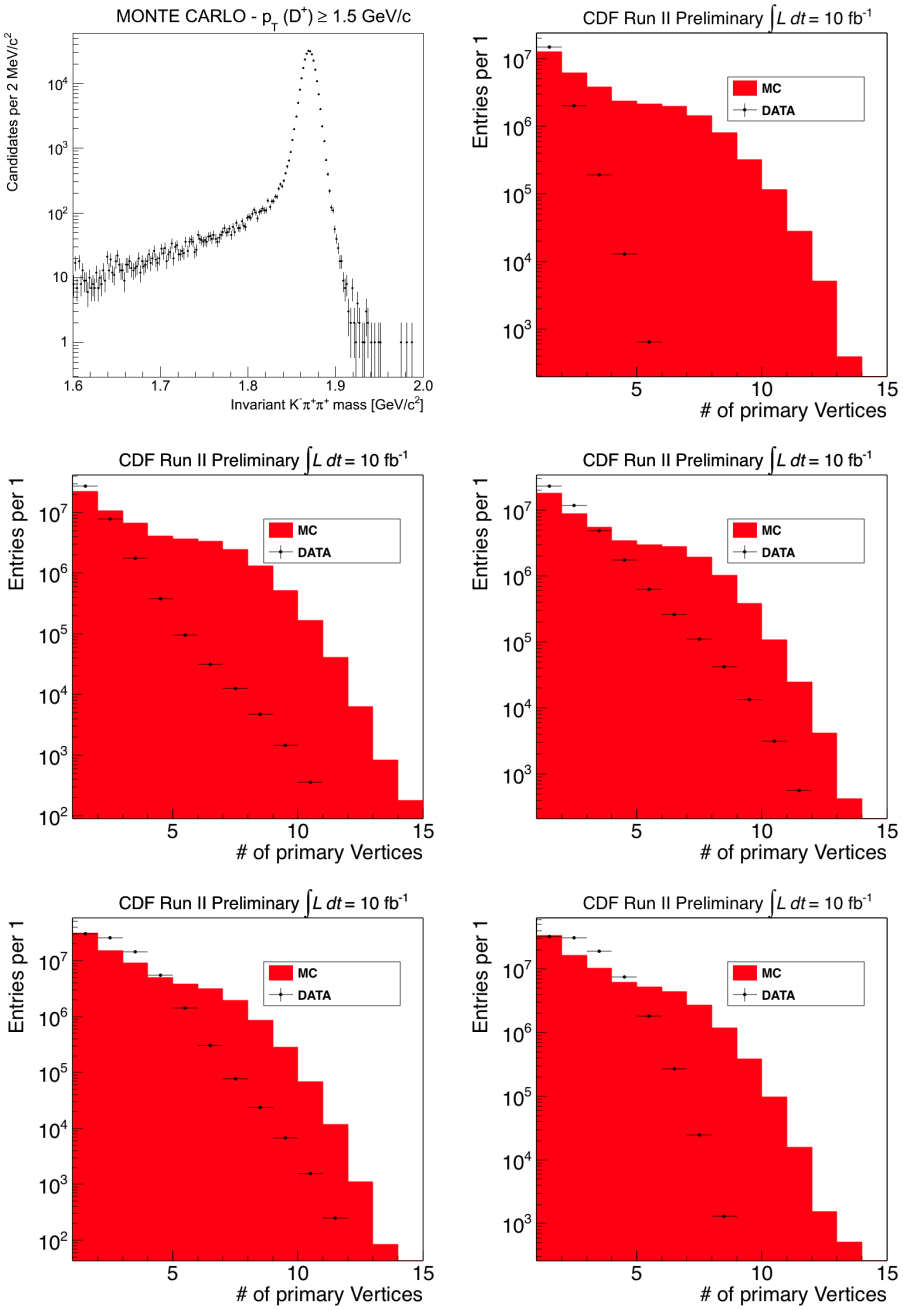


Figure 6.11: $K^-\pi^+\pi^+$ mass distribution of simulated candidates (top left). Distributions of primary-vertex multiplicity in simulation (red area) and data (black markers) for each data-taking-time period (all other panels).

in separating the two components. The shapes for the prompt and secondary impact-parameter distributions are determined using simulations, while the combinatorial background shape is determined using data.

For each component, mass and impact-parameter are independent variables. Thus, the likelihood function for $N$ candidates is:

$$\mathcal{L}(f_P, f_S) = \prod_{i=1}^{N} f_P F_{P,S}(m_i) F_P(d_{0,i}) + f_S F_{P,S}(m_i) F_S(d_{0,i}) + (1 - f_P - f_S) F_C(m_i) F_C(d_{0,i}) \tag{6.6}$$

where $m_i$ and $d_{0,i}$ are the mass and impact parameter, respectively, of the $i^{th}$ candidate, $F_{P,S}(m)$ is the $K^-\pi^+\pi^+$ mass shape common to the primary and secondary components; $F_P(d_0)$, $F_S(d_0)$ and $F_C(d_0)$ are the shapes of the $D^+$-impact-parameter distributions for the primary, secondary, and combinatorial components, respectively; and $F_C(m)$ is the mass shape for the combinatorial component. The free parameters are the prompt and secondary fractions, $f_P$ and $f_S$. While an extended likelihood would be more appropriate in a cross-section measurement, the size of the sample is such that in any transverse-momentum bin the additional uncertainty associated with the total number of candidates is irrelevant in the fit results. Hence, a simpler non-extended fit is preferred.

### 6.5.1 Modeling

The $D^+$ mass shapes are modeled from a single fit to the invariant $K^-\pi^+\pi^+$ mass distribution of the whole sample using a Gaussian shape modeled by simulation for the signal and an empirical shape for background. Primary and secondary signals are modeled with a sum of a Gaussian functions and the combinatorial background is modeled with a second-order polynomial:

$$F_{P,S}(m; \vec{\theta}_{P,S}) = \mathcal{G}(m; \mu_{P,S}, \sigma_{P,S}) \quad \text{and} \quad F_C(m; \vec{\theta}_{Cm}) = p_2(m; a, b, c) \tag{6.7}$$

To determine the impact-parameter shapes for the prompt and secondary candidates, the simulated samples described in Sec. 6.4.0.1 and 6.4.0.2 are used. For events restricted to each $p_T(D^+)$ bin, the impact-parameter line shape of prompt

and secondary candidates is parametrized with a sum of three Gaussians:

$$F_P(d_0;\vec{\theta}_P) = f_{P1}\cdot\mathcal{G}(d_0;\vec{\theta}_{P1}) + f_{P3}\cdot\mathcal{G}(d_0;\vec{\theta}_{P2}) + (1-f_{P1}-f_{P2})\cdot\mathcal{G}(d_0;\vec{\theta}_{P3}) \quad (6.8)$$

$$F_S(d_0;\vec{\theta}_S) = f_{S1}\cdot\mathcal{G}(d_0;\vec{\theta}_{S1}) + f_{S2}\cdot\mathcal{G}(d_0;\vec{\theta}_{S2}) + (1-f_{S1}-f_{S2})\cdot\mathcal{G}(d_0;\vec{\theta}_{S3}) \quad (6.9)$$

For the impact-parameter shape of the combinatorial component, the distribution of candidates reconstructed in the mass sidebands 1.7 – 1.8 GeV and 1.9 – 2.0 GeV is used. It is a sum of two Gaussian functions:

$$F_C(d_0;\vec{\theta}_C) = f_{C1}\cdot\mathcal{G}(d_0;\mu_{C1},\sigma_{C1}) + (1-f_{C1})\cdot\mathcal{G}(d_0;\mu_{C2},\sigma_{C2}) \quad (6.10)$$

Modeling of distributions in the lowermost transverse momentum bin, 1.5 – 2.5 GeV, requires special treatment because the combinatorial background shows two nearly symmetric structures in the impact-parameter distribution, as evident in Fig. 6.21. Such an effect is attributed to a bias resulting from the selection requirements implemented in this bin, as a result of the optimization procedure. No similar effects are reproduced in the MC for the prompt and secondary component, as shown in Fig. 6.12. Figure 6.13 shows the signal region before and after sideband subtraction for events restricted to the $p_T(D^+)$ bin 1.5 – 2.5 GeV, showing no unusual structures in the sideband-subtracted distribution. These structures do not affect the signal extraction, as long as they are well modeled in the fit. A sum of six Gaussian functions is empirically introduced to model them:

$$\begin{aligned} F_C(d_0;\vec{\theta}_C) &= f_1\cdot[f_{C1}\cdot\mathcal{G}_1 + f_{C2}\cdot\mathcal{G}_2 + (1-f_{C1}-f_{C2})\cdot\mathcal{G}_3] \\ &+ (1-f_1)\cdot[f_{C3}\cdot\mathcal{G}_4 + f_{C4}\cdot\mathcal{G}_5 + (1-f_{C2}-f_{C3})\cdot\mathcal{G}_6] \end{aligned} \quad (6.11)$$

Figures 6.14 and 6.15 show the shape parametrization for each component for candidates restricted to 3.5 – 4.5 GeV in transverse momentum for the even-numbered events.

### 6.5.2 Yield Extraction

The two-dimensional mass-IP fit is the core element of the measurement, since it allows the extraction of the raw signal yields from which cross-section results are derived. Therefore, a validation of the maximum-likelihood estimator - based on

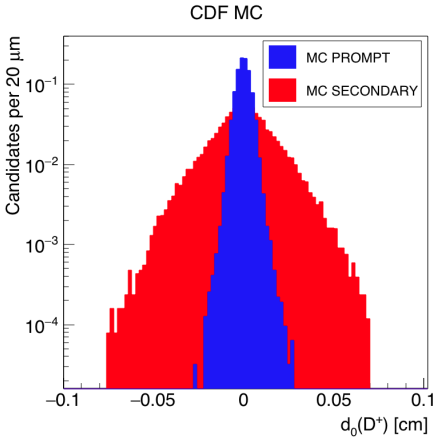


Figure 6.12: Impact-parameter distribution for simulated candidates restricted to $p_T(D^+)$ in 1.5 – 2.5 GeV.

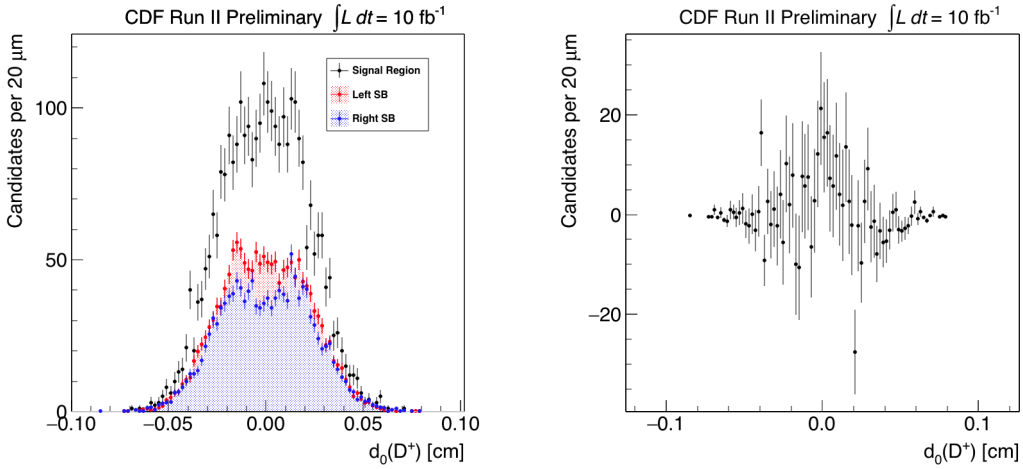


(a) Before sideband subtraction (b) After sideband subtraction

Figure 6.13: Impact-parameter distribution of candidates in the signal region before (a) and after (b) sideband subtraction for $p_T(D^+)$ in 1.5 – 2.5 GeV.

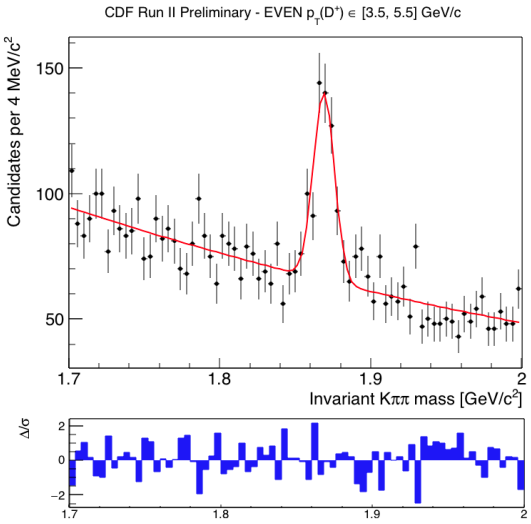


Figure 6.14: Shape parametrization for the signal and combinatorial background component in the invariant mass distribution for $p_T(D^+)$ in the range 3.5 – 4.5 GeV for the even-numbered events.

simulated pseudo-experiments - is performed. For each $p_T(D^+)$ bin and for each subsample (even- and odd-numbered events), an ensemble containing many pseudo-datasets is generated. Each ensemble is produced by randomly drawing numbers distributed according to the two-dimensional probability density function obtained in the analysis. In each, the true values for the fractions of primary and secondary $D^+$-mesons, determined by the fit to data, are input. Each of the pseudo-datasets is fit in the same way as the data and the distributions of the resulting estimates are studied. In Figs. 6.16 - 6.20 the pull distributions are shown for the various $p_T(D^+)$ bins. As expected, they approximate Gaussian distributions centred at zero with widths compatible with the statistical uncertainty determined by the fit to data. This shows that the maximum-likelihood estimator is unbiased and leads to reliable uncertainties.

The data fit results are summarized in Table 6.4 and fit projections are shown in Figures 6.21 - 6.25.

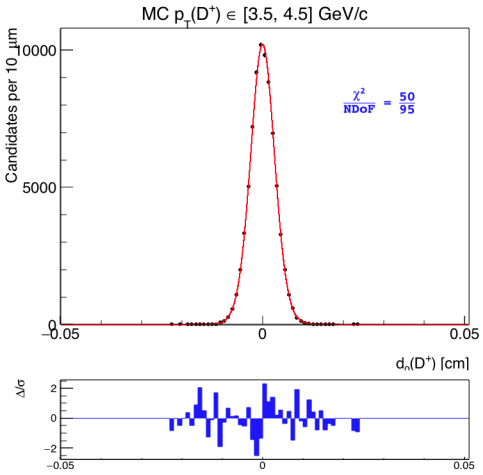


(a) Prompt $D^+$-mesons

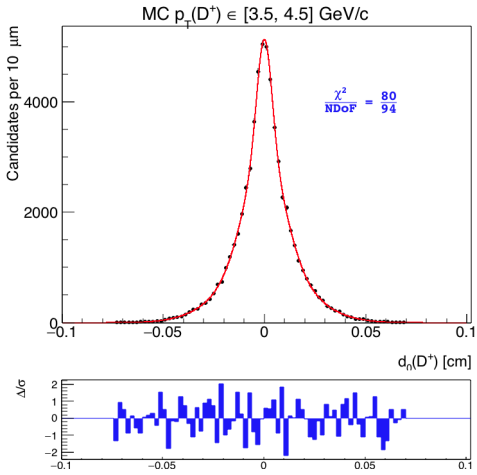


(b) Secondary $D^+$-mesons

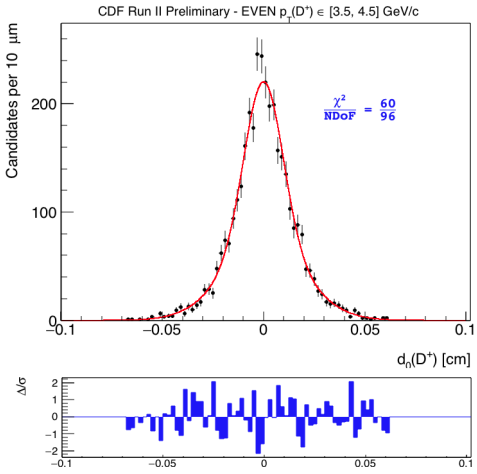


(c) Combinatorial background

Figure 6.15: Shape parametrization of the impact-parameter distribution for the $D^+$ prompt (a), secondary (b) and combinatorial component (c) for $p_T(D^+)$ in the range 3.5 – 4.5 GeV for the even-numbered events.

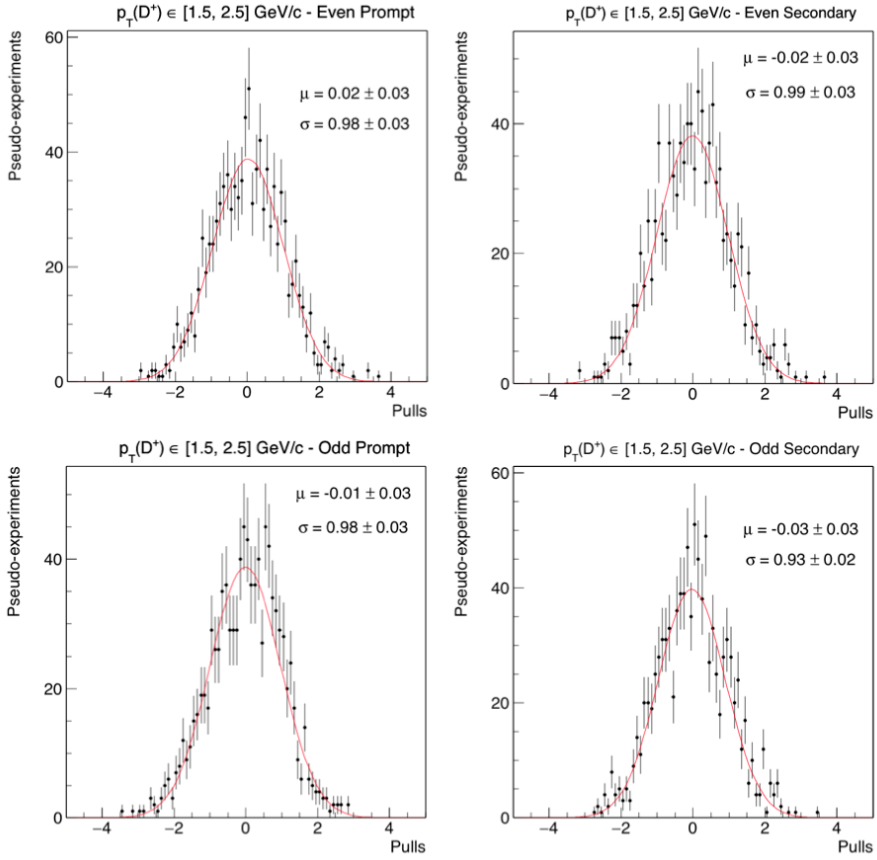


Figure 6.16: Pull distribution for the primary (left) and secondary (right) component for the even (top) and odd (bottom) pseudo-datasets of events restricted to the $p_T(D^+)$ range 1.5 – 2.5 GeV.

## 6.6 Efficiencies

The global efficiency for selecting and reconstructing a genuine $D^+$ signal decay, $\varepsilon(D^+)$, can be defined as the probability for a $D^+$ candidate to pass the trigger, reconstruction and offline-selection criteria. The estimation of $\varepsilon(D^+)$ is restricted to mesons reconstructed in the region $|y(D^+| \leq 1$:

$$\varepsilon(D^+) = \left. \frac{N_{\text{candidates}}(p_T) \text{ passing the Trig \& Rec}}{N_{\text{generated}}(p_T)} \right|_{|y|\leq 1} \tag{6.12}$$

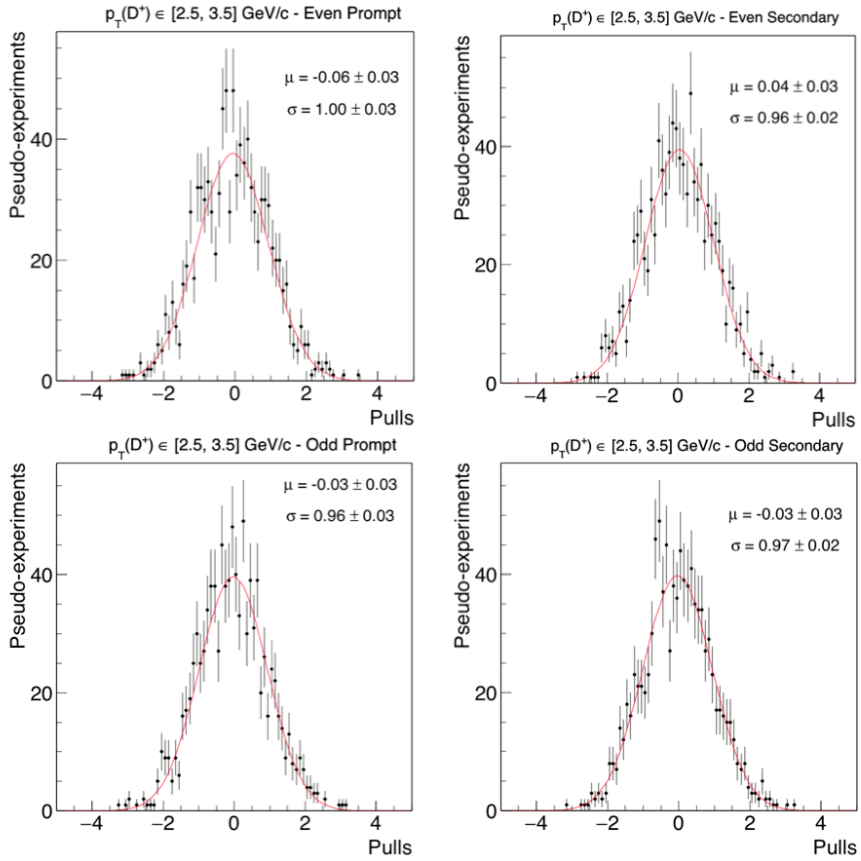


Figure 6.17: Pull distribution for the primary (left) and secondary (right) component for the even (top) and odd (bottom) pseudo-datasets of events restricted to the $p_T(D^+)$ range 2.5 – 3.5 GeV.

It is convenient to factorize the efficiency into the product of two main contributions: trigger, $\varepsilon_{\text{trig}}$, and reconstruction efficiency, $\varepsilon_{\text{rec}}$

$$\varepsilon(D^+) = \varepsilon_{\text{trig}} \times \varepsilon_{\text{rec}}(p_T) \tag{6.13}$$

The trigger efficiency is independent of features of the signal candidates and the event number. The reconstruction efficiency varies across $p_T$ ranges and between odd- and even-numbered events, which are selected with different offline criteria.

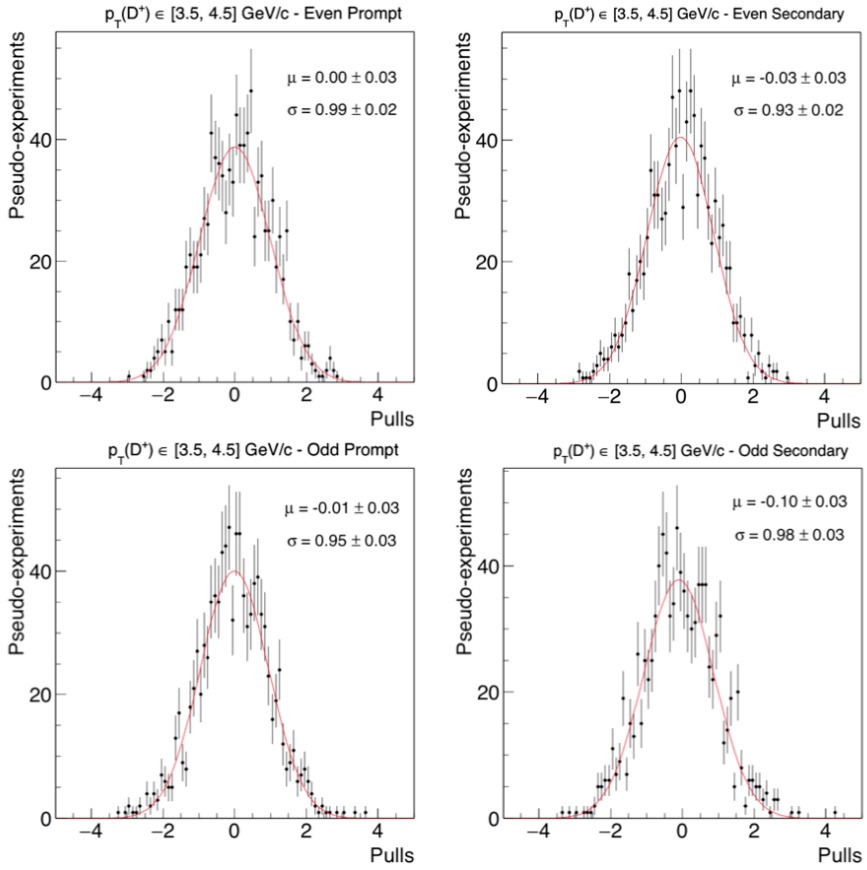


Figure 6.18: Pull distribution for the primary (left) and secondary (right) component for the even (top) and odd (bottom) pseudo-datasets of events restricted to the $p_T(D^+)$ range 3.5 – 4.5 GeV.

### 6.6.1 Trigger Efficiency

The term $\varepsilon_{\text{trig}}$ represents the correction for any inefficiency due to the online data selection and acquisition. It is specific for each trigger path: $\varepsilon_{\text{ZB}}$ and $\varepsilon_{\text{MB}}$.

#### 6.6.1.1 Zero Bias

The only possible source of inefficiency for the ZB trigger is the dead time incurred through the three-level trigger chain. However, each trigger path's integrated luminosity is automatically corrected for this dead time. Hence, the value stored in the luminosity database does not need to be corrected and $\varepsilon_{\text{ZB}} = 1$ [216].

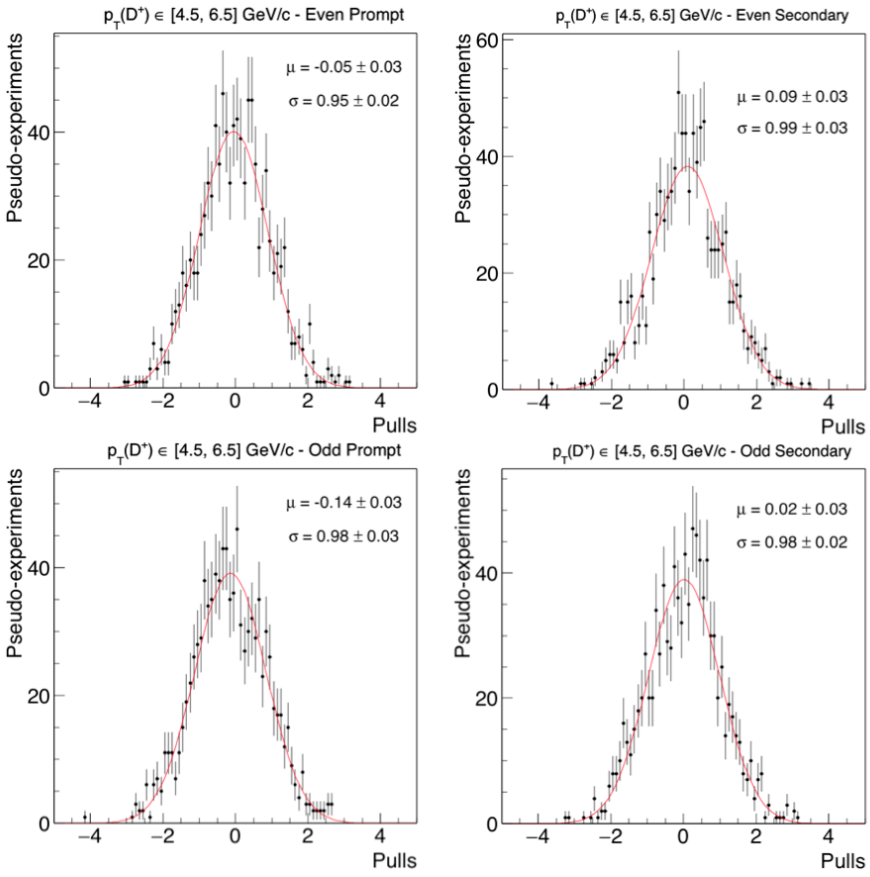


Figure 6.19: Pull distribution for the primary (left) and secondary (right) component for the even (top) and odd (bottom) pseudo-datasets of events restricted to the $p_T(D^+)$ range 4.5 – 6.5 GeV.

#### 6.6.1.2 Minimum Bias

Unlike ZB, the MB trigger efficiency is strongly dependent on beam conditions and event topology. After studying many event variables [217–219], it has been observed that it is mainly related to three quantities:

- the instantaneous luminosity, $L_{inst}$;
- the number of tracks in the event;
- the number of reconstructed primary vertices.

The quantities listed are closely related. If the luminosity increases, the number of interactions, the number of reconstructed primary vertices, the number of charged

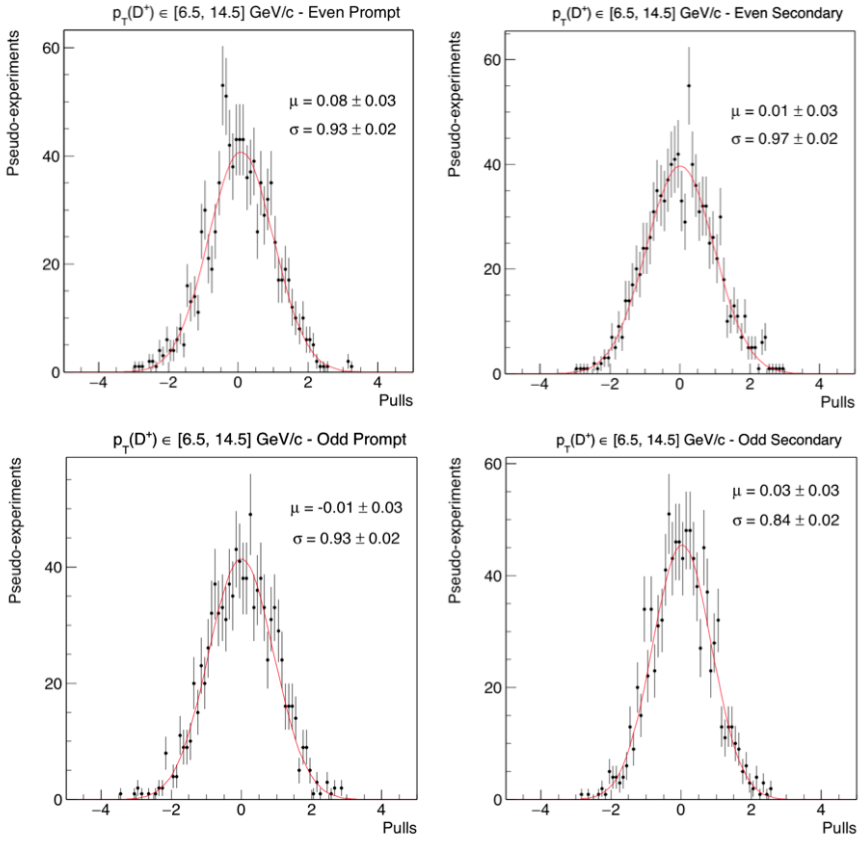


Figure 6.20: Pull distribution for the primary (left) and secondary (right) component for the even (top) and odd (bottom) pseudo-datasets of events restricted to the $p_T(D^+)$ range 6.5 – 14.5 GeV.

tracks and, hence, the probability of a coincidence in both East and West CLCs, grow up. Therefore, the efficiency rises as a function of these variables.

As $\varepsilon_{ZB} = 1$, it is possible to use the ZB data sample to evaluate $\varepsilon_{MB}$. In fact, each CDF event is labeled according to the trigger status of all the active triggers: if a particular ZB event has also been triggered by the MINBIAS trigger, the information is stored. Thus, the ratio of the number of $D^+$ candidates found in the ZB events with the MB trigger fired ($Y_{ZB\&MB}$) to the number of $D^+$ candidates found in the total ZB event-set ($Y_{ZB}$) represents the MB trigger efficiency for events with a $D^+$ candidate:

$$\varepsilon_{\mathrm{MB}}(D^+) = \frac{\mathrm{Y_{ZB\&MB}}}{Y_{\mathrm{ZB}}} \tag{6.14}$$

| $p_T$ [GeV/$c$] | Subsample | Primary yield | Secondary yield |
|---|---|---|---|
| 1.5 – 2.5 | Even | 170 ± 40 | 59 ± 76 |
| | Odd | 125 ± 40 | 83 ± 62 |
| 2.5 – 3.5 | Even | 366 ± 27 | 0 ± 40 |
| | Odd | 307 ± 34 | 17 ± 42 |
| 3.5 – 4.5 | Even | 301 ± 28 | 33 ± 33 |
| | Odd | 304 ± 28 | 66 ± 33 |
| 4.5 – 6.5 | Even | 384 ± 29 | 66 ± 29 |
| | Odd | 389 ± 29 | 50 ± 29 |
| 6.5 – 13.5 | Even | 278 ± 24 | 52 ± 19 |
| | Odd | 327 ± 27 | 46 ± 19 |

Table 6.4: Results of the 2D-fit for the five $p_T(D^+)$-bins.

with the corresponding uncertainty:

$$\sigma_{\varepsilon_{\mathrm{MB}}} = \sqrt{\frac{\varepsilon_{\mathrm{MB}}(1-\varepsilon_{\mathrm{MB}})}{Y_{\mathrm{ZB}}}} \tag{6.15}$$

The numerator and denominator of the ratio are extracted from a combined fit to the invariant $K^-\pi^+\pi^+$-mass-distribution of candidates from events that are selected by the ZB trigger and fired, or not, the MB trigger. The denominator of the ratio is evaluated as $Y_{\mathrm{ZB}} = Y_{\mathrm{ZB\&MB}} + Y_{\mathrm{ZB!MB}}$, where $Y_{\mathrm{ZB\&MB}}$ and $Y_{\mathrm{ZB!MB}}$ are the signal yields resulting from fits of ZB events that triggered MB or not. The fit is performed assuming the same modeling used for the signal-yield mass fits, described in Sec. 6.5.1. However, the background shape is the same for events that fire MB and those that don't. Figure 6.26 shows the results obtained for the inclusive sample of candidates with $p_T(D^+) \geq 1.5$ GeV. Possible $p_T$ dependencies for the MB efficiency are small enough to be safely neglected for the purposes of this analysis.

The result obtained is $\varepsilon_{\mathrm{MB}}(D^+) = 0.988 \pm 0.004$. Since the MB sample represents about 43% of the total, the overall effect of the MB trigger inefficiency is reduced to the level of $\mathcal{O}(10^{-3})$. Thus, the two subsamples (ZB and MB) can be safely combined into a sole merged sample because any uncertainty is negligible with respect to the final 5 - 10% uncertainties estimated for the $D^+$ yields. In principle, the MB trigger might be sensitive to the effects listed above also for events containing a $D^0$ candidate, but this is irrelevant since the efficiency is so high. As a result, $\varepsilon_{\mathrm{MB}}$ is assumed to be unity and the corresponding uncertainty is treated as a systematic

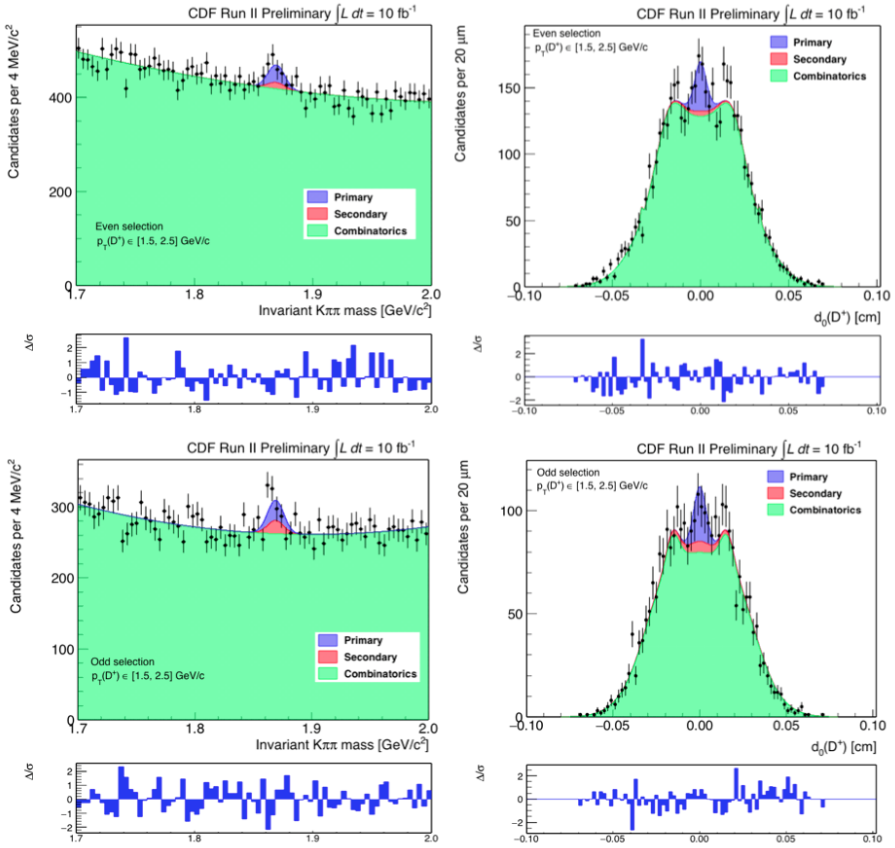


Figure 6.21: Distributions of the $K^-\pi^+\pi^+$-invariant mass (left) and impact parameter (right) with fit projections overlaid for the even subsample (top) and odd subsamples (bottom) of events restricted to the $p_T(D^+)$ range 1.5 – 2.5 GeV.

effect.

### 6.6.2 Reconstruction Efficiency

In order to measure the differential production cross-section $d\sigma/dp_T$ of $D^+$ mesons - *averaged* over a given $p_T$ interval and *integrated* over [-1,+1] in $y$ - the yield of signal decays observed in data needs to be divided also by the offline selection and reconstruction efficiency, $\varepsilon_{\rm rec}$. Such a term differs across even and odd samples, transverse-momentum bins and defines a global reconstruction efficiency. In fact, it takes into account different corrections:

- detector response to the passage of particles;

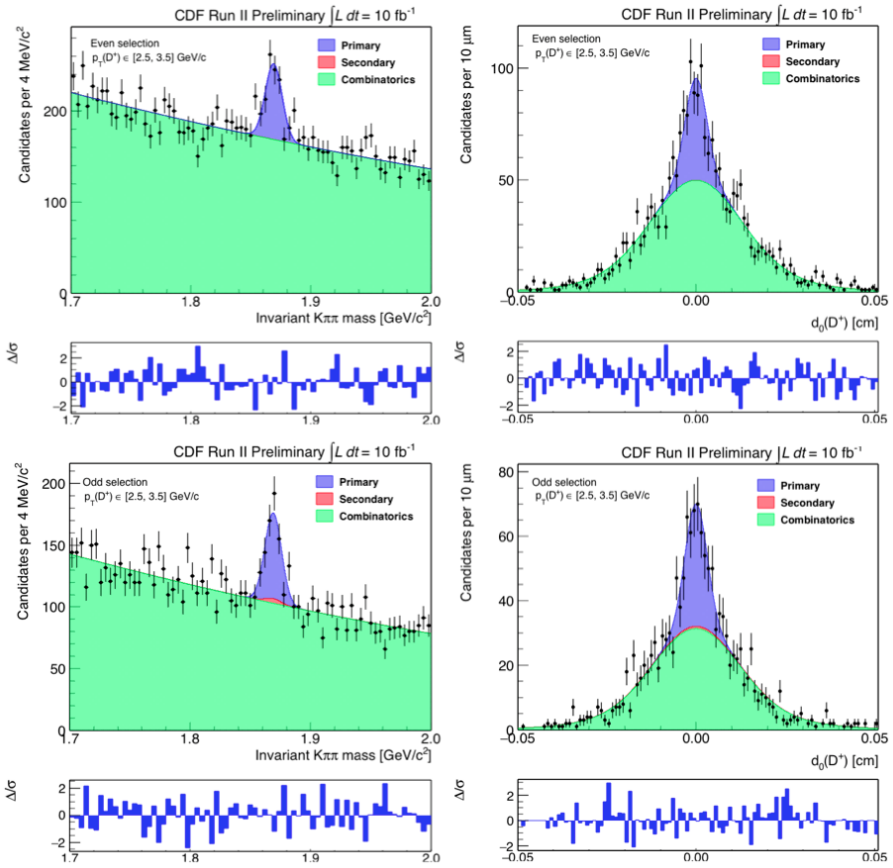


Figure 6.22: Distributions of the $K^-\pi^+\pi^+$-invariant mass (left) and impact parameter (right) with fit projections overlaid for the even subsample (top) and odd subsamples (bottom) of events restricted to the $p_T(D^+)$ range 2.5 – 3.5 GeV.

- tracking efficiency;
- efficiency and acceptance due to our selection of the candidates.

The reconstruction efficiency $\varepsilon_{\text{rec}}$ is determined from the signal samples simulated uniform in $y$ and with a $p_T$-spectrum described in Sec. 6.4.0.1. For each $p_T$ bin, the reconstruction efficiency is estimated as $\varepsilon_{\text{rec}}(p_T) = n(p_T)/N(p_T)$, where the denominator of the efficiency is the number $N$ of $D^+$ mesons generated in the $-1 < y < 1$ region and populating that $p_T$ bin and the numerator $n$ is the subset of $D^+$ that are reconstructed and meet the quality and offline-selection criteria. Table 6.5 summarizes the results obtained for the different $p_T(D^+)$ bins.

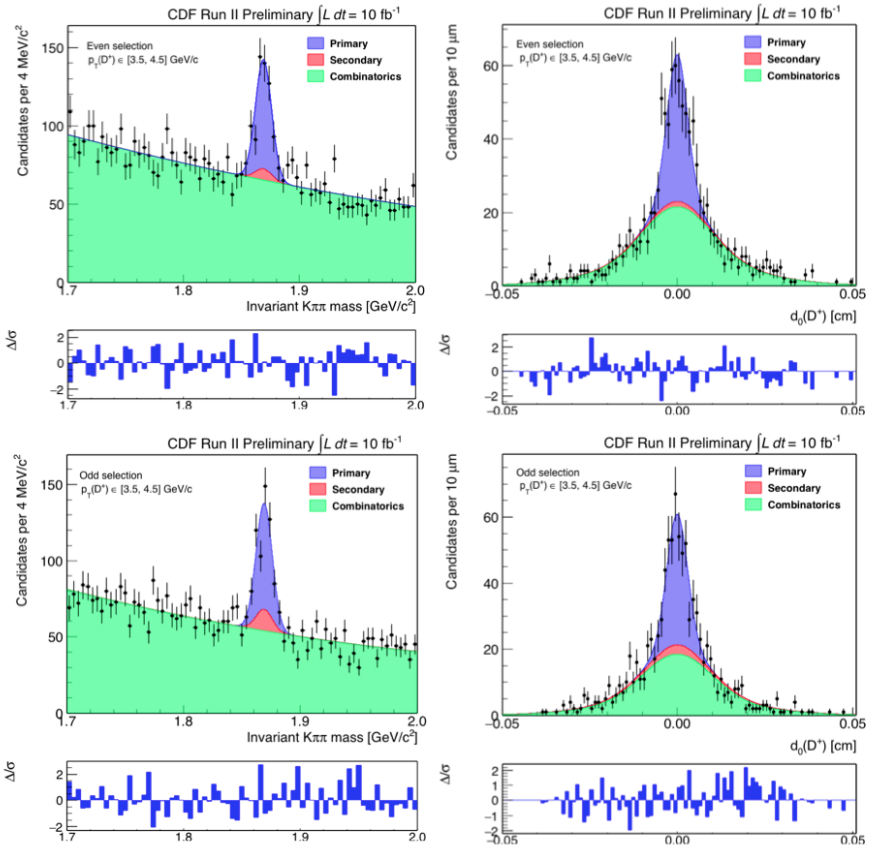


Figure 6.23: Distributions of the $K^-\pi^+\pi^+$-invariant mass (left) and impact parameter (right) with fit projections overlaid for the even subsample (top) and odd subsamples (bottom) of events restricted to the $p_T(D^+)$ range 3.5 – 4.5 GeV.

## 6.7 Systematic Uncertainties

The main sources of systematic uncertainties identified for this analysis and their estimated effects on the results are discussed in this section.

### 6.7.1 Luminosity

The integrated luminosity associated with the sample is obtained through the extrapolation of the total $p\bar{p}$ cross section from the measured value at $\sqrt{s} = 1.8$ TeV; the systematic uncertainty associated with this extrapolation is assessed in [216] to be $\sigma_{\mathcal{L}}^{sys} = 5.8\%$.

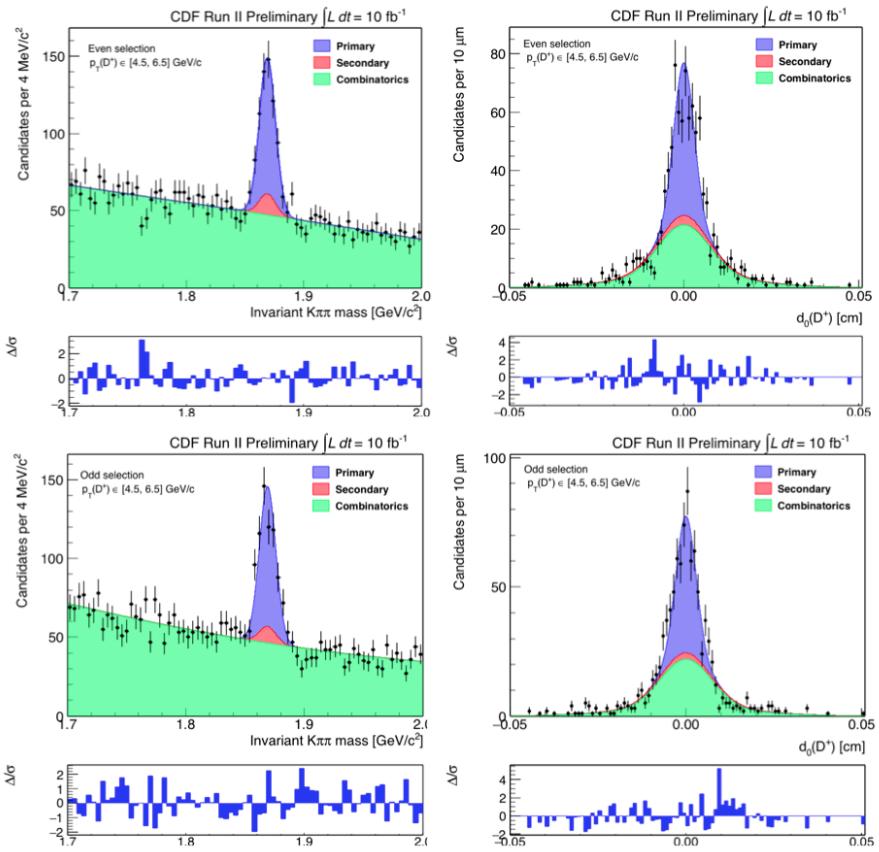


Figure 6.24: Distributions of the $K^-\pi^+\pi^+$-invariant mass (left) and impact parameter (right) with fit projections overlaid for the even subsample (top) and odd subsamples (bottom) of events restricted to the $p_T(D^+)$ range 4.5 – 6.5 GeV.

#### 6.7.1.1 Yield

Possible mismodelings affecting the mass and impact-parameter shapes could contribute to the systematic uncertainties. To assess the possible variations on the final results due to such mismodeling effects, the yield extraction is repeated using an alternative function to model more accurately the radiative tail of the distribution. The observed variations in results, $\Delta Y_{\text{sig}}$, are taken as systematic uncertainties.

To evaluate the effect of the combinatorial-background shape, the fit is repeated using an exponential function instead of a second-order polynomial function.

Variations, $\Delta Y_{\text{bkg}}$, from the measured values are taken as systematic uncertainties. Table 6.6 summarizes the values obtained for $\Delta Y_{\text{sig}}$ and $\Delta Y_{\text{bkg}}$ with $\sigma^{\text{sys}}_{\text{mass-shape}}$ indicating the sum in quadrature of the two contributions.

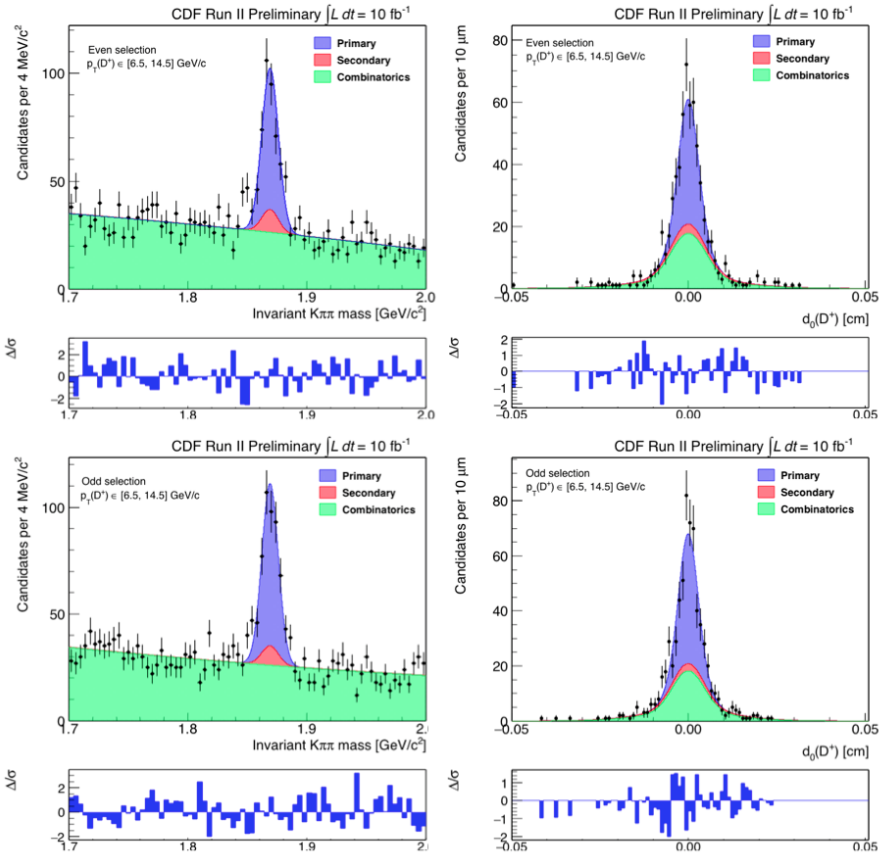


Figure 6.25: Distributions of the $K^-\pi^+\pi^+$-invariant mass (left) and impact parameter (right) with fit projections overlaid for the even subsample (top) and odd subsamples (bottom) of events restricted to the $p_T(D^+)$ range 6.5 – 14.5 GeV.

Variations in the final results may also occur due to mismodelings of the impact-parameter distributions. Thus, the impact-parameter fits are repeated with the inclusion of an additional Gaussian function to the prompt or secondary or combinatorial modeling. The resulting variations in the signal yields from the measured values, $\Delta Y_{\text{prompt}}$, $\Delta Y_{\text{sec}}$, and $\Delta Y_{\text{comb}}$ are taken as systematic uncertainties.

Table 6.7 summarizes the resulting values for $\Delta Y_{\text{prompt}}$, $\Delta Y_{\text{sec}}$ and $\Delta Y_{\text{comb}}$ with $\sigma^{\text{sys}}_{\text{IP-shape}}$ indicating the sum in quadrature of the two contributions.

Table 6.9 shows $\sigma^{\text{sys}}_{\text{shape}}$, which is the sum in quadrature of $\sigma^{\text{sys}}_{\text{mass-shape}}$ and $\sigma^{\text{sys}}_{\text{IP-shape}}$.

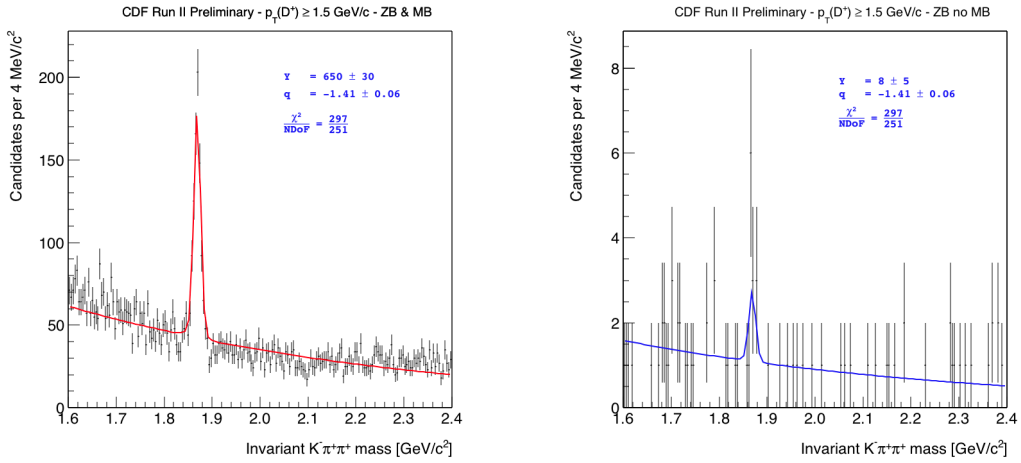


(a) $ZB$ AND $MB$ events (b) $ZB$ events

Figure 6.26: Result of the combined fit to the $K^-\pi^+\pi^+$-invariant-mass distribution for candidates that satisfied the ZB trigger and that fired (a) or not (b) the MB trigger.

| $p_T(D^+)$ [GeV/$c$] | Subsample | $\varepsilon_{\text{rec}}(D^+)$[%] |
|---|---|---|
| 1.5–2.5 | Even | 0.331 ± 0.011 |
| | Odd | 0.267 ± 0.010 |
| 2.5–3.5 | Even | 1.142 ± 0.026 |
| | Odd | 1.020 ± 0.025 |
| 3.5–4.5 | Even | 2.098 ± 0.047 |
| | Odd | 2.110 ± 0.047 |
| 4.5–6.5 | Even | 3.936 ± 0.073 |
| | Odd | 3.936 ± 0.073 |
| 6.5–14.5 | Even | 7.46 ± 0.15 |
| | Odd | 7.36 ± 0.15 |

Table 6.5: Reconstruction efficiency as a function of $p_T(D^+)$.

#### 6.7.1.2 Trigger efficiency

As reported in Sec. 6.6.1.2, the efficiency of the `MINBIAS` trigger is (98.8 ± 0.4)%. In the analysis the ZB and MB samples are combined. Since the ZB efficiency is 1, the total trigger efficiency is assumed to be 100% and the 0.4% uncertainty is treated as a systematic uncertainty for the final result. The MB sample is 43% of the total sample; thus, the final uncertainty associated with the trigger efficiency is estimated

| $p_T(D^+)$ [GeV/$c$] | Subsample | $\Delta Y_{\text{sig}}$ | $\Delta Y_{\text{bkg}}$ | $\sigma^{\text{sys}}_{\text{mass-shape}}$ |
|---|---|---|---|---|
| 1.5–2.5 | Even | 1.2% | 0.15% | 1.2% |
| | Odd | 1.1% | 0.052% | 1.1% |
| 2.5–3.5 | Even | 1.3% | 0.023% | 1.3% |
| | Odd | 1.4% | 0.10% | 1.4% |
| 3.5–4.5 | Even | 0.9% | 0.034% | 0.9% |
| | Odd | 1.1% | 0.030% | 1.1% |
| 4.5–6.5 | Even | 1.5% | 0.13% | 1.5% |
| | Odd | 1.3% | 0.092% | 1.3% |
| 6.5–14.5 | Even | 1.1% | 0.060% | 1.1% |
| | Odd | 1.3% | 0.048% | 1.3% |

Table 6.6: Systematic uncertainties associated with biases in the yield measurements due to possible mismodelings of the mass shapes.

| $p_T(D^+)$ [GeV/$c$] | Subsample | $\Delta Y_{\text{prompt}}$ | $\Delta Y_{\text{sec}}$ | $\Delta Y_{\text{comb}}$ | $\sigma^{\text{sys}}_{\text{IP-shape}}$ |
|---|---|---|---|---|---|
| 1.5–2.5 | Even | 0.05% | 0.020% | 0.10% | 0.11% |
| | Odd | 0.06% | 0.09% | 0.13% | 0.17% |
| 2.5–3.5 | Even | 0.20% | 0.05% | 0.04% | 0.21% |
| | Odd | 0.15% | 0.07% | 0.07% | 0.18% |
| 3.5–4.5 | Even | 0.03% | 0.08% | 0.10% | 0.13% |
| | Odd | 0.021% | 0.03% | 0.09% | 0.10% |
| 4.5–6.5 | Even | 0.12% | 0.09% | 0.04% | 0.16% |
| | Odd | 0.14% | 0.04% | 0.04% | 0.15% |
| 6.5–14.5 | Even | 0.06% | 0.13% | 0.07% | 0.16% |
| | Odd | 0.07% | 0.15% | 0.06% | 0.18% |

Table 6.7: Systematic uncertainties associated with the variations in impact-parameter shape, which can affect the yield measurement.

to be $\sigma^{\text{sys}}_{\varepsilon_{\text{trig}}} \sim 0.17\%$.

#### 6.7.1.3 Reconstruction efficiency

The CDF simulation is known to reproduce unreliably a number of relevant effects, namely the *conditional* efficiency for associating SVX hits to tracks that have been reconstructed in the COT and the details of the evolution of dead or noisy SVX channels as a function of data-taking time. Therefore, the value of the efficiency $\varepsilon_{\text{rec}}$ obtained from simulation and listed in Table 6.5 is used as the nominal value

for the reconstruction efficiency, but a generous systematic uncertainty - derived from control data samples - is added to account for these effects. It is convenient to partition the reconstruction associated with the numerator of the efficiency into three factorisable steps:

1. The three final-state tracks are reconstructed in the COT and meet the COT fiducial and quality requirements. It is crucial that, at this level, no information from the SVX is used. In the following description such tracks are labeled as *silicon-unbiased* tracks.

2. Silicon hits are associated to these silicon-unbiased tracks. A silicon-quality criterion is imposed on all three tracks requiring at least three axial and three stereo hits associated to each.

3. $D^+$ candidates that meet these requirements are used in further analysis and undergo the subsequent optimization. The resulting number of $D^+$ candidates represents simulated signal yields that mirror those observed in the analysis of experimental data.

The CDF Monte Carlo simulates reliably steps (1) and (3) [215], but not step (2). To include the effects of such mismodeling in the list of systematic uncertainties, it is assumed that the global efficiency for reconstructing a signal candidate $\varepsilon_{\rm rec}(D^+)$ can be factorized into the product of three conditional efficiencies, each corresponding to one of the three steps above:

$$\varepsilon_{\rm rec}(D^+) = \varepsilon_{\rm COT}(D^+) \times \varepsilon_{\rm SVX|COT}(D^+) \times \varepsilon_{\rm off}(D^+) \tag{6.16}$$

The systematic uncertainty is evaluated by comparing conditional[4] tracking efficiencies $\varepsilon_{\rm SVX|COT}$ derived from simulation with those derived from control samples. The largest observed discrepancy between the value of $\varepsilon_{\rm SVX|COT}$ per single track predicted by the simulation and that measured in data is determined. It is also assumed that the simulation reproduces correctly correlations of efficiencies between particles from the same decay. The validity of this assumption is tested and discussed later. The estimate of the systematic uncertainty therefore reduces to finding a sufficiently large sample of silicon-unbiased tracks, whose kinematic distributions

[4]Conditional means with respect to the COT.

mirror those of the $D^+$ tracks, and measuring which fraction of these tracks can be successfully associated with silicon information. Control samples of muon tracks from $J/\psi$-meson decays and soft pions ($\pi_s$) from $D^{*+} \to D^0(\to K^-\pi^+)\pi_s$ decays are studied.

#### 6.7.1.4 Conditional Silicon Single-track Efficiency Using $J/\psi$ Muons

A large sample of muon tracks from $J/\psi$ decays - collected by the dimuon trigger over the same data-taking period of the $D^+$ data - is introduced. Appendix C summarizes the details of the selection requirements. Out of the sample of muon tracks (consistent with coming from a $J/\psi$ decay) reconstructed as fiducial COT-only tracks, the fraction of those able to pass the silicon quality criteria is measured. This fraction is the *conditional silicon-efficiency for a single track* $\varepsilon_{\text{SVX|COT}}(\mu)$.

In order to test the reliability of the simulation in reproducing the conditional silicon-efficiency, a sample of $J/\psi$ mesons is generated in the same kinematic conditions as observed in data. Only muons reconstructed as in data are selected. For a proper data-to-simulation comparison, the simulated events are reweighted so that the $\cot\theta(\mu)$ distribution reproduces that observed in data. No further reweighting is needed in the $p_T(J/\psi)$ and $p_T(\mu)$ distributions, as shown in Fig. 6.27. MC efficiencies - $\varepsilon_{\text{SVX|COT}}(\mu)$ - as a function of $p_T(\mu)$ are then compared to the corresponding ones observed in data in various data-taking periods. Results are shown in Figure 6.28. For each data-taking period, a Scale Factor (SF) - corresponding to the ratio between the values of the plateaus resulting from fits to data and to simulated events - is measured.

However, the data-based values of $\varepsilon_{\text{SVX|COT}}(\mu)$ are not sufficient to probe discrepancies between Monte Carlo and data across the whole phase-space of interest. No muon-based efficiency is available for muons with transverse momentum below 1.5 GeV - phase space largely populated by $D^+$ tracks. This is due to the minimum transverse momentum needed for a muon to reach efficiently muon detectors. Figure 6.29 shows the transverse momentum distribution of the $D^+$ decay products for different $p_T(D^+)$ bins for one data-taking period. A significant fraction of $D^+$ decay products have $p_T < 1.5$ GeV.

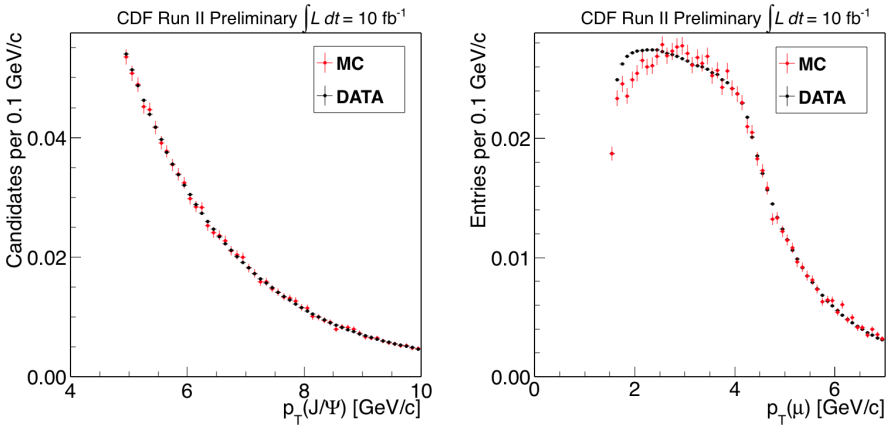


Figure 6.27: The $p_T(J/\psi)$ and $p_T(\mu)$ distributions in both data (black) and simulated events (red) for the time-integrated sample.

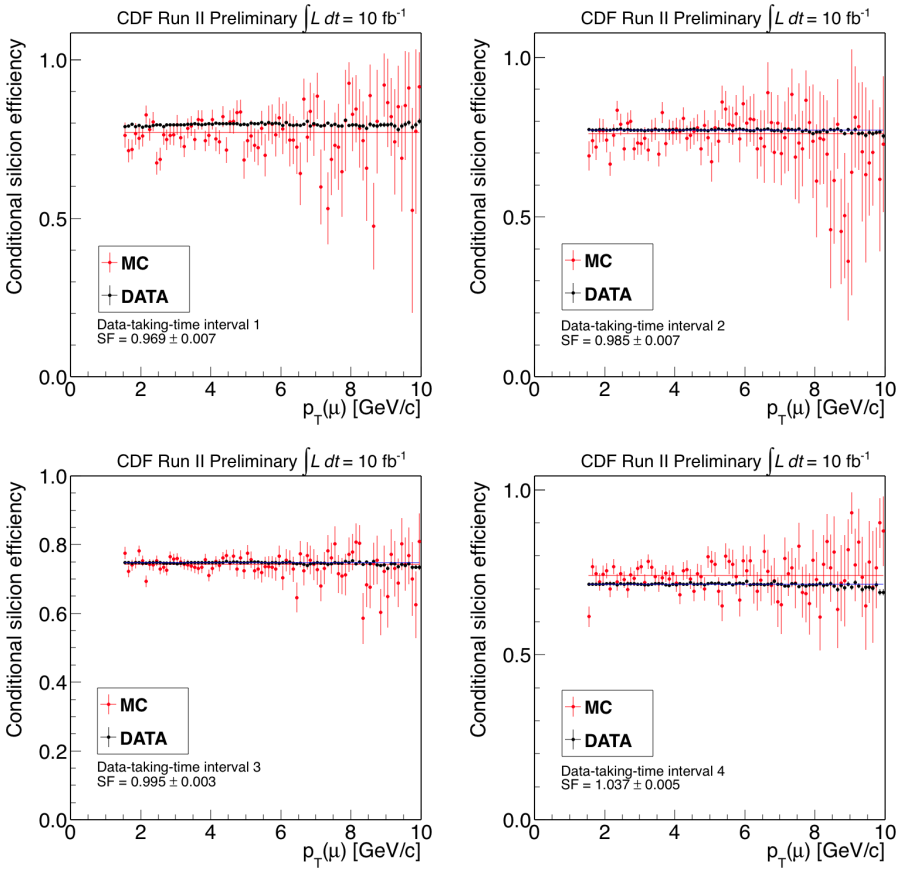


Figure 6.28: Conditional silicon single-track efficiency as a function of $p_T(\mu)$ for the first four data-taking periods, as observed in muons from $J/\psi$ decays - data (black) and simulated events (red).

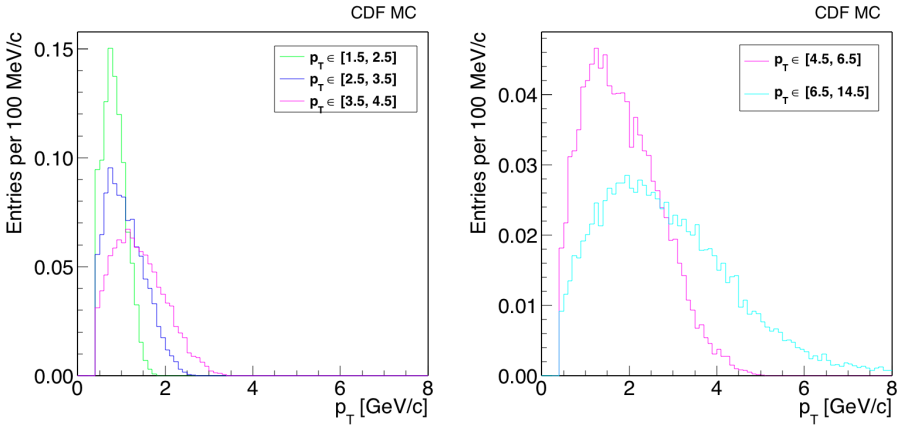


Figure 6.29: Transverse momentum distribution of $D^+$ decay products for different $p_T(D^+)$ bins for one data-taking period.

#### 6.7.1.5 Conditional Silicon Single-track Efficiency Using Soft Pions

The extraction of the conditional silicon efficiency is, therefore, extended to soft pions - $\pi_s^+$ - from the $D^{*+} \to \pi_s^+ D^0 (\to K^- \pi^+)$ sample. The momentum of the soft pion is expected to probe efficiently the low-momentum regime. Appendix C summarizes the details of the selection requirements. The reconstructed decay products of the $D^0$ are required to meet the trigger requirements. Similar to the efficiency study with muons, a sample of $D^{*+}$ decays with the same kinematic conditions as observed in data is generated. In addition, to improve data-to-MC agreement, the $cot\theta(\pi)$-distribution is reweighted to that observed in data. No further reweighting is needed in the $p_T(D^{*+})$ and $p_T(\pi)$ distributions, as shown in Fig. 6.30. The resulting distributions of $\varepsilon_{\mathrm{SVX|COT}}(\mu)$ as a function of $p_T(\pi)$ are then compared in data and MC. Because of the small size of the available simulated sample, data-to-MC comparisons cannot be performed in different data-taking periods. Thus, the time-integrated sample is used. Figure 6.31 reports the resulting scale factors between the plateau values fit to data and to simulated events.

Table 6.8 lists all scale factors. The maximum observed SF corresponds to a systematic uncertainty of 3.7% on the reconstruction efficiency per single track. Therefore, for a $D^+$ decaying into three particles, a conservative systematic uncertainty of 11.5% is inferred for all the $p_T(D^+)$ bins. This is the dominant systematic uncertainty of this measurement.

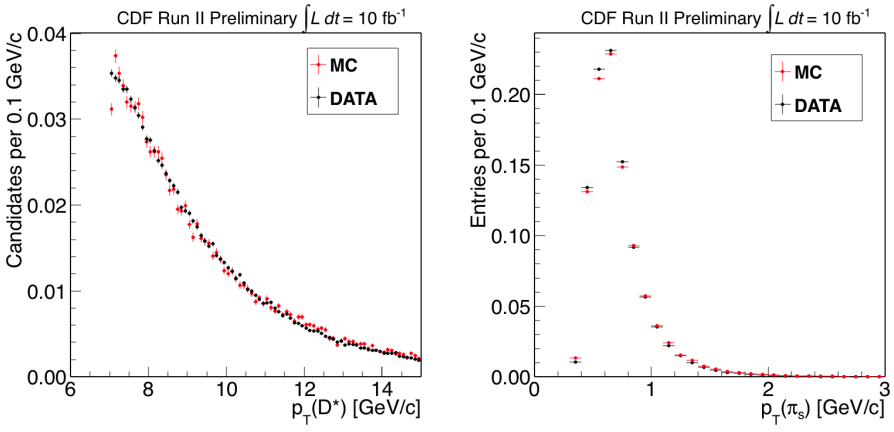


Figure 6.30: The $p_T(D^*)$ and $p_T(\pi)$ distributions in both data (black) and simulated events (red) for the time-integrated sample.

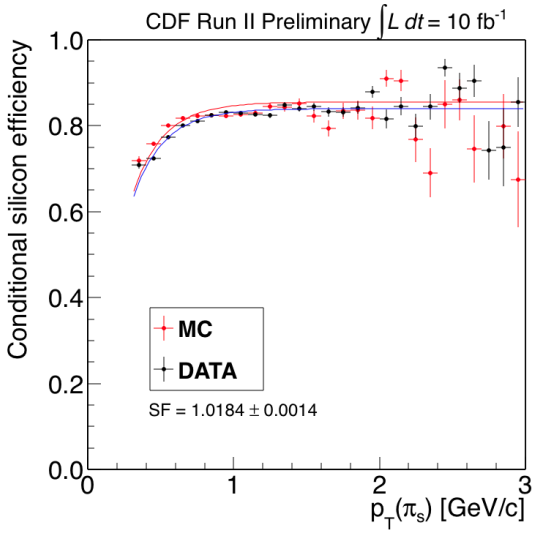


Figure 6.31: Conditional silicon single-track efficiency as a function of $p_T(\pi)$ as observed in the time-integrated sample for soft pions from $D^{*+} \to \pi_s^+ D^0$: data (black) and simulated events (red).

| Sample | Data-taking periods | $SF$ |
|---|---|---|
| $J/\psi$ | 1 | 0.969 ± 0.007 |
| $J/\psi$ | 2 | 0.985 ± 0.007 |
| $J/\psi$ | 3 | 0.995 ± 0.003 |
| $J/\psi$ | 4 | 1.037 ± 0.005 |
| $D^*$ | Time-integrated | 1.0184 ± 0.0014 |

Table 6.8: Conditional-silicon single-track efficiency scale factors for the control samples.

#### 6.7.1.6 Total Systematic Uncertainties

Table 6.9 summarizes the systematic uncertainties. The last column reports the sum in quadrature of all relevant contributions.

| $\sigma^{\text{sys}}_{\mathcal{L}}$ [%] | $\sigma^{\text{sys}}_{\text{shape}}$ [%] | $\sigma^{\text{sys}}_{\varepsilon_{\text{trig}}}$ [%] | $\sigma^{\text{sys}}_{\varepsilon_{\text{rec}}}$ [%] | $\mathcal{B}(D^+ \to K^-\pi^+\pi^+)$ [%] | $\sigma^{\text{sys}}_{\text{tot}}$ [%] |
|---|---|---|---|---|---|
| 5.8 | 0.9 - 1.5 | 0.17 | 11.5 | 0.24 | 13 |

Table 6.9: Summary of systematic uncertainties.

## 6.8 Results

Putting together all the ingredients according to Eq. (6.1) the differential cross sections for each bin of $p_T$ for even or odd subsamples can be measured. Values obtained independently in the even and odd samples are consistent, as shown in Figure 6.32 where only the statistical uncertainty has been included.

After averaging over even and odd samples, it's possible to measure the global differential cross-section. The measured differential cross sections, averaged over each $p_T$ bin and integrated over the rapidity range $|y| < 1$, are shown in Table 6.10 and displayed in Fig. 6.33. In each bin, the data point is displayed at the $p_T$ value at which the differential cross section equals its average over that $p_T$ bin, as determined using predictions from Ref. [206]. These effective $p_T$ values are also listed in Table 6.10. The observed cross sections are compatible with those predicted in recent calculations [206]. While the individual measurement points lie within the band of theoretical uncertainty, the experimental spectrum is systematically shifted to high $p_T$ -values as compared with theory. Hence, these results may help to further refine

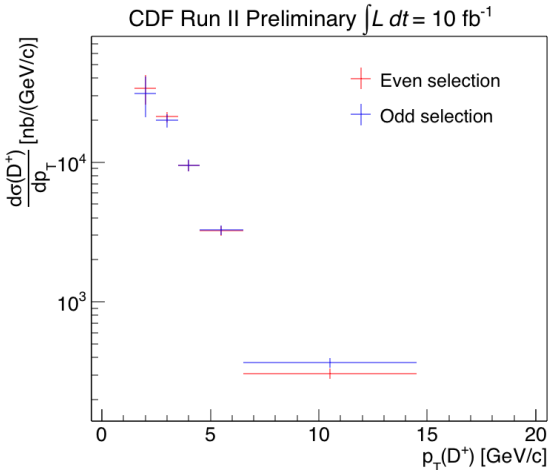


Figure 6.32: Measured $D^+$ production cross-section as a function of $p_T(D^+)$ separately for even- and odd-numbered events. Only the statistical uncertainty has been considered.

the shape of the theoretical cross section as a function of transverse momentum. The results may also be helpful for understanding backgrounds in astrophysical neutrino experiments at a few PeV, where most background sources are suppressed and the contributions from charm hadrons produced in the interaction of cosmic rays and atmospheric nuclei could be important.

| $p_T$ range [GeV/$c$] | Eff. $p_T$ [GeV/$c$] | $d\sigma(D^+, \lvert y\rvert < 1)/dp_T$ [$\mu$b/GeV/$c$] | $\sigma_i(D^+, \lvert y\rvert < 1)$ [$\mu$b] |
|---|---|---|---|
| 1.5 – 2.5 | 2.04 | $32.7 \pm 6.5 \pm 4.2$ | $32.7 \pm 6.5 \pm 4.2$ |
| 2.5 – 3.5 | 2.98 | $20.6 \pm 1.8 \pm 2.7$ | $20.6 \pm 1.8 \pm 2.7$ |
| 3.5 – 4.5 | 3.97 | $9.50 \pm 0.84 \pm 1.2$ | $9.50 \pm 0.84 \pm 1.2$ |
| 4.5 – 6.5 | 5.38 | $3.23 \pm 0.26 \pm 0.42$ | $6.46 \pm 0.52 \pm 0.84$ |
| 6.5 – 14.5 | 9.19 | $0.34 \pm 0.03 \pm 0.04$ | $2.69 \pm 0.22 \pm 0.35$ |

Table 6.10: Results for $D^+$-meson cross sections. All cross-section values are integrated over the range $|y| < 1$. The second column lists the "effective $p_T$" values at which the point-value of the cross section equals the predicted $p_T$-averaged value over the bin, as determined using Ref. [206]. Values in the third column are averaged over each $p_T$ bin. The first contribution to the uncertainties is statistical, the second systematic.

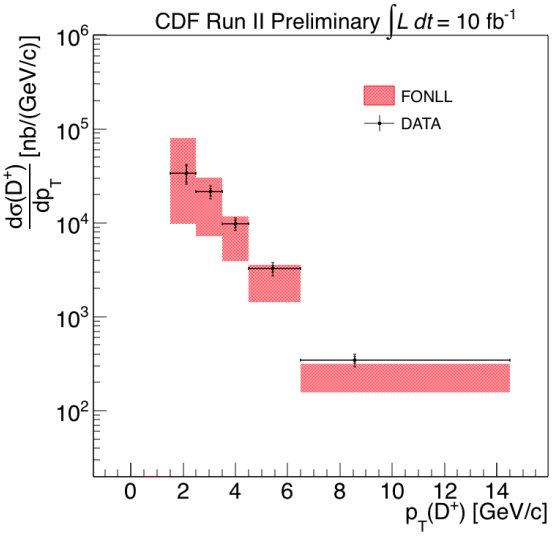


Figure 6.33: Measured $D^+$ production cross-section as a function of $p_T(D^+)$. In each bin, the data point is displayed at the $p_T$ value at which the differential cross section equals its average over that $p_T$ bin, as determined using predictions from Ref. [206]. These effective $p_T$ values are also listed in Table 6.10.

### 6.8.1 Comparison with Early CDF Run II Measurements

At higher transverse momentum, where the previous CDF measurements are available [74], the current measurements agree with earlier results. A direct comparison of the current results to the previous measurement based on early Run II data is not straightforward because of the different bin choices used in the two analyses. Also, the previous result published the cross section at a given $p_T$ value within each $p_T$ bin while for this result the cross section averaged across each $p_T$ bin is reported. Theoretical prediction can be used as a reference to normalize both the measurements to, allowing indirectly a comparison of the two results. To quantify the agreement, a weighted average of the Ratio=Data/Theory - calculated from the different $p_T$ bins - for both the measurements is performed and reported in Table 6.11. The agreement with the previous measurement is within less than half a standard deviation. For the purpose of showing the compatibility, the FONLL prediction can be used to transform the differential cross section from the average over a $p_T$ interval to the point value at the centre of the interval in a way similar to what was done in the previous result. In this way all the points, old and new, can be plot on the same scale with the theoretical prediction superimposed. Figure 6.34 shows the final plot

with both the measurements and the FONLL prediction.

CDF Run II Preliminary

| Current <R=Data/Theory> | Past<R=Data/Theory> | $\Delta/\sigma$ |
|---|---|---|
| 1.57±0.30 | 1.33±0.41 | 0.47 |

Table 6.11: Comparison between the previous [74] and the present CDF measurements.

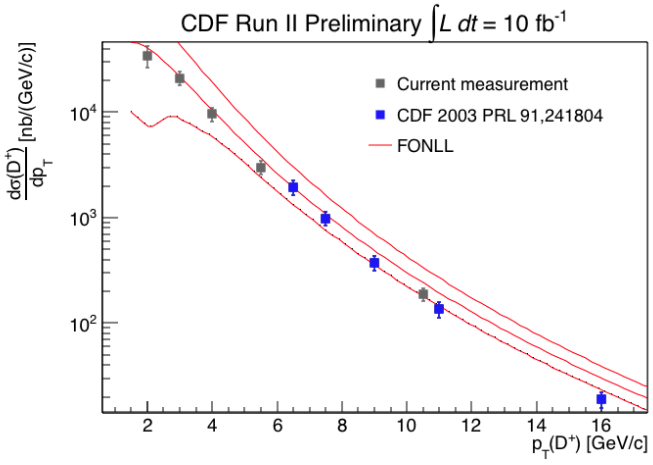


Figure 6.34: $D^+$ production cross section as a function of $p_T(D^+)$ at CDF Run II. For the purpose of showing the compatibility, the FONLL prediction can be used to transform the current differential cross section from the average over a $p_T$ interval to the point value at the centre of the interval in a way similar to what was done in the previous result. Theoretical predictions [206] are also shown.

# Chapter 7

# Conclusions

In this thesis all the activities I performed during my DPhil in particle physics at the University of Oxford are reported. I have presented results on Higgs physics and muon momentum performance with the ATLAS Collaboration and on charm physics with the CDF Collaboration.

*Higgs Physics at ATLAS.* The latest constraints on the signal strength of the off-shell Higgs boson production and the Higgs boson total width in the $ZZ \to \ell\ell\nu\nu$ and $ZZ \to 4\ell$ final states are presented, where $\ell$ stands for either an electron or a muon. The data were collected by the ATLAS experiment in 2015 and 2016 at the Large Hadron Collider, and they correspond to an integrated luminosity of 36.1 fb$^{-1}$. An observed (expected) upper limit on the off-shell Higgs signal strength, defined as the event yield normalised to the Standard Model prediction, of 5.3 (4.4) is obtained at 95% confidence level (CL) in the $ZZ \to \ell\ell\nu\nu$ channel. After the combination with similar results from the $ZZ \to 4\ell$ channel the reported observed (expected) limit is 3.8 (3.4) at 95% CL. Assuming the ratio of the Higgs boson couplings to the Standard Model predictions is independent of the momentum transfer of the Higgs production mechanism considered in the analysis, a combination with the on-shell signal-strength measurements yields an observed (expected) 95% CL upper limit on the Higgs boson total width of 14.4 (15.2) MeV.

Different assumptions can lead to different interpretations of these results. Assuming that the total width of the Higgs boson is as expected in the SM, and the coupling scale factors associated with on- and off-shell VBF production and the $H^* \to ZZ$ decay are the same, the same combination can be interpreted as a limit on

the ratio of the off-shell to the on-shell couplings to gluons $R_{gg} = \mu^{ggF}_{off-shell}/\mu^{ggF}_{on-shell}$. An observed (expected) limit of 4.3 (4.1) at 95% CL on $R_{gg}$ is obtained.

*Muon Momentum Performance at ATLAS.* The ATLAS simulation includes the best knowledge of the detector geometry, material distribution, and physics modeling of the muon interaction with the material of the ATLAS sub-detectors. However, this is not enough to reproduce the muon momentum scale(resolution) of data at the needed level of permille(percent) precision for important measurements, such as the Higgs boson mass or the $W$ boson mass. Additional corrections are applied to achieve such data/MC agreement. They are based on $J/\psi \to \mu\mu$ and $Z \to \mu\mu$ decays. A new independent validation of these corrections is possible using the $\Upsilon \to \mu\mu$ resonance. At ATLAS this is challenging as the momentum resolution is not sufficient to fully resolve the $\Upsilon(1S)$, $\Upsilon(2S)$ and $\Upsilon(3S)$ resonances. Results in this thesis are based on the analysis of $\sqrt{s}$ = 13 TeV $pp$ collision events corresponding to an integrated luminosity of 36.5 fb$^{-1}$ collected by the ATLAS detector in 2015 and in 2016. They demonstrate that the $\Upsilon$ resonance is a reliable validation channel. The corrected MC is in very good agreement with data, with the momentum scale within the scale systematics of 0.05% in the barrel region and up to 0.25% in the forward region, $|\eta| \sim 2.5$. Although within systematic uncertainties, a slight bias is evident in the scale result where the $\Upsilon(1S)$ peak estimated in MC is systematically lower than the corresponding value estimated in data indicating possible overcorrection effects. The muon momentum resolution is measured to be of 1.7% and 2.9% in the centre of the detector and in the endcaps, respectively.

The observed level of agreement demonstrates that the ATLAS simulation provides a very accurate description of the momentum scale and resolution in all $\eta$ regions, over a wide $p_T$ range.

*Charm Physics at CDF.* A measurement of the $D^+$-meson production cross section as a function of the transverse momentum in proton-antiproton collisions at 1.96 TeV centre-of-mass energy is reported. Results are based on the full dataset collected by the CDF detector at FERMILAB in Tevatron Run II and corresponding to 10 fb$^{-1}$ of integrated luminosity. Fully reconstructed $D^+ \to K^-\pi^+\pi^+$ decays in the central rapidity region $|y| < 1$ with transverse momentum down to 1.5 GeV are used. This is a range previously unexplored in $p\bar{p}$ collisions, close to a kine-

matic range where perturbative-QCD is challenging. Inelastic $p\bar{p}$-scattering events are selected online using minimally biasing requirements followed by an optimized offline selection. The $K^-\pi^+\pi^+$ mass distribution is used to identify the $D^+$ signal, and the $D^+$ transverse impact-parameter distribution is used to separate prompt production, occurring directly in the hard-scattering process, from secondary production from $b$-hadron decays. The final number of prompt $D^+$ candidates is 2950 corresponding to a total cross section $\sigma(D^+, 1.5 < p_T < 14.5 \text{ GeV}, |y| < 1) = 71.9 \pm 6.8(\text{stat}) \pm 9.3(\text{syst}) \ \mu\text{b}$. While the measured cross sections are consistent with theoretical estimates in each $p_T$ bin, the shape of the observed $p_T$ spectrum is softer than the expectation from QCD. The results are unique in $p\bar{p}$ collisions and can improve the shape and uncertainties of future predictions. In addition, in searches for astrophysical neutrinos, knowledge of charm production cross-sections may improve estimations of background rates from neutrinos produced in decays of charm hadrons from cosmic-ray interactions with atmospheric nuclei.

# Appendices

# Appendix A

# Muon Momentum Resolution and Scale at ATLAS

*In this appendix I show some of the Public Plots on the muon momentum scale and resolution I produced for the ICHEP2016 and Moriond2017 conferences. They were also shown in a poster I presented at LHCC2017 and at ICNFP2017. These plots are based on muons from $J/\psi \to \mu\mu$ and $Z \to \mu\mu$ decays collected by the ATLAS Collaboration in 2016 and are complementary to the ones shown for the $\Upsilon \to \mu\mu$ in Sec. 3.3.2.1.*

The plots reported in this Appendix are based on the same muon momentum corrections described in Sec. 3.3.2.1. The fitting procedure for the $Z$ and $J/\psi$ resonances is described in Sec. 8.2 of [133].

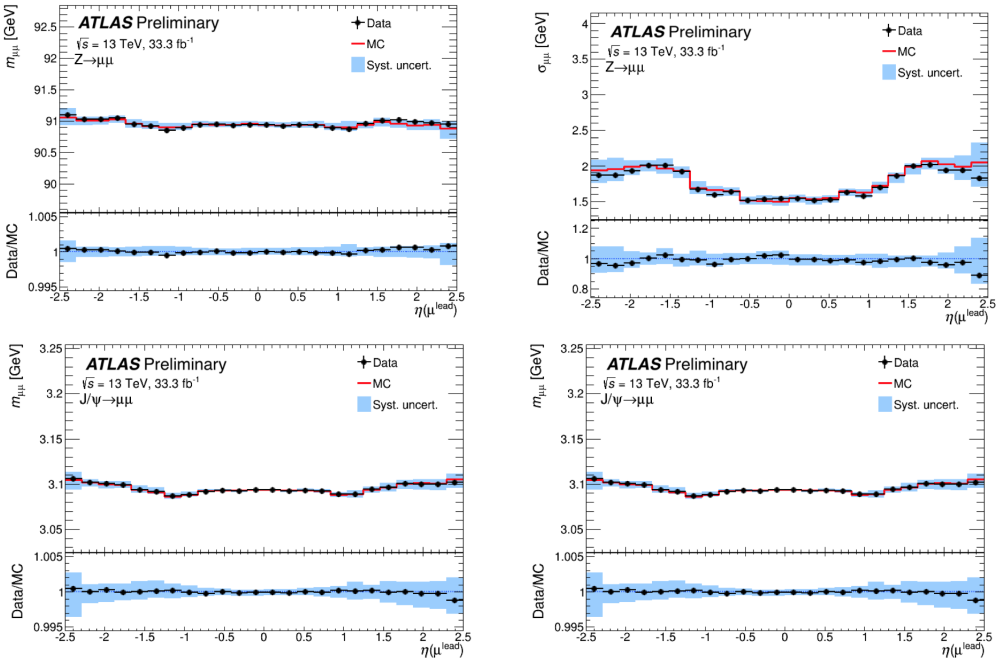


Figure A.1: Fitted $Z$ (top) and $J/\psi$ (bottom) mean mass (left) and dimuon invariant mass resolution (right) of the dimuon system for CB muons from $Z \to \mu\mu$ decays collected in 2016 and for the corrected simulation as a function of the pseudorapidity of the highest-$p_T$ muon. The upper panels show the fitted mean mass value for data (black) and corrected simulation (red). The lower panel shows the data/MC ratio. The error bars represent the statistical uncertainty; the blue shaded bands represent the systematic uncertainty in the correction and the systematic uncertainty in the extraction method added in quadrature.

# Appendix B

# Simulation for the Off-shell Production of the Higgs Boson

*In This Appendix some information on the higher-order theoretical corrections and on the simulation of $ZZ$ final states in the electroweak production mode used in the ATLAS analysis on the off-shell production of the Higgs boson are provided.*

## B.1 Simulation and Theoretical Corrections for the $gg \to (H^* \to) ZZ \to 4f$ Process

As explained in Sec. 4.3.1, the NLO and NNLO $K$-factors for the $gg \to ZZ$ processes are calculated with respect to the pure LO calculations and thus, they cannot be applied directly to the SHERPA MC samples, which are generated with up to one hard jet from the matrix element. LO samples are then introduced to apply the theoretical corrections.

The LO MC generators gg2VV [49,220] and MCFM (Monte Carlo for FeMtobarn processes) [51, 52] are introduced for the different final states considered in this analysis: the MCFM samples are used for the $4\ell$ analysis, while the gg2VV samples are used for the $2\ell 2\nu$ channel. The QCD renormalisation and factorisation scales are set to $m_{ZZ}/2$. The CT10 next-to-next-to-leading-order (NNLO) [122] parton distribution functions (PDFs) are used by gg2VV and MCFM since the LO of the $gg \to VV$ process is part of the NNLO calculation for the $pp \to ZZ$ process. The

default parton showering and hadronisation option for the events processed with the full detector simulation is Pythia 8 [123] with the "power shower" option [123], as it was largely studied in Run 1 [221]. The MCFM samples used are summarized in Table B.1, while the gg2VV samples used are summarized in Table B.2 and the SHERPA samples are summarized in Table B.3.

| **MCFM samples** | | | | |
|---|---|---|---|---|
| Process | | DSID | Events | cross-section |
| $gg \to H^* \to ZZ$ | ggH_ZZ_2e2mu_m4l130 | 344828 | 475000 | 0.107810 fb |
| | ggH_ZZ_4e_m4l130 | 344830 | 449000 | 0.053890 fb |
| | ggH_ZZ_4mu_m4l130 | 344832 | 453000 | 0.053884 fb |
| $gg \to ZZ$ | gg_ZZ_2e2mu_m4l100 | 344833 | 494000 | 2.524 fb |
| | gg_ZZ_4e_m4l100 | 344834 | 497000 | 1.254 fb |
| | gg_ZZ_4mu_m4l100 | 344835 | 494000 | 1.254 fb |
| $gg \to (H^* \to) ZZ$ | ggH_gg_ZZ_2e2mu_m4l130 | 344233 | 495000 | 2.288 fb |
| | ggH_gg_ZZ_4e_m4l130 | 344821 | 500000 | 1.139 fb |
| | ggH_gg_ZZ_4mu_m4l130 | 344823 | 50000 | 1.139 fb |
| $gg \to (H^* \to) ZZ(\mu_{off-shell} = 5)$ | ggH_gg_ZZ_5SMW_2e2mu_m4l130 | 344824 | 496000 | 2.457 fb |
| | ggH_gg_ZZ_5SMW_4e_m4l130 | 344825 | 498000 | 1.224 fb |
| | ggH_gg_ZZ_5SMW_4mu_m4l130 | 344826 | 498000 | 1.224 fb |
| $gg \to (H^* \to) ZZ(\mu_{off-shell} = 10)$ | ggH_gg_ZZ_10SMW_2e2mu_m4l130 | 344229 | 500000 | 2.802 fb |
| | ggH_gg_ZZ_10SMW_4e_m4l130 | 344230 | 500000 | 1.396 fb |
| | ggH_gg_ZZ_10SMW_4mu_m4l130 | 344231 | 500000 | 1.396 fb |

Table B.1: List of MCFM samples used in the $4\ell$ analysis along with the cross sections. Events are generated with the ATLAS fast simulation assuming $\Gamma_H = \Gamma_H^{SM}$ or $\Gamma_H = 5 \times \Gamma_H^{SM}$ or $\Gamma_H = 10 \times \Gamma_H^{SM}$. For the larger-than-SM-width samples only truth events are available. Only events with $m_{4\ell} > 130(100)$ GeV are generated for $gg \to (H^* \to) ZZ \to 4\ell$ ($gg \to ZZ$) sample. DSID is the Dataset ID.

| **gg2VV samples** | | | | |
|---|---|---|---|---|
| Process | | DSID | Events | cross-section |
| $gg \to H^* \to ZZ$ | gg2vvPy8EG_1SMW_ZZ_2l2v | 344784 | 992000 | 6.599 fb |
| $gg \to ZZ$ | gg2vvPy8EG_gg_ZZ_bkg_2l2v | 344783 | 993000 | 31.720 fb |
| $gg \to (H^* \to) ZZ$ | gg2vvPy8EG_1SMW_gg_ZZ_2l2v | 344785 | 994000 | 35.330 fb |
| $gg \to (H^* \to) ZZ(\mu_{off-shell} = 5)$ | gg2vvPy8EG_5SMW_SC_gg_ZZ_2l2v | 344786 | 997000 | 37.490 fb |
| $gg \to (H^* \to) ZZ(\mu_{off-shell} = 10)$ | gg2vvPy8EG_10SMW_SC_gg_ZZ_2l2v | 344787 | 992000 | 42.020 fb |

Table B.2: List of gg2VV samples used in the $2\ell 2\nu$ analysis. Events are generated with the ATLAS fast simulation assuming $\Gamma_H = \Gamma_H^{SM}$ or $\Gamma_H = 5 \times \Gamma_H^{SM}$ or $\Gamma_H = 10 \times \Gamma_H^{SM}$. For the larger-than-SM-width samples only truth events are available. DSID stays for Dataset ID. All the samples assume a 125-GeV-SM Higgs, i.e. technically the extension '$ggH125$'.

A preliminary consistency check of the $m_{ZZ}$ distribution of the MCFM and SHERPA samples is performed. In Figure B.1 the shape comparison MCFM-SHERPA

| **Sherpa samples** | | | | |
|---|---|---|---|---|
| Process | | DSID | Events | cross-section |
| $gg \to H^* \to ZZ$ | gglllOnlyHiggs_130M4l | 345712 | 49000 | 0.60 fb |
| $gg \to ZZ$ | gglllNoHiggs_130M4l | 345709 | 499000 | 10.6 fb |
| $gg \to (H^* \to) ZZ$ | gglll_130M4l | 345706 | 991400 | 10.0 fb |
| $gg \to H^* \to ZZ$ | ggllvvZZOnlyHiggs | 345726 | 99000 | 1.92 fb |
| $gg \to ZZ$ | ggllvvZZNoHiggs | 345725 | 294000 | 6.99 fb |
| $gg \to (H^* \to) ZZ$ | ggllvvZZ. | 345723 | 295000 | 7.11 fb |

Table B.3: List of Sherpa $gg$ samples used for both the analyses, $4\ell$ and $2\ell 2\nu$. Events are simulated with the ATLAS fast simulation.

for the $4\ell$ channel is shown. The discriminating variables used in both the analyses are defined in Sec. 4.4 - 4.5. An additional shape comparison MCFM-Sherpa and gg2VV-Sherpa is shown in Figures B.2, B.3 for the discriminant distribution of both the analyses, the Matrix-Element-Method discriminant (MEM) in the $4\ell$ channel and the transverse mass ($m_T^{ZZ}$) in the $2\ell 2\nu$ channel. The comparison is performed out-of-the-box, without any QCD higher-order theoretical corrections. The comparison shows an overall agreement and no re-weighting is needed. Minor deviations are observed, especially in the low mass range. The difference is due to the additional 1-jet matrix element calculation included in the Sherpa generator, as shown in [116]. This was explicitly validated by removing the 1-jet element calculations in Sherpa and a consistent spectrum was observed. After the application of the higher-order QCD theoretical corrections to the MCFM and gg2VV samples, a better agreement is achieved.

In more detail, the strategy to apply the higher-order QCD corrections to have the appropriate predictions in terms of both normalization and kinematic distributions can be summarized in three steps:

1. The higher-order QCD corrections are applied to the LO MC samples, MCFM for the $4\ell$ channel and gg2VV for the $2\ell 2\nu$ channel, as a function of $m_{ZZ}$ after the implementation of a fiducial selection. The corrected $m_{ZZ}$-differential distributions are then used as cross section references.

2. In the same fiducial phase space defined before, the $m_{ZZ}$ differential distributions of the Sherpa samples are re-weighted to the corrected NLO $m_{ZZ}$

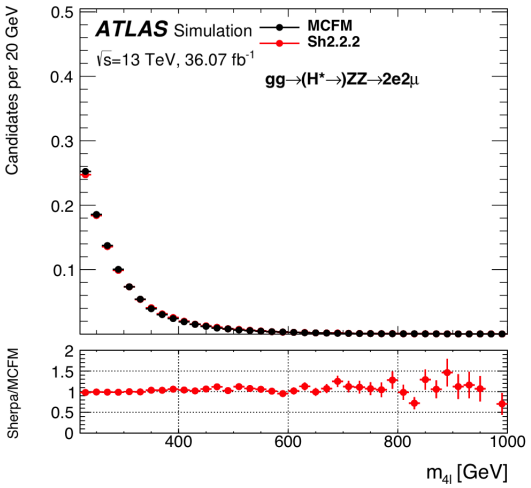


(a) $gg \to (H^* \to)ZZ \to 2e2\mu$

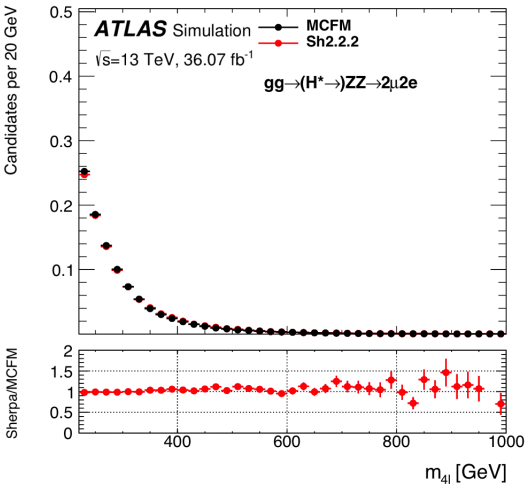


(b) $gg \to (H^* \to)ZZ \to 2\mu 2e$

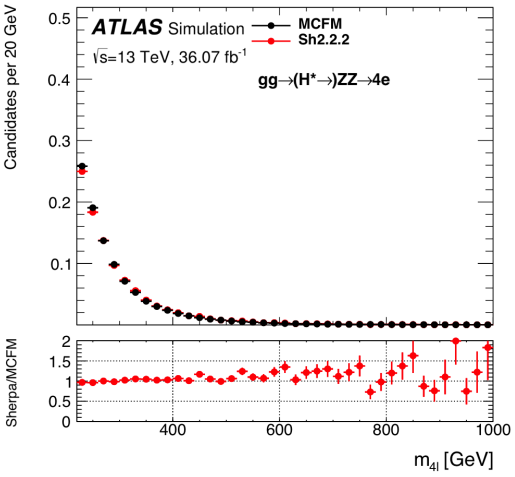


(c) $gg \to (H^* \to)ZZ \to 4e$

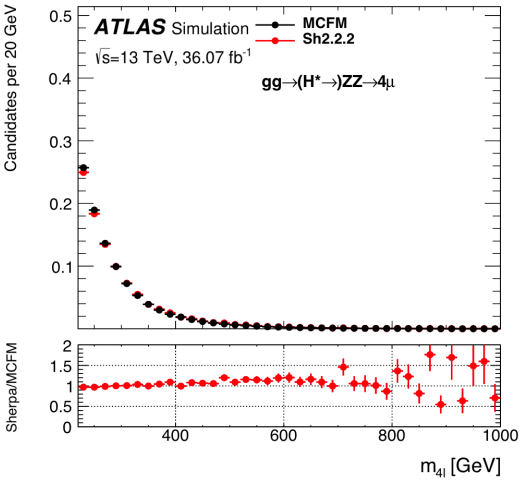


(d) $gg \to (H^* \to)ZZ \to 4\mu$

Figure B.1: Shape comparison of the $m_{4\ell}$ distribution between the SHERPA (red) and MCFM (blue) samples for the various $gg \to (H^* \to)ZZ \to 4\ell$ (with $l = e, \mu$) processes. The comparison is performed out-of-the-box, without any higher-order QCD theoretical corrections.

-differential distributions from the previous step. The appropriate weights for the off-shell signal, the continuum background and their interference are derived during this step. The distributions of the various weights to be applied to the SHERPA predictions are shown as a function of $m_{ZZ}$ in Figures B.4, B.5, B.6.

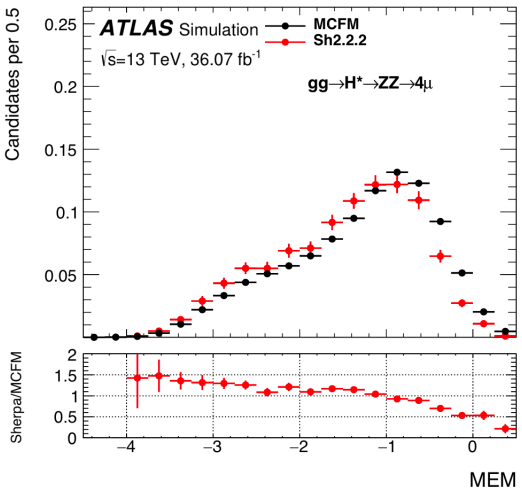


(a) $gg \to H^* \to ZZ \to 4\mu$ signal

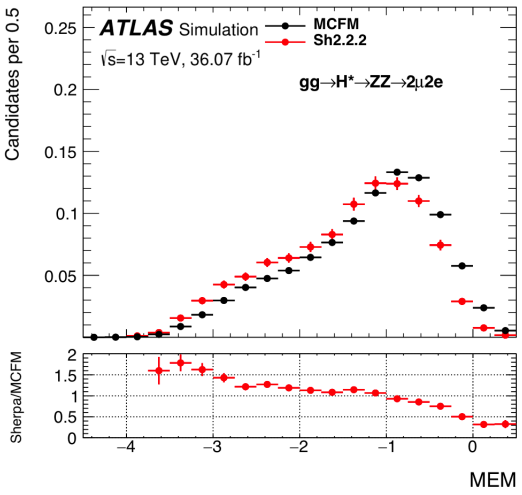


(b) $gg \to H^* \to ZZ \to 2\mu 2e$ signal

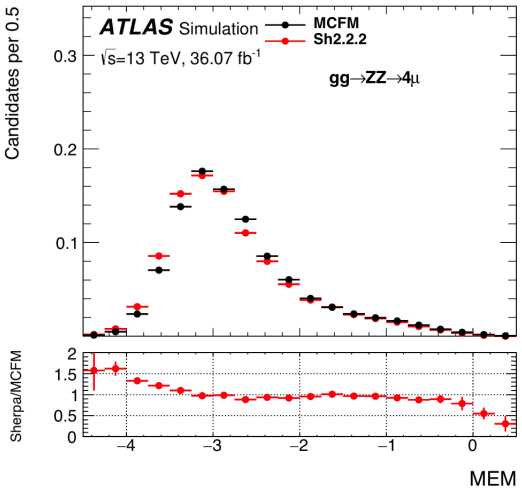


(c) $gg \to ZZ \to 4\mu$ background

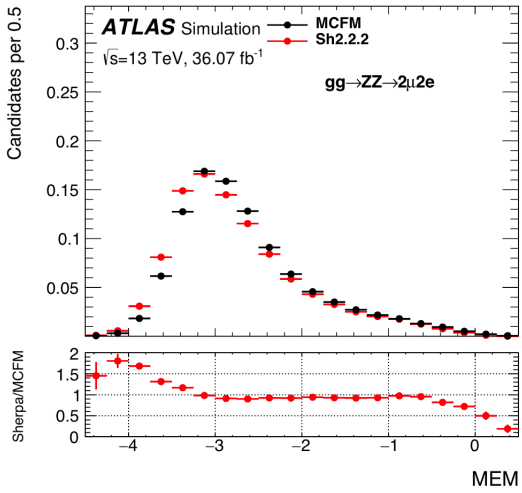


(d) $gg \to ZZ \to 2\mu 2e$ background

Figure B.2: Shape comparison of the Matrix-Element-Method discriminant (MEM) distribution between the SHERPA (red) and MCFM (blue) samples for the $gg \to H^* \to ZZ \to 4\mu$ off-shell signal (a) and the $gg \to ZZ \to 4\mu$ background (c), for the $gg \to H^* \to ZZ \to 2\mu 2e$ off-shell signal (b) and the $gg \to ZZ \to 2\mu 2e$ background (d). The comparison is performed out-of-the-box, without any higher-order QCD theoretical corrections.

3. The weights as function of $m_{ZZ}$ are then applied, on an event-per-event basis, to the SHERPA samples and the kinematic distributions of interest for the $4\ell$ and $2\ell 2\nu$ channels are derived. These SHERPA corrected kinematic variables

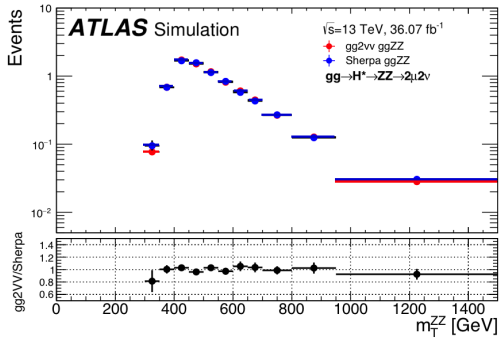


(a) $gg \to H^* \to ZZ \to 2\mu 2\nu$ signal

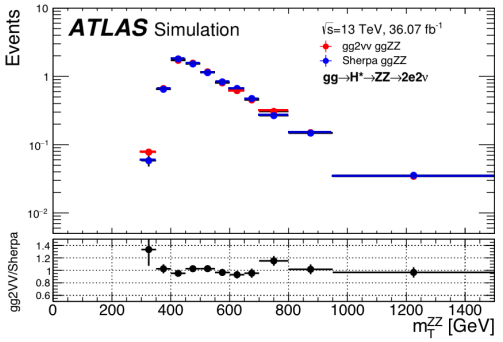


(b) $gg \to H^* \to ZZ \to 2e2\nu$ signal

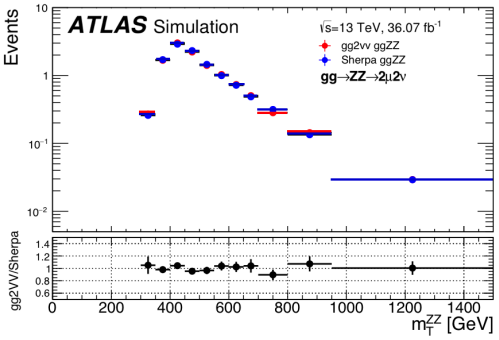


(c) $gg \to ZZ \to 2\mu 2\nu$ background

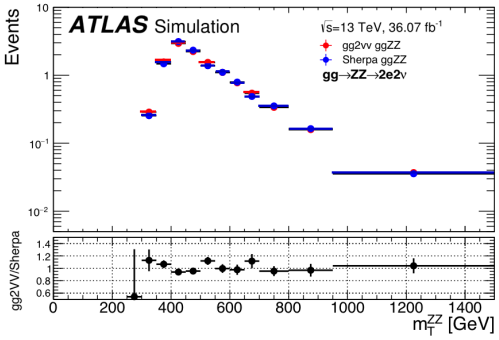


(d) $gg \to ZZ \to 2e2\nu$ background

Figure B.3: Shape comparison of the transverse-mass ($m_T^{ZZ}$) distribution between the SHERPA (blue) and gg2VV (red) samples for the $gg \to H^* \to ZZ \to 2\mu 2\nu$ off-shell signal (a) and the $gg \to ZZ \to 2\mu 2\nu$ background (c), for the $gg \to H^* \to ZZ \to 2e2\nu$ off-shell signal (b) and the $gg \to ZZ \to 2e2\nu$ background (d). The comparison is performed out-of-the-box, without any higher-order QCD theoretical corrections.

are then used to obtain the final results. In Sec. 4.3.3 it is explained how the weights are applied. As a sanity check, after the application of the theoretical corrections the main kinematic variables in the MCFM(gg2VV) and SHERPA samples are compared again. A good agreement is observed.

Following the parametrization reported in Sec. 4.3.3, when higher-order QCD corrections are applied in the step n.1 described above, the $SBIr$ sample can be

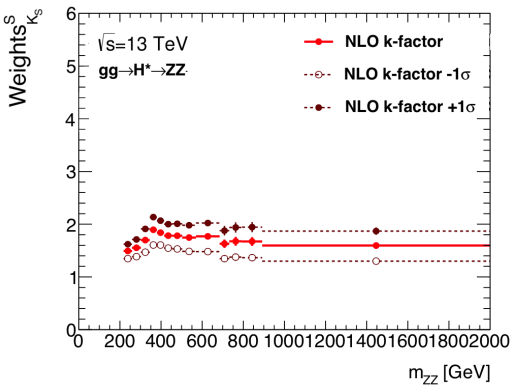


(a) Weights with $K^S_{NLO/LO}(m_{ZZ})$

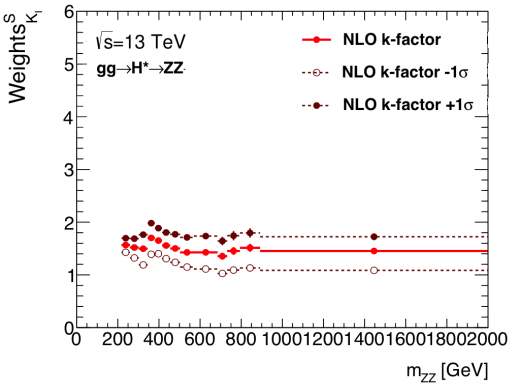


(b) Weights with $K^I_{NLO/LO}(m_{ZZ})$

Figure B.4: NLO/LO correction weights to be used for the SHERPA samples of the $gg \to H^* \to ZZ$ signal: (a) with $K$-factors for the signal process applied, (b) with $K$-factors for the interference process applied. Both the central values (red solid line) and the $\pm 1\sigma$ QCD scale uncertainties are shown (dashed lines).

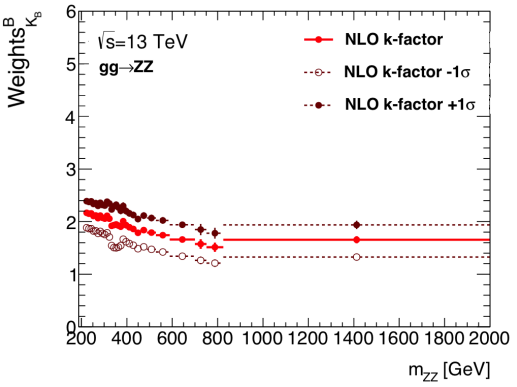


(a) Weights with $K^B_{NLO/LO}(m_{ZZ})$

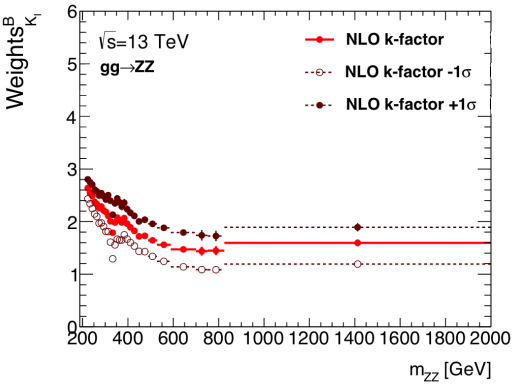


(b) Weights with $K^I_{NLO/LO}(m_{ZZ})$

Figure B.5: NLO/LO correction weights to be used for the SHERPA samples of the $gg \to ZZ$ continuum background: (a) with $K$-factors for the background process applied, (b) with $K$-factors for the interference process applied. Both the central values (red solid line) and the $\pm 1\sigma$ QCD scale uncertainties are shown (dashed lines).

constructed using the following weighting function:

$$\begin{aligned} \sigma_{gg\to(H^*\to)VV}(\mu_{off-shell}) &= \mu_{off-shell} \cdot K^S(m_{VV}) \cdot \sigma^{SM}_{gg\to H^*\to VV} \\ &+ \sqrt{\mu_{off-shell}} \cdot K^I(m_{VV}) \cdot \sigma^{SM}_{gg\to VV,\,\text{Interference}} \\ &+ K^B(m_{VV}) \cdot \sigma_{gg\to VV,\,\text{cont}} \end{aligned} \tag{B.1}$$

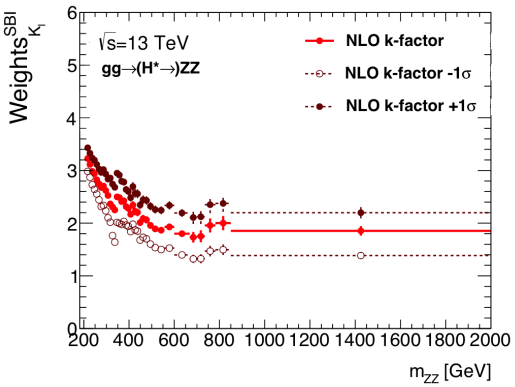


Figure B.6: NLO/LO correction weights to be used for the SHERPA samples of the $gg \to (H^* \to) ZZ$ process with $K$-factors for the interference process, $K^I_{NLO/LO}(m_{ZZ})$, applied. Both the central values (red solid line) and the $\pm 1\sigma$ QCD scale uncertainties are shown (dashed lines).

where the $K$-factors are calculated as described in Sec. 4.3.1.

As a direct simulation of an interference MC sample is not possible, Eq. (4.9) is used to obtain:

$$\begin{aligned} \sigma_{gg\to(H^*\to)VV}(\mu_{off-shell}) &= \mu_{off-shell} \cdot K^S(m_{VV}) \cdot \sigma^{SM}_{gg\to H^*\to VV} \\ &- \sqrt{\mu_{off-shell}} \cdot K^I(m_{VV}) \cdot \sigma^{SM}_{gg\to H^*\to VV} \\ &+ \sqrt{\mu_{off-shell}} \cdot K^I(m_{VV}) \cdot \sigma^{SM}_{gg\to (H^*\to)VV} \\ &+ K^B(m_{VV}) \cdot \sigma_{gg\to VV,\text{cont}} - \sqrt{\mu_{off-shell}} \cdot K^I(m_{VV}) \cdot \sigma_{gg\to VV,\text{cont}} \end{aligned} \tag{B.2}$$

Thus, the $SBIr$ sample is constructed from five individual samples:

- $K^S(m_{VV}) \cdot \sigma^{SM}_{gg\to H^*\to VV}$: the signal sample with the higher-order corrections for the signal process applied;
- $K^I(m_{VV}) \cdot \sigma^{SM}_{gg\to H^*\to VV}$: the signal sample with the higher-order corrections for the interference applied;
- $K^B(m_{VV}) \cdot \sigma_{gg\to VV,\text{cont}}$: the background sample with the higher-order corrections for the background process applied;
- $K^I(m_{VV}) \cdot \sigma_{gg\to VV,\text{cont}}$: the background sample with the higher-order corrections for the interference applied;

- $K^I(m_{VV}) \cdot \sigma^{SM}_{gg\to(H^*\to)VV}$: the $SBI$ sample with the higher-order corrections for the interference applied.

In the final analysis, the NLO corrected SHERPA samples are used for the parametrization, following the reweighting procedure described above. The parametrization reported above explains why it was necessary to derive also interference weights to be applied to the signal and the background samples.

## B.2 Simulation and Theoretical Corrections for the $q\bar{q} \to ZZ \to 4f$ Process

As explained in Sec. 4.3.4 NLO EW corrections are applied to the SHERPA samples for the $q\bar{q} \to ZZ$ background. The required quantities are derived from the initial-state quarks and the outgoing $Z$ bosons. The re-weighting method followed is taken from [163] and validated in [164]. In a strict sense the corrections are valid only for the leading order process above the corresponding diboson production threshold and with both vector bosons produced on-shell. Experimentally, this is achieved by requiring $s > \sqrt{(m_{V1}^{PDG} + m_{V2}^{PDG})^2}$ in the centre-of-mass frame of the diboson system. In this analysis this simplifies to $m_{ZZ} > 2 \cdot m_Z^{PDG}$. However, the analysis selections don't apply a rigorous on-shell-Higgs cut. In the $4\ell$ channel only a mass requirement is made with 50 GeV $< m_{l1l2} <$ 106 GeV for the first lepton pair, $m_{l1l2}$, and 50 GeV $< m_{l3l4} <$ 115 GeV for the second lepton pair, $m_{l3l4}$. This selection of course allows also for off-shell $Z$ bosons to be produced, which are not covered by the EW correction calculations. Since EW effects in events with off-shell $Z$ bosons are expected to be of the same size as in events with on-shell $Z$ bosons, the kinematics of such events can be extracted in the same way, but enlarging the EW-correction-weights uncertainty up to 100% to be conservative. Such events with off-shell $Z$ bosons only amount to 0.03% of the selected events for the $4\ell$ channel and even less for the $2\ell 2\nu$ channel where a stricter selection requirement on the dilepton mass is applied, 76 GeV $< m_{ll} <$ 106 GeV. Weights are computed at LO QCD since the (NLO QCD) × (NLO EW) corrections are not known. In events with high QCD activity, additional systematic uncertainties are considered, following the recommendations in [163].

## B.3 Correlation Between the $gg \to ZZ \to 4f$ and $q\bar{q} \to ZZ \to 4f$ Processes

Correlations between PDF uncertainties for the $gg \to ZZ \to 4f$ and $q\bar{q} \to ZZ \to 4f$ processes are evaluated using the CT10 PDF set using POWHEG NLO program. Events are selected with the requirements of $p_T^l > 5$ GeV and $|\eta| < 2.8$ at generator-level. The correlation between two different PDFs, at a given value of $(x, Q^2)$[1], in the Monte Carlo representation is evaluated using the formula expressed below from [222]:

$$\rho(\sigma^{gg}, \sigma^{q\bar{q}}) = \frac{\sum_i^{N_{eig}} (\sigma_i^{gg} - \sigma_0^{gg})(\sigma_i^{q\bar{q}} - \sigma_0^{q\bar{q}})}{\sqrt{\sum_i^{N_{eig}} (\sigma_i^{gg} - \sigma_0^{gg})^2 \sum_i^{N_{eig}} (\sigma_i^{q\bar{q}} - \sigma_0^{q\bar{q}})^2}} \tag{B.3}$$

where the sum is performed over the $N_{eig}$ eigenvectors or PDF replicas[2], $\sigma_i^{gg}$ and $\sigma_i^{q\bar{q}}$ are the uncertainties calculated at the $i^{th}$ eigenvector, while $\sigma_0^{gg}$ and $\sigma_0^{q\bar{q}}$ correspond to the values obtained by the central PDF value of the CT10 PDF set, which coincide with the MC average values. The PDF uncertainties themselves are derived from the envelope of the CT10, MSTW and NNPDF sets, but this envelope doesn't allow us to evaluate correlations of PDF systematics. However, since PDF correlations are generally independent of the PDF set chosen, the considerations above apply without any restriction.

The correlation between the off-shell $gg \to H^* \to ZZ$ signal and the $q\bar{q} \to ZZ$ background in the high-mass region is estimated to be -0.2. Hence these two PDF sets will be treated as uncorrelated for the extraction of the off-shell signal strength. Using the same equation, Eq. B.3 with the appropriate PDF uncertainties for the processes of interest, it is possible to estimate also the correlation between the off-shell and the on-shell $gg \to ZZ$ and $q\bar{q} \to ZZ$ processes. Results are summarized in Sec. 5.3.3 and Sec. 5.3.4, after providing the final results.

[1] Structure functions are generally provided as a function of the momentum transfers squared $Q^2$ and the Bjorken scaling variable $x = \frac{Q^2}{2M\nu}$ where $\nu$ is the energy loss between the scattering electrons, $M$ is the mass of the target nucleon and $q$ is the 4-momentum-transfer vector of the exchanged virtual photon in a electron-nucleon deep inelastic scattering.

[2] Modern sets of PDFs provide a representation of their associated uncertainties based on either the Hessian or the MC methods supplementing their central PDF member with additional error members, the so called eigenvectors or MC replicas.

## B.4 $ZZ$ Final States in the Electroweak Production Mode

In Table B.4 the Vector Boson Fusion samples used in the $4\ell$ analysis are reported, while the VBF samples used in the $2\ell 2\nu$ analysis are given in Table B.5.

| **MadGraph** $q\bar{q} \to ZZ \to 4\ell + jj$ **samples** | | | |
|---|---|---|---|
| Process | DSID | Events | cross-section |
| VBFH125_ZZ_4l_m4l130 | 345070 | 300000 | 0.125 fb |
| VBFH125_bkg_4l_m4l100 | 345276 | 299000 | 0.672 fb |
| VBFH125_sbi_4l_m4l130 | 345071 | 289000 | 0.636 fb |
| VBFH125_sbi5_4l_m4l130 | 345072 | 300000 | 0.775 fb |
| VBFH125_sbi10_4l_m4l130 | 345277 | 300000 | 1.002 fb |

Table B.4: List of $q\bar{q} \to ZZ \to 4\ell + jj$ MadGraph5 samples used in the $4\ell$ analysis. Events are simulated with the ATLAS fast simulation.

| **MadGraph** $q\bar{q} \to ZZ \to 2\ell 2\nu + jj$ **samples** | | | | |
|---|---|---|---|---|
| Process | DSID | Events | Filter efficiency | cross-section |
| VBFH125_ZZ_llnn_MET80 | 345067 | 497000 | 0.612 | 1.129 fb |
| VBFH125_bkg_llnn_MET80 | 345274 | 491000 | 0.309 | 1.441 fb |
| VBFH125_sbi_llnn_MET80 | 345068 | 496000 | 0.422 | 2.195 fb |
| VBFH125_sbi5_llnn_MET80 | 345069 | 497000 | 0.464 | 2.431 fb |
| VBFH125_sbi10_llnn_MET80 | 345275 | 495000 | 0.529 | 2.907 fb |

Table B.5: List of $q\bar{q} \to ZZ \to 2\ell 2\nu + jj$ MadGraph samples used in the $2\ell 2\nu$ analysis. Events are simulated with the ATLAS fast simulation. Cross section numbers are for individual neutrino flavor, they need to be scaled up by a factor of three for a proper normalization.

# Appendix C

# Auxiliary Samples Used for the $D^+$-meson Cross Section at CDF

*In this appendix the two selections for the auxiliary samples needed to evaluate the conditional silicon single-track efficiency are reported.*

### C.0.1 $D^*$ Sample Selection

$D^{*+} \to D^0(\to K^-\pi^+)\pi_s^+$ decay candidates are reconstructed with a kinematic fit to tracks selected in the two-track-triggered hadronic sample as shown in Table C.1. Restricting to $D^0 \to K^-\pi^+$ candidates with $1.7 < m_{K\pi} < 1.8$ GeV, it's possible to study the invariant mass of the selected $D^0$ candidates that are combined with a third track reconstructed using explicitly only COT-information. Finally the $p_T$ distribution of $\pi_s$ candidates under the $D^{*+}$ peak, 2.009 - 2.012 GeV, is determined, before and after the requirement of SVX hits for the soft pion. The ratio of the two distributions yields the conditional silicon single-track efficiency as a function of $p_T$.

### C.0.2 $J/\psi$ Sample Selection

$J/\psi \to \mu^+\mu^-$ candidate decays are reconstructed with a kinematic fit to candidate muons selected in the dimuon-triggered sample as shown in Table C.2. The dimuon mass of all pairs of candidate muons reconstructed in the tracker using the COT-information only is calculated. $J/\psi$ candidates are selected by restricting to an interval approximately $2\sigma$-wide around the peak, 3.073 – 3.121 GeV. Additionally,

| | | |
|---|---|---|
| $D^0$ daughters: | COT axial hits | $\geq 25$ |
| | COT stereo hits | $\geq 25$ |
| | SVX z hits | $\geq 1$ |
| | SVX SAS hits | $\geq 2$ |
| | SVX $r-\varphi$ hits | $\geq 3$ |
| | $p_T$ | $\geq 2$ GeV/c |
| | at radius R = 133 cm, $\lvert z\rvert$ | $\leq 155$ cm |
| | at radius R = 10.645 cm, $\lvert z\rvert$ | $\leq 47.25$ cm |
| $D^0$ candidate: | $m_{\pi\pi}$ | $\in [1.7; 1.8]$ GeV/$c^2$ |
| $\pi_s$: | $\eta$ | $\in$ [-1; 1] |
| | COT axial hits | $\geq 25$ |
| | COT stereo hits | $\geq 25$ |
| | SVX z hits | $\geq 1$ |
| | SVX SAS hits | $\geq 2$ |
| | SVX $r-\varphi$ hits | $\geq 3$ |
| | at radius R = 133 cm, $\lvert z\rvert$ | $\leq 155$ cm |
| | at radius R = 10.645 cm, $\lvert z\rvert$ | $\leq 47.25$ cm |
| $D^{\star+}$ candidate: | $m_{D^0\pi_s}$ | $\in [2.009; 2.012]$ GeV/$c^2$ |

Table C.1: Offline selection for $D^{*+} \to D^0(\to K^-\pi^+)\pi_s^+$ candidates in the two-track-trigger sample.

candidates are selected in two side-bands of the $J/\psi$ peak, 3.073 – 3.013 GeV and 3.147 – 3.181 GeV. This is needed to evaluate sideband-subtracted $p_T$-distributions of dimuons under the $J/\psi$ peak, before and after applying the SVX requirements. The ratio of the two distributions yields the average efficiency as a function of $p_T$.

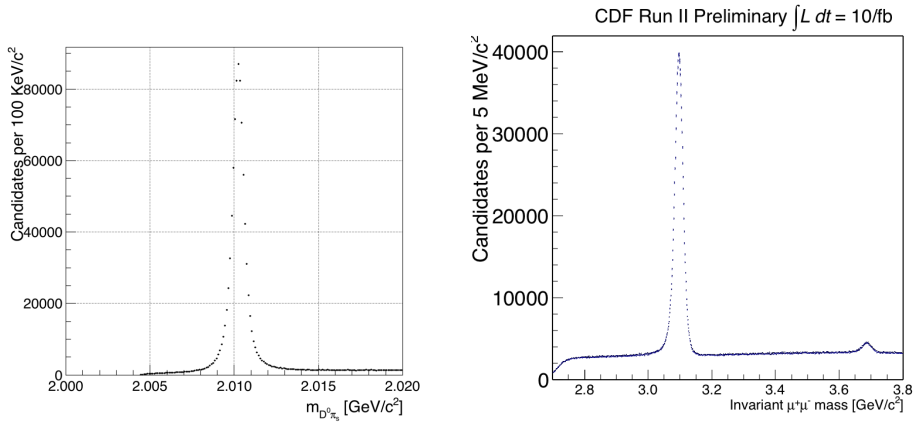


Figure C.1: Invariant $D^0\pi_s$ mass distribution (left) of $D^{\star+}$ candidates in the hadronic sample and $\mu^+\mu^-$ mass in the $J/\psi$ sample (right). In both plots, candidates are selected through the SVX requirements.

| | | |
|---|---|---|
| $\mu\mu$: | COT axial hits | $\geq 25$ |
| | COT stereo hits | $\geq 25$ |
| | SVX z hits | $\geq 1$ |
| | SVX SAS hits | $\geq 2$ |
| | SVX $r-\varphi$ hits | $\geq 3$ |
| | $p_T$ | $\geq 1.5$ GeV/c |
| | at radius R = 133 cm, $\lvert z\rvert$ | $\leq 155$ cm |
| | at radius R = 10.645 cm, $\lvert z\rvert$ | $\leq 47.25$ cm |
| $J/\psi$ candidate: | $m_{\mu\mu} \in [3.073; 3.121]$ GeV/$c^2$ | |

Table C.2: Offline selection for $J/\psi \to \mu^+\mu^-$ candidates in the two-track-trigger sample.

# Appendix D

# Additional Activities

*In this chapter I briefly summarize some additional activities I carried out during my DPhil, in parallel with the research described in the previous chapters.*

In parallel to the software-based research contributions described in the previous chapters, during my DPhil I also contributed to:

- *Data-taking Operations.* After I moved to CERN, I got involved in the Run 2 data-taking operations in the ATLAS Control Room (ACR). In 2017 I was an Inner Detector shifter, while in 2018 I became a Shift Leader, responsible for the shift crew and data taking during the shift. On the $2^{nd}$ of December 2018 I was the last ATLAS Shift Leader for the physics program in Run 2. We celebrated the moment with a cake. A memory photo is shown in Fig. D.1. The two experiences were complementary. As an Inner Detector shifter I learned how to prioritize issues that can happen during data-taking operations, focusing on a specific sub-detector. The experience as a Shift Leader was really intense. I had several night shifts, during which I learned how to coordinate and supervise several activities and issues on-going in the various sub-detectors. Data-taking operations are like an adventure in the forest, you never know what can happen when your start your 8-hour night shift. Tonight the DAQ system could temporary fail, tomorrow it is the muon system with some chambers not properly working etc. It is crucial to be proactive since several minutes with a detector not properly working correspond to some information, or even worse, data lost. I for sure will never forget busy nights

in the ATLAS Control Room drinking 3-4 coffee, with a white CERN Globe outside, covered with soft snow.

The ATLAS Collaboration evaluates individual contributions in the various areas (detectors performance, data-taking operations etc.) allocating to ATLAS members Operation Task Planner (OTP) quota in different Classes. In only 1.5 years as a shifter in the ATLAS Control Room I was allocated a quota of 83.73 Class 1 OTP corresponding to 77 shifts - 48 of them were night shifts. In addition, I was allocated a quota of 2.80 Class 2 OTP and for my muon performance work, described in Chapter 3, I was allocated a quota of 0.33 Class 3 OTP from 2016 to 2019.


Figure D.1: Celebrating the dump of the last physics fill of the LHC Run 2 in the ATLAS Control Room with all the shift crew - December 2, 2018.

- *Outreach Activities.* As a physicist I strongly believe outreach is part of our duties to correctly inform people of our goals, how we plan to achieve them and, last but not least, how careful we are about safety. It is beneficial for both the audience and us.

  Since 2016 I have worked with 3 high schools in Italy: Liceo Scientifico and Classico of Montesarchio, Benevento and Cervinara. Having worked with the LIGO, CDF and ATLAS collaborations, in 2016 I gave a 90-minute outreach seminar on the two Nobel discoveries of Gravitational Waves and the Higgs

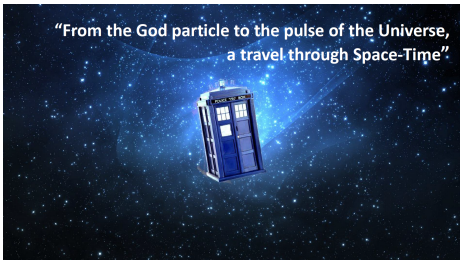


(a) Flyer.

(b) Audience.

Figure D.2: Outreach event in Italy, February 2017.

Boson in Montesarchio: "From the God particle to the pulse of the Universe, a travel through Space-Time" [223]. The flyer of the event and a photo with the students are shown in Figures D.2. The seminar was aimed at ~200 high school students. I also asked to give two 90-minute training courses aimed at high school professors in the province of Benevento to prepare the professor cohort for possible questions from the students after the seminar [224]. In 2017 I gave two lectures aimed at high school students on modern searches in physics. In 2019 I worked with the Italian Master of the same high schools and some professors on a multi-cultural project: "From Democritus' atom to Particle Physics". It was a program of 8 lectures over the academic year where students started with Latin literature and Greek philosophy and the project finished with my lectures on CERN physics. I tried to show them the invisible particles Democritus was only imagining. It was a fascinating trip for them and for me as well. I collaborated with colleagues in philosophy and literature in a way that they synchronized and prepared their programs over the year with my lectures.

In addition, in 2017 I also gave a public lecture aimed at a general audience in

Cervinara with ~100 people [225]. While in the UK I gave a public talk aimed at a general audience in Oxford [226], St Catherine's MCR Colloquia, and I showed an outreach poster during a public event organized at St Catherine's College.

At CERN, I am an official ATLAS guide. I show students/people the magic behind the scenes of the ATLAS detector - ATLAS Control Room and ATLAS cavern - and of CERN. In addition, in 2017 and 2018 I was invited to represent the British young community during the visit to CERN of the (at that time) *UK Secretary of State for Foreign and Commonwealth Affairs, Hon. Boris Johnson* and *Dr Patrick Vallance, Chief Scientific Adviser to the UK Government*.

- *Academic Activities*. In 2016, while flying to Chicago for a conference, I had an idea for a summer student program for undergraduate students. I proposed this idea to some people at the conference getting some funding and starting this International program with CAIF (the Cultural Association of Italians at Fermilab), the University of Oxford and the University of Pisa, **Mo$\nu$ingKnowledge17** [227]. We got 59 applications from all over the world for 3 positions. Following the successful 2017 program, in 2018 a new program was created, **ConnectingKnowledge18** [228] and Harvard joined the Mo$\nu$ingKnowledge18 program [229] [230] for a total of 8 students. The University of Chicago and Argonne joined the organizing committee, as well. We got 120 applications for 9 positions. In 2019 the University of Heidelberg joined the ConnectingKnowledge19 program. In 2018, as part of the program, I organized 2 weeks of lectures in Oxford on instrumentation and modern searches in physics from neutrino to collider physics. The flyers of the two programs are shown in Fig. D.3.

- *ATLAS Collaboration Activities*. Since March 2019 I have been selected for a 2-year appointment as a member of the **ATLAS Early Career Scientist Board**, a group of 7 young scientists. We work with the Spokesperson and the ATLAS management to improve the life of the ATLAS members, with a special focus on the early career physicists.

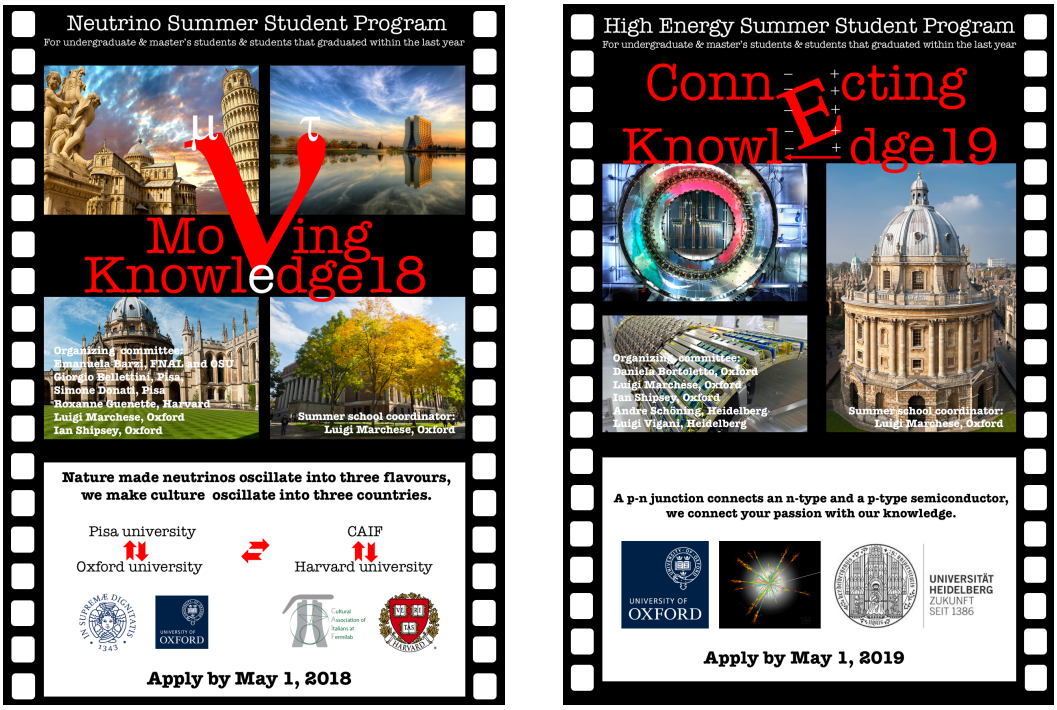


(a) MoνingKnowledge18 program. (b) ConnectingKnowledge19 program.

Figure D.3: Flyer of the Oxford Summer student programs in 2018 and in 2019.

# Bibliography


[1] S. Weinberg, *The Making of the standard model*, Eur. Phys. J. **C 34** (2004) 5-13.

[2] T. W. B. Kibble, *The Standard Model of Particle Physics*, (2014) arXiv:1412.4094.

[3] UA1 Collaboration, G. Arnison *et al.*, *Experimental Observation of Lepton Pairs of Invariant Mass Around 95 GeV/$c^2$ at the CERN SPS Collider*, Phys. Lett. **B 126** (1983) 398-410.

[4] UA2 Collaboration, M. Banner *et al.*, *Observation of Single Isolated Electrons of High Transverse Momentum in Events with Missing Transverse Energy at the CERN $\bar{p}p$ Collider*, Phys. Lett. **B 122** (1983) 476-485.

[5] UA2 Collaboration, P. Bagnaia *et al.*, *Evidence for $Z^0 \to e^+e^-$ at the CERN $\bar{p}p$ Collider*, Phys. Lett. **B 129** (1983) 130-140.

[6] P. W. Higgs, *Broken Symmetries, Massless Particles And Gauge Fields*, Phys. Lett. **12** (1964) 132.

[7] P. W. Higgs, *Broken Symmetries And The Masses Of Gauge Bosons*, Phys. Rev. Lett. **13** (1964) 508.

[8] G. Altarelli and M. W. Grunewald, *Precision electroweak tests of the Standard Model*, Physics Reports **403-404** no. 0, (2004) 189 - 201, CERN - the second 25 years.

[9] ATLAS Collaboration, *Observation of a new particle in the search for the Standard Model Higgs boson with the ATLAS detector at the LHC*, Phys. Lett. **B 716** (2012) 1.

[10] CMS Collaboration, *Observation of a new boson at a mass of 125 GeV with the CMS experiment at the LHC*, Phys. Lett. **B 716** (2012) 30.

[11] CMS Collaboration, *Observation of a new boson with mass near 125 GeV in pp collisions at $\sqrt{s}$ = 7 and 8 TeV*, JHEP **06** (2013) 081.

[12] A. Purcell, *Go on a particle quest at the first CERN webfest. Le premier webfest du CERN se lance a' la conquiete des particules*, (2012) BUL-NA-2012-269.

[13] A. Pich, *The Standard model of electroweak interactions* (2008) arXiv:0705.4264.

[14] J. Goldstone, *Field theories with Superconductor solutions*, Il Nuovo Cimento (1955-1965) **19** (Jan, 1961).

[15] F. Englert and R. Brout, *Broken symmetry and the mass of gauge vector mesons*, Phys. Rev. Lett. **13** (1964) 321 - 323.

[16] G. Guralnik, C. Hagen, and T. Kibble, *Global conservation laws and massless particles*, Phys. Rev. Lett. **13** (1964) 585 - 587.

[17] M. Tanabashi *et al.* [Particle Data Group], Phys. Rev. **D 98**, 030001 (2018).

[18] S. Bethke, *Determination of the QCD Coupling $\alpha_S$*, J. Phys. G **26** (2000) R27.

[19] Planck Collaboration, P. Ade *et al.*, *Planck 2013 results. I. Overview of products and scientific results*, Astron. Astrophys. **571** (2014) A1.

[20] M. Klasen, M. Pohl, and G. Sigl, *Indirect and direct search for dark matter*, Prog. Part. Nucl. Phys. **85** (2015) 1 - 32.

[21] M. Gonzalez-Garcia and M. Maltoni, *Phenomenology with Massive Neutrinos*, Phys. Rept. **460** (2008) 1 - 129.

[22] P. Langacker, *Introduction to the Standard Model and Electroweak Physics*, arXiv:0901.0241.

[23] N. Arkani-Hamed, A. Cohen, E. Katz, and A. Nelson, *The Littlest Higgs*, JHEP **0207** (2002) 034.

[24] Z. Chacko, H.-S. Goh, and R. Harnik, *The Twin Higgs: Natural electroweak breaking from mirror symmetry*, Phys. Rev. Lett. **96** (2006) 231802.

[25] A. Salam and J. A. Strathdee, *Supersymmetry and Nonabelian Gauges*, Phys. Lett. **B 51** (1974) 353 - 355.

[26] L. Randall and R. Sundrum, *A Large mass hierarchy from a small extra dimension*, Phys. Rev. Lett. **83** (1999) 3370 - 3373.

[27] A. Djouadi, *The Anatomy of electro-weak symmetry breaking. II. The Higgs bosons in the minimal supersymmetric model*, Phys. Rept. **459** (2008) 1 - 241.

[28] G. Branco, P. Ferreira, L. Lavoura, M. Rebelo, M. Sher, *et al.*, *Theory and phenomenology of two-Higgs-doublet models*, Phys. Rept. **516** (2012) 1 - 102.

[29] A. Das and S. SenGupta, *Lightest Kaluza-Klein graviton mode in a back-reacted Randall-Sundrum scenario*, Eur. Phys. J. **C 76** (2016) no. 8, 423.

[30] ATLAS Collaboration, *Search for heavy ZZ resonances in the $l^+l^-l^+l^-$ and $l^+l^-\nu\bar{\nu}$ final states using proton-proton collisions at $\sqrt{s}$ = 13 TeV with the ATLAS detector*, Eur. Phys. J. **C 78** (2018) 293.

[31] Matthias Neubert, *Effective Field Theory and Heavy Quark Physics*, Lectures presented at TASI 2004, arXiv:hep-ph/0512222.

[32] A. Djouadi, *The Anatomy of electro-weak symmetry breaking. I: The Higgs boson in the standard model*, Phys. Rept. **457** (2008) 1 - 216.

[33] ATLAS and CMS Collaborations, *Combined Measurement of the Higgs Boson Mass in pp Collisions at $\sqrt{s}$ = 7 and 8 TeV with the ATLAS and CMS Experiments*, Phys. Rev. Lett. **114** (2015) 191803.

[34] ATLAS Collaboration, *Measurement of the Higgs boson mass in the $H \to ZZ^* \to 4\ell$ and $H \to \gamma\gamma$ channels with $\sqrt{s}$ = 13 TeV pp collisions using the ATLAS detector*, Phys. Lett. **B 784** (2018) 345.

[35] ATLAS Collaboration, *Measurements of Higgs boson production and couplings in diboson final states with the ATLAS detector at the LHC*, Phys. Lett. **B 726** (2013) 88.

[36] ATLAS Collaboration, *Evidence for the spin-0 nature of the Higgs boson using ATLAS data*, Phys. Lett. **B 726** (2013) 120.

[37] CMS Collaboration, *Study of the Mass and Spin-Parity of the Higgs Boson Candidate via its Decays to Z Boson Pairs*, Phys. Rev. Lett. **110** (2013) 081803.

[38] CMS Collaboration, *Measurement of the properties of a Higgs boson in the four-lepton final state*, Phys. Rev. **D 89** (2014) 092007.

[39] ATLAS Collaboration, *Combined measurements of Higgs boson production and decay using up to 80 fb$^{-1}$ of proton-proton collision data at $\sqrt{s}$ = 13 TeV collected with the ATLAS experiment*, submitted to Phys. Rev. D (2019), arXiv:1909.02845.

[40] ATLAS Collaboration, *Observation of $H \to b\bar{b}$ decays and $VH$ production with the ATLAS detector*, Phys. Lett. **B 786** (2018) 59.

[41] ATLAS Collaboration, *Observation of Higgs boson production in association with a top quark pair at the LHC with the ATLAS detector*, Phys. Lett. **B 785** (2018) 173.

[42] LHC Higgs Cross Section Working Group, S. Heinemeyer, C. Mariotti, G. Passarino and R. Tanaka (Eds.), *Handbook of LHC Higgs Cross Sections: 4. Deciphering the Nature of the Higgs Sector*, (2016), 1480.

[43] LHC Higgs Cross Section Working Group, *Handbook of LHC Higgs Cross Sections: 3. Higgs Properties*, CERN Report CERN-2013-004, 2013.

[44] CMS Collaboration, *Precise determination of the mass of the Higgs boson and tests of compatibility of its couplings with the standard model predictions using proton collisions at 7 and 8 TeV*, Eur. Phys. J. **C 75** (2015) 212.

[45] ATLAS Collaboration, *Measurement of the Higgs boson mass from the $H \to \gamma\gamma$ and $H \to ZZ^* \to 4l$ channels with the ATLAS detector using 25 fb$^{-1}$ of pp collision data*, Phys. Rev. **D 90** (2014) 052004.

[46] CMS Collaboration, *Measurements of properties of the Higgs boson decaying into the four-lepton final state in pp collisions at $\sqrt{s}$ = 13 TeV*, JHEP **11** (2017) 047.

[47] LHC Higgs Cross Section Working Group, *Handbook of LHC Higgs Cross Sections: 1. Inclusive Observables*, CERN Report CERN-2011-002, 2013.

[48] CMS Collaboration, *Limits on the Higgs boson lifetime and width from its decay to four charged leptons*, Phys. Rev. **D 92** (2015) 072010.

[49] N. Kauer and G. Passarino, *Inadequacy of zero-width approximation for a light Higgs boson signal*, JHEP **08** (2012) 116.

[50] N. Kauer, *Inadequacy of zero-width approximation for a light Higgs boson signal*, Mod. Phys. Lett. **A 28** (2013) 1330015.

[51] F. Caola and K. Melnikov, *Constraining the Higgs boson width with ZZ production at the LHC*, Phys. Rev. **D 88** (2013) 054024.

[52] J. M. Campbell, R. K. Ellis, and C. Williams, *Bounding the Higgs width at the LHC using full analytic results for $gg \to e^-e^+\mu^-\mu^+$*, JHEP **04** (2014) 060.

[53] C. Englert and M. Spannowsky, *Limitations and Opportunities of Off-Shell Coupling Measurements*, Phys. Rev. **D 90** (2014) 053003.

[54] G. Cacciapaglia, A. Deandrea, G. D. La Rochelle, and J.-B. Flament, *Higgs couplings: disentangling New Physics with off-shell measurements*, Phys. Rev. Lett. **113** (2014) 201802.

[55] A. Azatov, C. Grojean, A. Paul, and E. Salvioni, *Taming the off-shell Higgs boson*, JETP **147(3)** (2015).

[56] M. Ghezzi, G. Passarino, and S. Uccirati, *Bounding the Higgs Width Using Effective Field Theory*, Proceedings of Science PoS **LL2014 072** (2014).

[57] C. Englert, Y. Soreq and M. Spannowsky, *Off-Shell Higgs Coupling Measurements in BSM scenarios*, (2014) arXiv:1410.5440.

[58] H. E. Logan, *Hiding a Higgs width enhancement from off-shell gg ($\to h^*$) $\to ZZ$ measurements*, Phys. Rev. **D 92**, 075038 (2015).

[59] J. M. Campbell, R. K. Ellis, and C. Williams, *Bounding the Higgs width at the LHC: complementary results from $H \to WW$*, Phys. Rev. **D 89** (2014) 053011.

[60] CMS Collaboration, *Constraints on the Higgs boson width from off-shell production and decay to Z-boson pairs*, Phys. Lett. **B 736** (2014) 64.

[61] ATLAS Collaboration, *Constraints on the off-shell Higgs boson signal strength in the high-mass ZZ and WW final states with the ATLAS detector*, Eur. Phys. J. **C 75** (2015) 335.

[62] CMS Collaboration, *Measurements of the Higgs boson width and anomalous $HVV$ couplings from on-shell and off-shell production in the four-lepton final state*, Phys. Rev. **D 99** (2019) 112003.

[63] ATLAS Collaboration, *Constraints on off-shell Higgs boson production and the Higgs boson total width in $ZZ \to 4\ell$ and $ZZ \to 2\ell 2\nu$ final states with the ATLAS detector*, Phys. Lett. **B 786** (2018) 223.

[64] R. Gauld, J. Rojo, L. Rottoli, and J. Talbert, J. High Energy Phys. 11 (2015) 009 ; P. Lipari, Astropart. Phys. **1**, 195 (1993); L. Pasquali, M. Reno, and I. Sarcevic, Phys. Rev. D **59**, 034020 (1999); R. Enberg, M.H. Reno, and I. Sarcevic, Phys. Rev. D **78**, 043005 (2008); P. Gondolo, G. Ingelman, and M. Thunman, Astropart. Phys. **5**, 309 (1996); A.M. Martin, M.G. Ryskin, and A.M Stasto, Acta Phys. Polon. B**34**, 3273 (2003); M.V. Garzelli, S. Moch, and S. Sigl, J. High Energy Phys. 10 (2015) 115; G. Gelmini, P. Gondolo, and G. Varieschi, Phys. Rev. D **61**, 036005 (2000).

[65] ALICE Collaboration, *Measurement of charm production at central rapidity in proton-proton collisions at $\sqrt{s}$ = 2.76 TeV*, JHEP **07** (2012) 191.

[66] LHCb Collaboration, *Prompt charm production in pp collisions at $\sqrt{s}$ = 7 TeV*, Nucl. Phys. **B 871** (2013) 20.

[67] LHCb Collaboration, *Measurements of prompt charm production cross-sections in pp collisions at* $\sqrt{s}$ *= 13 TeV*, JHEP **1603** (2016) 159.

[68] ALICE Collaboration, *D-meson production in proton-proton collisions with ALICE at the LHC*, Nuclear and Particle Physics **Proceedings** 294296 (2018) 32-36.

[69] ALICE Collaboration, *Open-charm measurements in pp and Pb-Pb collisions at central rapidity with ALICE*, ALICE PRC 94 (2016) 054908.

[70] CDF Collaboration, CDF Note 5859, (2002).

[71] CDF Collaboration, *Measurement of the* $B^+$ *total cross section and* $B^+$ *differential cross section* $d\sigma/dp_T$ *in* $p\bar{p}$ *collisions at* $\sqrt{s}$ *= 1.8 TeV.*, Phys. Rev. **D 65**, 052005 (2002).

[72] B.A. Kniehl, G. Kramer, I. Schienbein, and H. Spiesberger, *Hadroproduction of D and B mesons in a massive VFNS*, AIP Conf. Proc. 792, (2005) 867.

[73] B.A. Kniehl, G. Kramer, I. Schienbein and H. Spiesberger, *Reconciling Open-Charm Production at the Fermilab Tevatron with QCD*, Phys. Rev. Lett. **96** (2006) 012001.

[74] CDF Collaboration, *Measurement of Prompt Charm Meson Production Cross Sections in* $p\bar{p}$ *Collisions at* $\sqrt{s}$ *= 1.96 TeV*, Phys. Rev. Lett. **91** (2003) 241804.

[75] CDF Collaboration, *Measurement of the* $D^+$*-meson production cross section at low transverse momentum in* $p\bar{p}$ *collisions at* $\sqrt{s}$ *= 1.96 TeV*, Phys. Rev. **D 95**, 092006 (2017).

[76] O. S. Bru ning, P. Collier, P. Lebrun, S. Myers, R. Ostojic, J. Poole, and P. Proudlock, *LHC Design Report*, CERN Yellow Reports: Monographs. CERN-2004-003 (2004).

[77] ATLAS Collaboration, *The ATLAS Experiment at the CERN Large Hadron Collider*, JINST **3** (2008) S08003.

[78] ATLAS Collaboration, *ATLAS Insertable B-Layer Technical Design Report*, ATLAS-TDR-19, (2010) and *ATLAS Insertable B-Layer Technical Design Report Addendum*, ATLAS-TDR-19-ADD-1 (2012).

[79] CERN, *The CERN accelerator complex - Complexe des acclrateurs du CERN*, OPEN-PHO-ACCEL-2016-013 (2016).

[80] S. van der Meer,*Calibration of the effective beam height in the ISR*, CERN-ISR-PO-68-31. ISR-PO-68-31, CERN (1968).

[81] F. Meloni on behalf of the ATLAS Collaboration, *Primary vertex reconstruction with the ATLAS detector*, ATL-PHYS-PROC-2016-163 (2016).

[82] ATLAS Collaboration, *Performance of pile-up mitigation techniques for jets in pp collisions at* $\sqrt{s}$ *= 8 TeV*, Eur. Phys. J. **C 76** (2016) no. 11, 581.

[83] ATLAS Collaboration, *Luminosity Public Results Run 2*, URL: https://twiki.cern.ch/twiki/bin/view/AtlasPublic/LuminosityPublicResultsRun2

[84] M. Schott and M. Dunford, *Review of single vector boson production in pp collisions at* $\sqrt{s}$ *= 7 TeV*, Eur. Phys. J. C (2014) 74:2916.

[85] J. Pequenao, *Computer generated image of the whole ATLAS detector*, CERN-GE-0803012 (2008) URL: https://cds.cern.ch/record/1095924.

[86] ATLAS Collaboration, *ATLAS inner detector: Technical design report. Vol. 1 and Vol. 2*, CERN-LHCC-97-16, ATLAS-TDR-4 and CERN-LHCC-97-17 (1997).

[87] ATLAS Collaboration, *ATLAS pixel detector : Technical Design Report*, CERN-LHCC-98-013; ATLAS-TDR-11(1998).

[88] Ahmad, A. *et al.*, *The Silicon microstrip sensors of the ATLAS semiconductor tracker*, Nucl. Instrum. Meth. **A 578** (2007) 98 - 118.

[89] E. Hines on behalf of the ATLAS Collaboration, *Performance of Particle Identification with the ATLAS Transition Radiation Tracker*, Proceedings for the Meeting of the Division of Particles and Fields of the American Physical Society (DPF) 2011, arXiv:1109.5925.

[90] C. W. Fabjan and F. Gianotti, *Calorimetry for particle physics*, Rev. Mod. Phys. **75** (2003) 1243 - 1286.

[91] N. Nikiforou on behalf of the ATLAS Collaboration, *Performance of the ATLAS Liquid Argon Calorimeter after three years of LHC operation and plans for a future upgrade*, Proceedings for the 3rd International Conference on Advancements in Nuclear Instrumentation Measurement Methods and their Applications (ANIMMA 2013) 2013, arXiv:1306.6756.

[92] J. Pequenao, *Computer generated image of the ATLAS calorimeter*, CERN-GE-0803015 (2008) URL: https://cds.cern.ch/record/1095927.

[93] R. M. Brown, D. J. A. Cockerill, *Electromagnetic calorimetry*, NIMA 666 (2012) 4779.

[94] Z. Meng on behalf of the ATLAS LAr Collaboration, *Performance of the ATLAS liquid argon calorimeter*, Proceedings for the 5th International Conference PLHC2010, in Physics at the LHC2010 pp. 406 - 408 (2010).

[95] B. Sotto-Maior Peralva on behalf of the ATLAS Collaboration, *Calibration and Performance of the ATLAS Tile Calorimeter*, Proceeding for the International School on High Energy Physics : Workshop on High Energy Physics in the near Future (LISHEP 2013) pp. 17 - 24 (2013).

[96] ATLAS Collaboration, *ATLAS muon spectrometer: Technical Design Report*, CERN-LHCC-97-22, ATLAS-TDR-10 (1997).

[97] J. Pequenao, *Computer generated image of the ATLAS Muon subsystem*, CERN-GE-0803017 (2008) URL: https://cds.cern.ch/record/1095929.

[98] ATLAS Collaboration, *Monitored Drift Tubes Chambers for Muon Spectroscopy in ATLAS*, ATL-MUON-94-044. ATL-M-PN-44 (1994).

[99] T. Argyropoulos, K. A. Assamagan, B. H. Benedict, V. Chernyatin, E. Cheu, J. Deng, A. Gordeev, I. G. Eschrich, V. Grachev, K. Johns, S. Junnarkar, A. Kandasamy, V. Kaushik, A. Khodinov, A. Lankford, X. Lei, R. M. Garcia, K. Nikolopoulos, P. OConnor, C. L. Parnell-Lampen, W. Park, V. Polychronakos, R. Porter, M. Purohit, M. Schernau, B. K. Toggerson, and D.

Tompkins, *Cathode strip chambers in ATLAS : Installation, commissioning and in situ performance*, in 2008 IEEE Nuclear Science Symposium Conference Record, pp. 2819 - 2824 (2008).

[100] G. Cattani, on behalf of the ATLAS RPC group, *The Resistive Plate Chambers of the ATLAS experiment: performance studies*, Journal of Physics: Conference Series **280** (2011) no. 1, 012001.

[101] K. Nagai, on behalf of the ATLAS Collaboration , *Thin gap chambers in ATLAS*, Nuclear Instruments and Methods in Physics Research Section A: Accelerators, Spectrometers, Detectors and Associated Equipment **384** (1996) no. 1, 219 - 221.

[102] ATLAS Collaboration, *Letter of Intent for the Phase-I Upgrade of the ATLAS Experiment*, CERN-LHCC-2011-012. LHCC-I-020 (2011).

[103] ATLAS Collaboration, *Technical Design Report for the Phase-I Upgrade of the ATLAS TDAQ System*, CERN-LHCC-2013-018. ATLAS-TDR-023 (2013).

[104] W. Lampl, S. Laplace, D. Lelas, P. Loch, H. Ma, S. Menke, S. Rajagopalan, D. Rousseau, S. Snyder, and G. Unal, *Calorimeter Clustering Algorithms: Description and Performance*, ATL-LARG-PUB-2008-002. ATL-COM-LARG-2008-003 (2008).

[105] A. Sidoti, *Minimum Bias Trigger Scintillators in ATLAS Run II*, Journal of Instrumentation **9** (2014) no. 10, C10020.

[106] A. Buckley, T. Eifert, M. Elsing, D. Gillberg, K. Koeneke, A. Krasznahorkay, E. Moyse, M. Nowak, S. Snyder, and P. van Gemmeren, *Implementation of the ATLAS Run 2 event data model*, Journal of Physics: Conference Series **664** (2015) no. 7, 072045.

[107] ATLAS Collaboration, *ATLAS computing: Technical design report*, CERN-LHCC-2005-022, ATLAS-TRD-017.

[108] R. Brun *et al.*, *GEANT: Simulation Program For Particle Physics Experiments. User Guide and Reference Manual*, CERN-DD-78-2-REV, CERN-DD-78-2 (1978).

[109] ATLAS Collaboration, *The ATLAS simulation Infrastructure*, Eur. Phys. J. **C 70** (2010) 823.

[110] S. Agostinelli *et al.*, *GEANT4, a simulation toolkit*, Nucl. Instrum. Meth. **A 506** (2003) 250.

[111] S. Alioli, P. Nason, C. Oleari and E. Re, *NLO Higgs boson production via gluon fusion matched with shower in POWHEG*, JHEP **04** (2009) 002.

[112] P. Nason and C. Oleari, *NLO Higgs boson production via vector-boson fusion matched with shower in POWHEG*, JHEP **02** (2010) 037.

[113] T. Gleisberg *et al.*, *Event generation with SHERPA 1.1*, JHEP **02** (2009) 007.

[114] F. Cascioli, P. Maierhfer and S. Pozzorini, *Scattering Amplitudes with Open Loops*, Phys. Rev. Lett. **108** (2012) 111601.

[115] A. Denner, S. Dittmaier and L. Hofer, *COLLIER - A fortran-library for one-loop integrals*, Proceedings of Science PoS **LL2014** (2014) 071.

[116] F. Cascioli *et al.*, *Precise Higgs-background predictions: merging NLO QCD and squared quark-loop corrections to four-lepton + 0,1 jet production*, JHEP **01** (2014) 046.

[117] A. D. Martin, W. J. Stirling, R. S. Thorne and G. Watt, *Parton distributions for the LHC*, Eur. Phys. J. **C 63** (2009) 189.

[118] L. A. Harland-Lang, A. D. Martin, P. Motylinski and R. S. Thorne, *Parton distributions in the LHC era: MMHT 2014 PDFs*, Eur. Phys. J. **C 75** (2015) 204.

[119] R. D. Ball *et al.*, *Parton distributions for the LHC Run II*, JHEP **04** (2015) 040.

[120] S. Schumann and F. Krauss, *A Parton shower algorithm based on Catani-Seymour dipole factorisation*, JHEP **03** (2008) 038.

[121] J. Alwall et al., *The automated computation of tree-level and next-to-leading order differential cross sections, and their matching to parton shower simulations*, JHEP **07** (2014) 079.

[122] J. Gao *et al.*, *CT10 next-to-next-to-leading order global analysis of QCD*, Phys. Rev. **D 89** (2014) 033009.

[123] T. Sjstrand, S. Mrenna and P. Z. Skands, *A brief introduction to PYTHIA 8.1*, Comput. Phys. Commun. **178** (2008) 852.

[124] T. Sjostrand, S. Mrenna and P. Z. Skands, *PYTHIA 6.4 physics and manual*, JHEP **05** (2006) 026.

[125] ATLAS Collaboration, *Summary of ATLAS Pythia 8 tunes, ATL-PHYS-PUB-2012-003* (2012).

[126] D. J. Lange, *The EvtGen particle decay simulation package* Nucl. Instrum. Meth. **A 462** (2001) 152.

[127] ATLAS Collaboration, *Vertex Reconstruction Performance of the ATLAS Detector at $\sqrt{s}$ = 13 TeV*, ATL-PHYS-PUB-2015-026 (2015).

[128] S. Marti-Garcia on behalf of the ATLAS Collaboration, *Alignment of the ATLAS Inner Detector*, ATL-PHYS-SLIDE-2016-882 (2016).

[129] ATLAS Collaboration, *ATLAS Inner Detector Alignment Performance with February 2015 Cosmic Ray Data*, ATL-PHYS-PUB-2015-009 (2015).

[130] ATLAS Collaboration, *Electron efficiency measurements with the ATLAS detector using the 2015 LHC protonproton collision data*, ATLAS-CONF-2016-024 (2016).

[131] ATLAS Collaboration, *Electron and photon reconstruction and performance in ATLAS using a dynamical, topological cell clustering-based approach*, ATL-PHYS-PUB-2017-022 (2017).

[132] ATLAS Collaboration, *Electron reconstruction and identification in the ATLAS experiment using the 2015 and 2016 LHC proton-proton collision data at $\sqrt{s}$ = 13 TeV*, Eur. Phys. J. **C 79** (2019) 639.

[133] ATLAS Collaboration, *Muon reconstruction performance of the ATLAS detector in protonproton collision data at $\sqrt{s}$ = 13 TeV*, Eur. Phys. J. **C 76** (2016) no. 5, 292.

[134] ATLAS Collaboration, *Validation of the muon momentum corrections for the ATLAS simulation using the $Y \to \mu\mu$ channel based on 36.5 $fb^{-1}$ collision data collected in 2015 and 2016*, ATL-PHYS-PUB-2019-018 (2019).

[135] ATLAS Collaboration, *Public Muon Spectrometer Plots for Collision Data*, https://twiki.cern.ch/twiki/bin/view/AtlasPublic/MuonPerformancePublicPlots.

[136] ATLAS Collaboration, *Performance of the ATLAS Trigger System in 2010*, Eur. Phys. J. **C 72** (2012) 1849.

[137] M. Oreglia, *A Study of the Reactions $\psi' \to \gamma\gamma\psi$* , SLAC-R-0236 (1980).

[138] ATLAS Collaboration, *Measurement of the muon reconstruction performance of the ATLAS detector using 2011 and 2012 LHC proton-proton collision data*, Eur. Phys. J. **C 74** (2014) 3130.

[139] M. Cacciari, G. P. Salam and G. Soyez, *The anti-$k_t$ jet clustering algorithm*, JHEP **04** (2008) 063.

[140] M. Cacciari, G. P. Salam and G. Soyez, *FastJet User Manual*, Eur. Phys. J. C **72** (2012) 1896.

[141] ATLAS Collaboration, *Jet energy scale measurements and their systematic uncertainties in proton-proton collisions at $\sqrt{s}$ = 13 TeV with the ATLAS detector*, Phys. Rev. **D 96** (2017) no. 7, 072002.

[142] ATLAS Collaboration, *Tagging and suppression of pileup jets with the ATLAS detector*, ATLAS-CONF-2014-018 (2014).

[143] ATLAS Collaboration, *Selection of jets produced in 13TeV proton-proton collisions with the ATLAS detector*, ATLAS-CONF-2015-029 (2015).

[144] ATLAS Collaboration, *Characterisation and mitigation of beam-induced backgrounds observed in the ATLAS detector during the 2011 proton-proton run*, JINST **8** (2013) P07004.

[145] ATLAS Collaboration, *Jet energy resolution in proton-proton collisions at $\sqrt{s}$ = 7 TeV recorded in 2010 with the ATLAS detector*, Eur. Phys. J. **C 73** no. 3, (2013) 2306.

[146] ATLAS Collaboration, *Performance of b-Jet Identification in the ATLAS Experiment*, JINST **11** (2016) no. 04, P04008.

[147] ATLAS Collaboration, *Performance of b-Jet identification in the ATLAS experiment*, JINST **11** (2016) P04008.

[148] ATLAS Collaboration, *Optimisation of the ATLAS b-tagging performance for the 2016 LHC Run*, ATL-PHYS-PUB-2016-012 (2016).

[149] A. Policicchio on behalf of the ATLAS Collaboration, *BSM searches in ATLAS*, ATL-PHYS-PROC-2015-010 (2015).

[150] ATLAS Collaboration, *Performance of missing transverse momentum reconstruction with the ATLAS detector using proton-proton collisions at* $\sqrt{s}$ *= 13 TeV*, Eur. Phys. J. **C 78** (2018) 903.

[151] G. Passarino, *Higgs CAT*, Eur. Phys. J. **C 74** (2014) 2866.

[152] ATLAS Collaboration, *Combination of Searches for Invisible Higgs Boson Decays with the ATLAS Experiment*, Phys. Rev. Lett. **122** (2019) 231801.

[153] F. Caola, K. Melnikov, R. R ontsch and L. Tancredi, *QCD corrections to ZZ production in gluon fusion at the LHC*, Phys. Rev. **D 92** (2015) 18.

[154] F. Caola, M. Dowling, K. Melnikov, R. Rontsch and L. Tancredi, *QCD corrections to vector boson pair production in gluon fusion including interference effects with off-shell Higgs at the LHC*, JHEP **087** (2016) 23.

[155] J. M. Campbell and R. K. Ellis *Higgs Constraints from Vector Boson Fusion and Scattering*, JHEP **04** (2015) 030.

[156] LHC Higgs Cross Section Working Group, *Handbook of LHC Higgs Cross Sections: 2. Differential distributions*, CERN Report CERN-2012-002, 2012.

[157] ATLAS Collaboration, *High Mass Offshell HNNLO 13TeV*, URL: https://twiki.cern.ch/twiki/bin/view/LHCPhysics/HighMassOffshellHNNLOv213TeV.

[158] F. Caola, K. Melnikov, R. Rontsch and L. Tancredi, *QCD corrections to ZZ production in gluon fusion at the LHC*, Phys. Rev. **D 92** (2015) 18.

[159] F. Caola, M. Dowling, K. Melnikov, R. Rontsch and L. Tancredi, *QCD corrections to vector boson pair production in gluon fusion including interference effects with off-shell Higgs at the LHC*, JHEP **087** (2016) 23.

[160] T. Gleisberg and S. Höche, *Comix, a new matrix element generator*, JHEP **12** (2008) 039.

[161] B. Biedermann, A. Denner, S. Dittmaier, L. Hofer and B. Jger, *Electroweak corrections to* $pp \to \mu^+\mu^- e^+ e^- + X$ *at the LHC: a H. Johann H. Khniggs background study*, Phys. Rev. Lett. **116** (2016) 161803.

[162] B. Biedermann, A. Denner, S. Dittmaier, L. Hofer and B. Jager, *Next-to-leading-order electroweak corrections to the production of four charged leptons at the LHC*, JHEP **01** (2017) 033.

[163] S. Gieseke, T. Kasprzik and J. H. Khn, *Vector-boson pair production and elctroweak correction in HERWIG++*, Eur. Phys. J. **C 74** (2018) no. 8, 2988.

[164] J. Meyer and T. Kasprzik, *Reweighting method to incorporate higher order electroweak corrections into resonant heavy gauge boson pair production predictions*, ATL-COM-PHYS-2014-152 (2014).

[165] P. Nason and G. Zanderighi, $W^+W^-, WZ$*and* $ZZ$ *production in the POWHEG-BOX-V2*, Eur. Phys. J. C **74** (2014) 2702.

[166] H.-L. Lai *et al.*, *New parton distributions for collider physics*, Phys. Rev. **D 82** (2010) 074024.

[167] ATLAS Collaboration, *Measurement of the* $Z/\gamma$ *boson transverse momentum distribution in pp collisions at* $\sqrt{s} = 7$ *TeV with the ATLAS detector*, JHEP **09** (2014) 145.

[168] R. Gavin, Y. Li, F. Petriello and S. Quackenbush, *FEWZ 2.0: A code for hadronic Z production at next-to-next-to-leading order*, Comput. Phys. Commun. **182** (2011) 2388.

[169] P. Z. Skands, *Tuning Monte Carlo Generators: The Perugia Tunes*, Phys. Rev. **D 82** (2010) 074018.

[170] M. Aaboud *et al.*, *Measurement of inclusive and differential cross sections in the $H \to ZZ^* \to 4l$ decay channel in pp collisions at $\sqrt{s}$ = 13 TeV with the ATLAS detector*, JHEP **10**, (2017) 132.

[171] ATLAS Egamma Combined Performance Group, *Electron Identification*, URL: https://twiki.cern.ch/twiki/bin/view/AtlasProtected/EGammaIdentificationRun2#Electron_identification.

[172] ATLAS Muon Combined Performance Group, *MCPAnalysisGuidelinesMC15*, URL: https://twiki.cern.ch/twiki/bin/viewauth/AtlasProtected/MCPAnalysisGuidelinesMC15.

[173] ATLAS Collaboration, *Properties of Jets and Inputs to Jet Reconstruction and Calibration with the ATLAS Detector Using Proton-Proton collisions at $\sqrt{s}$ = 13 TeV*, ATL-PHYS-PUB-2015-036 (2015).

[174] ATLAS Collaboration, *Tagging and suppression of pileup jets with the ATLAS detector*, ATLAS-CONF-2014-018 (2014).

[175] ATLAS JetEtMiss Performance Group, *Usage of Jets in analyses: rebuilding and systematics*, URL: https://twiki.cern.ch/twiki/bin/view/AtlasProtected/%20JetEtmissRecommendations2016.

[176] ATLAS Collaboration, *Selection of jets produced in 13 TeV proton-proton collisions with the ATLAS detector*, ATLAS-CONF-2015-029 (2015).

[177] ATLAS JetEtMiss Performance Group, *Usage of Missing Etmiss in analyses: rebuilding and systematics*, URL: https://twiki.cern.ch/twiki/bin/view/AtlasProtected/METUtilities.

[178] ATLAS Collaboration, *Study of $\ell\ell$ + MET final state in HZZ group with proton-proton collisions at $\sqrt{s}$ = 13 TeV: objects definition and background estimation*, ATL-COM-PHYS-2015-1275 (2015).

[179] ATLAS Collaboration, *Luminosity determination in pp collisions at $\sqrt{s}$ = 8 TeV using the ATLAS detector at the LHC*, Eur. Phys. J. **C 76** (2016) 653.

[180] ATLAS Collaboration, *Measurement of the Inelastic ProtonProton Cross Section at $\sqrt{s}$ = 13 TeV with the ATLAS detector at the LHC*, Phys. Rev. Lett. **117** (2016) 182002.

[181] ATLAS Egamma Combined Performance Group, *Electron recommendations*, URL: https://twiki.cern.ch/twiki/bin/view/AtlasProtected/LatestRecommendationsElectronIDRun2.

[182] ATLAS Collaboration, *Electron efficiency measurements with the ATLAS detector using the 2015 LHC proton-proton collision data*, ATLAS-CONF-2016-024 (2016).

[183] ATLAS Muon Combined Performance Group, *Muon recommendations*, URL: https://twiki.cern.ch/twiki/bin/view/AtlasProtected/%20MCPAnalysisGuidelinesMC15#MCP_recommendations..

[184] ATLAS Collaboration, *Measurement of the Higgs boson mass in the $H \to ZZ^* \to 4\ell$ and $H \to \gamma\gamma$ channels with $\sqrt{s}$ = 13 TeV pp collisions using the ATLAS detector*, ATLAS-CONF-2017-046 (2017).

[185] ATLAS Collaboration, *Muon reconstruction performance of the ATLAS detector in proton-proton collision data at $\sqrt{s}$ = 13 TeV*, Eur. Phys. J. **C 76** (2016) 292.

[186] ATLAS Collaboration, *Jet energy scale measurements and their systematic uncertainties in proton-proton collisions at $\sqrt{s}$ = 13 TeV with the ATLAS detector*, Phys. Rev. **D 96** (2017) 072002.

[187] ATLAS JetEtMiss Performance Group, *Usage of Etmiss in analyses: rebuilding and systematics*, URL: https://twiki.cern.ch/twiki/bin/viewauth/AtlasProtected/%20EtmissRecommendationsRel20p7.

[188] ATLAS Collaboration, *Expected performance of missing transverse momentum reconstruction for the ATLAS detector at $\sqrt{s}$ = 13 TeV*, ATL-PHYS-PUB-2015-023 (2015).

[189] ATLAS Collaboration, *Optimisation of the ATLAS b-tagging performance for the 2016 LHC Run*, ATL-PHYS-PUB-2016-012 (2016).

[190] G. Cowan, K. Cranmer, E. Gross and O. Vitells, *Asymptotic formulae for likelihood-based tests of new physics*, Eur. Phys. J. **C 71** (2011) 1554.

[191] G. Cowan, *Statistical Data Analysis*, Oxford science publications. Clarendon Press, (1998).

[192] A. L. Read, *Presentation of search results: The CL(s) technique*, J. Phys. **G 28** (2002) 2693 - 2704.

[193] ATLAS Collaboration, *Measurement of the Higgs boson coupling properties in the $H \to ZZ^* \to 4\ell$ decay channel at $\sqrt{s}$ = 13 TeV with the ATLAS detector*, JHEP **03** (2018) 095.

[194] W. Verkerke and D. P. Kirkby, *The RooFit toolkit for data modeling*, eConf **C0303241** (2003), MOLT007.

[195] L. Moneta, K. Belasco, K. S. Cranmer, S. Kreiss, A. Lazzaro, D. Piparo, G. Schott, W. Verkerke and M. Wolf, *The RooStats Project*, Proceedings of Science PoS **ACAT2010** (2010) 057.

[196] R. Barbieri, A. Pomarol, R. Rattazzi and A. Strumia, *Electroweak symmetry breaking after LEP1 and LEP2*, Nucl. Phys. B **703** (2004) 127.

[197] M. Gillioz, R. Grober, C. Grojean, M. Muhlleitner and E. Salvioni, *Higgs Low-Energy Theorem (and its corrections) in Composite Models*, CERN-PH-TH/2012-176; KA-TP-26-2012; SFB/CPP-12-43; ZU-TH 09/12; LPN12-062 (2012).

[198] C. Grojean, E. Salvioni, M. Schlaffer and A. Weiler, *Very boosted Higgs in gluon fusion*, JHEP **1405** (2014) 022.

[199] ATLAS Collaboration, *ATLAS Higgs to ZZ Workshop at Oxford* https://indico.cern.ch/event/710733/ Oxford, April 2018.

[200] ATLAS Collaboration, *Off-shell Higgs boson couplings measurements using $H \to ZZ \to 4\ell$ events at High Luminosity LHC*, ATL-PHYS-PUB-2015-024 (2015).

[201] ATLAS Collaboration, *Technical Design Report for the ATLAS Inner Tracker Strip Detector*, Tech. Rep. CERN-LHCC-2017-005. ATLAS-TDR-025, CERN, 2017.

[202] ATLAS Collaboration, *Technical Design Report for the ATLAS Inner Tracker Pixel Detector*, Tech. Rep. CERN-LHCC-2017-021. ATLAS-TDR-030, CERN, 2018.

[203] LCC Physics Working Group, *Physics case for the 250 GeV Stage of the International Linear Collider*, DESY-17-155, KEK Preprint 2017-31, LAL 17-059, SLAC-PUB-17161 (2017).

[204] R. Contino *et al.*, *Physics at a 100 TeV pp collider: Higgs and EW symmetry breaking studies*, CERN Yellow Rep. (2017) no.3, 255-440, CERN-TH-2016-113.

[205] P. Giacomelli, *The Higgs boson at the FCC*, talk at ICHEP2018 (2018) URL: https://indico.cern.ch/event/686555/contributions/2971566/attachments/1682031/2703684/HiggsmeasurementsFCCICHEP2018_169.pdf.

[206] Theoretical predictions are from the calculations at next-to-leading order in the strong-interaction coupling and next-to-leading threshold logarithm by M. Cacciari and P. Nason, J. High Energy Phys. **09** (2003) 006 and updates at http://www.lpthe.jussieu.fr/ cacciari/fonll/fonllform.html.

[207] CDF Collaboration, *The CDF II Detector: Technical Design Report*, FERMILAB-Pub-96/390-E (1996).

[208] CDF Collaboration, *A first look at the CLC Luminosity measurements*, CDF note 6052, (2002).

[209] S. Klimenko, J. Konigsberg and T. Liss, *Averaging of the inelastic cross-section measured by the CDF and the E811 experiments*, CDF Note 6314, (2003).

[210] CDF Collaboration, CDF Note 6165, (2003).

[211] CDF Collaboration, CDF Note 9509, (2008).

[212] CDF Collaboration, *Description of Bgenerator II*, CDF Note 5092, (1999).

[213] P. A. Movilla Fernandez, *Performance of the CDF calorimeter simulation in Tevatron Run II*, AIP Conf. Proc., vol. 867, pp. 487 - 494, (2006).

[214] R. Veenhof, *Garfield, a drift chamber simulation program*, International Conference on Programming and Mathematical Methods for Solving Physical Problems, Dubna, Russia, 14 - 19 Jun (1993).

[215] CDF Collaboration, *Measurement of the Track Reconstruction Efficiency in the COT Using a MC Track Embedding Technique* CDF Note 6394 (2003).

[216] CDF Collaboration, CDF Note 6314 (2003).

[217] CDF Collaboration, CDF Note 5861 (2003).

[218] CDF Collaboration, CDF Note 6054 (2003).

[219] CDF Collaboration, CDF Note 8594 (2003).

[220] N. Kauer *Interference effects for $H \to WW/ZZ \to l\nu l\nu$ searches in gluon fusion at the LHC*, JHEP **12** (2013) 082.

[221] ATLAS Collaboration, *Study of higher-order QCD corrections in the $gg \to H \to VV$ process*, tech.rep. ATL-PHYS-PUB-2016-006, CERN (2016).

[222] S. Carrazza, S. Forte, Z. Kassabov, J. I. Latorre and J. Rojo, *An unbiased Hessian representation for Monte Carlo PDFs*, Eur. Phys. J. **C 75** (2015) 369.

[223] http://www.fermimontesarchio.gov.it/dalla-particella-di-dio-al-battito-delluniverso/.

[224] http://www.fermimontesarchio.gov.it/seminario-di-formazione-sulla-fisica-moderna/.

[225] http://www.ilcaudino.it/cervinara-dalla-particella-di-dio-al-battito-delluniverso-dibattito-culturale/.

[226] https://allevents.in/oxfordshire/st-catz-mcr-colloquia-monumental-physics-with-luigi-marchese/330542130694562.

[227] http://movingknowledge.physics.ox.ac.uk.

[228] http://oxfordsummerprogram.physics.ox.ac.uk/ConnectingKnowledge.html.

[229] http://oxfordsummerprogram.physics.ox.ac.uk/MovingKnowledge.html.

[230] http://oxfordsummerprogram.physics.ox.ac.uk.